Bioorthogonal nanomaterials to probe adhesive protein function

Laura Elizabeth Wilkins

A thesis submitted in fulfilment of the requirements for the degree of
Doctor of Philosophy

Department of Chemistry, University of Warwick.

September 2018

Table of Contents

Acknowledgements

First and foremost I would like to thank my supervisors Professor Matthew Gibson and Dr Nick Waterfield. I've been fortunate enough to work with Matt in some capacity since the third year of my MChem degree, and he has always provided me with his time and the relentless optimism that is required often in the academic sphere. Even when he has an infinite list of things to take care of, he always seems to find the energy to help his group members. Nick, with whom I have been unfortunate in working less closely, has helped many times in instilling me with the confidence and excitement of working on the *Photorhabdus* project and at the Gibbet Hill Campus (which can be unnerving for a chemist!) I would also like to thank the Leverhulme trust for making my PhD, and the PVC project, possible.

I would also like to thank those who have made my work possible in the Department of Chemistry. Marc Walker whose expertise in XPS is boundless. The TEM team, especially Houari Amari, have been part of the reason I found TEM to be the most interesting and rewarding type of analysis. I'd like to thank Dr Ivan Prokes, Dr Lijiang Song, Mr Philip Aston, Dr Dan Lester for their training and help in NMR, MS, ICP and GPC. Thanks also to Dan and David Hammond for their help with and the tricky upkeep of the TGA machines.

Up at the Gibbet hill campus, Dr Muhammad Hasan has had endless patience in setting up our new lab, as well as training all of us chemists, and still managing to do his own work! The Proteomics RTP team, Cleidi Zampronio and Juan Hernandez-Fernaud, have been wonderful. The Waterfield group – especially Joe Healey, Alexia Hapeshi and Max Addison – have been great in our PVC project collaboration, and as colleagues in the lab. Joe especially has been my life sciences counterpart, and accordingly has been a massive help in everything PVC. Thank you to everyone else up in life sciences – Blessing Anonye, Ian Hands-Portman, Pratik Gurnani, Andy Lunn to name a few.

The Gibson group has been wonderful both in and out of work. Henry for your sarcastic, but heartfelt, help in pretty much everything for the last 4 years. Trisha Bailey, queen of the Gibson group bat cave, has been excellent in looking after everything in the cell lab and helping everyone else at the same time. Chris Stubbs for everything PVA, and for that inevitable fast food fix after a conference social. Alice Fayter for her x-ray and ice-shaping assay expertise, as well as providing a much-needed shoulder to whinge on (/to) many a day. Dr Caroline Biggs for everything SPLAT. Dr Sarah-Jane Richards for her gold nanoparticle wizardry. Drs Antonio Laezza and Collette Guy for all their synthetic advice. And generally thank you to everyone else in the Gibson group for both helping with science and with putting a fresh, fun perspective on working in academia - Ben Graham, Marie Grypioti, Julia Lipecki, Ben Martyn and everyone else who has been a part of our lab, even if briefly.

Thank you also to those in the Chemistry department who I've had the pleasure of working with in a teaching or other capacity. To my advisory board, Professor Tim Bugg and Dr Manuela Tosin, for your excellent advice. Dr Nick Barker for his incredibly inspirational, infectious dedication to outreach work. Dr Russ Kitson, Dr Gerard Willey as well as the other academics, technicians and the UG/PG students I had the pleasure of teaching, for making the experience really fun and educational. I plan on taking forward everything I've learnt in my PhD to teaching in the future! Thank you to those in the MAS department, Dr Nikola Chemel, Dr Claudia Blindauer, Naomi Grew, my MAS MSc coursemates and all the others for your support on the MSc programme and in my PhD programme as well.

Claire, Becky, Seb for our pre-work exercise routine motivation. Claire especially for making me get away from my desk or fumehood and relax when required! I'd also like to thank the other physicists – Andrew, Kerrie, John, Harry, Tim, Lauren, Annie, Alex – for providing much needed fun at regular intervals. To my other friends, in the Chamber Choir, from Japanese Classes (Yasmin!) from my MChem, from Brass Society, and Freya, Tori and Annie, for putting up with me – your friendship has made everything so much easier. To Dad, Mum and David for your support and love throughout the whole process.

In particular, I'd like to thank those who helped me prepare for the massive changes in my post-PhD life. Alex, May, Tim Bugg and the others who supported me unwaveringly when I first decided I would study medicine after my PhD. Also to those who helped me in shadowing and volunteer work and made me see the light at the end of the tunnel that made everything worth working for.

Finally, to Alex, who has been with me from the beginning. Who has been with me through the good and the bad, has always believed in me, and has kept me able to do the things important to me – from music and travel to science and volunteering – while always providing me with a cup of green tea, a smile and a hug.

Declarations

This thesis is submitted to the University of Warwick in support of my application for the degree of Doctor of Philosophy in Chemistry. It has been composed by myself and has not been submitted in any previous form for any degree at any other University.

The work presented was carried out by the author except in the case of collaborative research, as outlined below.

Chapter 3:

- All recombinant AFP protein was prepared by Dr Muhammad Hasan at the University of Warwick. Dr Hasan also ran all SDS-PAGE gels used in *this* chapter.
- All XPS and data analysis was performed by Dr Marc Walker at the University of Warwick.
- All PVA polymers were prepared and characterized by Christopher Stubbs. "Splat" assays and analysis was also performed by Christopher Stubbs.
- All sucrose sandwich assays into ice shaping was performed by Alice Fayter.
- All "splat" assays and analysis of AFP-containing samples was performed by Dr Caroline Biggs.
- All thermal hysteresis assays were performed by Dr Peter Davies at Queen's University, Kingston, Ontario, Canada.

Chapter 4:

- Recombinant PVC*lumt*_Pvc13 and PVC*pnf*_Pvc13 tail fibre proteins were prepared by Joseph Healey of the Waterfield group.

- All XPS and data analysis was performed by Dr Marc Walker at the University of Warwick.

- Orbitrap mass spectrometry was performed in the University of Warwick Proteomics RTP by Cleidi Zampronio. Perseus and Scaffold analysis was performed by me.

- All A549 and SW480 cells were prepared in the Gibson cell lab, passaged and cultured by Trisha Bailey, but I undertook all assays.
- CACO2 cells were provided ready for lysis by Blessing Anonye of the Unnikrishnan group, but lysed and used by me.
- Recombinant PVC*unit4*_Pvc13 tail fibre protein was prepared by Dr Alexia Hapeshi of the Waterfield group. THP1 and S2 cells were also provided ready for lysis by Dr Alexia Hapeshi, but lysed and used by me. *Caenorhabditis elegans* were provided by the Waterfield lab, and lysate preparation was performed jointly with Alexia Hapeshi.
- CryoEM reconstructions of PVCs were performed by Franziska Leidreiter at the Max Planck Institute of Molecular Physiology, Dortmund, Germany.

Abbreviations

%	Percent
°C	Degrees celsius
3-D	3-Dimensional
Å	Angström
Ab	Antibody
Ach	Acetylcholine
AChE	Acetylcholine esterase
ACVA	4,4-Azobis(4-cyanovaleric acid)
AFM	Atomic force microscopy
AFP	Antifreeze protein
All	Allyl-β-D-galactose
AR2G	Amine reactive second-generation (BLI sensor)
ATRP	Atom transfer radical polymerisation
AU	Arbitrary units
AuNP	Gold nanoparticle
BCA	Bicinchoninic acid
BG	Benzylguanine (6-((4-(aminomethyl)benzyl)oxy)-7H-purin-2-amine)

BLI	Bio-layer interferometry
Boc	*tert*-Butyloxycarbonyl protecting group
BSA	Bovine serum albumin
CLIO	Iron nanoparticles cross-linked with dextran
cm	Centimetre
ConA	Concanavalin A
CryoEM	Cryo-electron microscopy
CTA	Chain transfer agent
CTx	*Vibrio cholera*e toxin
Cy3	Cyanine 3 dye
Cy5	Cyanine 5 dye
Cys	Cysteine
Đ	Dispersity (Mw/Mn)
DCM	Dichloromethane
DLS	Dynamic light scattering
DMAP	4-(Dimethylamino)pyridine
DMF	Dimethylformamide
DMP or DDMAT	2-(Dodecylthiocarbonothioylthio)-2-methylpropionic acid

DMSO	Dimethyl sulfoxide
DNA	Deoxyribonucleic acid
DP	Degree of polymerisation
DTE	Dithioerythritol
DTT	Dithiothreitol
EDC	Ethyl-3-(3-dimethylaminopropyl)carbodiimide
EDTA	Ethylenediaminetetraacetic acid
ESI	Electrospray ionisation
EthD-1	Ethidium homodimer 1
eV	Electron volts
F-12K	Kaighn's medium
FBS	Fetal bovine serum
FeNP	Iron nanoparticles
FimH	*E. coli* adhesive pili protein
FITC	Fluorescein isothiocyanate
FLAG-tag	FLAF octapeptide tag
FRET	Förster resonance energy transfer
FTIR	Fourier-transform infrared
g	Grams

G	Relative centrifugal force
GHO	Global Health Observatory
GM-1	Monosialotetrahexosylganglioside
GPCR	G-protein coupled receptor
GPI	Glycosylphosphatidylinosityl
GTPase	Enzyme that cleaves GTP to form di/monophosphate
GTP	Guanosine triphosphate
Halo-tag	Modified haloalkane dehalogenase tag
HEA	*N*-hydroxyethyl acrylamine
HEPES	4-(2-hydroxyethyl)-1-piperazineethanesulfonic acid
His-tag	Polyhistidine peptide tag
hrs	Hours
HSA	Human serum albumin
ICP	Inductively coupled plasma
IJ	Infective juvenile (nematode)
IMAC	Immobilised metal ion affinity chromatography
IPTG	Isopropyl β-D-1-thiogalactopyranoside
IRI	Ice recrystallisation inhibition
$\mathbf{K_D}$	Equilibrium dissociation constant

k_{OFF}	Dissociation rate constant
k_{ON}	Association rate constant
LB	Lysogeny broth
LC	Liquid chromatography
logP	Logarithm (base 10) of P-value (statistics)
M	Moles per litre
m/z	Mass/charge
MALDI	Matrix-assisted laser desorption ionisation
max	Maximum
mg	Milligrams
MGA	Mean grain area crystal size
MIC50	Minimum concentration at which 50 % of target molecules are inhibited by analyte
mins	Minutes
mL	Millilitres
mm	Millimetre
mM	Millimoles per litre
mmol	Millimoles
M_n	Number average molecular weight

mol	Moles
MRI	Magnetic resonance imaging
MS	Mass spectrometry
Ms	Milliseconds
MTT	3-(4,5-Dimethylthiazol-2-yl)-2,5-diphenyltetrazolium bromide
M_w	Weight average molecular weight
Mw	Molecular weight (g.mol^{-1})
n/a	Not applicable
NADH	Nicotinamide adenine dinucleotide
NHS	*N*-Hydroxysuccinimide
nm	Nanometre
nM	Nanomoles per litre
NMR	Nuclear magnetic resonance
NP	Nanoparticle
NTA	Nα,Nα-*Bis*(Carboxymethyl)-L-lysine hydrate
OES	Optical emission spectroscopy
PBS	Phosphate-buffered saline
PDB	Protein Database

PEG	Poly(ethylene glycol)
PET	Positron emission tomography
PFP	Pentafluorophenol
pH	Logarithmic scale (base 10) denoting acidity of solution
pHEA	Poly(*N*-hydroxyethyl acrylamine)
PIP	Phosphatidylinositol
pM	Picomoles per litre
pmoles	Picomoles
ppm	Parts per million
PtdIns	Phosphatidylinositol
pTLAm	Poly(thiolactone acrylamine)
PVA	Poly(vinyl alcohol)
PVAc	Poly(vinyl acetate)
PVC	*Photorhabdus* virulence cassette
PVP	Poly(vinylpyrrolidone)
RAFT	Reversible addition fragmentation-transfer
RCA_{120}	Ricin Communis Agglutinin-120
RNA	Ribonucleic acid
rpm	Revolutions per minute

s	Seconds
s0	Denominator of T-statistic
SDS	Sodium dodecylsulphate
PAGE	Poly(acrylamide) gel electrophoresis
SEC	Size-exclusion chromatography
SiNPs	Silica nanoparticles
SPR	Surface plasmon resonance
STM	Scanning tunelling microscopy
t-test	Statistical test that compares the means of two distributions to test if they are different to each other
TBS	Tris-buffered saline
TBS-T	Tris-buffered saline with 0.1 % Tween-20 by volume
TCO	Trans-cyclooctene
TEA	Triethylamine
TEM	Transmission electron microscopy
TF	Transferrin
TGA	Thermogravimetric analysis
TH	Thermal hysteresis
Theo	Theoretical

THF	Tetrahydrofuran
TLAm	Thiolactone acrylamide
Tris	*tris*(Hydroxymethyl)aminomethane
Tz	1,2,4,5-Tetrazene
UCSF	University College San Francisco
UV	Ultraviolet
UV-Vis	Ultraviolet-visible
VEGF	Vascular endothelial growth factor
XPS	X-ray photoelectron spectroscopy
µg	micrograms
µL	Microlitre
µM	Micromoles per litre
µm	Micrometre
$\boldsymbol{v}$	Frequency

List of Figures

List of Schemes

List of Equations

List of Tables

Abstract

Tools to understand the mechanisms of protein binding to cell surface proteins are of interest to enable the manipulation of such proteins, such as for therapy and drug delivery. In particular, bioorthogonal techniques are of interest as they can be used to probe protein structure and function in their native environment with minimal structural perturbation, as described in Chapter 1. This work seeks to develop such bioorthogonally-designed materials (polymers and nanoparticles) in order to study adhesive proteins.

In Chapter 2, using controlled radical polymerisation and "click"-like chemistries, doubly-functionalised glycopolymers with sequential variation in carbohydrate density, side chain length and secondary functionality were synthesized to probe the binding activity of an adhesive pathogenic toxin (*Vibrio cholerae* toxin subunit B). This revealed a new approach whereby sterically large secondary units enabled selectivity towards a toxin to be introduced.

In chapter 3, a small (<5 nm diameter) gold nanoparticle (AuNP) scaffold was used as the basis for the development of a dendrimeric ice binding protein (antifreeze protein type III). Two different bioorthogonal immobilization strategies were developed to probe AFP capture to NP surfaces. Optimum AFP activity was observed only for covalent SNAP-tag conjugates. Furthermore, this was critically compared to a fully-synthetic AFP mimic; poly(vinyl alcohol) coated gold nanoparticles.

Chapter 4 reports a detailed investigation into the function of adhesive protein fibres from an insect pathogen, using the nanoparticle tools developed here. Recombinant his-tagged fibres were immobilized and evaluated for whole-cell binding to a range of cell lines, and also lipid and glycan arrays. Furthermore, proteomics used to identify insect and mammalian cell protein targets. This resulted in the first ever description of Pvc13 tail fibre protein function, which may help elucidate its pathogenicity and a potential application in drug delivery.

In summary, novel nanomaterials were developed in order to probe adhesive protein structure and function. These materials must be delicately designed to avoid an impact on native protein function, and to exploit the material properties to their full effect.

1.Introduction

1.1. Protein structure and function

Biomacromolecules are responsible for a vast range of functions from intracellular processes to organism-wide signalling and providing physical structure. Proteins, involved in most cellular processes, are produced as a distinct sequence chosen from canonical amino acid residues as defined in the DNA or RNA of the productive organism. Proteins have a hierarchical structure, with four specific layers of structure adding up to a final quaternary structure (see Figure 1-1). It is this final, fully processed, quaternary structure that defines the function of the protein *in vivo* and its capacity to interact with other proteins, macromolecules and ligands.[1,2] However, this quaternary structure is also in turn defined in the original primary structure produced by the ribosome. The primary amino acid sequence (with side chains) or post-translational modifications, with different hydrophobicity, polarity and charge, determine the interactions that can occur with other amino acids both locally and further away in the primary sequence. The amino acids presented on the surface of the protein, and in its active or adhesion sites, are those residues that we can target to alter its function *in vivo*.

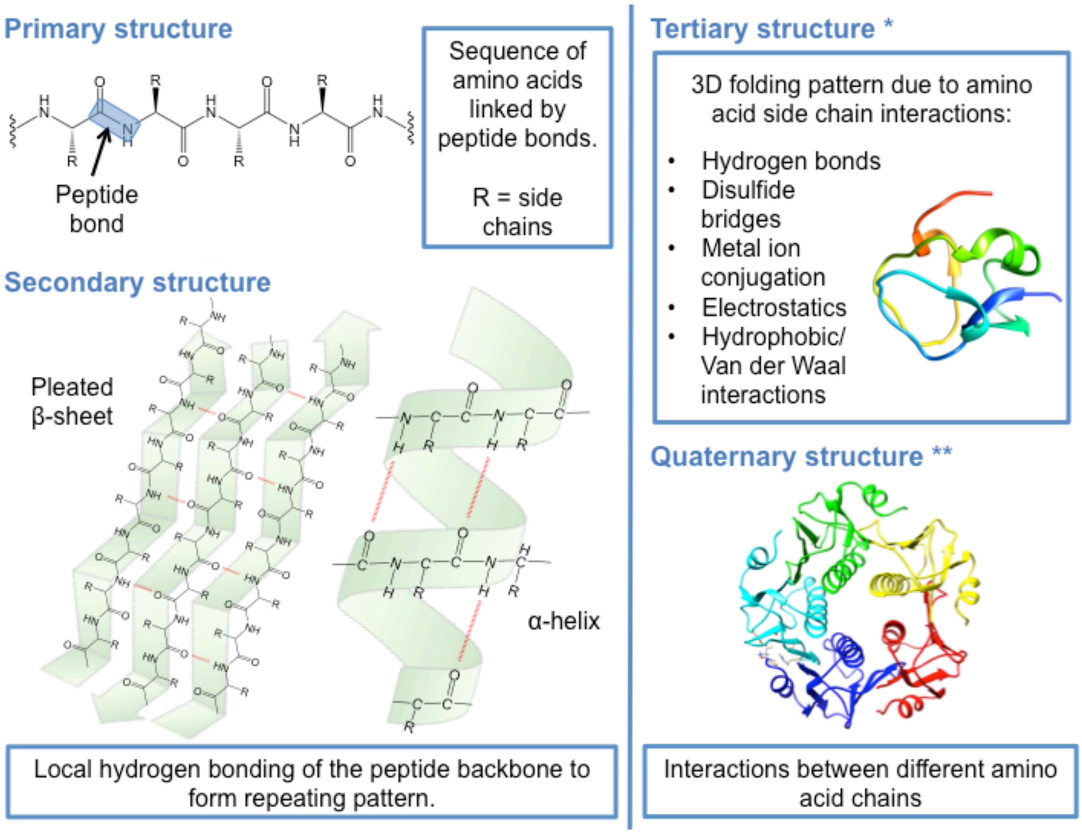

Figure 1-1. Hierarchical protein structures. *From Howard et al[3]. **From Merrit et al.[4].

Many proteins have an active site that binds to a selective ligand partner, including enzymes, which serve as catalysts for biochemical reactions, and antibodies (Abs), which bind specifically to antigens found on cell surfaces or in solution for immunological purposes. The 3-D structure of the active site is essential in the maintenance of these proteins' function.

Proteins engage in various forms of interactions with other molecules: hydrogen bonding, disulfide bridges, metal ion-conjugations, other electrostatic interactions or hydrophobic interactions (see Figure 1-2). Of particular interest to those in the drug design sphere is knowledge of the active site amino acid side chains with which the native ligand forms interactions, so that synthetic molecules may be designed to mimic these interactions or even out-compete the native ligand.

Synthetic macromolecules (polymers, nanoparticles) have therefore been proposed to target biomacromolecules, with their capacity to tune both the overall size and surface properties of the materials (such as hydrophobicity, density of functionality and 3-D organisation) as well as the specific functionalities installed to mimic the active site ligand binding.

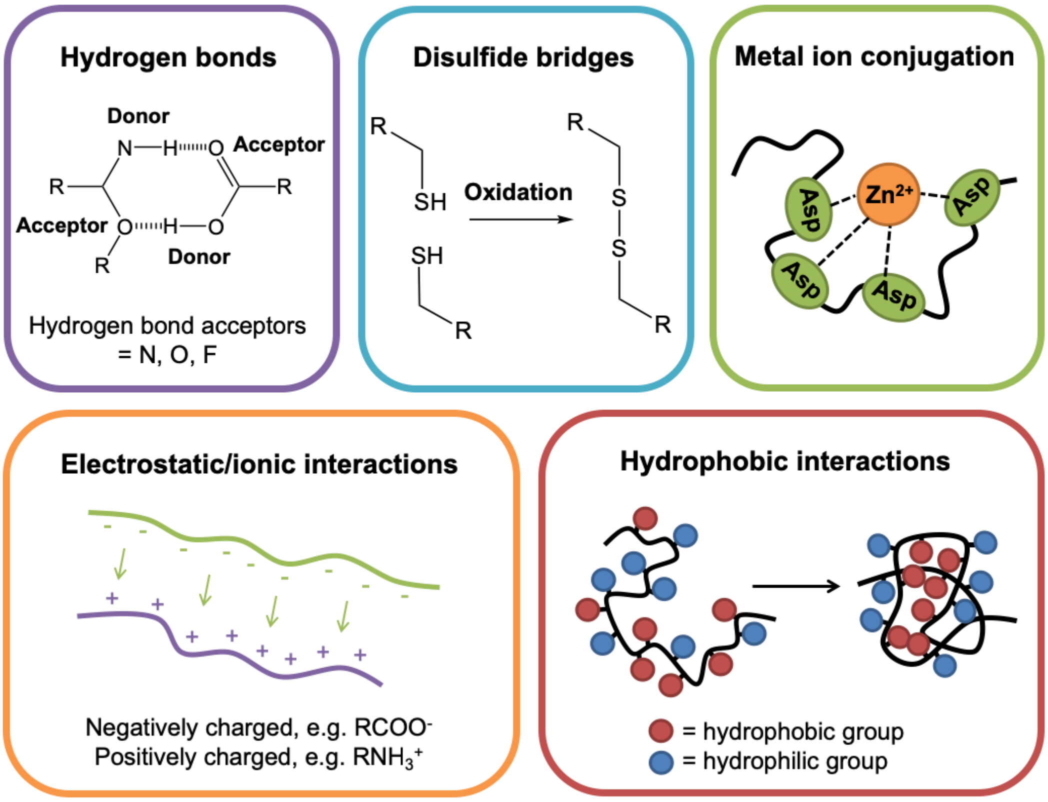

Figure 1-2. Different types of interactions in which proteins engage.

1.1.1. The biological basis of bioorthogonal chemistry

Bioorthogonal chemistry is a term coined by Bertozzi referring to chemical reactions which may occur *in vivo* without adversely affecting native processes.[5–7] It is defined as follows:

> *"The two components are non-interacting (orthogonal) to the functionality presented in biological systems. Further, the reaction must proceed in water at neutral or near-neutral pH at temperatures ranging from 25 to 37 °C without any cytotoxic reagents or byproducts."*[8]

These bioorthogonal techniques are utilised to further the understanding of native biochemical processes such as the activity of proteins, glycans and lipids, with the introduction of a bioorthogonal probe allowing the researcher to monitor a target macromolecule. Such chemistries must be extremely selective for their target, and must not alter other biochemical processes in order to allow effective study of the target macromolecule.[5–7] They must also exhibit rapid kinetics on a timescale of minutes to reduce competition with native cellular reactions.[8]

These chemistries often require two steps: the first being the introduction of a reactive functionality to the target, and the second being a reactive probe to couple with this functionality (such as a dye).[9] In studying protein structure and function, the use of recombinant proteins can provide a different synthetic approach.

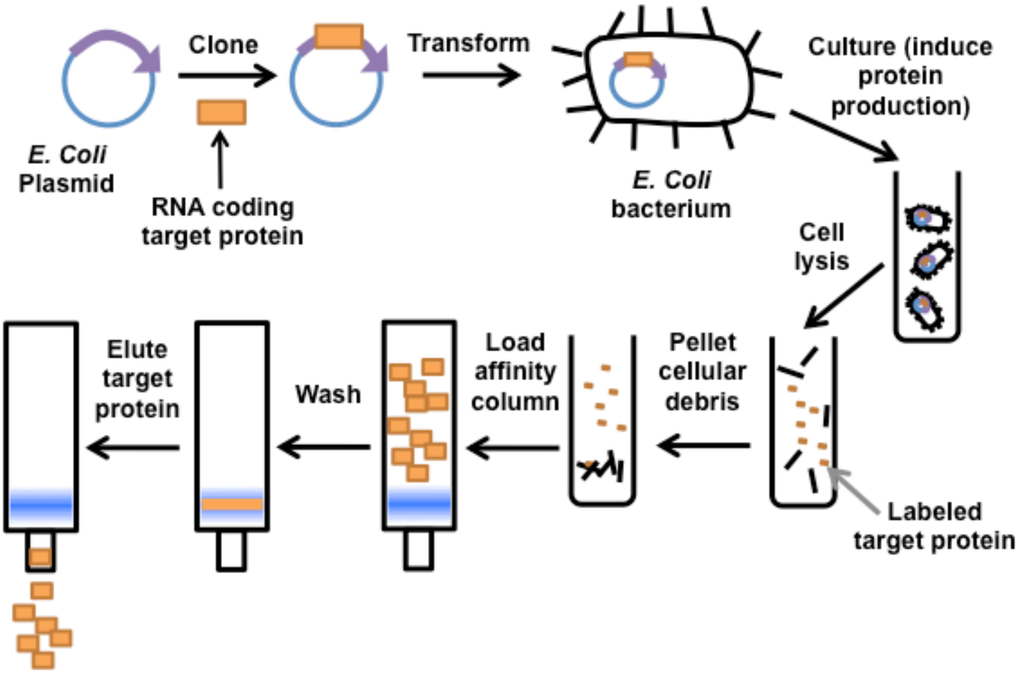

Figure 1-3. Workflow for production of recombinant protein using *E. coli* plasmid vector.

Recombinant proteins are necessary in biochemistry both to reduce costs and to produce a satisfactory yield of proteins for study. *Escherichia coli* is well-established as a prokaryotic factory for recombinant protein.[10–13] This process involves selecting the gene for the protein of interest, cloning this gene into a plasmid, transforming this plasmid into *E. coli* and inducing this protein to be produced by the bacteria before purifying it (see Figure 1-3). Each of the steps in this workflow involves careful consideration of which reagents should be used. Of particular interest herein, to facilitate the purification step of soluble protein production, an affinity tag is often introduced into the gene cloned into the plasmid vector (at either the C- or N-terminus of the protein, whichever is not buried in the protein's final structure) to allow this protein to be selectively separated from *E. coli*'s other cellular components.[10]

The expression of a peptide tag (a short amino acid sequence) or a fusion partner (a large polypeptide) allows the production of a chimeric protein that can be detected or isolated via its affinity tag and can even enhance solubility.[10,14] Alternatively, unnatural amino acids can be used, though these methods can be laborious and expensive.[15–17] For example, the amber stop codon (TAG in DNA, UAG in mRNA and CUA in tRNA) normally terminates translation by recruitment of release factor 1 of 2 (RF1 or RF2).[18] However, the suppression of this stop codon has allowed the use of modified UAG-tRNAs to incorporate unnatural amino acids into *E. coli*.

Small peptide tags include the poly-His-, FLAG- and Strep II tags, and these tags generally have commercially-available antibodies to allow Western Blot detection.[10,14] The His-tag is ubiquitously included in many plasmids, and the facile technique of immobilised metal ion affinity chromatography (IMAC) is extensively used to capture His-tagged proteins.[14,19–23] Cysteine is commonly a target for bioorthogonal labelling, but this is not possible if the amino acid is involved in the protein's active site or if a newly-introduced cysteine becomes involved in intermolecular disulfide bonds or affects native disulfide bridges.[9,24] It is still commonly used, however, due to the bioorthogonality of such chemistries, as well as the low frequency of cysteine in eukaryote proteins, and accessible on the protein surface (see Figure 1-4).[25,26]

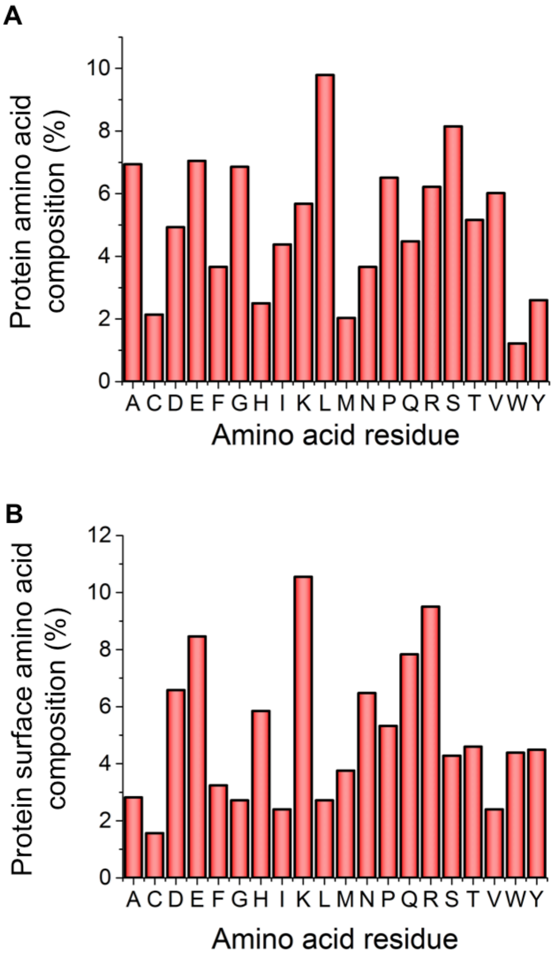

Figure 1-4. Amino acid frequency in protein structure. Amino acids are signified by their single letter (ie. C = cysteine). A) Mammalian non-membrane protein amino acid composition, from Gaur, 2014[25]. B) Amino acid composition on protein surface of a nonredundant library of 3-D protein structure, from Lins *et al.*[26]

Fusion partners can also enhance the solubility of purified proteins: examples include Maltose-binding protein[27], thioredoxin[28], glutathione S-transferase[29], SNAP[30] and SUMO[31]. Several of these tags have been proposed to possess intrinsic chaperone activity that accentuate this solubility enhancement.[27,30] These tags also vary in their attachment to their substrates, with SNAP binding covalently to a benzylguanine group whilst maltose binding protein binds electrostatically.[30,32–37] Alternatively, several fusion tags respond to stimuli such as temperature and calcium concentration, thus eliminating the need for purification by chromatography.[10,38,39]

Bioorthogonal tags can be used to immobilise proteins to surfaces and materials such that their function can be probed. Site-specific protein labelling with such tags also ensure that, if the structure is known, the active site can be made available for functional studies. Pull down assays are a well-established technique to assess the binding of a “bait” protein immobilised on beads (for example, his-tagged proteins attached to Ni-NTA groups on magnetic nanoparticles) to target proteins in solution.[10] Tags can also enable to use of specific dyes, meaning that the binding of protein to an array can be assessed by fluorescence measurements.

The development of novel synthetic tools to exploit the presence of these affinity tags is of interest as these techniques are cheap, facile and well understood: these chemistries are explored further in the following sections.

1.2. Synthetic bioorthogonal techniques

Bioorthogonal chemistries are utilised to introduce a probe onto a protein that is then monitored to elucidate protein function *in vivo* or *in vitro*.[9,40–42] Synthetic chemistries, rather than biological techniques, can afford a wide variety of functionalities interacting specifically in an affordable manner (see Figure 1-5 and Table 1-1). In particular, bioorthogonal techniques may be used to immobilise proteins onto a surface, such as a biochip, for further study, or specifically introduce a label.[43] Labels can allow the tracking of protein localisation in cells, protein-protein interactions or protein binding to glycan or lipid arrays.

A combination of biological and chemical conjugation can be achieved through enzyme chemistry, wherein a reactive functional group is introduced to the protein which can then "click" to a reactive chemical probe.[24,44] As stated by Bertozzi:

> *"A good click reaction satisfies many criteria: it should be high yielding, produce minimal byproducts, and be stereospecific when applicable. Further, it should involve readily available starting materials, take place in benign solvents (ideally water) or under solvent-free conditions, and allow simple isolation of products. In practice, click reactions tend to have large negative free energies and hence involve carbon-heteroatom bond-forming processes. Thus, unlike many conventional synthetic reactions, the power of click chemistry lies in its simplicity and ease of use."*[8]

"Click" chemistries are those 'spring-load'-like reactions between otherwise stable functionalities, and their power thus comes from its simplicity.[45] For example, lipoic acid ligase can be used to acylate a specific lysine with lipoic acid or, more usefully, with modified lipoic acid analogues that may be chemically conjugated by "click".[24] Herein, however, enzymatic techniques will not be considered, as their use can add another layer of complexity to an already-complex field. "Click" chemistries alone can, however, be adapted to be bioorthogonal.

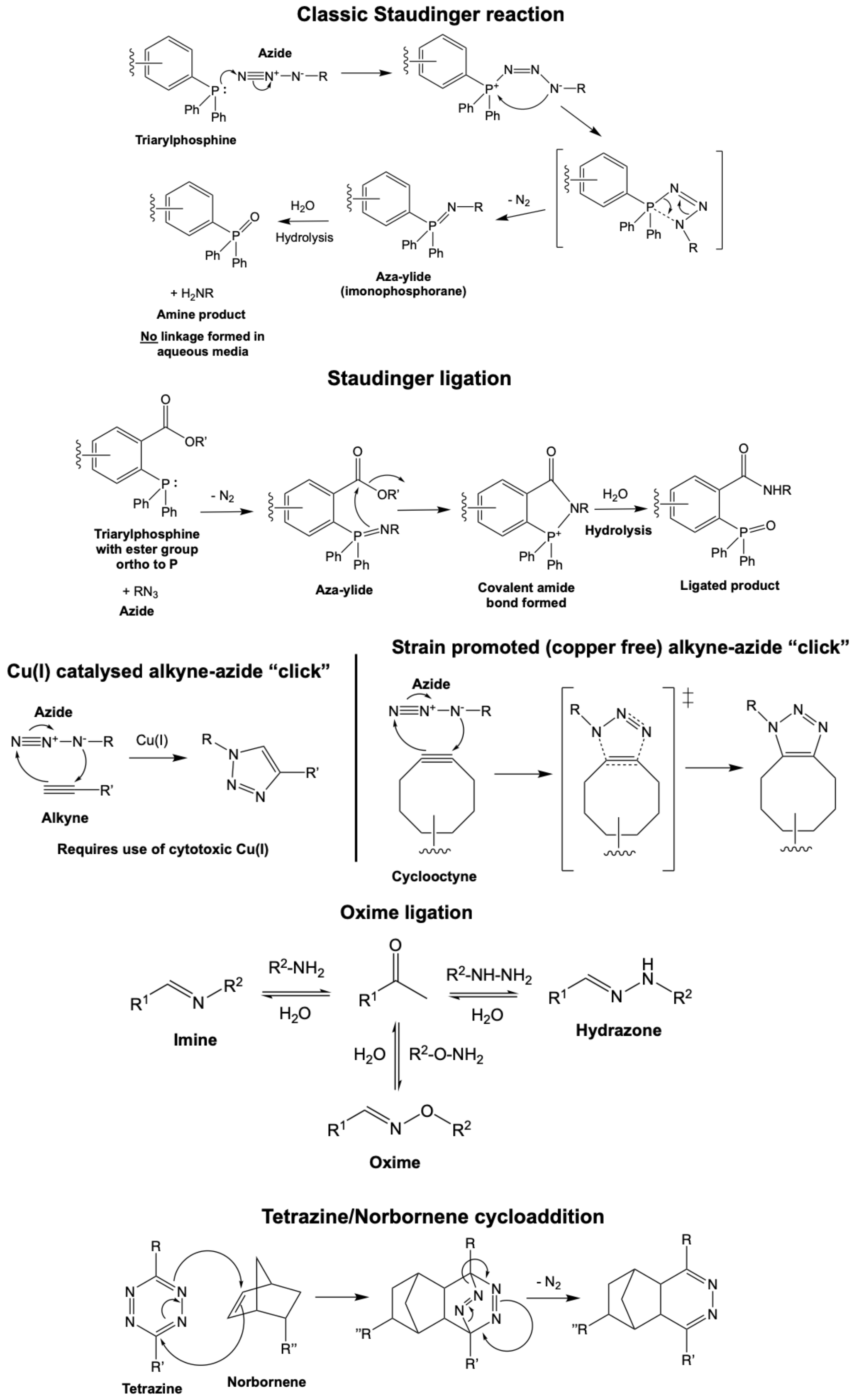

Figure 1-5. Schemes for proposed bioorthogonal chemistries and their non-bioorthogonal precursors.

Table 1-1. Proposed bioorthogonal strategies.

Reaction type	Functionality	Advantages	Limitations
Oxime/ hydrazone ligation	Ketone/ aldehyde condensation with amine nucleophiles	Takes place at ambient temperature, aqueous media at physiological pH. Specificity as native ketones and aldehydes are not present on cell surface. Fast. High-yielding.	Competition with carbonyl (though not favoured). Competition with native aldehydes/ketones (eg. Glucose/pyruvate). Difficult to implement aldehyde.
Staudinger ligation	Azide with triarylphosphine	Takes place at ambient temperature, aqueous media at physiological pH. Functionalities not present in biological systems. "Traceless" versions exist without phosphine oxide in product. No azide present in biological systems. Small azide does not hinder modified substrate.	Azides may be reduced by thiols/disulfides, especially in basic conditions. Phosphines may reduce disulfides (though less at physiological conditions). Slow reaction kinetics ($k = 10^{-3}\ M^{-1}\ s^{-1}$) require high triarylphosphine concentration (> 250 µM)
Strain-promoted alkyne/azide "click" ([3+2] cycloaddition)	Azide with strained alkyne	Takes place at ambient temperature, aqueous media at physiological pH. Functionalities not present in biological systems.	First generation (without fluorine on cyclooctyne) exhibits slow kinetics ($k = 10^{-3}\ M^{-1}\ s^{-1}$), and poorly soluble.

		Small azide does not hinder modified substrate. Does not require use of cytotoxic copper (I) catalyst. Gem-difluorinated cyclooctyne has similar kinetics to copper catalysed "click" ($k = 10^{-1}$ M^{-1} s^{-1})	
Tetrazine/ norbornene cycloaddition (inverse Diels-Alder)	Tetrazine (Tz) with norbornene	Takes place at ambient temperature, aqueous media at physiological pH. Functionalities not present in biological systems. High yield, rapid kinetics	Competition via Michael additions from biological nucleophiles
Tetrazine/ strained alkene (eg. Trans-cyclooctene, TCO) (inverse Diels-Alder)		Takes place at ambient temperature, aqueous media at physiological pH. Functionalities not present in biological systems. Rapid kinetics	Competition via Michael additions from biological nucleophiles Possibility for non-specific modification of surface lysines

Various chemistries exist to non-specifically label proteins, such as EDC/NHS coupling, but the use of non-specific labelling has the potential to affect native protein function by blocking proteins' active sites or affecting folding.[9,46] Alternatively, specific tags on proteins can be used as a template for site-specific labelling. For example, terminally-introduced cysteine residues allow the introduction of maleimides of α-halo acids or the use of 2-cyanobenzothiazole condensation, the poly-His tag conjugates to a nickel atom (or cobalt) bound to an NTA-group, and the larger

SNAP-tag can react specifically with a benzylguanine group.[19,24,30,47] Bioorthogonal chemistries used to interact with proteins require delicate conditions to avoid affecting protein structure and function, and thus must proceed specifically, in high yields, rapidly and in aqueous solution.[9]

The Staudinger ligation is a gold-standard bioorthogonal strategy developed by Bertozzi *et al.* from the Staudinger reaction, previously used for cell-surface engineering or bioconjugate preparation.[5–7,48–51] This reaction involves the ligation of a phosphane reagent containing the chosen probe to the protein target via an aza-ylide intermediate moiety, forming a stable amide bond in aqueous media at high yields. These functionalities are not present in biological systems, thus affording perfect selectivity, though they proceed slowly and the phosphine-probes may oxidise in air. Bertozzi and Raines also developed the traceless Staudinger ligation, wherein the phosphine oxide moiety is no longer present in the final modified product, which may be preferable for preparation of protein microarrays.[5,50]

Various other ligation mechanisms also exist, which typically involve a capture step to bring two specific reactive functionalities together in an unstable intermediate, followed by the ligation step.[52,53] The oxime ligation, for example, involves the condensation of an oxyamine and an aldehyde/ketone, and occurs rapidly at high yields.[52,54] However, the introduction of an aldehyde functionality (more common than the ketone) to a protein can be challenging.[9,55] Other novel ligation strategies, such as using tetrazines or quandricyclanes, are also beginning to make the leap from synthetic to *in vivo* work.[9,56–58]

Bertozzi *et al.* also developed the second landmark bioorthogonal chemistry: the copper-free click reaction (so called as the use of activated reagents negates the need for cytotoxic copper catalysts), as a more rapid alternative to the Staudinger ligation.[59] This reaction uses a strained cyclooctyne ring to interact with an azide, with the 17 ° deviation from the preferred geometry being sufficient to activate the reaction.[5,35] There are limitations to this method, including possible nucleophilic addition with cellular nucleophiles (for example, glutathione or oxidised cysteines), the hydrophobicity of the cyctooctyne ring and a relatively slow rate of reaction.[24] However, the use of polymers to enhance solubility and the implementation of substituents, ring fusion and heteroatoms have increased the rate of this reaction sufficiently to allow its use *in vivo* and in imaging studies.[5,24,35,60,61]

Other potential cycloaddition and click strategies exist, such as norbornenes and tetrazole photoclicks, but again these techniques have yet to be tested extensively *in vivo* to fully assess biocompatibility: the latter being suggested as a non-bioorthogonal photo-crosslinking reagent due to lack of specificity.[62–66] Finally, the Diels-Alder reaction is a well-understood diene/dienophile reaction that proceeds in aqueous solution, but its slow rate, reversibility and susceptibility to hydrolysis makes it difficult to use in forming a stable bioconjugate.[24]

The Staudinger ligation or copper-free click chemistries are therefore currently the gold standard when it comes to bioorthogonal chemistry whilst more investigation is required to validate the use of other strategies. Thus the introduction of an affinity tag, via protein recombination, during the protein synthesis step is incredibly useful.

1.3. Polymeric bioconjugates

Polymers have found their uses in biological systems due to their ability to mimic biological macromolecules[67–70], biocompatibility[71–74], and capacity to contain triggerable functionalities[75–79]. In particular, polymers are useful in many fields as they can both mimic the local structure of a biomacromolecules and bulk properties such as amphiphilicity[70]. Bioorthogonal chemistry can serve as a toolbox with which biocompatible, bio-functional polymers can be produced.[24,80–85]

Protein therapeutics, though potentially useful in toxin elimination or mimickry of native proteins, are often intrinsically instable and vulnerable to degradation, in oral delivery where they are destroyed by the digestive system, and in injectables where they are rapidly renally excreted.[86] Polymer conjugation can enhance the retention of these protein therapeutics, reduce immunological, proteolytic or other reactions by masking the protein surface, as well as provide the opportunity for targeted delivery.[86–88] Increasing the size of the protein by conjugation slows kidney ultrafiltration and promotes accumulation into target, permeable, tissues by the EPR (enhanced permeation and retention) effect.[87–89]

Protein/polymer conjugation by PEGylation has been used extensively in bioconjugates, as adding a PEG chain onto a biologic has been shown to increase stability, reduce aggregation and enhance solubility (see Figure 1-6).[86,89–98] Various PEGylated therapeutics have so far been approved (such as PEG-alpha interferon 2b developed by Scherling Plough's PEG-Intron, and PEG-alpha interferon 2a developed by Hoffman-La Roche's Pegasys) or filed for approval (such as PEG-granulocyte colony stimulating factor developed by Amgen, and PEG-human growth hormone antagonist developed by Pharmacia).[86]

There exist a variety of enzymatic or chemical strategies for PEGylation, which can each confer different functional properties on the resultant conjugate, such as through the conjugation of protein surface lysine ε-amino groups to activated PEG, though this occurs non-specifically and results in multiple, non-specific polymer/protein linkages.[86,89,90,93,98] Studies by Abuchowski *et al.*[99,100] have demonstrated enhanced retention of PEGylated (1900 and 5000 Da) albumin, as a reduction in antibody production that leads to free albumin removal, or catalase, as a reduction in both antibodies and proteolysis, and enhanced enzymatic activity (around tenfold higher) relative to free catalase over the course of 3 days.

In particular, many studies have shown interest in PEGylation of interferon protein for treatment of hepatitis C or cancer.[94,101,102] For example, Bailon *et al.*[103] synthesized monoPEGylated interferon R-2a (with a 40 kDa branched PEG), with PEGylated at one of interferon's 4 lysine residues (Lys31, 121, 131 and 134). These conjugates were found to have 70-fold increased serum half-life and severalfold increased antitumor activity in mice, relative to free interferon.

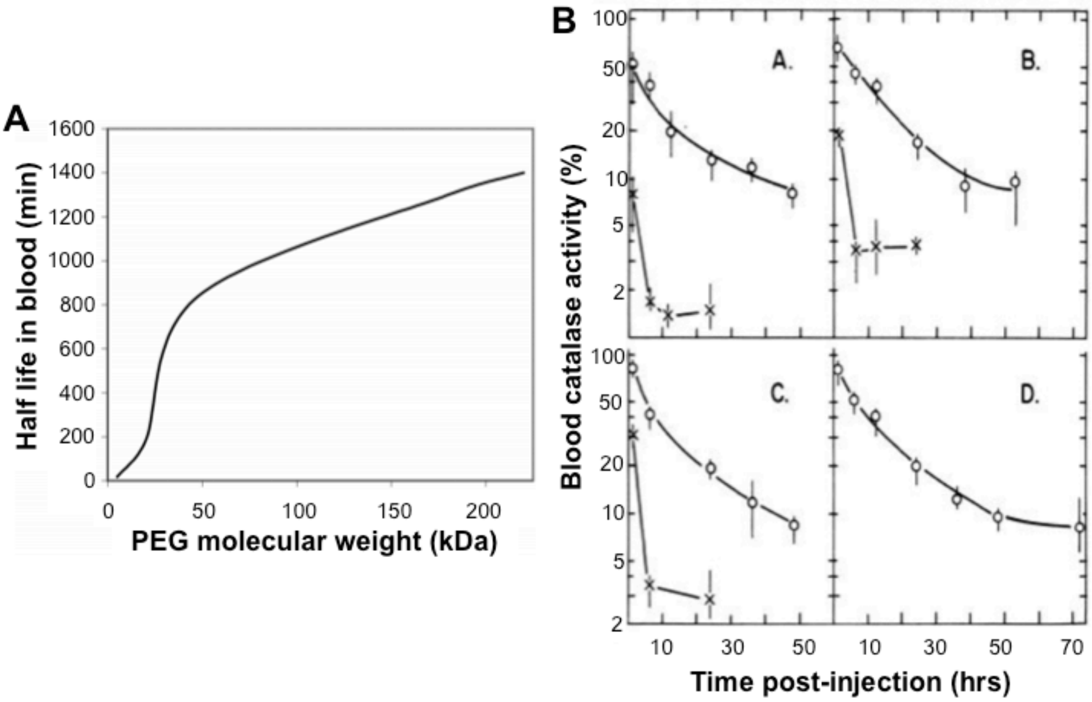

Figure 1-6. Stability in blood of PEG and PEG_{5000}-interferon conjugates. A) PEG molecular weight dependence on half life in blood after intravenous administration. Figure taken from Caliceti and Veronese[89]. B) Retention of catalase activity in blood of Acatalasemic mice, of catalase (X) and PEG_{5000}-catalase (O). Individual points are an average of four animals. Half of the animals in the investigated were injected by the tail vein with either 100 perborate units of free catalase or PEG_{5000}-catalase conjugate. Animals were then injected thrice weekly (day 2, 4 and 7). After 15 mins, 6-, 12-, 24-, 36- and 48-hrs, 0.15 mL of blood was taken from the eye orbit and assayed according to Feinstein's protocol. Different sets of animals were used for each bleed, except for the same animals used for the 15 minute and final bleed. This

assay was performed after the first (B.1), 13th (B.2), 26th (B.3) and 39th (B.4) injection. Figure taken from Abuchowski *et al.*[100]

Oxytocin is used to prevent post-partum haemorrhaging, but it is unstable in aqueous solution, especially at elevated temperatures.[104] Polymer-peptide conjugates formed using reversible disulfide bridges between the protein and a dithiophenol maleimide-functionalised polymer showed greater stability than native protein (less than 5 % of free oxytocin remained after 28 days incubated at 50 °C relative to ~90 % when attached to a conjugate), though further assays are required to assess biocompatibility and activity relative to the native protein.[104] Shi *et al.*[105] demonstrated azidized testis-specific protease 50 immobilisation via alkyne-azide "click" onto propargyl-containing polymer nanofibres, developed from a copolymer of 5-methyl-5-propargyloxycarbonyl-1,3-dioxan-2-one and *L*-lactide. These fibres attached specifically to the azide groups on the protein, with reversible detachment (with 75 % efficient reattachment) under exposure to a solution of pH 2.2.

These studies demonstrate the capacity to develop fully bioorthogonal techniques to form polymer bioconjugates. There are, however, multiple points at which a polymer can be functionalised: the polymer backbone, side groups off the polymer backbone, through the addition of branching, or through the end groups. The inherent nature of polymers is such that there are a variety of chain lengths in any synthesized polymer mixture, and therefore dispersity exists in the number of functionalities if implemented in the polymer chain or through branching, and therefore it stands to reason that end group functionalisation is the best method to introduce one moiety to the polymer chain for a proposed 1:1 polymer:protein conjugate. Various studies have looked into developing specific bioorthogonal strategies to form these 1:1, site-specific bioconjugates.[95,106–112]

Reynhoult *et al.*[113] developed a hybrid triblock structure, with a synthetic polystyrene (PS)-*b*-PEG$_{113}$ conjugated to myoglobin or horseradish peroxidase. ATRP was used to provide the copper catalyst, and the bromide at the chain end of the was converted to an azide to allow "click" onto the alkyne-terminal Zn-conjugating protoporphyrinIX cofactor to allow subsequent protein attachment. The resultant conjugates formed different structures (vesicles, micellar rods, vesicles, toroids, figure of eights or octopuses) depending on the ratio of the diblock elements of the synthetic polymer unit: for example, increasing the chain length of the polystyrene resulted in a shift from micelle to micellar rod structure. The obvious drawback of this strategy, despite the delicate design of the bioconjugate, is the use of the ATRP polymerisation and copper “click” methods, and the subsequent presence of cytotoxic copper.

Lim *et al*[53]. propose the novel bioorthogonal pair of *p*-nitrodiphenylazirine and dimethyl fumarate, and their use in lysozyme conjugation under biological conditions. The reaction involves rapid (~2 minute) “click” of an azirine to an alkene initiated by 302 nm UV light, though the use of visible light may be possible upon the adding of auxochromic groups to the azirine’s phenyl rings to make them photoactive. Simon *et al*[114] successfully introduced an N-terminal azido-homoalanine and a C-terminal cysteine into a designed ankyrin repeat protein with high yield (30 mg) and stability. These doubly-modified proteins allowed PEGylation (20 kDa PEG) at the N-terminus and Alexa488 fluorophore at the C-terminus, and the final conjugate showed promising binding activity and kinetics with tumour cells, with an approximately fourfold increase in the association constant (k_{on}) of the conjugate relative to non-PEGylated protein (4×10^4 M^{-1} s^{-1}) and a similar dissociation constant (k_{off}).

The drawback of these techniques is unfortunately limits on simplicity and biocompatibility, with the use of copper, UV light and unnatural amino acids.[53,113,114] There is a therefore definite need to address these drawbacks and develop fully bioorthogonal, facile polymer/protein bioconjugates.

1.3.1. RAFT Polymerisation

Biothogonal polymer synthesis requires the use of techniques that afford control over molecular weight, dispersity and architecture. Many synthetic techniques exist that produce such polymers (termed controlled radical polymerisation) by delaying termination of the propagating polymer chains by establishing a dynamic equilibrium between dominant polymer chains and active radicals.[205-207] The majority of the chains, as dormant species, must be activated in order to chain extend, but do not terminate.

The work herein makes use of reversible addition-fragmentation chain transfer (RAFT) polymerisation. RAFT utilises free radical polymerisation, with a chain transfer agent (CTA) that is transferred between chains during propagation to mediate chain growth.[208-214] This technique is versatile (tolerant of a wide variety of monomer structures, solvents and initiators), resulting in polymers with low dispersity.[210-214] In particular, RAFT polymerisation generates polymers with predictable end-group functionality (based on the CTA used), which can be used in post-polymerisation modification.[209]

1.4. Nanoparticles

Nanoparticles (NPs) have a large surface area:volume ratio, but are sufficiently small enough to be colloidally stable, soluble and functionalisable, in size ranges typically 1 to 100 nm.[115,116] Unlike polymers, their shape, size and softness/hardness can be tuned as properties of the nanoparticle core.[115,117] Studies have shown their use as contrast agents, drug delivery vehicles, diagnostic tools or as theranostic agents.[115,117,118] A variety of nanoparticle types exist from metallic and magnetic to quantum dots, polymeric and silica.

1.4.1. Types of nanoparticle core

Mimicking the self-assembly of biomacromolecules underlies the development of polymeric nanoparticles, which must be carefully designed to achieve the desired size, shape and surface functionality.[118–122] In particular, polymeric nanoparticles may serve as excellent drug delivery vehicles due to their ability to encapsulate active agents, thereby affording physical protection to reduce degradation and enhance efficacy, an opportunity for targeted delivery, and a size compatible with intracellular delivery (1-100 nm).[123]

Amphiphilic polymers, synthetically or naturally-derived, self-assemble in polar solvent to enhance hydrophobic functionalities' interactions with bulk solvent and bury hydrophobic functionalities.[119] Block copolymers in particular serve as a good building block for self-assembled nanoparticles. For example, AB diblocks (containing two separated A and B repeat units) form micelles, worms, polymersomes and hollow tubes. Changes in the block ratio/length, hydrophobic/hydrophilic block positioning or functional groups used result in changes in structure.[120] The polymer nanoparticle preparation procedure can determine whether nanospheres or nanocapsules form, with the former being a packed matrix of polymer with constituents dispersed throughout, and the latter a polymeric vesicle (polymersome) with an inner cavity containing any active agent (see Figure 1-7).[119]

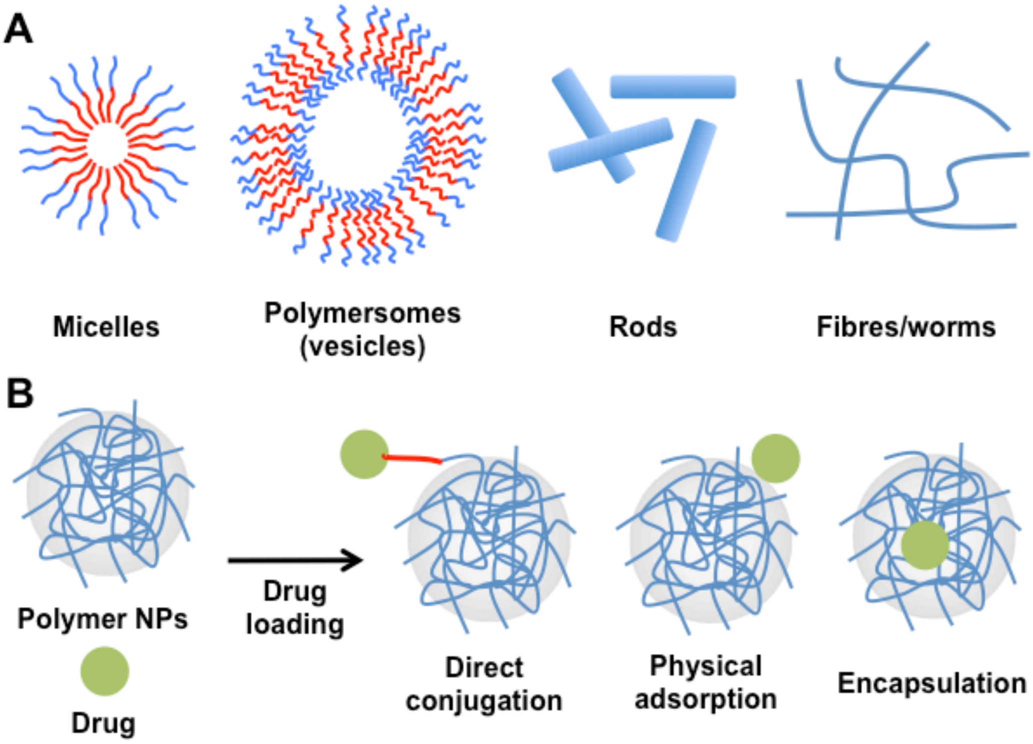

Figure 1-7. Polymer NP structures (A) and incorporation of drugs (B). Figure based on Zhao *et al.*[123]

Metallic nanoparticles (Au, Ag, Cu etc., see Table 1-2) are easily synthesized, purely from metal precursors, in a range of shapes and sizes, afford easy functionalisation (forming stable covalent-like thiol bonds) and have been shown to be biocompatible.[118] Conductive electrons also oscillate along the particle surface, with their resonant frequency being a function of surface composition.[118] This is termed surface plasmon resonance (SPR).

Magnetic nanoparticles (Fe, Mn, Co etc.) have potential as MRI contrast agents, are biocompatible, though they have been found to accumulate in biological tissue.[118] Silica nanoparticles have lower density than metallics, are biocompatible and have potential optical properties such as fluorescence.[118] Of interest herein are these colloidal inorganic nanoparticles, consisting of an inorganic core dispersed in a solvent, with surface conjugation of organics or biomolecules generating a hybrid material that can have specific surface function and greater biocompatibility in addition to NP properties such as fluorescence, magnetic moment or solubility.[45,116,124–129]

Table 1-2. Colloidal NP cores.

Core type	Properties	Advantages
Metallic **(Au, Ag, Cu)**	Surface plasmon resonance determined by composition, size, shape. Covalent-link bonds with thiols.	Facile synthesis of range of sizes/shapes. Easily functionalised. Biocompatible (low cytotoxicity, except in oxidation to Ag^+) Can be used in cell-labelling, diagnostics.
Magnetic **(Fe, Mn, Ni)**	Ferromagnetic/ superparamagnetic.	Biocompatible (low cytotoxicity). Accumulates in target tissue Can be used in MRI or as recyclable catalysts.
Silica **(SiO_2)**	Low density Optical properties	Able to encapsulate compounds. Biocompatible (low cytotoxicity) Can be used in drug delivery, biosensors or fluorescence imaging.

1.4.2. Bioconjugation to nanoparticles

The use of NPs as a scaffold for protein conjugation combines the properties of the NPs with those of the conjugated proteins.[116] The challenge of nanoparticle bioconjugates stems from their non-uniform nature: there are several coating molecules or conjugates present on individual NPs, but the number of surface functionalities available for further conjugation or activity varies widely and is dependent on the surface area they cover, and these details can only be obtained as a statistical distribution.[45,115,130] Different coatings, such as different numbers of DNA molecules attached to the core, may be separated by techniques such as gel electrophoresis, but this can be laborious and unnecessary for application of these materials.[45] Nanoparticle design benefits from simplicity, with layers of conjugate molecules linked together by at their terminals. Conjugation techniques must consider desired surface density, orientation upon attachment, and the length of linker required to give full access for biomolecule activity (see Figure 1-8).[130]

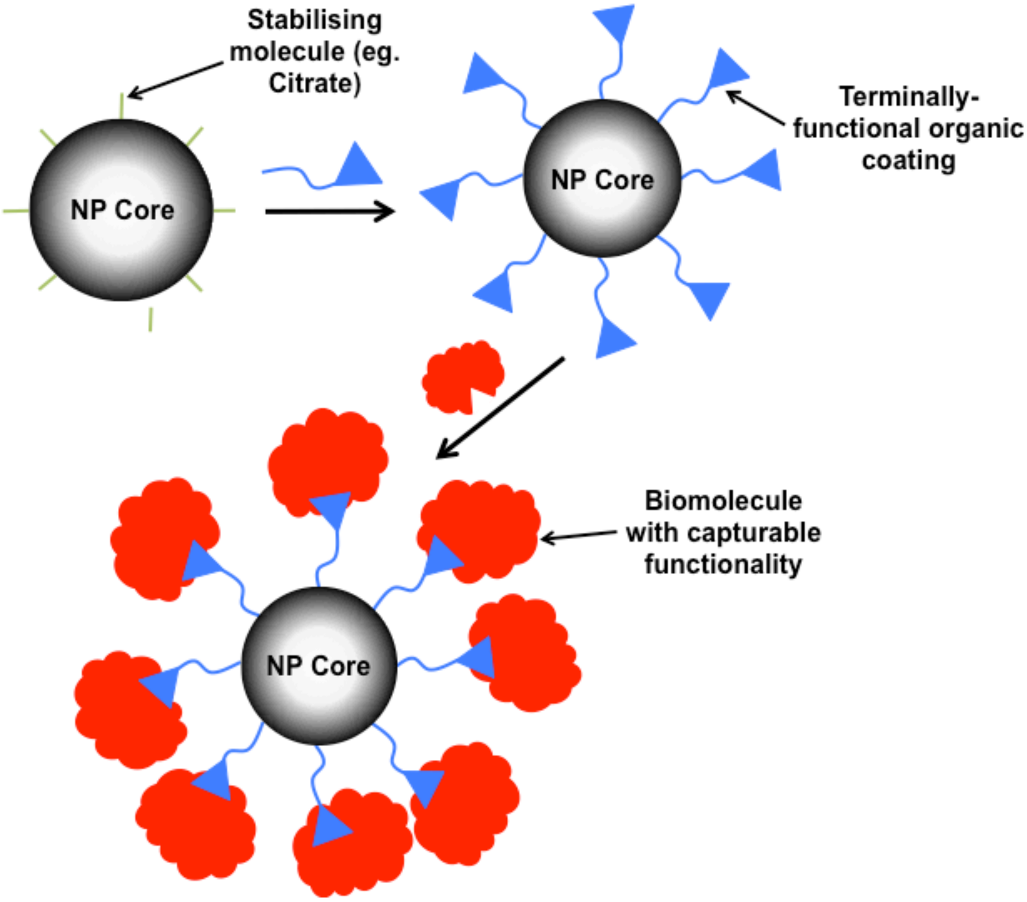

Figure 1-8. Typical nanoparticle layer-by-layer bioconjugate concept.

The surface functionalisation of the nanoparticles, or the NP's corona, determines the interaction with the environment: coatings affect colloidal stability, surface functionality and any targeting of biomolecules.[45,130,131] In particular, we are interested in the interactions between NPs and native biomolecules through covalent bonds, hydrogen bonds, acidity, electrostatics, coulombic forces or van der Waals, though the delivery mechanism has an affect on this, with many injectables becoming coating with serum albumin in the body.[116,130] Polymer coatings can sterically stabilise NPs, with dispersity of shape or patchy coating risking aggregation, but terminal carboxylic acids can stabilise via electrostatic repulsion.[45] After coating, unconjugated coatings must be removed from the reaction mixture, or the modified NPs purified (for example, by specific column chromatography) to avoid false positives, or potential crosslinking and subsequent NP aggregation.[45,130]

The conjugation of enzymes to a nanoparticle surface has been shown in several studies to enhance their activity relative to free enzyme, which suggests a potential application as nanofactories able to rapidly, repeatedly perform the enzyme's function.[116] When attached to a surface, enzyme activity is reduced due to steric hindrance, slower diffusion, or alterations in conformation due to attachment. Attachment to NPs potentially affords greater flexibility than surface immobilisation, allowing both an increase in activity and long-term enzyme stability. There is therefore particular interest in developing enzyme-NP constructs as well as other biomolecule/NP constructs.

Bioconjugation strategies must have several properties, similar to the definition of bioorthogonality. Though difficult to achieve in practice, ideal chemistries would result in a predictable and reproducible number of functionalities present on the NP surface (valence), ie. minimal dispersity.[115] This also means a reliable distance and attachment point on the linker attaching the biomolecule, and controlled orientation to allow retention of both NP and biomolecule function. These chemistries must be bioorthogonal: proceeding selectively under rapid, mild aqueous conditions. Finally, we desire these linkages to be stable, but with triggerable lability if required for, for example, drug delivery.

Bioconjugation to nanoparticles can be through direct binding to an inorganic NP core via, for example, thiol groups, electrostatic adsorption of positive to negative macromolecules, specific covalent linkages of functionality pairs, or non-covalent receptor/ligand systems.[45,115,130,132–145] Biomolecules may also be encapsulated in the nanoparticle core, but we are interested only in surface-functionalisation here. Direct biomolecule/nanoparticle strategies usually involve dative bonds, but they require delicate design of all components to ensure NP stability in reaction conditions, and avoidance of steric hindrance that may alter biomolecule function.

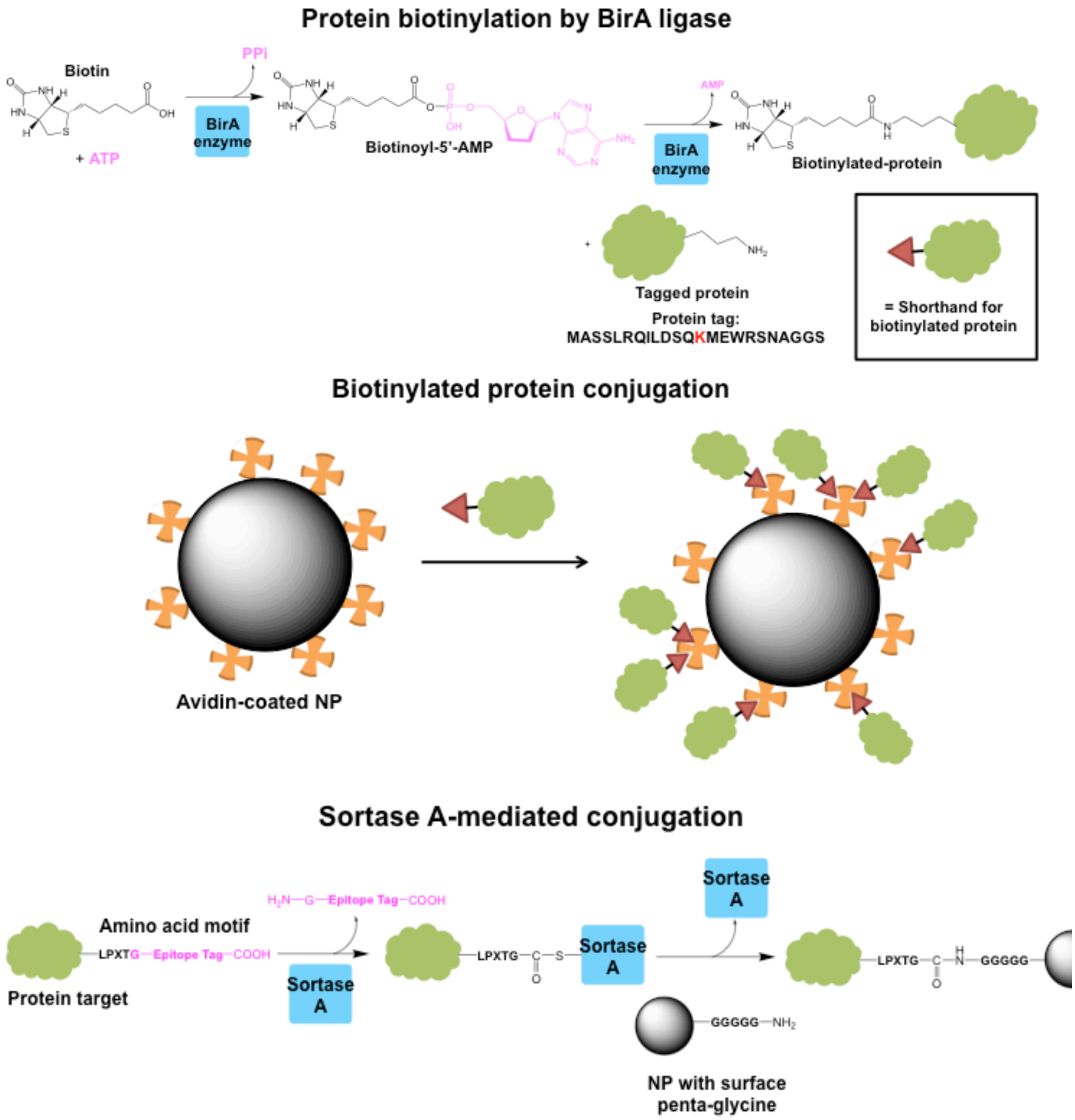

Figure 1-9. Select enzymatic conjugation strategies. Note that there are various biotinylation strategies used depending on the desired coupling. Shown here is the site-specific enzymatic strategy using BirA ligase to attach biotin to a lysine residue in a 23 amino acid tag on the (C- or N-) terminal of a recombinant protein in aqueous solvent; another method is the non-site-specific EDC/NHS coupling in organic solvents.

As with polymer bioconjugation strategies, there are many studies using enzymatic strategies to form the NP linkage.[118,146–149] Biotin/avidin coupling is commonly used for bioconjugation due to its specificity and extremely high affinity despite it being a non-covalent interaction (see Figure 1-9).[115,118] The chemistry has been applied to many different reporters, but with often heterogeneity in labeling and poor control of the binding site. Biotin ligase systems have enabled site-specfic labelling, such as BirA ligase transferring biotin to a specific lysine side chain which have then been applied to labelling of live cells using streptavidin-coated quantum dots. As another example, Sortase A enzyme (from *Staphylococcus aureus*) is a transpeptidase used to covalently ligate proteins specifically to glycine groups (see Figure 1-9).[149,150] These enzymatic strategies are generally very specific and mild, but they can induce aggregation and add another layer of complexity to this already-complex chemistry.

EDC/NHS coupling (between amines and carboxylic acids, activated by ethyl-3-(3-dimethylaminopropyl)carbodiimide) is commonly used due to its simplicity, but it is often called "shotgun labelling" due to lack of specificity (see Figure 1-11).[115] EDC activation of surface carboxylic acids forms an unstable, less-soluble, *o*-acylisourea intermediate that can undergo rapid hydrolysis. This can be stabilized by increasing EDC concentration, though the increase in surface intermediate formation can destabilize the NP in solution. Alternatively, sulfinated succinimides such as N-hydroxysuccinimide (NHS) can convert the intermediate to a more stable sulfonated succinimidyl ester intermediate without the need for excess EDC. Although this chemistry can, efficiently, multivalently display biomolecules on NP surfaces, they are totally non-specific, forming uncontrolled, multiple, random linkages between NP surface carboxylic acids, and any surface amines on the protein target. This can drastically affect the structure and function of the protein conjugated, and therefore these shotgun labeling techniques are best avoided.

Site-specific "click" chemistries potentially application to these purposes include 1,3-dipolar cycloadditions, Diels-Alder cycloadditions, Staudinger ligations and inverse electron demand Diels-Alder reactions (see Figures 1-5 and 1-10).[130,151] These chemical bioconjugation methods each have their advantages and disadvantages: for example, the Staudinger ligation between esters and azides requires no catalyst, but is slow and may have low coupling yields.[5]

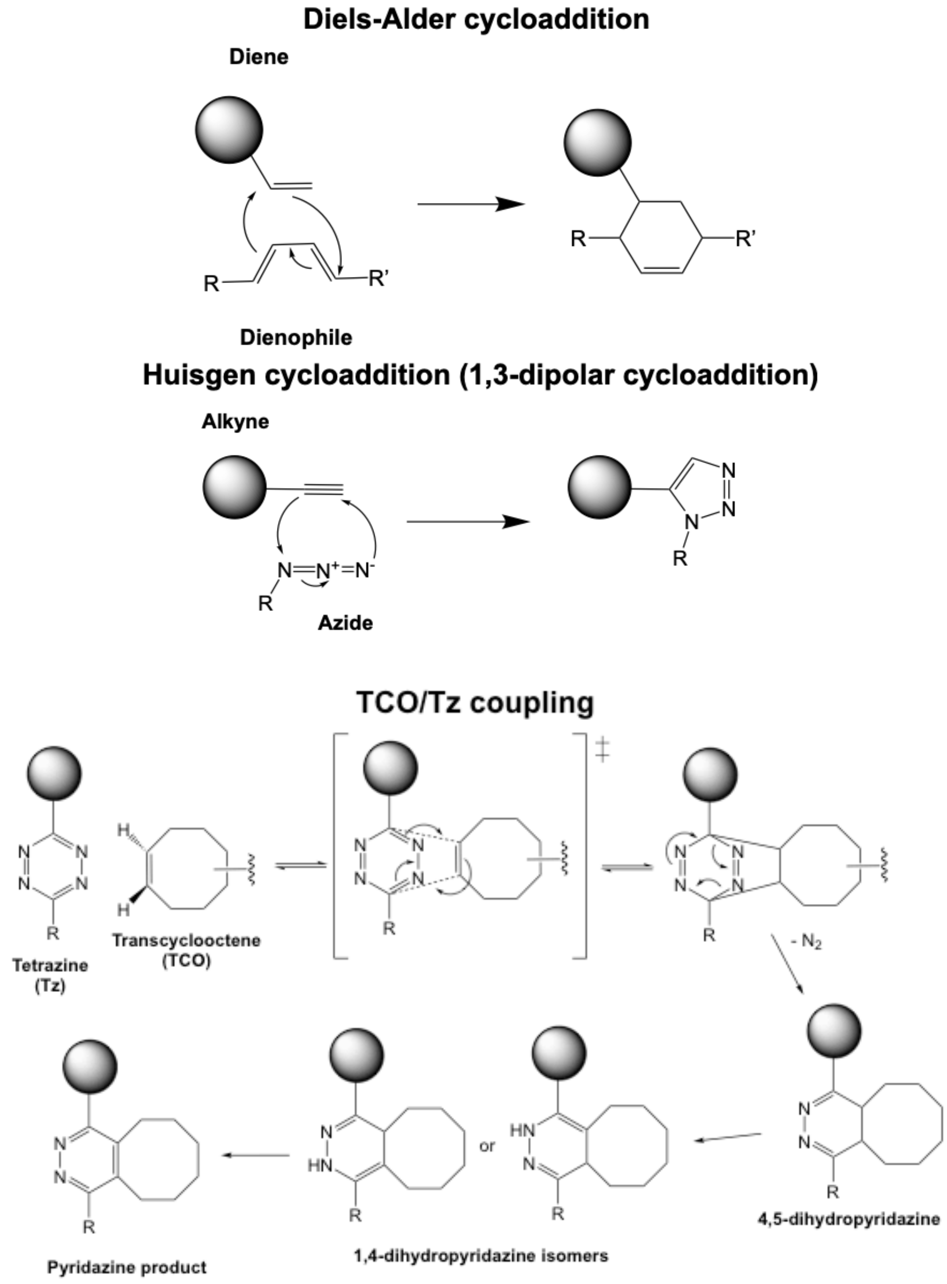

Figure 1-10. Select chemical conjugation strategies.

Copper catalysed "click" has been used by a variety of research groups to functionalise NPs, with the obvious drawback being the use of a cytotoxic copper catalyst (see Figure 1-5).[133,134,144,145,151,152] Lin *et al.*[151] showed a method of conjugating C-terminal alkynated proteins to azido groups on a silica oxide-coated magnetic iron oxide nanoparticle surface via Cu(I)-catalysed alkyne azide [2+3] cycloaddition. The activity of this site-specifically alkynated protein was higher than that exhibited by random linkages to amine groups: the EDC/NHS strategy showed significantly lower fluorescent intensity in a protein microarray relative to the cycloadditions method.

Copper "click" was used to conjugate human serum albumin (HSA) to iron oxide NPs by Polito *et al.*[145]. The protein has one unpaired cysteine at which alkyne acrylamide was added by Michael addition, and the protein was attached to an azide-terminal tetraethylene glycol linker on the NP surface via copper-catalysed "click". Anti-HSA antibody assays showed agglomerisation of the nanoparticles in a time- and dose-dependent manner relative to HSA concentration, suggesting that this method retained protein activity.

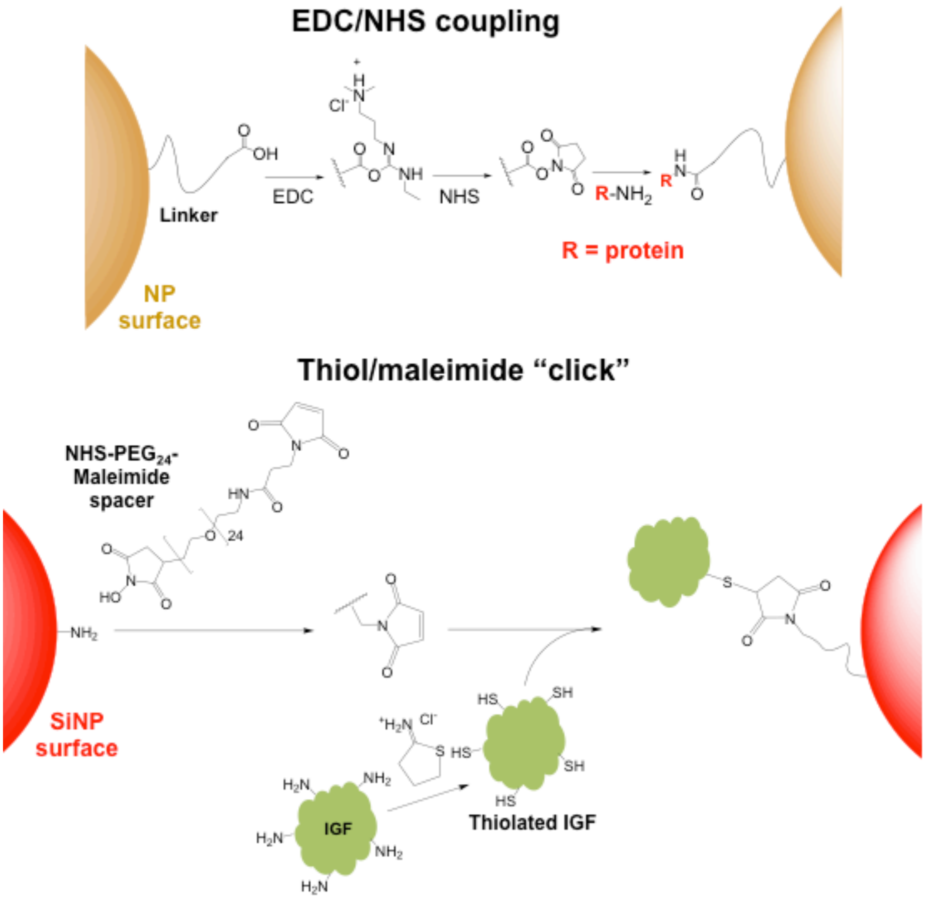

Figure 1-11. Select non-site-specific conjugation strategies.

Examples of copper-free bioorthogonal linkages also exist in the literature (see Figure 1-5).[118,153–156] Nanoparticles are reported to respond to tumours' enhanced permeability and retention (termed the EPR effect)s, meaning they are observed to accumulate specifically in these tissues.[153,154] These techniques require the pre-targeting of conjugates. Koo *et al.*[153] introduced unnatural azido-sialic acids (by intra-tumoral injection of tetraacetylated N-azidoacetyl-*d*-mannosamine). Successful azido-sialic acid incorporation was confirmed by staining of modified a549 (human adenocarcinoma) cells and tumour-specific attachment of dibenzyl cyclooctyne-terminated, PEGylated liposomes dose-dependently in mice, with an approximately 20-fold increase in near infrared fluorescence intensity in excised, azide-sialic acid decorated mouse tumours. Alternatively, studies have used copper-free click for biomolecule attachment: Feldborg *et al.*[156] found this technique to be faster than copper "click", Michael addition, and oxime ligation to liposomes with tumour targeting peptide, dependent on where the relevant functionalities were introduced onto the PEG polymer linker. All these liposome-immobilisation reactions were found to require at least 1 hour to reach a plateau, however.

Although bioorthogonal strategies usually require pre-modification of the target biomolecule, the addition of unnatural amino acids with azide groups can be difficult in proteins, so alternative, more facile, procedures have also been developed. Pasold *et al.*[157] displayed a beautifully simple method wherein fluorescent SiNPs were surface functionalised with maleimide groups using a PEG_{24} linker (see figure 1-11). Thiolated insulin-like growth factor was produced by incubation with 2-iminothiolane, desalted and reacted with the SiNP surface maleimide groups via a simple mixing procedure, followed by cysteine solution to block any free surface maleimide and washing. These IGF-1@SiNPs showed biocompatibility, cell viability and enhanced cell attachment and metabolic activity on a collagen-based tissue culture scaffold (with 120 µm infiltration after 7 days and ~5-fold increase in chondrocyte metabolic activity relative to the control without collagen).

Alternatively, easily-implemented, reliable affinity tags present in recombinant proteins can be used to selectively capture these proteins when paired with the appropriate chemistries.[118,158] Cysteine residues are readily functionalisable if present on the protein surface (see Figure 1-12).[118,159] Disulfide bonds can spontaneously form in a stable manner, and this has seen wide application. Soft-soft thiol interactions and Michael addition to a maleimide are both spontaneous, simple and occur rapidly. Such thiols are easily introduced to peptide via site-directed mutagenesis, but their use can be non-specific if other unpaired surface cysteines exist, and it can affect protein structure and function.[159]

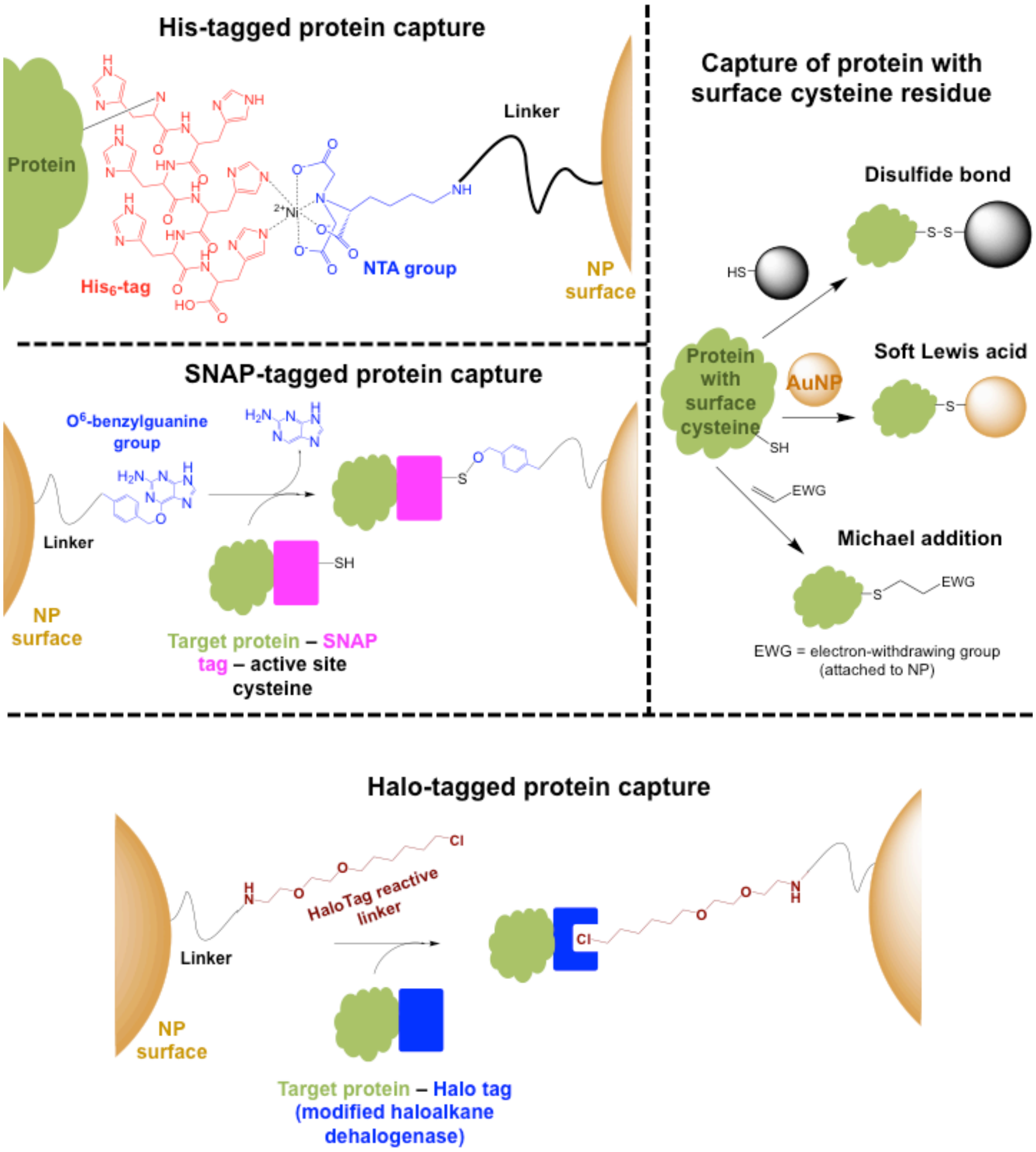

Figure 1-12. Select conjugation strategies utilising short peptide or fusion protein tags.

Hexahistidine-tags (His-tags) are an obvious choice for site-specific conjugation due to their easy, common use in affinity purification of recombinant proteins, with many studies using Ni-NTA (Ni-bis-nitrilotriacetic acid) groups to biocompatibly, selectively capture His-tagged proteins (see Figure 1-12).[19–23,118,159,160] This tag is small, specific and can be attached at either protein terminal. For example, Lai *et al.*[19] used a fluorescent Ni-NTA-probe (formed of NTA conjugated with a fluorophore and arylazide, followed by Ni^{2+} ion coordination) to show the intracellular location of a His-tagged DNA repair protein, Xeroderma pigmentosum group A. Despite the ease of their use, His-tag capture is limited due to the non-covalent nature of the linkage, such that the binding affinity is low and could lead to dissociation; though this reversibility can be a positive as purified proteins can be isolated from Ni-NTA resins using imidazole solution.

Other larger and non-toxic peptide tags may also be useful for selective protein capture without the risk of steric issues due to attachment to the main protein structure, such as SNAP-tag and Halo-tag, and these tags have been used previously to detect bioreactive small molecules in vivo (see Figure 1-12).[30,158,161,162] These tags are directional, efficient and site-specific, but their larger sizes have the potential to be immunogenic.[118] The Halo-tag is a modified haloalkane dehalogenase (a 33 kDa bacterial enzyme) that can covalently interact via an active site aspartate reside with chloroalkane linkers, termed Halo-tag ligands, bound to a variety of molecules such as dyes or surfaces.[158,162] This reaction has been used to detect cellular membrane potassium ion dynamics, using a potassium-detecting fluorescent probe conjugated to a GPCR/Halo-tag fusion protein. In this study by Hirata *et al.*[163], the full probe construct assembled at the cellular membrane onto the membrane-bound GPCR/Halo-tag, via a Halo-tag-ligand/K^+ probe, and fluorescence turned on in response to the infusion of high [K^+] buffer solution.

The SNAP-tag (a mutant of the human 19 kDa O^6-alkylguanine-DNA alkyltransferase) reacts selectively with O^6-benzylguanine groups via an active site cysteine residue, and has therefore been used to form semi-synthetic fluorescent probes for small molecule detection in cellular environments.[30,32–34,36,163–165] Srikun *et al.*[34] synthesized a boronate-capped SNAP-Peroxyl-Green probe able to biocompatibly detect intracellular hydrogen peroxide. In this work, an organelle-targeting protein/SNAP tag fusion protein was produced and attached to a H_2O_2-reactive fluorescent probe via a covalent interaction with a terminal benzylguanine or benzyl-2-chloro-6-aminopyrimidine group. This strategy allows the detection of H_2O_2 in specific subcellular locations, such as the plasma membrane or nucleus, by confocal microscopic visualization of fluorescence changes. Bannwarth *et al.*[165] proposed a calcium sensor consisting of Indo-1 dye fused to SNAP-tag fusion protein (again using a subcellular location-targeting protein) using the indole ester group (previously used in Indo-1-NP conjugation) coupled to benzylguanine amine. Confocal microscopy could again be used to detect subcellular levels of small molecules (in this case Ca^{2+}).

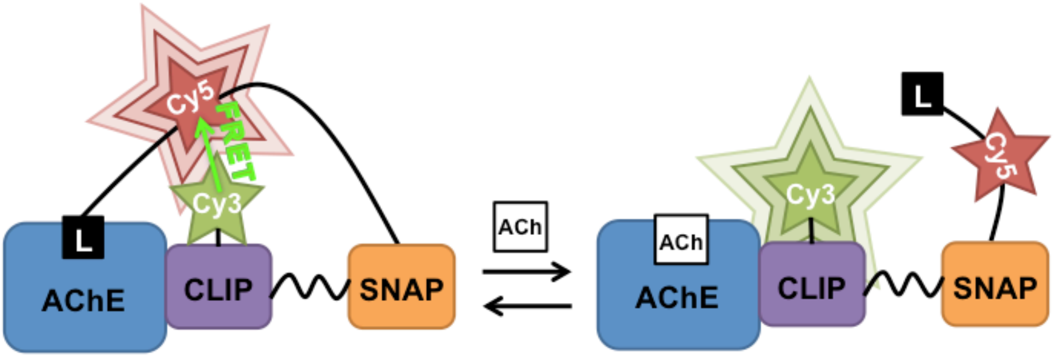

Figure 1-13. The SNIFIT labelling strategy. Figure reproduced from Ueda et al.[158]

Johnsson *et al.*[166] developed a larger fusion construct of acetylcholinesterase (AChE), CLIP tag labeled with a Förster resonance energy transfer (FRET) donor, and SNAP tag tethered to a FRET acceptor and AChE ligand, altogether called Ach-SNIFIT (see Figure 1-13). This SNIFIT protein shows a change in fluorescence depending on whether the FRET donor and acceptor are in close proximity (1-10 nm). The FRET donor and acceptor are two fluorescent groups, with the donor excited at the wavelength applied to the sample, and the acceptor only able to emit upon excitation by the wavelength emitted by the donor when it is close enough. This means that, when acetylcholine (Ach) is present, it displaces the SNAP-tag-tethered AChE ligand from the AChE active site, resulting in an increased distance between the FRET donor and acceptor, which is detected as a change in the ratio of fluorescence emitted by the donor and acceptor molecules: this this construct serves as an exquisitely-designed detector of applied ACh. In this way, the SNIFIT fusion protein, also an option for NP conjugation can be used in the detection of larger, more complex molecules than the SNAP-tag concept alone.[164,166–168]

It is clear that many fully bioorthogonal techniques exist for the nanoparticle bioconjugation. However, there is a need to further develop techniques to be applied in situ in biological systems, and this is challenging as it requires expertise in both molecular biology and chemistry.

1.4.3. Gold nanoparticle conjugates

Gold nanoparticles (AuNPs) are the most stable metal nanoparticles, and have a variety of other useful properties for bioconjugation.[169] Historically they have been used medicinally since the middle ages for their anti-inflammatory activity, such as against rheumatoid arthritis.[130] AuNPs can be easily synthesized in a wide variety of shapes, sizes and hardness (see Figure 1-14).[115,118,130,169–175] AuNPs have also shown catalytic properties, electrochemical application, facile characterisation by dynamic light scattering, and the capacity to be detected (for NPs ≥ 100 nm) strongly by dark-field microscopy.[169,173,176,177] AuNPs are able to both exhibit fluorescence when fluorescent markers are attached, or quench fluorescence, depending on the distance of the fluorophore's linker to the AuNP surface.[115,169]

Due to their high biocompatibility and low cytotoxicity, biological applications have included cell-labelling, gene therapy, nucleotide delivery and biosensing.[118] In particular, TEM has been extensively used to detect the intracellular localisation of AuNPs in cellular uptake studies.[178–182] For example, Gunduz *et al.*[182] showed intracellular AuNP accumulation on mammalian cells over the course of 2 months' incubation, with no detectable cell death, but elevated endoplasmic reticulum stress. TEM as a technique is used to determine AuNP size, shape and dispersity as AuNPs have very high contrast under the electron beam.[169,171,173,178–181,183] Scanning tunnelling microscopy and atomic force microscopy may also be used for these purposes. X-ray photoelectron spectroscopy (XPS) and inductively coupled plasma linked to either mass spectrometry (ICP-MS) or optical emission spectroscopy (ICP-OES) are used to determine Au concentration in complex mixtures, with XPS able to determine changes in Au oxidation state after coating.[169]

Spherical AuNPs are coloured red in water, reflecting the surface plasmon resonance (SPR) where visible light is broadly absorbed in the 517-575 nm region (though AuNPs < 2 nm diameter do not show a visible SPR maximum).[130,169] This SPR is due to collective oscillation of electrons at the AuNP surface (6s electrons) that happen to resonate with a visible light wavelength. The maximum peak of SPR (SPR_{max}) changes as a function of AuNP shape, size, the thickness and composition of surface functionality and the dielectric properties of the medium surrounding the AuNPs.[115,118,130,169,172] Therefore change in surface functionality, resulting in a shift in SPR_{max}, can be detected by UV-Vis spectroscopy.

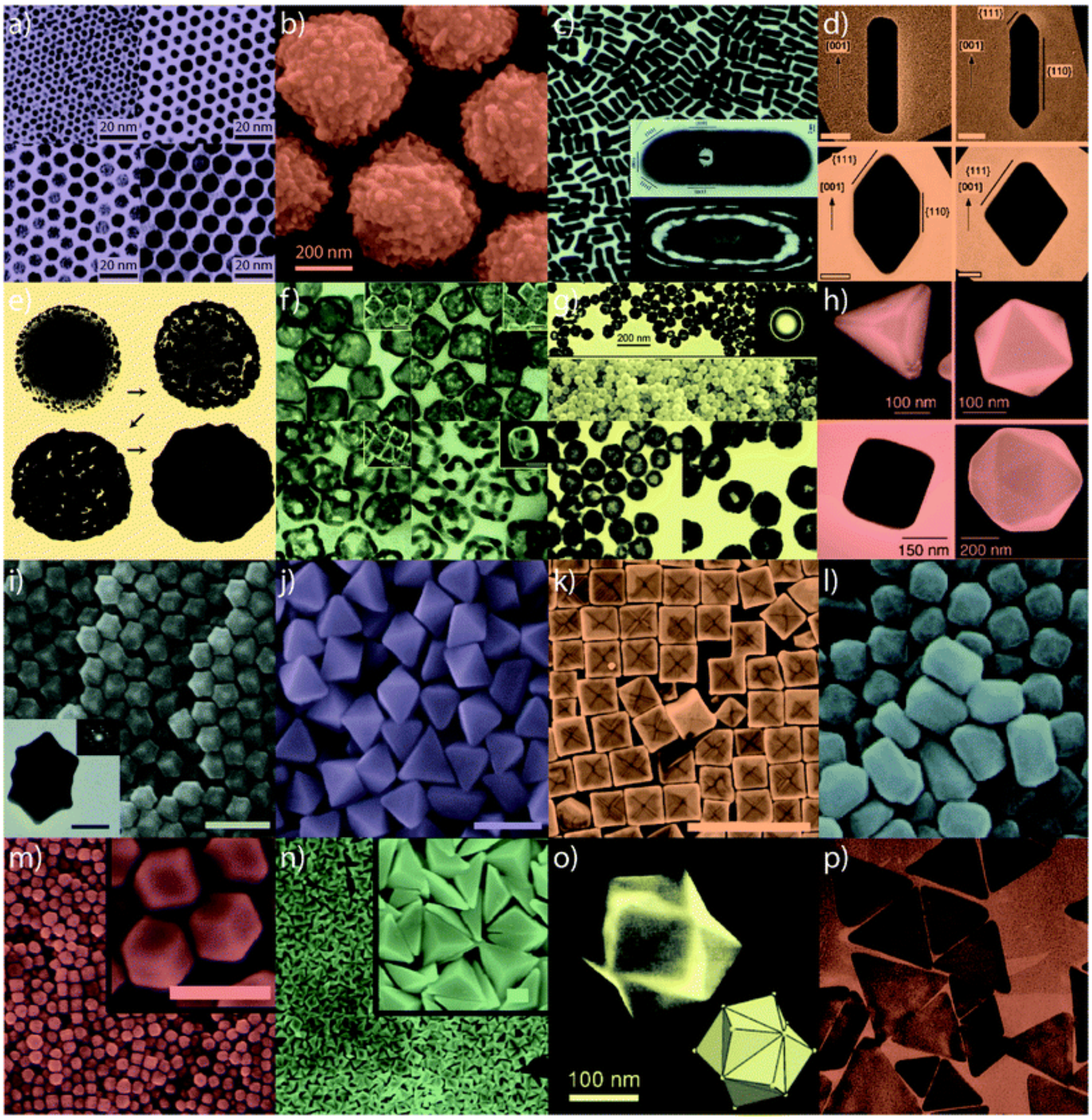

Figure 1-14. Various AuNP shapes and sizes. Small (a) and large (b) nanospheres, (c) nanorods, (d) sharpened nanorods, (e) nanoshells, (f) nanocages/frames, (g) hollow nanospheres, (h) tetrahedra/octahedra/cubes/icosahedra, (i) rhombic dodecahedra, (j) octahedra, (k) concave nanocubes, (l) tetrahexahedra, (m) rhombic dodecahedra, (n) obtuse triangular bipyramids, (o) trisoctahedra, and (p) nanoprisms. Figure taken from Dreaden *et al.*[184]

Colloidal AuNPs, as other metallic NPs, form bioorthogonal, stable linkages with, and thus can be stabilised in solution by thiols, citrate, phosphines, amines (eg. Lysine) and even isocyanide, attached to the AuNP surface through a simple mixing procedure.[118,130,151,169,171] Thiols are reported to form the strongest bonds, as a covalent-like Au-S bond, and as such it is predicted than dithiothreitol (DTT) has the capacity to strip of surface functionality via displacement using the small DTT ligand.[169,185] Recent studies have shown this displacement is dependent on ligand affinity, and is not wholly efficient.[169] Luo *et al.*[186] recently presented a possible displacement of small molecules via a Staudinger ligation-like displacement, wherein thiol-derivatized Rhodamine B dye was displaced with organic azide molecules, as detected by the dye's fluorescence when released into solution. Au-S bonds form through reductive elimination of the thiol hydrogen to form hydrogen gas or water, whilst disulfides are reported to be split upon chemisorption to the AuNP surface.[130]

This thiol-Au linkage has been used for the attachment of both thiol-terminated polymers (the majority being PEG or PVP) and small molecules to the AuNP surface, used either alone or as linkers for further modification, with a representative change in SPR_{max} observed.[115,169,179,181,187] As with other metallic NPs, AuNP show greater stability upon coating.[169,188] These structures also allow tuning of the coating density and thickness, as well as tuning properties such as hydrophobicity, patchiness and linker length: longer linkers result in greater stability but slower interaction with external stimuli.[169,188] UV-Vis has successfully detected a wide range of surface modification, from antibodies (Abs) directly attached to the AuNP surface, followed by the binding of these AuNP-surface Abs to their target proteins (such as anti-biotin conjugated via an oligonucleotide linker, IgG1, to biotin).[189] This is detected as the AuNP solution changing colour from red to blue upon the increase in size or aggregation (due either to a decrease in colloidal stability or AuNP clustering) of the AuNPs. Other methods for detection of surface functionality include IR and TGA, which can also be used to determine the average number of surface functionalities.[169]

Glyco-AuNPs have been widely investigated due to the facility of their synthesis, their capacity to incorporate both NP core properties and glycan biofunctionality, and their ability to mimic cell-surface glycan clusters.[151,169,188,190–193] This is of particular interest due to glycans being pivotal in the infection mechanisms of various bacteria, bacterial toxins and poisons, and in the signalling and sugar uptake of cancer cells in tumours.[190,191,194,195] Lin *et al.*[193] demonstrated the binding of mannosylated AuNPs to the adhesive FimH protein on *Escherichia coli* pili. Richards *et al.*[188,191] have looked into glyco-AuNP coating dependent specific detection of bacterial lectins (specific glycan-binding proteins often involved in cellular adhesion), wherein both the choice of carbohydrate displayed, coating density and the linker length play an important role (see Figure 1-15).

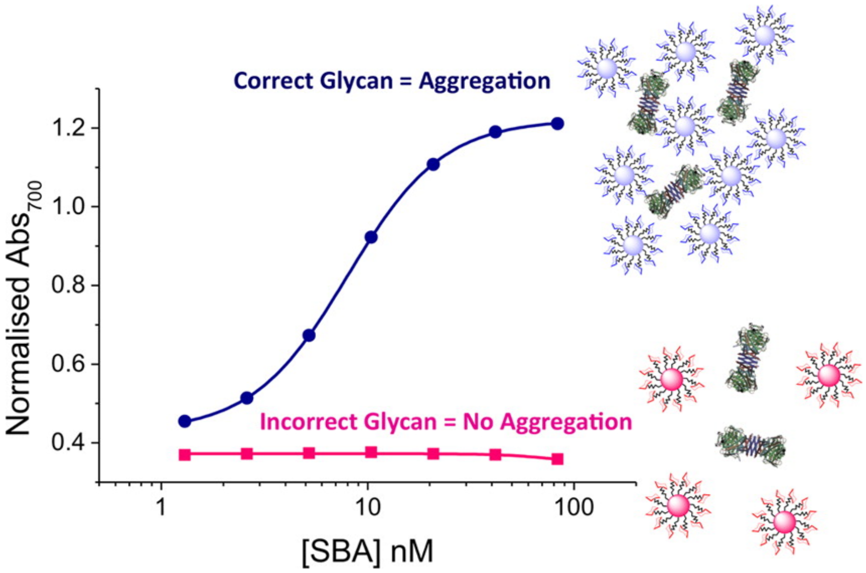

Figure 1-15. Aggregation of glycan-coated AuNPs in response to SBA lectin. Characteristic pink → blue colour change results from optimisation of AuNP coating for SBA interaction, suggesting their potential use in identification of target lectins. Figure taken from Richards *et al.*[188].

AuNPs also serve as biocompatible, easily-functionalised, bioconjugate scaffolds.[130,152,169,175,196–203] Thermally-stable DNA/AuNP conjugates were synthesized through direct Au-S linkages by Li *et al.*[198], using a variety of thiol structures: aliphatic and cyclic, mono- and bi-dentate. They found colloidal stability to be greater with higher DNA packing density (higher density with monodentate ligands) and aliphatic anchor structures, as determined by the slower release of DNA from the conjugates upon exposure to 85 °C heat. Studies by the Mirkin group have looked into DNA detection with oligonucleotide-AuNP conjugates, and their sequence-dependent stability.[196,197] In these studies, complementary oligonucleotide sequences on AuNPs caused aggregation of AuNPs coated with their respective target DNA, detected as a pink → blue solution colour shift.[189]

In another study, by Clark *et al.*[199], 80 nm gold was coated with transferrin (Tf) via an acid-cleavable linker, to allow crossing of the blood brain barrier by receptor-mediated transcytosis. These AuNPs were found in an *in vivo* mouse model to bind to transferrin receptors on one side of the blood brain barrier, and separate from the transferrin conjugate due to an increased acidity during the transcytosis process to enable crossing into the brain parenchyma. This trafficking was found to be enhanced relative to both Tf-AuNP conjugates with non-cleavable linkers, and Ab-AuNP conjugates with acid-cleavable linkers, suggesting both the Tf and acid-cleavage are needed. Biodistribution of AuNPs was determined in mouse brain tissue slices *via* the presence of silver-enhanced AuNP clusters in optical microscopy.

Tan *et al.*[175] used EDC/NHS chemistry to attach FITC-labelled anti-VEGF (vascular endothelial growth factor) antibody to carboxylic acid terminated, PEG-coated AuNPs (see Figure 1-11). The shape, size and dispersity of these bioconjugates were assessed by TEM and DLS, and protein valency was determined as a function of protein fluorescence versus AuNP absorbance spectra. ICP-MS assessed cell internalisation of the AuNP bioconjugates, and cell viability was shown to decrease dose-dependently with bioconjugate incubation. VEGF induces proliferation in human umbilical vein endothelial cells in a dose-dependent, temporal manner.[175] This is reduced by pre-incubation with free anti-VEGF Abs, which act by binding to cellular VEGF. Pre-incubation with anti-VEGF-PEG-AuNP bioconjugates showed partial retention of Ab function by decreasing cell proliferation, but unfortunately Au functionalised with anti-horseradish peroxidase control also showed this activity. It could be that the use of the uncontrolled, non-specific EDC/NHS coupling reaction for bioconjugation resulted in a loss of Ab function: ie. these results could be attributed to the presence of any Ab/AuNP bioconjugate.

AuNP bioconjugates may also been synthesized by more specific "click" or bioorthogonal techniques.[152,204] Copper-catalysed alkyne/azide chemistry has been used to attach azide-functionalised AuNPs with *Thermomyces lanuginosus* lipase, and successful conjugation and retention of the enzymatic activity relative to unconjugated lipase was confirmed through gel electrophoresis and a fluorometric activity assay respectively (see Figure 1-5).[152] Aufaure *et al.*[204] used inverse electron demand Diels-Alder chemistry, with an alkene-terminal 1-hydroxy-1,1-methylenebisphosphonate conjugated to AuNPs. Tetrazine 3,6-dipyridin-2-yl-1,2,4,5-tetrazine was then conjugated to the AuNPs in one-pot, bioorthogonal conditions, and verified by XPS. Following this experiment, 6-methyl-tetrazine-sulfo-cyanine 5 (a near IR probe) was then also successfully conjugated to the original modified AuNPs, as proof that this chemistry has possible application in the synthesis of materials for biological imaging.

Inspired by affinity chromatography techniques, the oligomeric histidine affinity tag has also been used to conjugate proteins to the AuNP surface (see Figure 1-12).[200,201]

In a study by Hainfeld *et al.*[201], a His-tagged adenovirus “knob” protein was attached to nickel-coordinated, NTA-dipeptide-thiol pre-conjugated to the surface of small (either 1.6 or 1.8 nm diameter, though the larger core showed greater conjugation success) AuNPs. Successful conjugation was verified by column chromatography, UV-Vis and TEM, and the conjugate retained protein receptor binding activity relative to unconjugated protein.

From these various examples, AuNPs are shown to be a good, stable, bioorthogonal scaffold for the attachment of biomolecules for the purposes of assessing protein structure and function.

1.5. Conclusions

There are a variety of scaffolds available for the conjugation of biological or biorthogonal moieties, but there is currently a dearth of fully biorthogonal techniques to fulfil these conjugations. Chemical techniques tend to have limitations to their efficacy or biocompatibility (for example through the use of UV light or copper), whilst the use of enzymatic strategies results in a further layer of complexity.

Herein, novel techniques are proposed to overcome these limitations, with “click”-like thiolactone polymer chemistry (**Chapter 2**) and protein tags on AuNP scaffolds (**Chapters 3 and 4**) in order to investigate protein function. These techniques aim to use close-to native protein structure with biocompatible synthetic techniques in order to explore protein function in systems comparable to *in vivo*.

1.6. References

(1) Stryer, L.; Berg, J. M.; Tymoczko, J. L. *Biochemistry*, 6th ed.; W. H. Freeman: New York, USA, 2006.

(2) Klotz, I. M.; Langerman, N. R.; Darnall, D. W. *Annu. Rev. Biochem.* **1970**, *39*, 25.

(3) Howard, E. I.; Blakeley, M. P.; Haertlein, M.; Haertlein, I. P.; Mitschler, A.; Fisher, S. J.; Siah, A. C.; Salvay, A. G.; Popov, A.; Dieckmann, C. M.; Petrova, T.; Podjarny, A. *J. Mol. Recognit.* **2011**, *24* (4), 724.

(4) Merritt, E. A.; Sarfaty, S.; Akker, F. Van Den; L’Hoir, C.; Martial, J. A.; Hol, W. G. J. *Protein Sci.* **1994**, *3* (2), 166.

(5) Sletten, E. M.; Bertozzi, C. R. *Acc. Chem. Res.* **2011**, *44* (9), 666.

(6) Sletten, E. M.; Bertozzi, C. R. *Angew. Chem., Int. Ed.* **2009**, *48* (38), 6974.

(7) Prescher, J. A.; Bertozzi, C. R. *Nat. Chem. Biol.* **2005**, *1* (1), 13.

(8) Baskin, J. M.; Bertozzi, C. R. *QSAR Comb. Sci.* **2007**, *26* (11–12), 1211.

(9) Chen, Y. X.; Triola, G.; Waldmann, H. *Acc. Chem. Res.* **2011**, *44* (9), 762.

(10) Rosano, G. L.; Ceccarelli, E. A. *Front. Microbiol.* **2014**, *5* (April), 1.

(11) Makrides, S. C. *Microbiol. Rev.* **1996**, *60* (3), 512.

(12) Baneyx, F. *Curr. Opin. Biotech*. **1999**, pp 411–421.

(13) Stevens, R. C. *Structure* **2000**, *8* (072/1), R177.

(14) Zhou, Q. *Biomedicines* **2017**, *5* (4), 64.

(15) Behrens, C. R.; Hooker, J. M.; Obermeyer, A. C.; Romanini, D. W.; Katz, E. M.; Francis, M. B. *J. Am. Chem. Soc.* **2011**, *133* (41), 16398.

(16) Jiang, M.; Jin, Y.; Yang, H.; Fu, H. *Sci. Rep.* **2016**, *6*, 1.

(17) Schoffelen, S.; Lambermon, M. H. L.; Eldijk, M. B. Van; Hest, J. C. M. Van.

Bioconjug. Chem. **2008**, *19*, 1127.

(18) Wals, K.; Ovaa, H. *Front. Chem.* **2014**, *2* (April), 1.

(19) Lai, Y.-T.; Chang, Y.-Y.; Hu, L.; Yang, Y.; Chao, A.; Du, Z.-Y.; Tanner, J. A.; Chye, M.-L.; Qian, C.; Ng, K.-M.; Li, H.; Sun, H. *Proc. Natl. Acad. Sci.* **2015**, *112* (10), 2948.

(20) Graff, R. A.; Swanson, T. M.; Strano, M. S. *Chem. Mater.* **2008**, *20* (5), 1824.

(21) Kubalek, E. W.; Le Grice, S. F. J.; Brown, P. O. *J. Struct. Biol.* **1994**, pp 117–123.

(22) Sigal, G. B.; Bamdad, C.; Barberis, A.; Strominger, J.; Whitesides, G. M. *Anal. Chem.* **1996**, *68* (3), 490.

(23) Lauer, S. A.; Nolan, J. P. *Cytometry* **2002**, *48* (3), 136.

(24) Braun, A. C.; Gutmann, M.; Lühmann, T.; Meinel, L. *J. Control. Release* **2018**, *273* (January), 68.

(25) Gaur, R. K. *IIOAB J.* **2014**, *5* (2), 6.

(26) Lins, L.; Thomas, A.; Brasseur, R. *Protein Sci.* **2003**, *12* (7), 1406.

(27) Kapust, R. B.; Waugh, D. S. *Protein Sci.* **1999**, *8*, 1668.

(28) LaVallie, E. R.; DiBlasio, E. A.; Kovacic, S.; Grant, K. L.; Schendel, P. F.; McCoy, J. M. *Nat. Biotechnol.* **1993**, *11*, 187.

(29) Smith, D. B.; Johnson, K. S. *Gene* **1988**, *67* (1), 31.

(30) Cole, N. B. *Curr. Protoc. Protein Sci.* **2013**, *73* (30), 1.

(31) Butt, T. R.; Edavettal, S. C.; Hall, J. P.; Mattern, M. R. *Protein Expr. Purif.* **2005**, *43* (1), 1.

(32) Abo, M.; Minakami, R.; Miyano, K.; Kamiya, M.; Nagano, T.; Urano, Y.; Sumimoto, H. *Anal. Chem.* **2014**, *86* (12), 5983.

(33) Wang, C.; Song, X.; Han, Z.; Li, X.; Xu, Y.; Xiao, Y. *ACS Chem. Biol.* **2016**, *11* (7), 2033.

(34) Srikun, D.; Albers, A. E.; Nam, C. I.; Iavarone, A. T.; Chang, C. J. *J. Am. Chem. Soc.* **2010**, *132* (12), 4455.

(35) Freidel, C.; Kaloyanova, S.; Peneva, K. *Amino Acids* **2016**, *48* (6), 1357.

(36) Montoya, L. A.; Pluth, M. D. *Anal. Chem.* **2016**, *88* (11), 5769.

(37) Yu, Y.; Xia, J. *Sci. China Chem.* **2016**, *59* (7), 853.

(38) Meyer, D. E.; Chilkoti, A. *Nat. Biotechnol.* **1999**, *17* (11), 1112.

(39) Banki, M. R.; Feng, L.; Wood, D. W. *Nat. Methods* **2005**, *2* (9), 659.

(40) Lang, K.; Chin, J. W. *ACS Chem. Biol.* **2014**, *9* (1), 16.

(41) Lang, K.; Chin, J. W. *Chem. Rev.* **2014**, *114* (9), 4764.

(42) King, M.; Wagner, A. *Bioconjug. Chem.* **2014**, *25* (5), 825.

(43) Lueking, A.; Cahill, D. J.; Müllner, S. *Drug Discov. Today* **2005**, *10* (11), 789.

(44) Sato, H.; Ikeda, M.; Suzuki, K.; Hirayama, K. *Biochemistry* **1996**, *35* (40), 13072.

(45) Sperling, R. A.; Parak, W. J. *Philos. Trans. R. Soc. A Math. Phys. Eng. Sci.* **2010**, *368* (1915), 1333.

(46) Chen, X.; Wu, Y.-W. *Org. Biomol. Chem.* **2016**, *14* (24), 5417.

(47) Northrop, B. H.; Frayne, S. H.; Choudhary, U. *Polym. Chem.* **2015**, *6* (18), 3415.

(48) Köhn, M.; Breinbauer, R. *Angew. Chem., Int. Ed.* **2004**, *43* (24), 3106.

(49) Gamblin, D. P.; Scanlan, E. M.; Davis, B. G.; Ligation, G. *Chem. Rev.* **2009**, *109*, 131.

(50) Liu, S.; Edgar, K. J. *Biomacromolecules* **2015**, *16* (9), 2556.

(51) Van Berkel, S. S.; Van Eldijk, M. B.; Van Hest, J. C. M. *Angew. Chem., Int. Ed.* **2011**, *50* (38), 8806.

(52) Hackenberger, C. P. R.; Schwarzer, D. *Angew. Chem., Int. Ed.* **2008**, *47* (52), 10030.

(53) Lim, R. K. V; Lin, Q. *Chem. Commun.* **2010**, *46* (42), 7993.

(54) Tang, L.; Yin, Q.; Xu, Y.; Zhou, Q.; Cai, K.; Yen, J.; Dobrucki, L. W.; Cheng, J. *Chem. Sci.* **2015**, *6* (4), 2182.

(55) Agten, S. M.; Dawson, P. E.; Hackeng, T. M. *J. Pept. Sci.* **2016**, *22* (5), 271.

(56) Kang, K.; Park, J.; Kim, E. *Proteome Sci.* **2017**, *15* (1), 1.

(57) Šečkute, J.; Devaraj, N. K. *Curr. Opin. Chem. Biol.* **2013**, *17* (5), 761.

(58) Sletten, E. M.; Bertozzi, C. R. *J. Am. Chem. Soc.* **2011**, *133* (44), 17570.

(59) Jewett, J. C.; Bertozzi, C. R. *Chem. Soc. Rev.* **2010**, *39* (4), 1272.

(60) Baskin, J. M.; Prescher, J. A.; Laughlin, S. T.; Agard, N. J.; Chang, P. V.; Miller, I. A.; Lo, A.; Codelli, J. A.; Bertozzi, C. R. *Proc. Natl. Acad. Sci.* **2007**, *104* (43), 16793.

(61) Chang, P. V.; Prescher, J. A.; Sletten, E. M.; Baskin, J. M.; Miller, I. A.; Agard, N. J.; Lo, A.; Bertozzi, C. R. *Proc. Natl. Acad. Sci.* **2010**, *107* (5), 1821.

(62) Li, Z.; Qian, L.; Li, L.; Bernhammer, J. C.; Huynh, H. V.; Lee, J. S.; Yao, S. Q. *Angew. Chem., Int. Ed.* **2016**, *55* (6), 2002.

(63) Salehi, Y.; Hamzehloueian, M. *Tetrahedron* **2017**, *73* (31), 4634.

(64) Vrabel, M.; Kölle, P.; Brunner, K. M.; Gattner, M. J.; López-Carrillo, V.; De Vivie-Riedle, R.; Carell, T. *Chem. - Eur. J.* **2013**, *19* (40), 13309.

(65) Song, W.; Yu, Z.; Madden, M. M.; Lin, Q. *Mol. Biosyst.* **2010**, *6* (9), 1576.

(66) Lim, R. K. V.; Lin, Q. *Sci. China Chem.* **2010**, *53* (1), 61.

(67) Reuter, J. D.; Myc, A.; Hayes, M. M.; Gan, Z.; Roy, R.; Qin, D.; Yin, R.; Piehler, L. T.; Esfand, R.; Tomalia, D. A.; Baker, J. R. *Bioconjug. Chem.* **1999**, *10*, 271.

(68) Kobayashi, A.; Kobayashi, K.; Akaike, T. *J. Biomater. Sci. Polym. Ed.* **1992**, *3* (6), 499.

(69) Jones, M. W.; Otten, L.; Richards, S. J.; Lowery, R.; Phillips, D. J.; Haddleton, D. M.; Gibson, M. I. *Chem. Sci.* **2014**, *5* (4), 1611.

(70) Graham, B.; Fayter, A. E. R.; Houston, J. E.; Evans, R. C.; Gibson, M. I. *J. Am. Chem. Soc.* **2018**, *140* (17), 5682.

(71) Wilkins, L. E.; Phillips, D. J.; Deller, R. C.; Davies, G. L.; Gibson, M. I. *Carbohydr. Res.* **2015**, *405*, 47.

(72) Muthiah, M.; Park, I. K.; Cho, C. S. *Biotechnol. Adv.* **2013**, *31* (8), 1224.

(73) Meyers, S. R.; Grinstaff, M. W. *Chem. Rev.* **2012**, *112* (3), 1615.

(74) Huang, Y.; Wang, D.; Zhu, X.; Yan, D.; Chen, R. *Polym. Chem.* **2015**, *6* (15), 2794.

(75) Won, S.; Hindmarsh, S.; Gibson, M. I. *ACS Macro Lett.* **2018**, *7* (2), 178.

(76) Zeng, X.; Qu, K.; Rehman, A. *Acc. Chem. Res.* **2016**, *49* (9), 1624.

(77) Xu, C.; Huang, Y.; Wu, J.; Tang, L.; Hong, Y. *ACS Appl. Mater. Interfaces* **2015**, *7* (36), 20377.

(78) Kolomanska, J.; Johnston, P.; Gregori, A.; Fraga Domínguez, I.; Egelhaaf, H. J.; Perrier, S.; Rivaton, A.; Dagron-Lartigau, C.; Topham, P. D. *RSC Adv.* **2015**, *5* (82), 66554.

(79) Paik, B. A.; Mane, S. R.; Jia, X.; Kiick, K. L. *J. Mater. Chem. B* **2017**, *5* (42), 8274.

(80) Jung, S.; Kwon, I. *Polym. Chem.* **2016**, *7* (28), 4584.

(81) Desai, R. M.; Koshy, S. T.; Hilderbrand, S. A.; Mooney, D. J.; Joshi, N. S. *Biomaterials* **2015**, *50* (1), 30.

(82) Mavila, S.; Eivgi, O.; Berkovich, I.; Lemcoff, N. G. *Chem. Rev.* **2016**, *116* (3), 878.

(83) Glassner, M.; Maji, S.; De La Rosa, V. R.; Vanparijs, N.; Ryskulova, K.; De Geest, B. G.; Hoogenboom, R. *Polym. Chem.* **2015**, *6* (48), 8354.

(84) Nagahama, K.; Kimura, Y.; Takemoto, A. *Nat. Commun.* **2018**, *9* (1).

(85) Wu, C.; Jin, Y.; Schneider, T.; Burnham, D. R.; Smith, P. B.; Chiu, D. T. *Angew. Chem., Int. Ed.* **2010**, *49* (49), 9436.

(86) Vicent, M. J.; Ringsdorf, H.; Duncan, R. *Adv. Drug Deliv. Rev.* **2009**, *61* (13), 1117.

(87) Borchmann, D. E.; Carberry, T. P.; Weck, M. *Macromol. Rapid Commun.* **2014**, *35* (1), 27.

(88) Qi, Y.; Chilkoti, A. *Curr. Opin. Chem. Biol.* **2015**, *28*, 181.

(89) Caliceti, P.; Veronese, F. M. *Adv. Drug Deliv. Rev.* **2003**, *55* (10), 1261.

(90) Roberts, M. J.; Bentley, M. D.; Harris, J. M. *Adv. Drug Deliv. Rev.* **2002**, *54* (4), 459.

(91) Debets, M. F.; Van Berkel, S. S.; Schoffelen, S.; Rutjes, F. P. J. T.; Van Hest, J. C. M.; Van Delft, F. L. *Chem. Commun.* **2010**, *46* (1), 97.

(92) Deiters, A.; Cropp, T. A.; Summerer, D.; Mukherji, M.; Schultz, P. G. *Bioorganic Med. Chem. Lett.* **2004**, *14* (23), 5743.

(93) Sato, H. *Adv. Drug Deliv. Rev.* **2002**, *54* (4), 487.

(94) Wang, Y.-S.; Youngster, S.; Grace, M.; Bausch, J.; Bordens, R.; Wyss, D. F. *Adv. Drug Deliv. Rev.* **2002**, *54* (4), 547.

(95) Foser, S.; Schacher, A.; Weyer, K. A.; Brugger, D.; Dietel, E.; Marti, S.; Schreitmüller, T. *Protein Expr. Purif.* **2003**, *30* (1), 78.

(96) Gopin, A.; Ebner, S.; Attali, B.; Shabat, D. *Bioconjug. Chem.* **2006**, *17* (6), 1432.

(97) Yu, H.; Nie, Y.; Dohmen, C.; Li, Y.; Wagner, E. *Biomacromolecules* **2011**, *12* (6), 2039.

(98) Kinstler, O.; Molineux, G.; Treuheit, M.; Ladd, D.; Gegg, C. *Adv. Drug Deliv. Rev.* **2002**, *54*, 477.

(99) Abuchowski, A.; van Es, T.; Palczuk, N. C.; Davis, F. F. *J. Biol. Chem.* **1977**, *252* (11), 3578.

(100) Abuchowski, A.; Mccoy, J. R.; Palczuk, N. C.; Van Es, T.; Davis, F. F. *J. Biol. Chem.* **1977**, *252* (11), 3582.

(101) Rajender Reddy, K.; Modi, M. W.; Pedder, S. *Adv. Drug Deliv. Rev.* **2002**, *54*, 571.

(102) Pasut, G.; Veronese, F. M. *Adv. Drug Deliv. Rev.* **2009**, *61* (13), 1177.

(103) Bailon, P.; Palleroni, A.; Schaffer, C. A.; Spence, C. L.; Fung, W. J.; Porter, J. E.; Ehrlich, G. K.; Pan, W.; Xu, Z. X.; Modi, M. W.; Farid, A.; Berthold, W. *Bioconjug. Chem.* **2001**, *12* (2), 195.

(104) Collins, J.; Tanaka, J.; Wilson, P.; Kempe, K.; Davis, T. P.; Mcintosh, M. P.; Whittaker, M. R.; Haddleton, D. M. *Bioconjug. Chem.* **2015**, *26* (4), 633.

(105) Shi, Q.; Chen, X.; Lu, T.; Jing, X. *Biomaterials* **2008**, *29* (8), 1118.

(106) Sala, A.; Ehrbar, M.; Trentin, D.; Schoenmakers, R. G.; Vörös, J.; Weber, F. E. *Langmuir* **2010**, *26* (13), 11127.

(107) Mero, A.; Schiavon, M.; Veronese, F. M.; Pasut, G. *J. Control. Release* **2011**, *154* (1), 27.

(108) Arnusch, C. J.; Branderhorst, H.; De Kruijff, B.; Liskamp, R. M. J.; Breukink, E.; Pieters, R. J. *Biochemistry* **2007**, *46*, 13437.

(109) Dijkgraaf, I.; Rijnders, A. Y.; Soede, A.; Dechesne, A. C.; Van Esse, G. W.; Brouwer, A. J.; Corstens, F. H. M.; Boerman, O. C.; Rijkers, D. T. S.; Liskamp, R. M. J. *Org. Biomol. Chem.* **2007**, *5* (6), 935.

(110) Dirks, A. J.; Van Berkel, S. S.; Hatzakis, N. S.; Opsteen, J. A.; Van Delft, F. L.; Cornelissen, J. J. L. M.; Rowan, A. E.; Van Hest, J. C. M.; Rutjes, F. P. J. T.; Nolte, R. J. M. *Chem. Commun.* **2005**, No. 33, 4172.

(111) Lühmann, T.; Schmidt, M.; Leiske, M. N.; Spieler, V.; Majdanski, T. C.; Grube, M.; Hartlieb, M.; Nischang, I.; Schubert, S.; Schubert, U. S.; Meinel, L. *ACS Biomater. Sci. Eng.* **2017**, *3* (3), 304.

(112) Lee, J. P.; Kassianidou, E.; MacDonald, J. I.; Francis, M. B.; Kumar, S. *Biomaterials* **2016**, *102*, 268.

(113) Reynhout, I. C.; Cornelissen, J. J. L. M.; Nolte, R. J. M. *J. Am. Chem. Soc.* **2007**, *129* (8), 2327.

(114) Simon, M.; Zangemeister-Wittke, U.; Plückthun, A. *Bioconjug. Chem.* **2012**, *23* (2), 279.

(115) Algar, W. R.; Prasuhn, D. E.; Stewart, M. H.; Jennings, T. L.; Blanco-Canosa, J. B.; Dawson, P. E.; Medintz, I. L. *Bioconjug. Chem.* **2011**, *22* (5), 825.

(116) Johnson, B. J.; Russ Algar, W.; Malanoski, A. P.; Ancona, M. G.; Medintz, I. L. *Nano Today* **2014**, *9* (1), 102.

(117) Xie, J.; Lee, S.; Chen, X. *Adv. Drug Deliv. Rev.* **2010**, *62* (11), 1064.

(118) Avvakumova, S.; Colombo, M.; Tortora, P.; Prosperi, D. *Trends Biotechnol.* **2014**, *32* (1), 11.

(119) Palao-Suay, R.; Gómez-Mascaraque, L. G.; Aguilar, M. R.; Vázquez-Lasa, B.; Román, J. S. *Prog. Polym. Sci.* **2016**, *53*, 207.

(120) Konishcheva, E.; Daubian, D.; Gaitzsch, J.; Meier, W. *Helv. Chim. Acta* **2018**, *101* (2), 1.

(121) Lecommandoux, S.; Borsali, R. *Polym. Int.* **2005**, *55*, 1161.

(122) Mouffouk, F.; Simão, T.; Dornelles, D. F.; Lopes, A. D.; Sau, P.; Martins, J.; Abu-Salah, K. M.; Alrokayan, S. A.; Rosa da Costa, A. M.; dos Santos, N. R. *Int. J. Nanomedicine* **2015**, *10*, 63.

(123) Zhao, H.; Lin, Z. Y.; Yildirimer, L.; Dhinakar, A.; Zhao, X.; Wu, J. *J. Mater. Chem. B* **2016**, *4* (23), 4060.

(124) Messerschmidt, C.; Hofmann, D.; Kroeger, A.; Landfester, K.; Mailï¿½nder, V.; Lieberwirth, I. *Beilstein J. Nanotechnol.* **2016**, *7* (1), 1296.

(125) Zielinska, E.; Tukaj, C.; Radomski, M. W.; Inkielewicz-Stepniak, I. *PLoS One* **2016**, *11* (10), e0164137.

(126) Poussard, S.; Decossas, M.; Le Bihan, O.; Mornet, S.; Naudin, G.; Lambert, O. *Int. J. Nanomedicine* **2015**, *10*, 1479.

(127) Costanzo, M.; Carton, F.; Marengo, A.; Berlier, G.; Stella, B.; Arpicco, S.; Malatesta, M. *Eur. J. Histochem.* **2016**, *60* (2), 107.

(128) Chalovich, J. M.; Eisenberg, E. *Curr. Opin. Chem. Biol.* **2010**, *14* (6), 828.

(129) Sista, P.; Ghosh, K.; Martinez, J. S.; Rocha, R. C. *Polym. Rev.* **2014**, *54* (4), 627.

(130) Sapsford, K. E.; Algar, W. R.; Berti, L.; Gemmill, K. B.; Casey, B. J.; Oh, E.; Stewart, M. H.; Medintz, I. L. *Chem. Rev.* **2013**, *113* (3), 1904.

(131) Erathodiyil, N.; Ying, J. Y. *Acc. Chem. Res.* **2011**, *44* (10), 925.

(132) Punna, S.; Kaltgrad, E.; Finn, M. G. *Bioconjug. Chem.* **2005**, *16* (6), 1536.

(133) Zhang, S.; Chan, K. H.; Prud'Homme, R. K.; Link, A. J. *Mol. Pharm.* **2012**, *9* (8), 2228.

(134) Duckworth, B. P.; Xu, J.; Taton, T. A.; Guo, A.; Distefano, M. D. *Bioconjug. Chem.* **2006**, *17* (4), 967.

(135) Haun, J. B.; Devaraj, N. K.; Hilderbrand, S. A.; Lee, H.; Weissleder, R. *Nat. Nanotechnol.* **2010**, *5* (9), 660.

(136) Peterson, V. M.; Castro, C. M.; Lee, H.; Weissleder, R. *ACS Nano* **2012**, *6* (4), 3506.

(137) Chung, H. J.; Reiner, T.; Budin, G.; Min, C.; Liong, M.; Issadore, D.; Lee, H.; Weissleder, R. *ACS Nano* **2011**, *5* (11), 8834.

(138) Tassa, C.; Shaw, S. Y.; Weissleder, R. *Acc. Chem. Res.* **2011**, *44* (10), 842.

(139) Sanjaya, K. C.; Ranzoni, A.; Watterson, D.; Young, P.; Cooper, M. A. *Biosens. Bioelectron.* **2015**, *67*, 769.

(140) Hou, S.; Choi, J. S.; Garcia, M. A.; Xing, Y.; Chen, K. J.; Chen, Y. M.; Jiang, Z. K.; Ro, T.; Wu, L.; Stout, D. B.; Tomlinson, J. S.; Wang, H.; Chen, K.; Tseng, H. R.; Lin, W. Y. *ACS Nano* **2016**, *10* (1), 1417.

(141) Du, L.; Qin, H.; Ma, T.; Zhang, T.; Xing, D. *ACS Nano* **2017**, *11* (9), 8930.

(142) Selvan, S. T.; Tan, T. T.; Ying, J. Y. *Adv. Mater.* **2005**, *17* (13), 1620.

(143) Yhee, J. Y.; Lee, S. J.; Lee, S.; Song, S.; Min, H. S.; Kang, S. W.; Son, S.; Jeong, S. Y.; Kwon, I. C.; Kim, S. H.; Kim, K. *Bioconjug. Chem.* **2013**, *24* (11),

1850.

(144) Binder, W. H.; Sachsenhofer, R.; Straif, C. J.; Zirbs, R. *J. Mater. Chem.* **2007**, *17* (20), 2125.

(145) Polito, L.; Monti, D.; Caneva, E.; Delnevo, E.; Russo, G.; Prosperi, D. *Chem. Commun.* **2008**, *8* (5), 621.

(146) Galbiati, E.; Cassani, M.; Verderio, P.; Martegani, E.; Colombo, M.; Tortora, P.; Mazzucchelli, S.; Prosperi, D. *Bioconjug. Chem.* **2015**, *26* (4), 680.

(147) Zhao, T.; Li, T.; Liu, Y. *Nanoscale* **2017**, *9* (28), 9841.

(148) Parker, C. L.; Yang, Q.; Yang, B.; McCallen, J. D.; Park, S. I.; Lai, S. K. *Acta Biomater.* **2017**, *63*, 181.

(149) Chan, L.; Cross, H. F.; She, J. K.; Cavalli, G.; Martins, H. F. P.; Neylon, C. *PLoS One* **2007**, *2* (11), 1.

(150) Van Lith, S. A. M.; Van Duijnhoven, S. M. J.; Navis, A. C.; Leenders, W. P. J.; Dolk, E.; Wennink, J. W. H.; Van Nostrum, C. F.; Van Hest, J. C. M. *Bioconjug. Chem.* **2017**, *28* (2), 539.

(151) Lin, P. C.; Ueng, S. H.; Yu, S. C.; Jan, M. D.; Adak, A. K.; Yu, C. C.; Lin, C. C. *Org. Lett.* **2007**, *9* (11), 2131.

(152) Brennan, J. L.; Hatzakis, N. S.; Tshikhudo, T. R.; Dirvianskyte, N.; Razumas, V.; Patkar, S.; Vind, J.; Svendsen, A.; Nolte, R. J. M.; Rowan, A. E.; Brust, M. *Bioconjug. Chem.* **2006**, *17* (6), 1373.

(153) Koo, H.; Lee, S.; Na, J. H.; Kim, S. H.; Hahn, S. K.; Choi, K.; Kwon, I. C.; Jeong, S. Y.; Kim, K. *Angew. Chem., Int. Ed.* **2012**, *51* (47), 11836.

(154) Lee, S.; Koo, H.; Na, J. H.; Han, S. J.; Min, H. S.; Lee, S. J.; Kim, S. H.; Yun, S. H.; Jeong, S. Y.; Kwon, I. C.; Choi, K.; Kim, K. *ACS Nano* **2014**, *8* (3), 2048.

(155) Gruttner, C.; Muller, K.; Teller, J. *IEEE Trans. Magn.* **2013**, *49* (1), 172.

(156) Feldborg, L. N.; Jølck, R. I.; Andresen, T. L. *Bioconjug. Chem.* **2012**, *23* (12), 2444.

(157) Pasold, J.; Zderan, K.; Heskamp, B.; Grüttner, C.; Lüthen, F.; Tischer, T.; Jonitz-Heincke, A.; Bader, R. *Int. J. Nanomedicine* **2015**, *10*, 1131.

(158) Ueda, T.; Tamura, T.; Hamachi, I. *ACS Sensors* **2018**, *3* (3), 527.

(159) Aubin-Tam, M. E.; Hamad-Schifferli, K. *Biomed. Mater.* **2008**, *3* (3), 1.

(160) Kim, J. S.; Velancia, A.; Liu, R.; Lin, W. *Bioconjug. Chem.* **2007**, *18* (2), 333.

(161) England, C. G.; Luo, H.; Cai, W. *Bioconjug. Chem.* **2015**, *26* (6), 975.

(162) Los, G. V; Encell, L. P.; Mcdougall, M. G.; Hartzell, D. D.; Karassina, N.; Simpson, D.; Mendez, J.; Zimmerman, K.; Otto, P.; Vidugiris, G.; Zhu, J. *ACS Chem. Biol.* **2008**, *3* (6), 373.

(163) Hirata, T.; Terai, T.; Yamamura, H.; Shimonishi, M.; Komatsu, T.; Hanaoka, K.; Ueno, T.; Imaizumi, Y.; Nagano, T.; Urano, Y. *Anal. Chem.* **2016**, *88* (5), 2693.

(164) Brun, M. A.; Griss, R.; Reymond, L.; Tan, K. T.; Piguet, J.; Peters, R. J. R. W.; Vogel, H.; Johnsson, K. *J. Am. Chem. Soc.* **2011**, *133* (40), 16235.

(165) Bannwarth, M.; Corêa, I. R.; Sztretye, M.; Pouvreau, S.; Fellay, Ci.; Aebischer, A.; Royer, L.; Ríos, E.; Johnsson, K. *ACS Chem. Biol.* **2009**, *4* (3), 179.

(166) Schena, A.; Johnsson, K. *Angew. Chem., Int. Ed.* **2014**, *53* (5), 1302.

(167) Masharina, A.; Reymond, L.; Maurel, D.; Umezawa, K.; Johnsson, K. *J. Am. Chem. Soc.* **2012**, *134* (46), 19026.

(168) Brun, M. A.; Tan, K. T.; Griss, R.; Kielkowska, A.; Reymond, L.; Johnsson, K. *J. Am. Chem. Soc.* **2012**, *134* (18), 7676.

(169) Daniel, M. C. M.; Astruc, D. *Chem. Rev.* **2004**, *104*, 293.

(170) Low, A.; Bansal, V. *Biomed. Imaging Interv. J.* **2010**, *6* (1), 3.

(171) Mori, T.; Hegmann, T. *J. Nanoparticle Res.* **2016**, *18* (10), 1.

(172) Haiss, W.; Thanh, N. T. K.; Aveyard, J.; Fernig, D. G. *Anal. Chem.* **2007**, *79* (11), 4215.

(173) Zheng, T.; Bott, S.; Huo, Q. *ACS Appl. Mater. Interfaces* **2016**, *8* (33), 21585.

(174) Ieong, N. S.; Brebis, K.; Daniel, L. E.; Reilly, R. K. O.; Gibson, M. I. *Chem. Commun.* **2011**, *47*, 11627.

(175) Tan, G.; Kantner, K.; Zhang, Q.; Soliman, M.; del Pino, P.; Parak, W.; Onur, M.; Valdeperez, D.; Rejman, J.; Pelaz, B. *Nanomaterials* **2015**, *5* (3), 1297.

(176) Huang, X.; El-Sayed, I. H.; Yi, X.; El-Sayed, M. A. *J. Photochem. Photobiol. B Biol.* **2005**, *81* (2), 76.

(177) Pache, C.; Bocchio, N. L.; Bouwens, A.; Villiger, M.; Berclaz, C.; Goulley, J.; Gibson, M. I.; Santschi, C.; Lasser, T. *Opt. Express* **2012**, *20* (19), 21385.

(178) Malatesta, M.; Zancanaro, C.; Costanzo, M.; Cisterna, B.; Pellicciari, C. *Eur. J. Histochem.* **2013**, *57* (3), 168.

(179) Freese, C.; Gibson, M.; Mainz, J. G. *Part. Fibre Toxicol.* **2012**, *9* (23), 1.

(180) Peckys, D. B.; De Jonge, N. *Nano Lett.* **2011**, *11* (4), 1733.

(181) Freese, C.; Unger, R. E.; Deller, R. C.; Gibson, M. I.; Brochhausen, C.; Klok, H. A.; Kirkpatrick, C. J. *Biomater. Sci.* **2013**, *1* (8), 824.

(182) Gunduz, N.; Ceylan, H.; Guler, M. O.; Tekinay, A. B. *Sci. Rep.* **2017**, *7* (February), 1.

(183) Azubel, M.; Koivisto, J.; Malola, S.; Bushnell, D.; Hura, G. L.; Koh, A. L.; Tsunoyama, H.; Tsukuda, T.; Pettersson, M.; Häkkinen, H.; Kornberg, R. D. *Science (80-.).* **2014**, *345* (6199), 909.

(184) Dreaden, E. C.; Alkilany, A. M.; Huang, X.; Murphy, C. J.; El-Sayed, M. A. *Chem. Soc. Rev.* **2012**, *41* (7), 2740.

(185) Tsai, D. H.; Shelton, M. P.; DelRio, F. W.; Elzey, S.; Guha, S.; Zachariah, M. R.; Hackley, V. A. *Anal. Bioanal. Chem.* **2012**, *404* (10), 3015.

(186) Luo, W.; Gobbo, P.; Gunawardene, P. N.; Workentin, M. S. *Langmuir* **2017**, *33* (8), 1908.

(187) Chen, Y.; Xianyu, Y.; Jiang, X. *Acc. Chem. Res.* **2017**, *50* (2), 310.

(188) Richards, S. J.; Gibson, M. I. *ACS Macro Lett.* **2014**, *3* (10), 1004.

(189) Rosi, N. L.; Mirkin, C. A. *Chem. Rev.* **2005**, *105* (4), 1547.

(190) Marradi, M.; Chiodo, F.; García, I.; Penadés, S. *Chem. Soc. Rev.* **2013**, *42* (11), 4728.

(191) Richards, S. J.; Fullam, E.; Besra, G. S.; Gibson, M. I. *J. Mater. Chem. B* **2014**, *2* (11), 1490.

(192) Tengdelius, M.; Gurav, D.; Konradsson, P.; Påhlsson, P.; Griffith, M.; Oommen, O. P. *Chem. Commun.* **2015**, *51* (40), 8532.

(193) Lin, C. C.; Yeh, Y. C.; Yang, C. Y.; Chen, C. L.; Chen, G. F.; Chen, C. C.; Wu, Y. C. *J. Am. Chem. Soc.* **2002**, *124* (14), 3508.

(194) Rodríguez, E.; Schetters, S. T. T.; Van Kooyk, Y. *Nat. Rev. Immunol.* **2018**, *18* (3), 204.

(195) Paszek, M. J.; Dufort, C. C.; Rossier, O.; Bainer, R.; Mouw, J. K.; Godula, K.; Hudak, J. E.; Lakins, J. N.; Wijekoon, A. C.; Cassereau, L.; Rubashkin, M. G.; Magbanua, M. J.; Thorn, K. S.; Davidson, M. W.; Rugo, H. S.; Park, J. W.; Hammer, D. A.; Giannone, G.; Bertozzi, C. R.; Weaver, V. M. *Nature* **2014**, *511* (7509), 319.

(196) Storhoff, J. J.; Elghanian, R.; Mirkin, C. A.; Letsinger, R. L. *Langmuir* **2002**, *18* (17), 6666.

(197) Stoeva, S. I.; Lee, J. S.; Thaxton, C. S.; Mirkin, C. A. *Angew. Chem., Int. Ed.* **2006**, *45* (20), 3303.

(198) Li, F.; Zhang, H.; Dever, B.; Li, X.-F.; Le, X. C. *Bioconjug. Chem.* **2013**, *24* (11), 1790.

(199) Clark, A. J.; Davis, M. E. *Proc. Natl. Acad. Sci.* **2015**, *112* (40), 12486.

(200) Aldeek, F.; Muhammed, M. A. H.; Palui, G.; Zhan, N.; Mattoussi, H. *ACS Nano* **2013**, *7* (3), 2509.

(201) Hainfeld, J. F.; Liu, W.; Halsey, C. M. R.; Freimuth, P.; Powell, R. D. *J. Struct. Biol.* **1999**, *127* (2), 185.

(202) Boyles, M. S. P.; Kristl, T.; Andosch, A.; Zimmermann, M.; Tran, N.; Casals,

E.; Himly, M.; Puntes, V.; Huber, C. G.; Lütz-Meindl, U.; Duschl, A. *J. Nanobiotechnology* **2015**, *13* (1), 1.

(203) Storhoff, J. J.; Mirkin, C. A. *Chem. Rev.* **1999**, *99* (7), 1849.

(204) Aufaure, R.; Hardouin, J.; Millot, N.; Motte, L.; Lalatonne, Y.; Guénin, E. *Chem. - Eur. J.* **2016**, *22* (45), 16022.

(205) Lu/Yang/Cai, - Lu, L.; Yang, N.; Cai, Y. *Chem. Comm.* **2005**, *0*, 5287.

(206) Congdon, T. R.; Notman, R.; Gibson, M. I. *Biomacromolecules* **2016**, *17* (9), 3033.

(207) Rudolph/Espeel/DuPrez - Rudolph, T.; Espeel, P.; Du Prez, F. E.; Schacher, F. H. *Polym. Chem.* **2015**, *6* (23), 4240.

(208) Skey, J.; Reilly, R. K. O. *Chem. Comm.* **2008**, *35,* 4183.

(209) Gibson, M. I.; Fröhlich, E.; Klok, H. *J. Polym. Sci, Part A: Polym. Chem.* **2009**, 47, 4332.

(210) Stamenović, M. M.; Espeel, P.; Baba, E.; Yamamoto, T.; Tezuka, Y.; Du Prez, F. E. *Polym. Chem.* **2013**, *4* (1), 184.

(211) Song, E.; Manganiello, M. J.; Chow, Y. H.; Bilal, G.; Convertine, A. J.; Stayton, P. S..; Schnapp, L. M.; Ratner, D. M. *Biomat.* **2012**, *33* (28), 6889.

(212) Cameron, N. R.; Spain, S. G.; Kingham, J. A.; Weck, S.; Albertin, L.; Barker, C. A. Battaglia, G.; Smart, T.; Blanazs, A. *Faraday Discussions* **2008**, *139*, 359.

(213) Richards, S. J.; Gibson, M. I. *ACS Macro Lett.* **2014**, *3* (10), 1004.

(214) Parry, A. L.; Clemson, N. A.; Ellis, J.; Bernhard, S. S. R.; Davis, B. G.; Cameron, N. R. *J. Am. Chem. Soc.* **2013**, *135* (25), 9362.

1.7. Thesis summary

The following chapters detail bioorthogonal approaches to the synthesis of materials (nanoparticles and polymers) in order to investigate the activity of adhesive proteins: namely, *Vibrio cholerae* toxin's adhesive subunit (CTxB), the ice-binding protein antifreeze type III, and the proposed adhesive protein segments of *Photorhabdus* bacteria's Photorhabdus virulence cassettes.

Chapter 2.

In the glycobiology sphere, there is interest in the development of multivalent glycan mimics that may have applications in anti-adhesive therapy against lectin proteins on pathogen cellular surfaces or pathogen toxins. Novel bifunctional glycopolymers with tuneable secondary functionality, carbohydrate density and linker length were described and tested against CTxB, and the more promiscuous ricin communis agglutinin to assess both binding capacity and lectin specificity. Glycopolymers with a sugar secondary functionality (glucosamine rather than benzylamine), low carbohydrate density (5 % of polymer repeat units), and linker length appropriate to interact with CTxB (allyl rather than hexenyl) were found to be more specific and active.

Chapter 3.

The impact of branching or multivalency on the activity of antifreeze-active macromolecules is of interest in the development of biocompatible cryopreservatives with enhanced ice recrystallisation inhibitory activity (IRI). The impact of tethering antifreeze compounds to a multivalent, dendrimer-like, small (~4 nm diameter) gold nanoparticle (AuNP) scaffold was investigated: (poly(vinyl acetate) polymer (PVA) and antifreeze type III protein (AFP). These studies showed this tethering to have either no impact on activity, with no significant difference between the activity of PVA and PVA/AuNP conjugates, or a slight increase in activity, with AFP/AuNP conjugates showing a ~10 % decrease in ice crystal sizes relative to free monomeric AFP of the same concentration.

Chapter 4.

The binding activity of a newly-described adhesive "tail fibre" segment of three different Photorhabdus virulence cassette proteins (PVC*lumt*_Pvc13, PVC*pnf*_Pvc13 and PVC*unit4*_Pvc13) was evaluated utilising cell incubation studies of protein/AuNP conjugates (assessed by ICP-OES), glycan and lipid arrays, and pull-down assays followed by quantitative proteomics. A variety of potential glycan and protein candidates were identified by the glycan and pull-down experiments respectively.

2. Doubly-modified thiolactone polymers with anti-adhesive activity against cholera toxin

2.1. Chapter Summary

Multivalent glycomaterials show enhanced binding affinity to lectins due to the cluster glycoside effect, but often lack selectivity towards the desired lectin target due to the need to simplify a complex glycan structure into monosaccharides presented on the polymer side chain. For example, cholera toxin has a deep galactose binding pocket with an allosteric site binding neuraminic acid on the native GM-1 glycan, which traditional non-specific glycopolymers do not target, and hence offer an opportunity to use polymer architecture to tune selectivity.

Herein we produce more precise mimics of the natural 3-D glycan structures by utilising thiolactone chemistry. This chemistry allowed the incorporation of two distinct sugar residues in sequence in order, with the aim to interact with both the primary and allosteric binding pockets of the cholera toxin subunit. The choice of secondary, non-binding unit dramatically influences the affinity and selectivity towards cholera toxin. Kinetic analysis by bio-layer interferometry further confirmed this effect with the residence times of these glycopolymers, with highest affinity and selectivity in the structures with a galactose-linker length appropriate for the CTx binding site, and secondary glucosamine residue.

These doubly-modified glycopolymers, developed using simply "click"-like chemistries, have the potential to further exploit the native structure of the lectins' binding pocket.

2.2. Introduction

A large proportion of essential cell-cell binding processes are mediated through the binding of sugar-binding proteins (lectins) to complex polysaccharides (glycans): processes from fertilisation to glycoprotein transport and cancer malignancy.[1–6] In particular, many pathogens exploit these native glycans in order to adhere to the human cell surface, and this adhesion is a key step in both infection and the immune response.[2,7–13] As examples, mycobacteria interacts with glycan receptors on host macrophages[14]; the first step of influenza infection is the binding to extracellular sialic acid receptors[7]; and HIV binds to native lectins via mannose moieties presented on an envelop glycoprotein[15]. The exact sequence of the glycan, including stereochemistry, serves as a code which is "read" by the native target cell in order to elicit a specific response.[13] In fact, it is only in the formation of these complex, sometimes branched, oligosaccharide chains that so few monosaccharide building blocks can be used for such a large number of specific targets in nature.[13] The lectin binding pocket is therefore finely tuned to maximise the number of hydrogen bonds and hydrophobic interactions that form with its specific glycan ligand, which makes any change in structure very disfavoured.

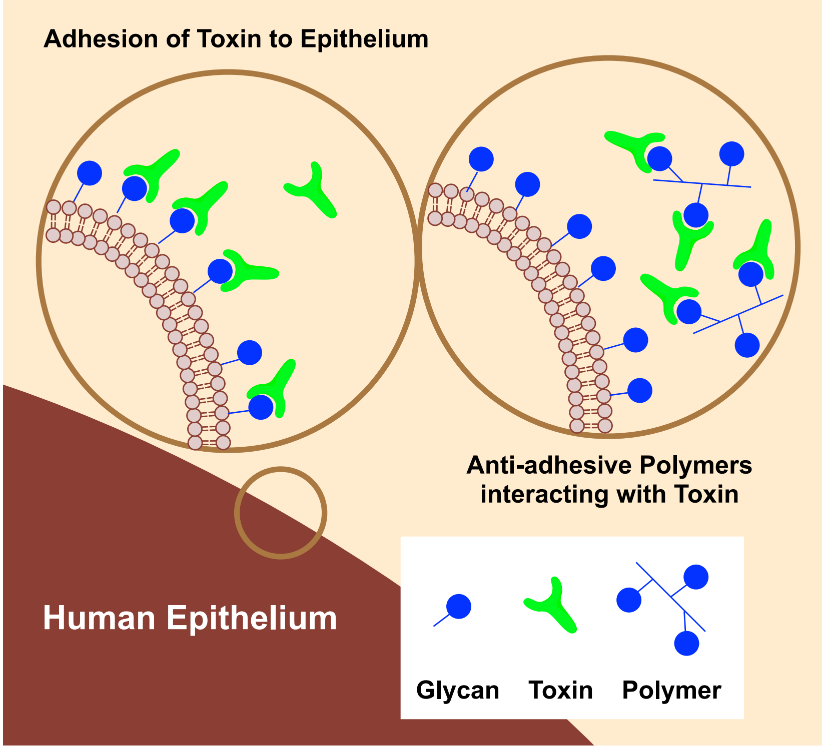

Figure 2-1. The principles of anti-adhesion therapy using anti-adhesive polymers.

In recent years, anti-adhesion therapy has been proposed as a technique circumventing the need for antibacterial therapies, which is desirable given the alarming increase in drug-resistant bacterial strains.[8,10] In particular, anti-adhesion therapy would involve interfering with the initial adhesion of pathogens to their hosts and therefore they avoid bactericidal methods that greatly enhance the likelihood of antibiotic resistance occurring (see Figure 2-1).[8,16] In this therapy, inhibitors can be designed to compete with the human host receptors for pathogen binding and thus need not be able to enter human cells or interact with them at all.

The physiological processes in which lectins are involved are adhesive or regulatory, with the multimeric structure of many of these lectins affording fine-tuning of the extent of response elicited. In monovalent form, glycan ligands bind only weakly to their lectins ($K_{D} = \text{mM}$) through noncovalent interactions.[13] In their multivalent form (as usually displayed on the cell surface) the affinities of these carbohydrates rises more than purely the multiple of their constituent residues (K_D = nM), and this is termed the cluster glycoside effect.[4,13,17–21] This effect is not fully understood; however it is hypothesized that it is largely an entropic effect of aggregation.[20]

Thus, multivalent synthetic systems such as polymers and nanoparticles, with the ability to display a large number of carbohydrate residues, have been applied to a range of lectin targets.[8,12,13,15,17,20,22–24] Reuter *et al.*[7] developed multivalent (dendritic polymers of various conformations) sialic acid polyacrylamides that had potentially at least 32-fold more activity in preventing influenza-induced agglutination of erythrocytes relative to monomeric sialic acid. By tuning the 3-D structure of these dendritic polymers, they found comb-branched and dendrigraft polymers have even more activity that more linear or spherical polymers, with up to 50,000-fold greater activity than the monomer.

Parry et al.[25] also exploited this cluster glycoside effect with glycopolymer-stabilised gold nanoparticles that were able to enhance antibody production in cancer cells. The Tn-antigen glycan (α-*N*-acetyl-*D*-galactosamine) is one of several core 1 mucin-type glycans overexpressed on the breast cancer cell surface. In this study, Parry *et al.* produced both polymers with a Tn-antigen glycan side chain and gold nanoparticles surface functionalised with this polymer to investigate the effect of the enhanced multivalency. They found the nanoparticles to have enhanced IgG antibody titre relative to the polymer after immunisation of New Zealand White rabbits, suggesting that these materials might be an avenue for the development of cancer vaccines.

2.2.1. Anti-adhesion of the Cholera Toxin lectin

Cholera is a highly contagious major waterborne disease that causes regular epidemics in areas of poor water access and sanitation, especially in cases of natural disaster where such infrastructure is heavily disrupted. It is estimated that 2.9 million cases, and 95,000 deaths, occur yearly worldwide (see Figure 2-2).[26] The gram-negative, motile *Vibrio cholerae* bacterium is responsible for the diarrheal symptoms of the disease, which cause severe dehydration and death within hours if not treated.[27,28] There is a lot of interest in developing anti-infectives to prevent cholera infection due to the limited scope of the current Vaxchora vaccine (which is currently only effective for serogroup 01).[16,29]

Cholera toxin (CTx, see Figure 2-3), produced by the bacterium *Vibrio cholerae* adheres to the human gut epithelium via GM-1 glycans presented on the cell surface.[28,30–36] This adhesion, as in all members of the AB_5 toxin family (containing five effectively-identical adhesive B subunits and one toxic A subunit), allows the toxin to enter the host cell, hijack its machinery and induce toxic effects.[34,37] The GM-1 receptor carries CTx from the plasma membrane to the endoplasmic reticulum to initiate this process.[37] This glycan is a branched pentasaccharide with a terminal galactose, and a sialic acid-terminated side chain proposed to also be key in CTx adhesion. The specific 3-D structure of this glycan is key in CTx adhesion: secreted *Vibrio cholerae* neuraminidases degrade the mucin layer of the gastrointestinal tract, converting higher-order gangliosides to GM-1.[30,33,36,38] That the presence of this enzyme is essential suggests that a locally-high concentration of GM-1 glycans is necessary to enable sufficient CTx attachment for successful infection: the five adhesive subunits of the toxin have the capacity to bind five GM-1 receptors at once.[31,39,40] Multivalency therefore seems a promising characteristic for designing a mimic of GM-1 for anti-CTx-adhesion effects.

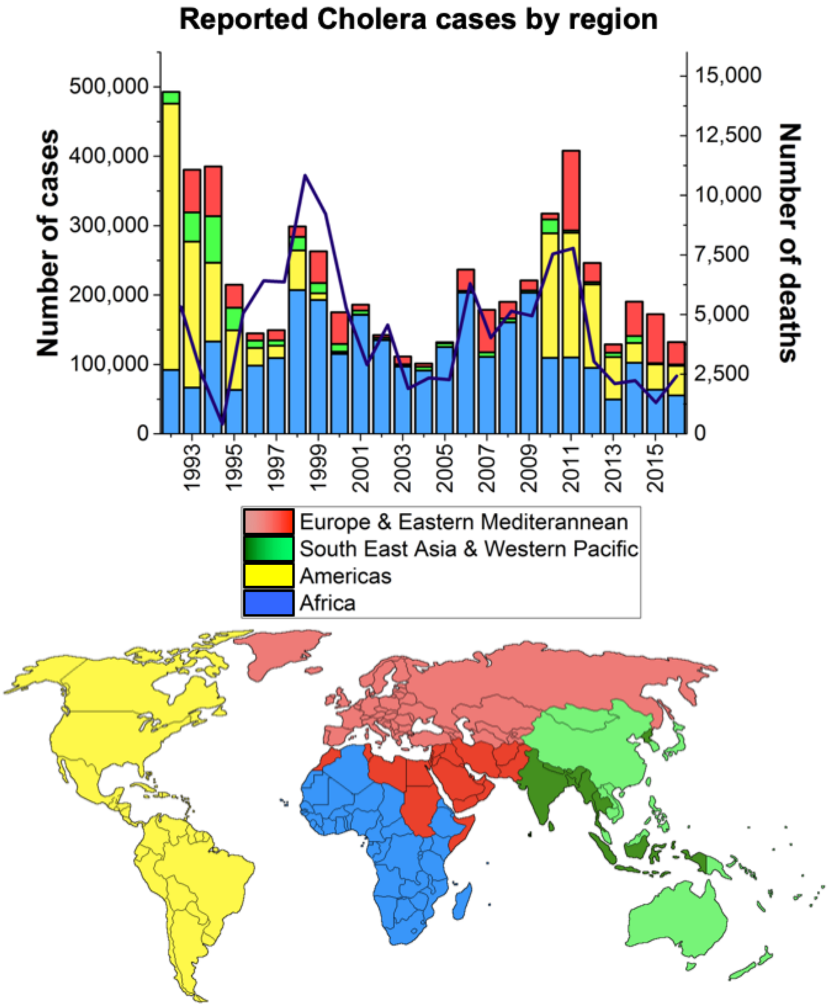

Figure 2-2. Worldwide Cholera cases by region. Data and regional definitions taken from Global Health Observatory (GHO).[64] It should be noted that these data include only cases and deaths as reported by the relevant countries' authorities.

In GM-1 binding, both branches show several hydrogen bonding interactions with CTx, with galactose buried deeply in the binding pocket, whilst sialic acid residue sits in a more spacious shallow pocket (see Figure 2-4).[29] ITC studies have shown that subnanomolar affinities are achieved for the CTx-GM-1 interaction due to the 3-D conformation of the glycan.[13]

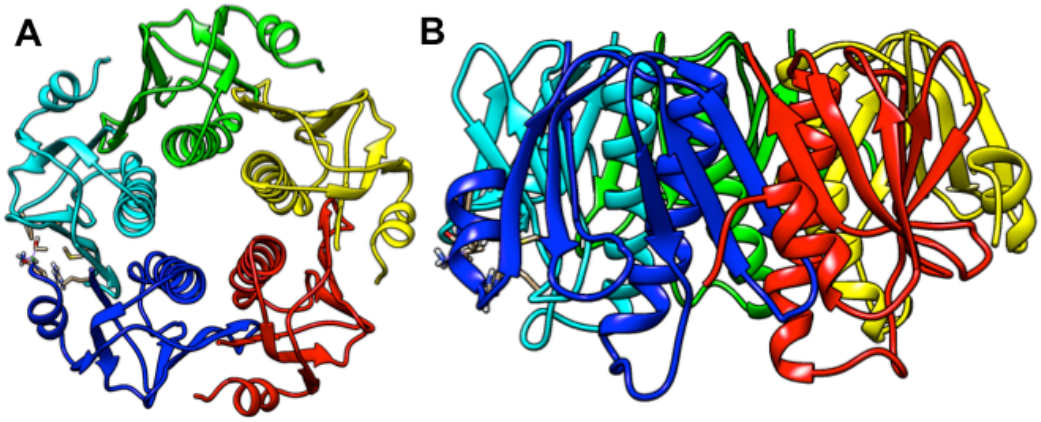

Figure 2-3. Structure of CTx B subunit from above (A) and side (B), showing barrel-like conformation. 2CHB PDB file visualised with UCSF Chimera software

It has so far proved very complex to form monovalent anti-infective ligands for CTx.[13,40–42] For example, work by Lanne et al.[43] displayed the negative effect of even small alterations to the structure of the sialic acid. In this study, modified GM-1 glycolipids modified with amides and alcohols at the C(1) of neuraminic acid were immobilized onto blotting membrane surfaces were then exposed to radiolabeled CTxB, and this showed that these modifications reduced binding, possibly due to a reduced capacity to form hydrogen bonds with the toxin. Bernardi *et al.*[40–42] also performed several studies into the structure-function relationship in developing both oligosaccharides and monomeric ligands. For example, monomeric GM-1 mimics were easily produced through the use of α-hydroxyacids to avoid the difficulty of incorporating the neuraminic acid moiety. The terminal galactose and α-hydroxyacids were attached to a commercially available cyclohexanediol scaffold representing the rest of the pentasaccharide. The highest affinity for GM-1 with these mimics, determined by fluorescence spectroscopy, was found to be K_D=190 mM, which shows significantly weaker binding than the native GM-1, K_D=4.61 pM.[39]

Due to the difficulty of developing a structure more well suited to CTx's binding pocket than GM-1, many groups have attempted to circumvent this difficulty with compounds displaying five GM-1 mimics to exploit the multivalency effect. Wang *et al.*[44] developed a pentavalent compound with 5 arms terminated by galactose on a pentacycle core, showing the importance of matching the length of the carbohydrate spacer (not too long or too short) to the CTx binding pocket. This rationale was extended to corannulene core-based pentavalent GM-1 oligosaccharide compounds synthesized by Mattarella *et al.*[45], which showed nanomolar IC_{50} values.

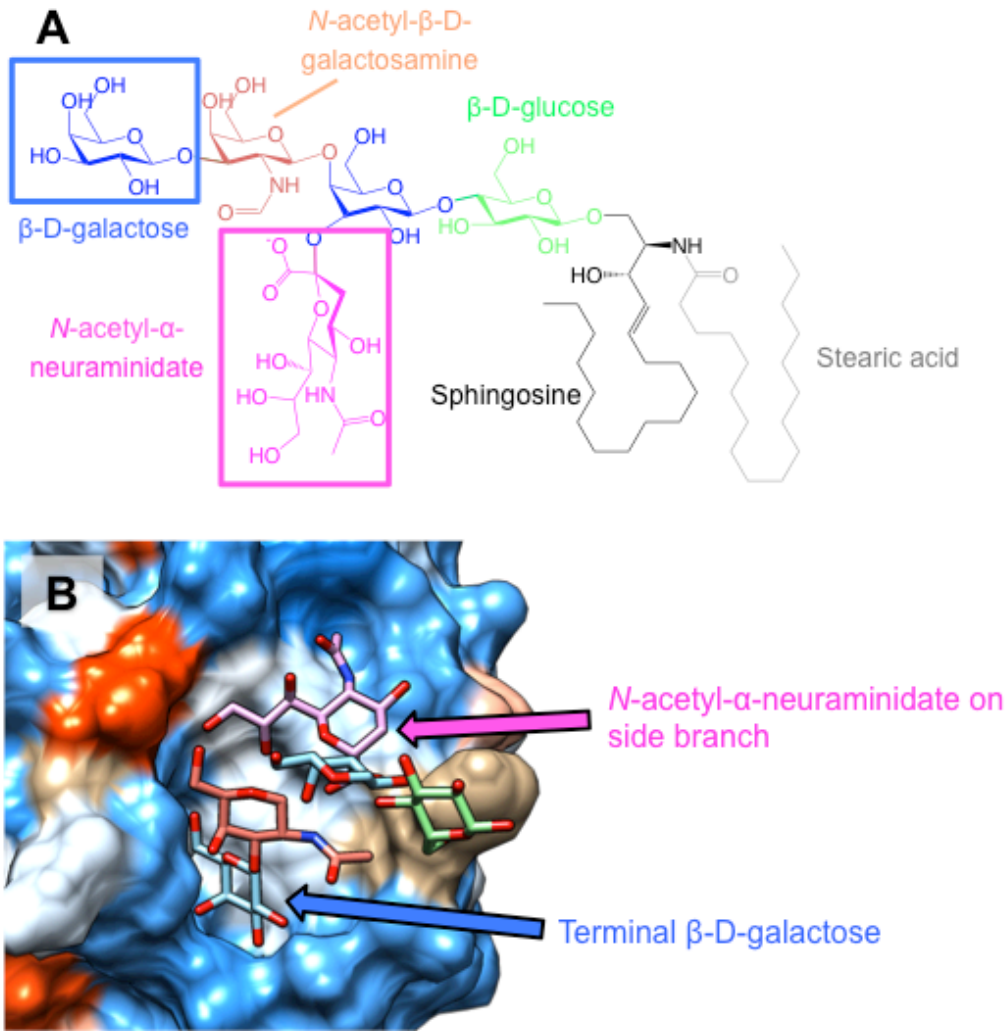

Figure 2-4. Structure of GM-1 bound to CTx adhesive binding pocket. A) Structure of GM-1 ligand. B) GM-1 bound to CTx, 2CHB PDB file visualised with UCSF Chimera software.

Polymers and nanoparticles have the potential to further exploit the cluster glycoside effect by displaying more than 5 moieties on one scaffold. With this rationale, the hope is that the effect of the very large number of carbohydrates displayed should override the reduced binding due to the less precise sequence control achieved in a polymer,.[41,46] The tunable properties of a polymer are very different to those available in small molecules: namely, average chain length, the choice of pre- or post-polymerisation addition of functionality, density of functionalisation.

Das *et al.*[16] developed GM-1-terminated polymers coated onto nanoparticles, and showed these materials to have promising anti-CTx activity *in vitro* and *in vivo*. This study, although presenting a promising mimic of native GM-1 binding, does not provide any understanding of how we might tune polymer structure to enhance CTx affinity *without* using the native GM-1 ligand.

The density of functionalisation and linker length to the polymer chain is key due to the freedom of movement required to allow multivalent bonding modes.[4,19] Fulton *et al.*[47] developed a library of glycopolymers with the ability to adapt galactosyl residue density in response to exposure to the CTx protein. In response to their application to various immobilised lectin templates in 96-well microplates, acylhydrazine-containing carbohydrates reversibly conjugated to aldehyde-functionalised polymers. In each well, the applied polymers with carbohydrates attached (galactose and/or mannose were pre-attached in each case) formed the specific glycopolymer composition able to interact with highest affinity with these lectin templates. Composition was determined by ^{1}H-NMR spectroscopic monitoring of the sugars' anomeric protons. This templating process enhanced the affinity of these glycopolymers to their target lectins, as determined by fluorescence titration of the isolated templated polymers, suggesting that lectins' exhibit higher binding for strategically placed carbohydrates over the carbohydrate-dense pretemplated glycopolymers. Richards *et al.* produced a series of poly(methacrylate)s with pentafluorophenyl groups on the sidechain, which were converted post-polymerisation with amine linkers of various lengths terminated with galactose residues.[23] This study showed higher affinities were obtained with the longer linker lengths optimized to the depth of the CTx pocket, suggesting that it is important to tune this length to the length of the native GM-1 glycan.

The next step in this rational design was to implement the 3-D GM-1 structure by interaction with CTx's shallow allosteric sialic acid binding pocket. Jones *et al.* previously developed a polymer capable of distinguishing PNA (a galactose-binding lectin) and CTx by implementing a branched functional motif in addition to terminal galactose on the sidechain of a methyl methacrylate polymer scaffold.[48] In this study, they developed a library of polymers with equivalent spacing between the galactose and sialic acid residues to the native GM-1, and found a chlorobenzyl branched group to grant 6-fold selectivity for CTx over PNA. Unfortunately, however, this selective compound had a relatively high MIC_{50} of 0.1 mM. Tran *et al.*[46] also synthesized acrylamides with hetero-bifunctional moieties attached to side chains of the polymers. The allosteric moieties were chosen out of utility rather than to mimic GM-1's branched sialic acid, but many of these molecules displayed sub mM IC_{50} values.

The evidence suggests that further mimicking GM-1's branched 3-D structure in the polymer's side chain may further enhance both selectivity and affinity: linker length, density of functionalisation and double modification are all key in designing CTx anti-adhesion compounds.

2.3. Chapter aims

There is a need for the design of glycopolymers tailored to bind specifically to the binding pocket of CTxB, involving the involvement of CTxB’s allosteric site. There are currently no studies looking into the 3D structure of the glycopolymer side chain for this application. To this end, the aims of this chapter are as follows:

- To synthesis a library of doubly-functionalised glycopolymers with terminal galactose, several carbohydrate densities, two different linker lengths and two different secondary moieties to interact.
- To determine the inhibitory activity of the glycopolymers with CTxB and a simpler lectin without an allosteric binding site (RCA_{120} has a shallow binding pocket) versus immobilised GM-1 glycan.
- To assess the binding kinetics of the glycopolymers with CTxB and RCA_{120}.
- To compare all binding assay data to determine the effect of linker length and allosteric moiety on lectin binding and selectivity.

2.4. Results and Discussion

2.4.1. Synthesis of poly-hydroxyethyl acrylamide-co-thiolactone acrylamide

In this study, we designed bifunctional glycopolymers aiming to interact with both the deep galactose-binding pocket and more-shallow sialic acid binding pocket of the CTx B subunit (CTxB). This double modification is implicated as a potential strategy to further increase affinity for CTx through rational design of a structure mimicking the 3-D structure of GM-1. Thiolactone-containing polymers have been extensively used as doubly modifiable scaffolds which can easily integrate a large variety of functional groups via "click"-like chemistry.[49–58] Though these polymers have yet to be used in biomedical application, their capacity to employ two functionalities using rapid, specific, versatile "click"-like chemistry means that the this chemistry could be suitable for the production of biorthogonal polymers. Thiolactone acrylamide was synthesized, following a well-established procedure previously described by Reinicke *et al.*, from the readily available homocysteine thiolactone hydrochloride in a typical two-phase system (1:1 dioxane:water) using sodium bicarbonate to deprotect the hydrochloride salt.[49,52] Acryloyl chloride (an acid chloride) was used to activate this compound overnight at room temperature, and the resulting monomer product was purified. Structure and purity were validated by ^{1}H and ^{13}C-NMR spectroscopy, the presence of the M+Na$^+$ peak at 194 m/z by ESI-MS, and FTIR.

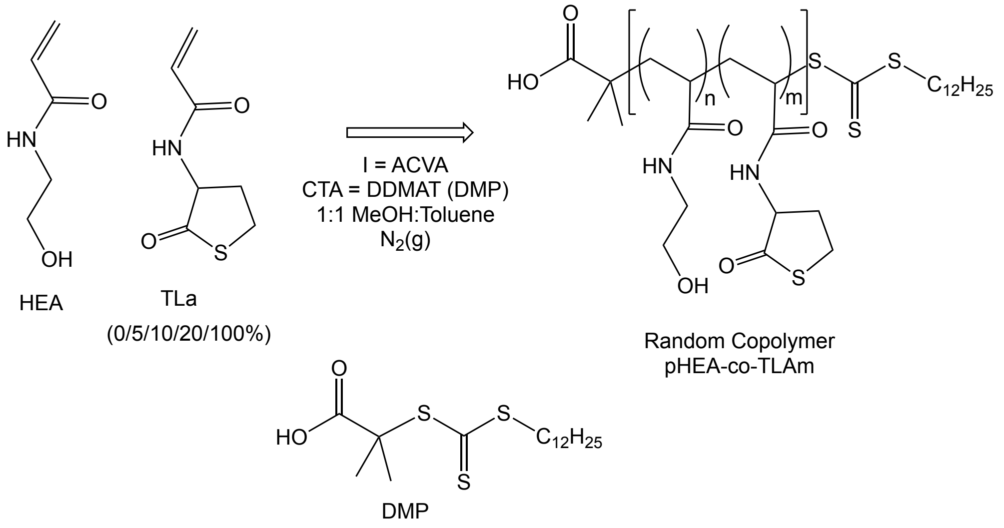

Scheme 2-1. RAFT polymerisation of pHEA-*co*-TLAm.

A library of polymers with different percentages of thiolactone acrylamide included in the chain was synthesized using RAFT (reversible addition fragmentation chain-transfer) copolymerisation with *N*-hydroxyethyl acrylamide (see Scheme 2-1). This method was chosen for chain length control and its tolerance of the thiolactone and acrylamide moieties. The molar ratio of thiolactone acrylamide was varied from 5-20 %, with homopolymers of both monomers also synthesized for characterisation. Polymers were assessed by SEC, NMR and FTIR to determine chain length, and dispersity, with all polymers displaying acceptable control (**Đ** < 1.3) (see Figure 2-5). The thiolactone acrylamide monomer displayed reduced reactivity to the *N*-hydroxyethyl acrylamide, as indicated by a relative reduction in conversion (see Table 2-1). ^{1}H-NMR displayed broadening of peaks in the polymer spectra, and the loss of the terminal vinyl peaks involved in polymer formation.

Kinetics experiments were not carried out to assess the structure of the polymer backbone, so it is possible that these copolymers may not be random, with some clustering of the thiolactone moieties. That the conversion of the TLAm monomer was consistently above that of the HEA monomer in all copolymers (see Table 2-1) suggests that the reactivity of TLAm may be greater than HEA, which in turn suggests that TLAm repeat unit clustering may well have occurred.

Table 2-1. Unmodified pHEA-*co*-TLAm polymers.

Polymer	**[M]/ [CTA] (total)**[a]	**% TLAm monomer feed**	**HEA Conversion (%)**[b]	**TLAm Conversion (%)**[b]	**$M_{n\ (THEO)}$ (g.mol^{-1})**[b]	**$M_{n\ (SEC)}$ (g.mol^{-1})**[c]	**Đ**[c]
pHEA	84	0	73	-	7,000	14,000	1.1
pHEA-*co*-TLAm (5 %)	100	5	98	100	11,000	8,100	1.3
pHEA-*co*-TLAm (10 %)	100	10	96	100	12,000	9,700	1.3

pHEA-*co*-TLAm (20 %)	100	20	76	84	9,700	9,200	1.3
pTLAm	100	100	-	30	4,700	7,200	1.2

[a] Monomer to RAFT agent molar ratio; [b] Determined by depletion of vinyl peaks in ^{1}H NMR using mesitylene as an internal standard (fortunately the vinyl peaks for HEA and TLAm were distinct by ^{1}H-NMR); [c] Determined by SEC.

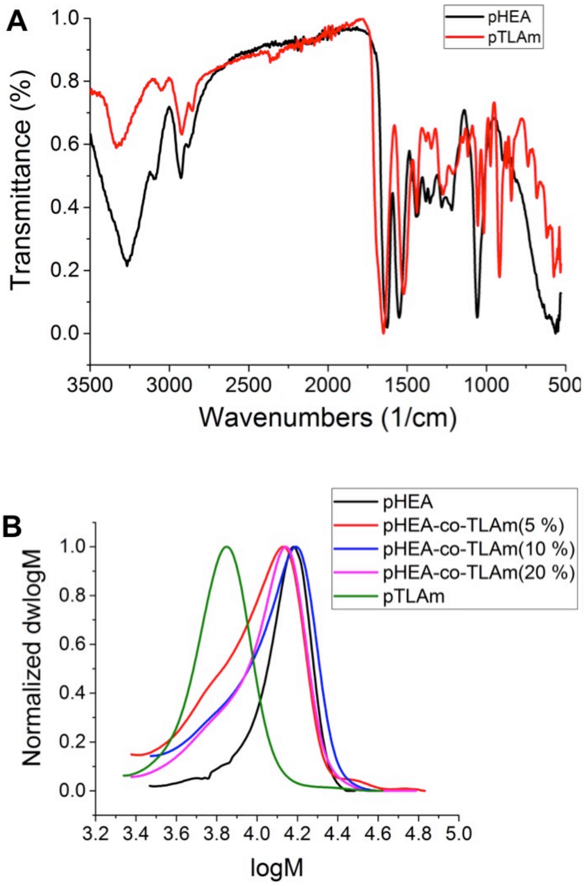

Figure 2-5. Difference in FTIR spectra (A) and SEC molecular weight distributions (B) between different proportions of TLAm in polymer. Of note in FTIR are the broad OH-peak at ~3250 cm^{-1} in pHEA and not pTLAm, and the obvious double C=O peak at ~1000 cm^{-1} in the pTLAm but not the pHEA spectrum.

2.4.2. Post-polymerisation double modification of thiolactone acrylamide-containing copolymers

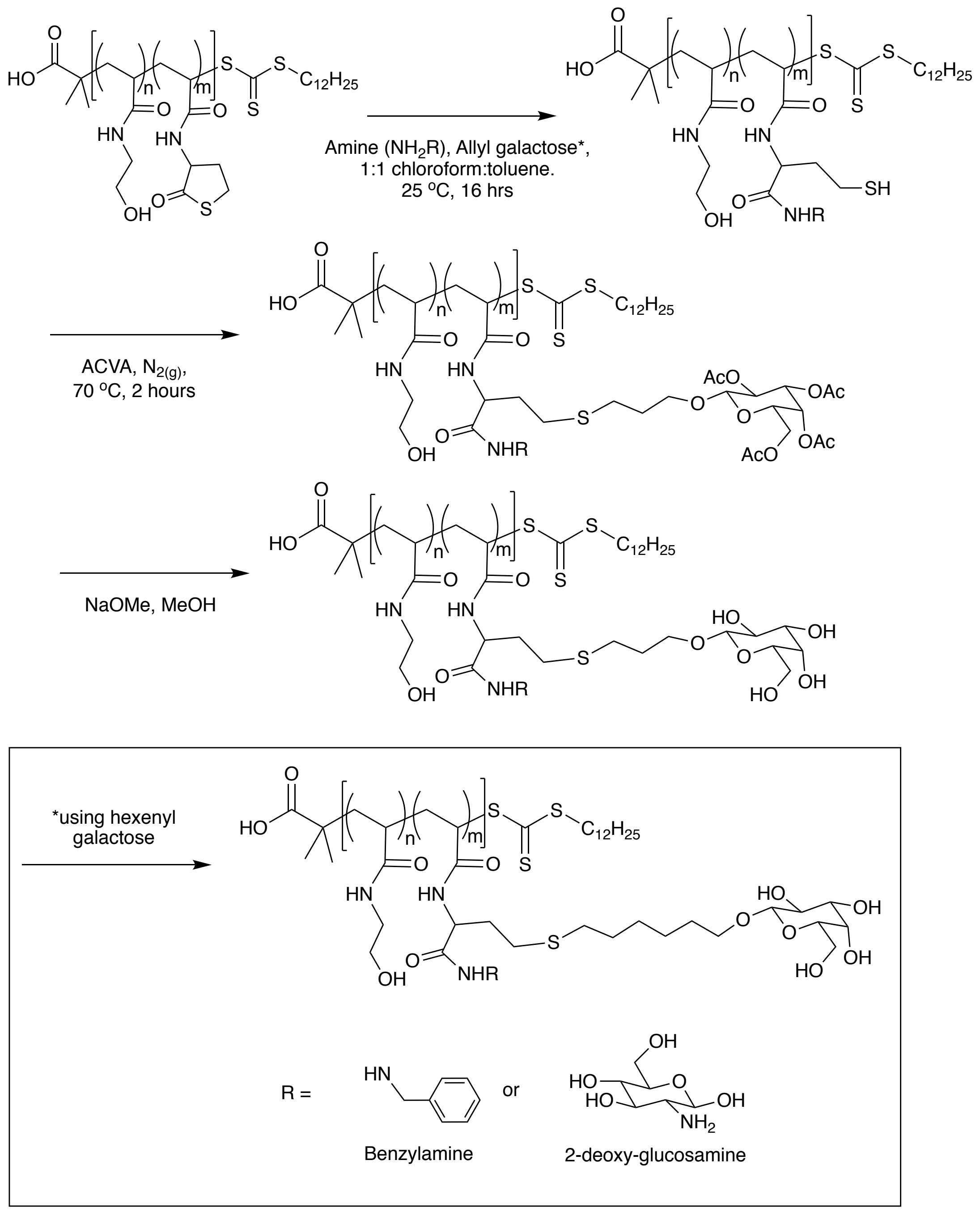

Scheme 2-2. Modification of pHEA-*co*-TLAm modified with primary amine, galactose with alkene linker, followed by deprotection.

The thiolactone-containing polymers were doubly modified in a one-pot, two-stage process to install functionalities in a manner mimicking the branched 3-D structure of GM-1 (See Scheme 2-2). The modification of the different percentages of thiolactone was undertaken to determine the effect of carbohydrate density on affinity. Two different linker lengths were also implemented for the galactose modifications to assess whether the allosteric modification did indeed have an effect. The length of the polymer chain to the terminal galactose is 12.7 and 16.5 Å for the allyl and hexenyl galactose respectively (the length of the entire GM-1 pentasaccharide chain is 16 Å, see Figure 2-6). This suggests that the allyl linker length is appropriate to allow binding of the secondary unit to the CTxB allosteric site whilst the galactose residue sits in the deeper galactose binding pocket. The hexenyl linker is therefore long enough to inhibit the interaction of the secondary unit to this allosteric site. In this way, carbohydrate density, presence of allosteric moiety and type of allosteric moiety could all be assessed for CTx binding in this study.

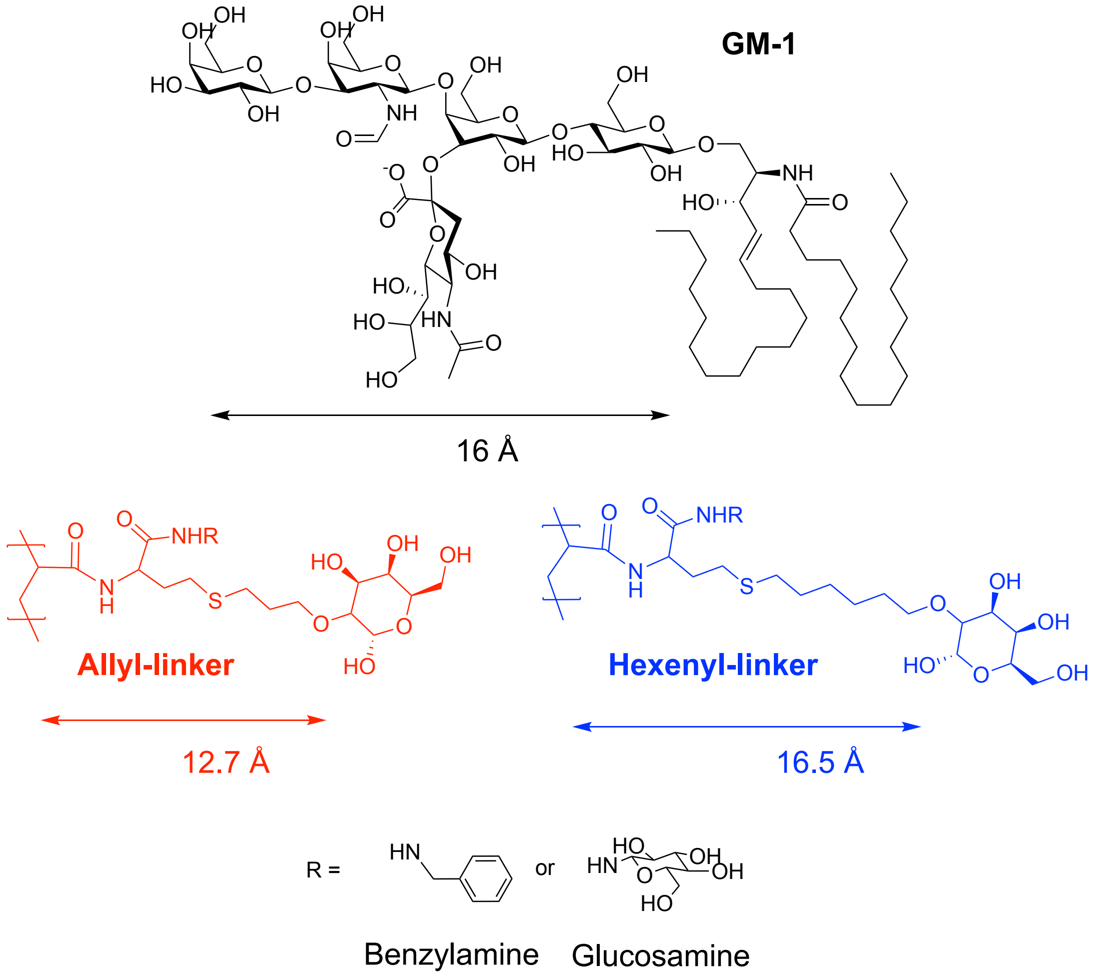

Figure 2-6.. Linker lengths of the native GM-1 ligand and synthesized polymers. Calculated according to methods used by Richards *et al.*[23]

The secondary modification (either 2-glucosamine or benzylamine) was incorporated first by ring-opening the thiolactone to release a free thiol. The primary, galactose-containing, functionality was then incorporated further down the thiolactone-derived side chain in a "thiol-ene" radical click mechanism with this free thiol, using ACVA as a radical source. The galactose compounds' acetate protecting groups were then removed by stirring overnight in sodium methoxide followed by dialysis.

Successful modification was confirmed by increase in Mn by SEC (see Figure 2-7 and Table 2-2, though these data are indicative of hydrodynamic volume, not raw molecular weight) with most samples showing no significant change in polydispersity (suggesting no undesirable side reactions such as disulfide formation), loss of thiolactone-indicative peaks by FTIR (suggesting ring-opening) and the presence of a shoulder on the carbonyl peak. There are shoulders visible on several of the SEC traces, potentially due to undesirable transesterification reactions taking place. The removal of acetate protecting groups was confirmed by loss of the large upfield peaks in ^{1}H-NMR and C-O peaks in FTIR. The solubility of the modified polymers (except the thiolactone acrylamide homopolymer) in water only after the deprotection step was both essential for protein activity assays, and indicates successful modification.

^{1}H-NMR analysis was not consistently useful in confirming modification due to the presence of polymer peaks at ~4.5-5.5 ppm (where we would expect to see sugar peaks). It should also be noted that most of the final, modified, polymers were only soluble in water (or D_2O), and therefore the change in the amide peak was not observable in most spectra due to it exchanging with deuterium in this solvent. The ^{1}H-NMR spectra for pHEA-*co*-TLAm(5 %) polymer's modification with 2-glucosamine then allyl-β-D-galactose or hexenyl-β-D-galactose had visible amide peaks despite the use of deuterium oxide solvent. These amide peaks showed a change in shape, suggesting the presence of the third amide (produced by the 2-glucosamine modification during thiolactone ring opening).

In addition to this, the pHEA-*co*-TLAm(5 %) (modified with glucosamine/hexenyl-β-D-galactose) was the only modified polymer readily soluble in methanol as well as water, so a ^{1}H-NMR was obtained in this solvent. The integral for this amide peak dropped tenfold (from 0.22 to 0.02 using a polymer peak as a standard integral). This suggests that the presence of the modification enables the amides to deuterium exchange more readily.

Table 2-2. Modified pHEA-*co*-TLAm polymers.

Precursor polymer	**Galactose linker (alkene)**	**Amine modification**	**$M_{n\,(THEO)}$ (g.mol^{-1})[a]**	**$M_{n\,(SEC)}$ (g.mol^{-1})[b]**	**Đ[d]**
pHEA-*co*-TLAm (5 %)	Allyl-β-D-galactose	Glucosamine	13,500	12,400	1.2
		Benzyslamine	13,100	10,500	1.3
	Hexenyl-β-D-galactose	Glucosamine	13,700	13,100	1.7[e]
		Benzylamine	13,300	15,000	1.2
pHEA-*co*-TLAm (10 %)	Allyl-β-D-galactose	Glucosamine	15,600	14,400	1.2
		Benzylamine	14,800	13,800	1.4
	Hexenyl-β-D-galactose	Glucosamine	16,000	16,600	1.4
		Benzylamine	15,300	13,900	2.0
pHEA-*co*-TLAm (20 %)	Allyl-β-D-galactose	Glucosamine	16,400	13,300	1.2
		Benzylamine	15,100	[c]	[c]
	Hexenyl-β-D-galactose	Glucosamine	17,100	14,100	1.3
		Benzylamine	15,900	9,300	1.3

[a] Determined by depletion of vinyl peaks in ^{1}H NMR using mesitylene as an internal standard (fortunately the vinyl peaks for HEA and TLAm were distinct by ^{1}H-NMR); [b] Determined by SEC; [c] Insufficient polymer to perform characterisation. [d] Determined by SEC. [e] A shoulder was evidently visible on the SEC of these products potentially due to transesterification, see Figure 2-25 in appendix.

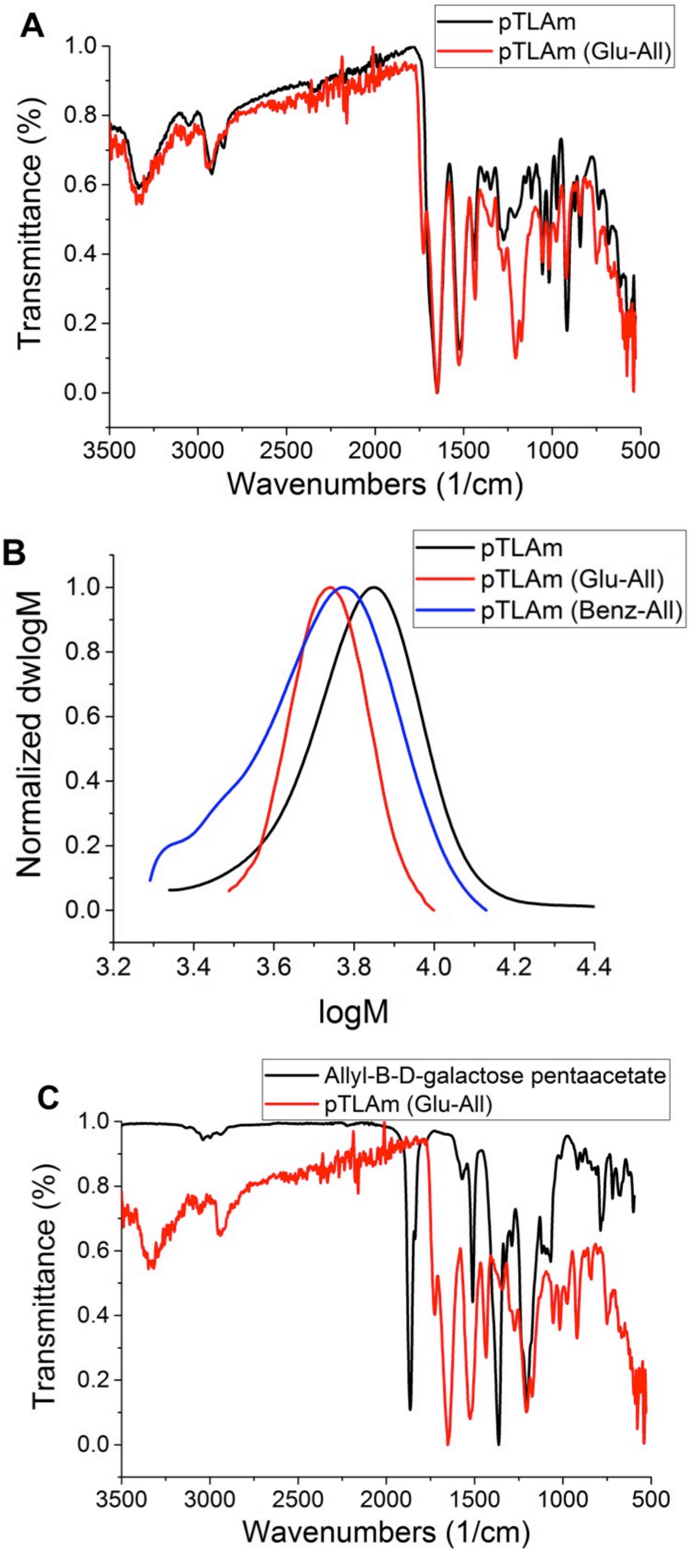

Figure 2-7. Representative modification of pTLAm polymer to form doubly-modified pTLAm product. A) FTIR showing change in pTLAm polymer upon modification: of note are peaks at 1600 (second overlapping C=O peak) and 1100-1200 cm^{-1} (C-O peaks from sugar modifications). B) SEC trace showing shift in molecular weight distribution upon modification; shoulder on pTLAm (Benz-All)

shows shoulder that may be caused by transesterification. C) FTIR showing the loss of acetate groups by the loss of the characteristic 1750 cm^{-1} C=O peak. Brackets denote (SecondaryModification-AlkeneGalactoseLinker).

2.4.3. Microplate assays to determine competitive binding

A fluorescence-linked binding assay was used to evaluate binding to CTxB and a galactose-binding lectin control. RCA_{120} has a shallow binding pocket and therefore it is useful to assess non-specific binding to terminal galactose but not the secondary binding moiety.[12,24,59] Herein, fluorescently-labelled lectin were incubated with a serial dilution of polymer concentrations. This mixture was then incubated on a high-binding microplate pre-surface-functionalised with GM-1 (prepared as previously described by Richards *et al.*[48]) and washed to remove unbound lectin. Fluorescence emission was assessed in a plate reader, with more fluorescence indicating more free lectin (not bound to the applied glycopolymers) and less fluorescence indicated higher affinity for the synthesized glycopolymers.

Representative binding curves are displayed (Figure 2-9 and minimum inhibitory concentrations (MIC_{50}) for all compounds are displayed in Figure 2-8 as total calculated galactose concentration. Compounds showing binding activity display a sigmoidal curve shape on increasing concentration, with a steep increase in binding as the binding of *some* lectin molecules facilitates further binding, and a maximum plateau at which point all lectin molecules are engaged. MIC_{50} values are calculated as the concentration at which this sharp increase occurs (at which 50% of toxin units are engaged), and therefore those compounds which do not display this sigmoidal binding activity do not have MIC_{50} values: thus, Figure 2-8 does not have any values for the polymers with benzylamine, or the hexenyl galactose at 10 and 20 % carbohydrate density, as these compounds showed no competitive binding activity (ie. Increased binding relative to the GM-1 ligand).

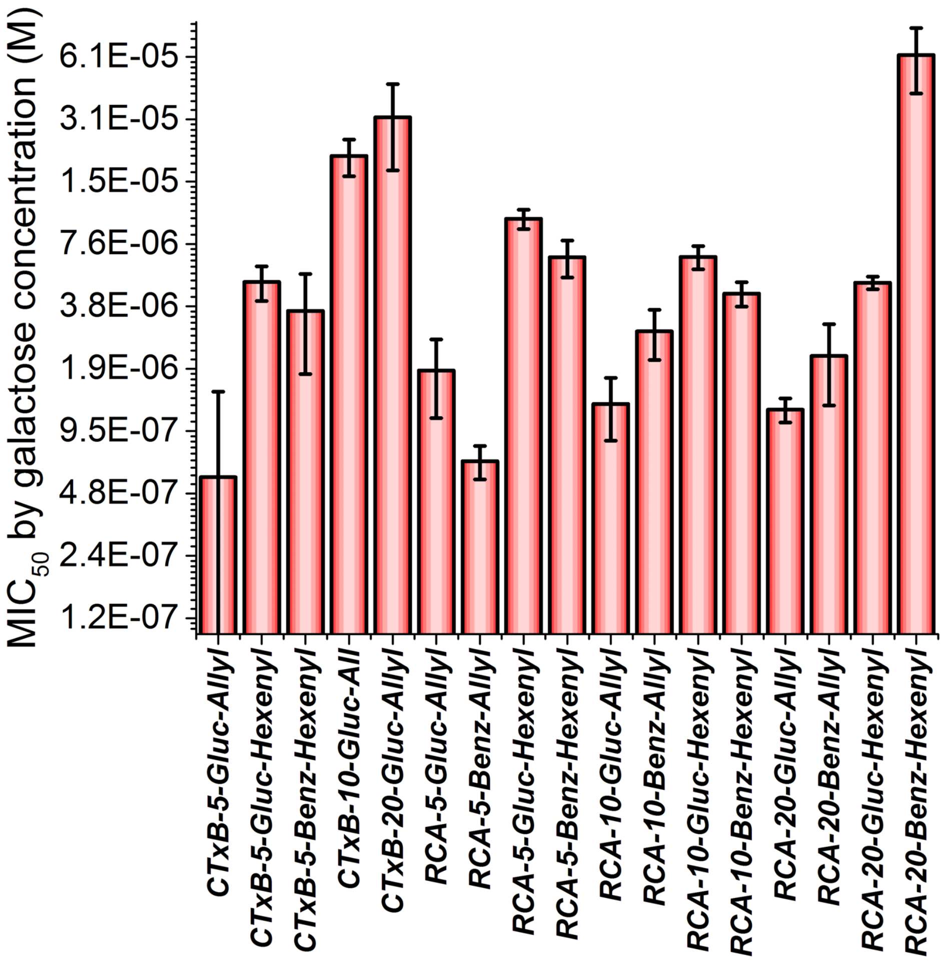

Figure 2-8. MIC50 values by galactose concentration, excluding those without sigmoidal curve fits. Axes labels for polymers are in the format TOXIN-TLAmDensity-SecondaryModification-AlkeneGalactoseLinker. Full data in appendix. Error from experiments performed in triplicate.

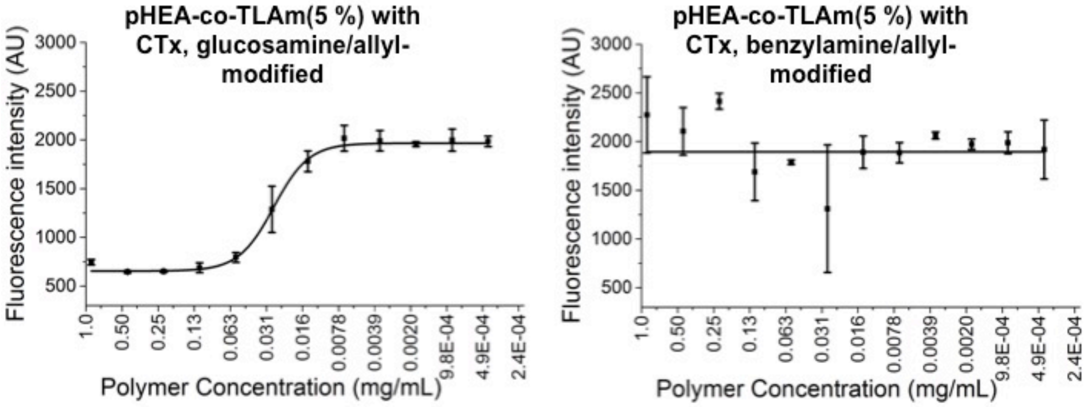

Figure 2-9. Representative Microplate assay binding curves (full set of curves in appendix, all assays undertaken in triplicate).

As the carbohydrate units were installed by post-polymerisation modification, any changes in activity due to linker length or secondary unit can be isolated as independent of changes in chain length, density or dispersity. The modified thiolactone acrylamide homopolymers showed no binding activity. This could be due to too-high carbohydrate density, or because these polymers were insoluble in aqueous media (HEPES buffer was used for all other solutions), and therefore were applied in DMSO (no other samples contained DMSO), which could have had other effects. These polymers were excluded from further study.

The RCA_{120} control displayed no significant preference for either secondary binding motif, as would be expected due to its shallow binding pocket having no capacity to interact beyond the terminal galactose. RCA_{120} binding also exhibited no significant differences between linker lengths. Conversely, the presence of the benzyl secondary unit dramatically decreased CTxB binding to the extent that no binding activity was observed at all, potentially due to this group not interacting favourably with the sialic acid allosteric site.

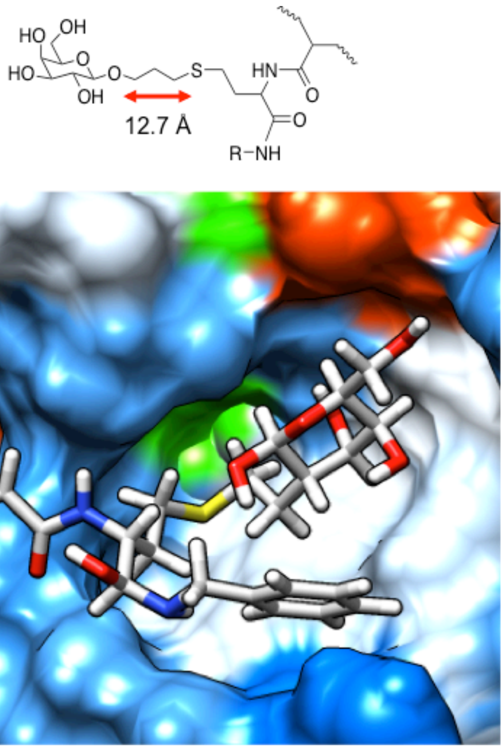

Figure 2-10. Model of shorter linker glycopolymers bound to CTxB binding pocket. Glycopolymer TLAm repeat unit modified with glucosamine and allyl-β-*D*-

galactose, fitting in CTxB binding pocket, produced using SwissDock online server[60].

The glucosamine-containing polymers with allyl (shorter) linkers had binding interactions with CTxB and RCA_{120} at all densities, but with affinity reducing with greater carbohydrate density. This reduced density could be favourable due to an increased freedom of movement allowing the side chain to exhibit a similar 3-D orientation to native GM-1, where the presence of more long ring-opened thiolactone-derived chains sterically inhibits lectin interaction.[19] As predicted (see Figure 2-10_, the longer linker length (the hexenyl galactose) cancels out the enhanced binding effect of the secondary functionality, meaning that both the benzyl and glucosamine had comparable activity with CTxB. This confirms the hypothesis that it is the secondary unit binding to the allosteric site eliciting the change in binding activity.

2.4.4. Bio-layer interferometry studies to determine kinetics of cholera toxin binding

In addition to a fluorescence-linked sorbent assay, bio-layer interferometry (BLI) was employed to understand the kinetics of binding over multiple, longer, timepoints. This assay was also employed to understand the affinity of these glycopolymers for CTxB rather than their capacity to inhibit GM-1 binding to CTxB. BLI is a label-free technique which analyses the interference pattern of white light reflected from two different layers. White light reflected off an internal standard layer is compared to white light reflected off the biosensor tip (which consists of the immobilized protein and any ligands that may be attached). In this way, it is able to detect changes in the binding of ligands to the biosensor probe during the assay, and thereby quantitatively and precisely measure ligand association and dissociation in real time. Such kinetic studies are essential in uncovering what is happening on a molecular level, analyzing a different aspect of ligand binding to competition assays (such as the fluorescence-linked sorbent assay). See Figure 2-11 for a demonstration of a typical BLI experiment.

Using the BLI system, lectins were immobilized onto BLI sensors with simple EDC/NHS coupling: this is desirable due to its utility, however it should be noted that this type of immobilization is non-specific and may lead to binding to random, multiple amine residues anywhere on the protein surface. Alternative methods, such as biotin-streptavidin, are available. Optimal lectin binding on the sensors was determined using a dilution series. A concentration series of polymers were applied to test dose-dependent activity, and a 2:1 model was selected as the closest available curve fitting for the raw data (see Figure 2-14 for representative curve fits).

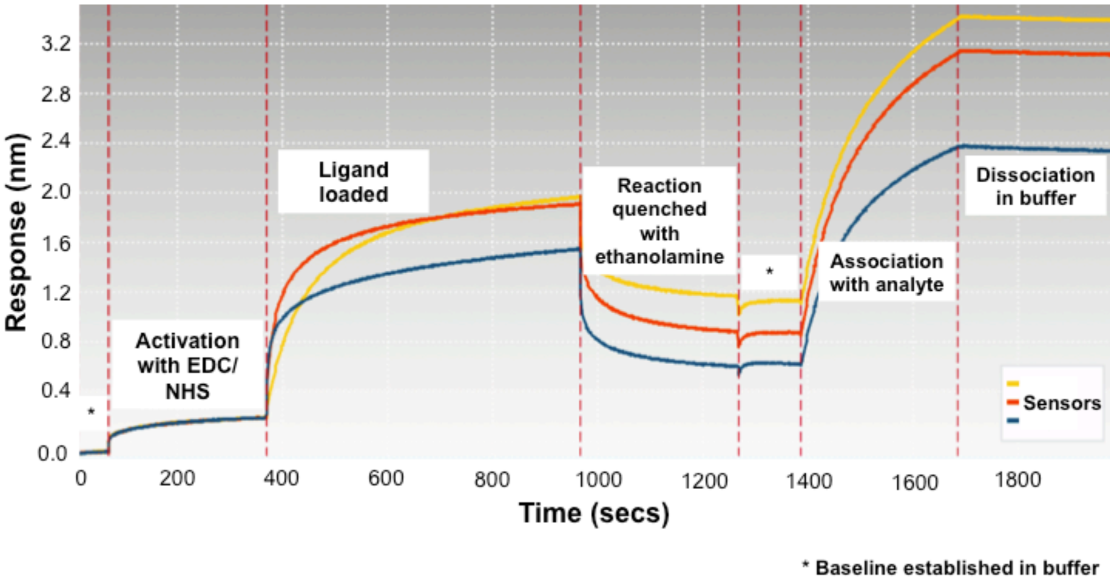

Figure 2-11. Typical curve observed on Octet system during BLI assay, with labels to indicate the different stages of the assay. These curves show the steps using amine-reactive sensors (to attach a ligand via EDC/NHS coupling).

From a cursory glance at the binding curves, we can assess the relative mass of polymer bound to the bound lectins as a simplistic measure of binding activity. These raw intensity values correlated closest to MIC_{50} values from the Microplate binding assays. For both RCA_{120} and CTxB, increases in carbohydrate density led to decreased activity (with less change between 10 and 20 %). For both lectins, the benzylic secondary unit also decreased activity (to a larger extent with CTxB), with a reduced decrease in activity for the hexenyl linker. In fact, with the longer hexenyl linker the binding activity with the secondary benzyl is increased. Conversely, the longer linker decreases activity with the 2-glucosamine secondary unit (see Figure 2-12); perhaps related to a positive interaction with the binding pocket that is not possible with the longer linker. This is supported by models of the CTxB binding site showing that only the shorter linker enables the secondary functionality to interact with CTxB's binding pocket in any capacity (see Figure 2-10).

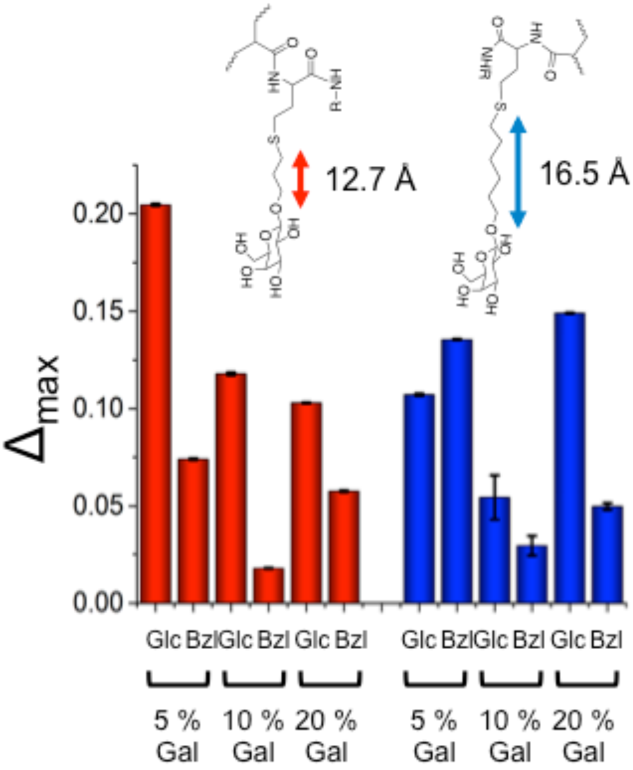

Figure 2-12. The effect of linker length on CTxB binding. Graph shows total mass of glycopolymer captured (Δ_{max}) by lectins immobilised on BLI probe (experiments performed in triplicate)

The strength of BLI, however, lies in understanding the kinetics of these binding interactions rather than the raw intensity of binding. K_D is the binding constant for a ligand interacting with a specific lectin, calculated from a concentration series. This constant is derived by dividing the association constant, k_{on}, by the dissociation constant, k_{dis}. The K_D of a particular ligand-lectin pairing is therefore led either by k_{on} or k_{dis} (see Figure 2-13). The parameter we are interested in most is the residence time of the polymer once bound to the lectin, defined as the average length of time a ligand spends in a binding pocket. This residence time is key as a high residence time of a proposed anti-adhesive agent could reduce CTx binding to its natural GM-1 target *in vivo* application.

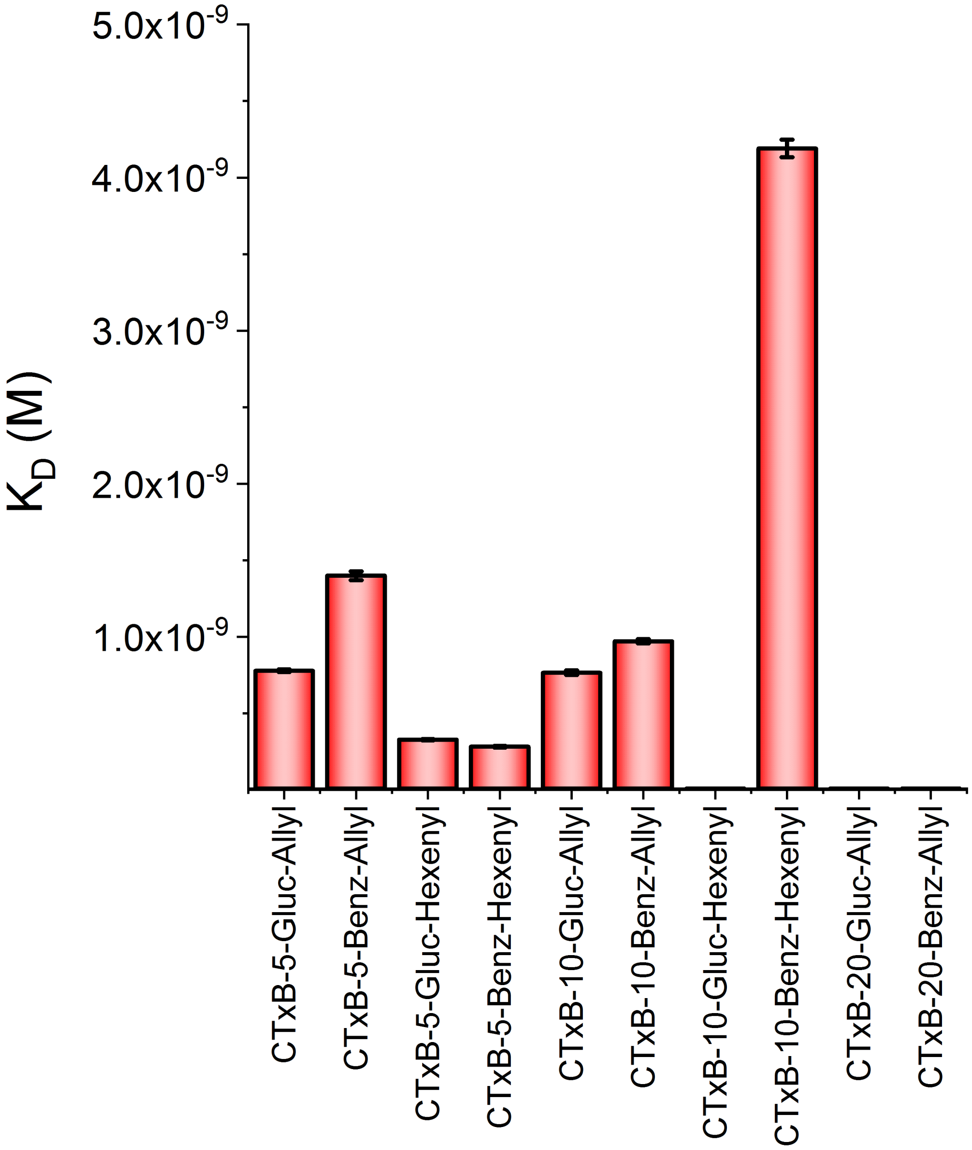

Figure 2-13. KD values by polymer concentration. Axes labels for polymers are in the format TOXIN-TLAmDensity-SecondaryModification-AlkeneGalactoseLinker. Full data in appendix. Due to the sensitivity limitations of the instrument, 1 x 10^{-12} is the minimum value (hence the abundance of this value).

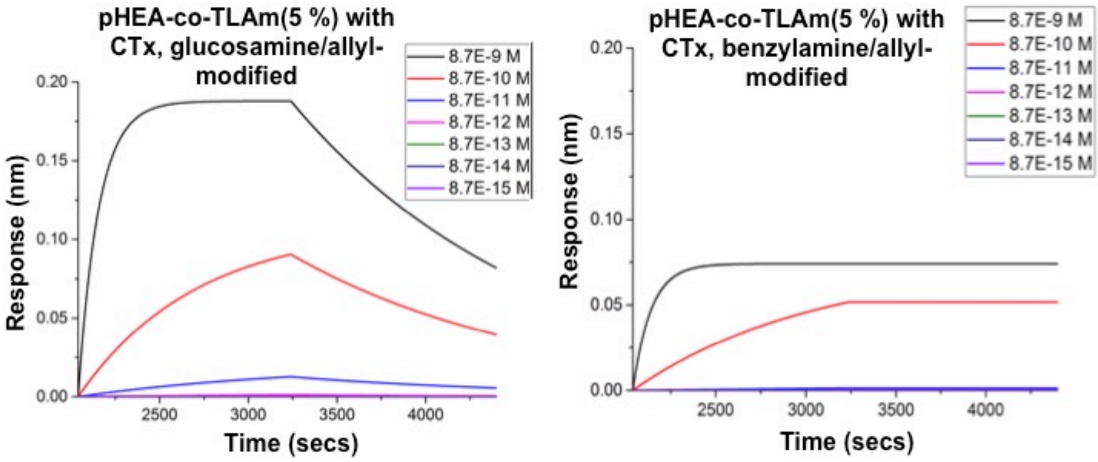

Figure 2-14. Representative BLI fitted response curves (full set of curves in appendix).

The K_D values obtained were estimated by the BLI's accompanying software, with slow dissociation constants resulting in low K_D values. One series of results did change with k_{on} (the association rate constant), which is the constant defining the kinetics of formation of the ligand-lectin complex: the RCA_{120} control with the hexenyl linker and benzyl secondary unit had slower binding with increases in carbohydrate density. All other samples showed no change in k_{on} despite changes in ligand structure.

With CTxB, there seemed to be no kinetic trend with carbohydrate density, with all glucose/allyl polymers showing fast dissociation regardless of density (see Figure 2-13). This suggests that, even if these polymers show high binding activity, their residence times in the binding pocket are low. In contrast, although the benzylic secondary unit showed lower binding activity, k_{dis} values were consistently lower than with the glucosamine unit, suggesting longer residence times (see Figure 2-42). This could be due to either more stable complex formation, or due to hydrophobic interactions barring the release of the polymer from the lectin's binding pocket.[61] No significant kinetic trends were observed with change in linker length.

With RCA_{120}, there were no obvious k_{dis} trends relating to linker length. Dissociation of polymers with benzylic rather than glucosamine secondary units, or with higher carbohydrate densities, was consistently slower than the glucosamine unit.

Previous studies have shown the native GM-1 ligand to have a dissociation rate constant (k_{dis}) of around 40 nM.[29] All the polymers herein had lower dissociation constants than this, suggesting that the residence times of the GM-1 are longer, perhaps due to other parts of the polymer chain interacting with other CTxB subunits. However, the relatively low values obtained are typical of multivalent systems, suggesting there is promise in the use of these doubly-modified polymers.

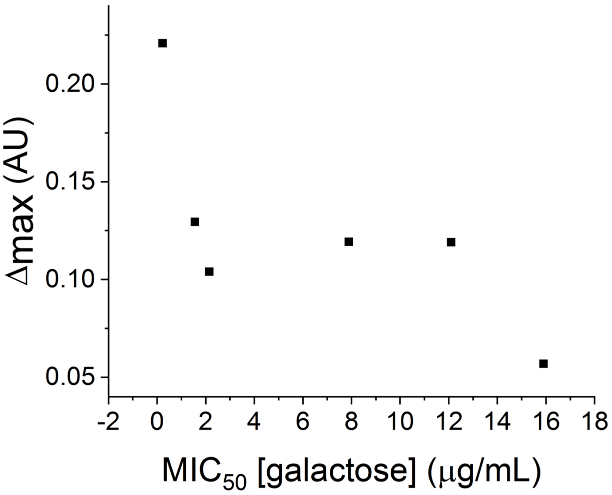

Figure 2-15. Plot of CTxB-binding MIC50 values (from fluorescence-linked sorbent assay) versus Δ_{max} (maximum mass of glycopolymer bound to CTxB probe, from BLI assay).

Due to the difference between the nature of the inhibitory and BLI assays, it is not expected that their results will necessarily agree: the former comparing the binding of immobilised GM-1 and the analyte to CTxB at one time point, and the latter showing the kinetics of binding to immobilised CTxB with no native GM-1 ligand present. Accordingly, the kinetic parameters did not agree with the inhibitory data, showing no link between inhibition of GM-1/CTxB binding and glycopolymers residence times in CTxB. There was potentially a correlation seen (in Figure 2-15) between the MIC_{50} values from inhibitory assays and the maximum response seen in the BLI assay (related to the mass of glycopolymers bound to the CTxB probe), with Δ_{max} (greater binding in the BLI association step) correlating to a lower MIC_{50} value (a lower concentration of glycopolymers required to inhibit GM-1/CTxB binding).

Although models produced using the SwissDock server (see Figure 2-10) support the rationale of designing a doubly functionalized glycopolymers in order to interact with both the galactose and neuraminic acid binding sites in the CTxB binding pocket, the experimental data suggest that the glycopolymers/lectin interaction is incredibly complex. These data do, however, show wide differences between the interactions with RCA and CTxB, suggesting that lectin discrimination and selectivity are possible using doubly functional glycopolymers.

2.5. Conclusions

This chapter demonstrated the synthesis of a library of doubly-modified glycopolymers with a variety of secondary modifications and linker lengths between the primary and secondary modifications and an analysis of their interaction with the CTxB lectin. Precursor copolymers of thiolactone acrylamide and *N*-hydroxyethyl acrylamide, with different percentage thiolactone incorporation, were polymerised by RAFT polymerisation. These polymers were subsequently modified in a one-pot, two step process with either benzylamine or 2-glucosamine, followed by allyl- or hexenyl-β-D-galactose.

Fluorescence-linked sorbent assays were performed to determine concentration-dependent lectin binding affinity, and BLI to determine the kinetics and residence times of polymer ligands in the lectin binding pockets. As expected, the glucosamine-containing polymers with shorter linker length and lower carbohydrate density had lower MIC_{50} values. This suggests that a hydrophilic secondary unit has favourable interactions with the CTxB allosteric site; the shorter linker length confirming that this effect is due to the secondary unit. In contrast, CTxB residence times by BLI were enhanced by a benzylic secondary unit, and not affected significantly by carbohydrate density or linker length.

The kinetic parameters from the BLI assay showed no link to the inhibitory assay data versus the native GM-1 ligand (the fluorescence-linked sorbent assay). A correlation was instead seen between the MIC_{50} values and Δ_{max} from the BLI assay (related to the mass of glycopolymers bound to the CTxB probe), which suggests that the amount of glycopolymers that binds during the association step may have an effect on capacity to inhibit CTxB's binding to its native GM-1 ligand. These data combined suggest that the 3-D structure of a GM-1 mimic has a dramatic effect on its interaction with CTxB and other galactose-binding lectins. Increased complexity through both tuning linker length and the use of bifunctional glycopolymers may have application as specific anti-adhesives against Cholera.

2.6. Materials and Methods

2.6.1. Materials

Ultra-pure water with resistance < 18 Ω, was obtained from a Milli-Q© Integral Water Purification System. All chemicals were purchased from Sigma-Aldrich and used as supplied unless otherwise stated. 15 and 40 nm citrate-stabilised gold colloid solution was purchased from BBI solutions. GM1-ganglioside was purchased from Carbosynth. Deuterated solvents used (methanol, chloroform, water) were purchased from Sigma-Aldrich). *n*-Hexane, THF, DMF and ethyl acetate were purchased from Fisher. The toxins used in fluorescence-linked assays were Cholera toxin B subunit, FITC-conjugate, lyophilized powder from Sigma-Aldrich and Fluorescein labelled Ricinus Communis Agglutinin I (RCA I, RCA120) from Vector Laboratories. HEPES buffer stock solution was prepared with the following concentrations, and adjusted to pH 7.5 using the minimum volume required of 0.1 M $HCl_{(aq)}$ and 0.1 M $NaOH_{(aq)}$: 10mM HEPES, 0.15 M NaCl, 0.1 mM $CaCl_2$ and 0.01 mM Mn^{2+}. The toxins using in bio-layer interferometry were Cholera toxin B subunit, lyophilized powder from Sigma-Aldrich and Unconjugated Ricinus Communic Agglutinin I (RCA I, RCA120) from Vector Laboratories.

2.6.2. Analytical Methods

^{1}H and ^{13}C-NMR spectra were obtained using a Bruker DPX-400 or Bruker DPX-300 NMR Spectrometer; all chemical shifts are reported in ppm (δ) relative to residual non-deuterated solvent. Mass spectrometry was carried out in pure methanol or water on the Agilent 6130B ESI-Quad instrument using electrospray in positive mode. FTIR spectroscopy was carried out on a Bruker Vector 22 FTIR spectrometer with a Golden gate diamond attenuated total reflection cell. SEC measurements were carried out on an Agilent 390-LC MDS instrument equipped with a dual angle light scatter (LS), 2 x PLgel Mixed D columns (300 x 7.5 mm) and a PLgel 5 μm guard column. The eluent was DMF or THF with 5 mmol NH_4BF_4 additive. Samples were run at 1ml/min at 50°C. Poly(methyl methacrylate) standards (Agilent EasyVials) were used for calibration between 955,000 – 550 gmol^{-1}. Analyte samples were filtered through a nylon membrane with 0.22 μm pore size before injection. Respectively, experimental molar mass (Mn_{SEC}) and dispersity ($Đ$) values of synthesized polymers were determined by conventional calibration using Agilent SEC software. Fluorescence plate readings were performed on a BioTek Synergy HT Microplate Reader. Bio-layer interferometry was performed on a ForteBio Octet Red 96 Bio-layer Interferometer using Dip and Read^{TM} Amine Reaction Second-Generation (AR2G) Biosensors.

2.6.3. Synthetic Methods

Synthesis of 2-(dodecylthiocarbonothioylthio)-2-methylpropionic acid (DMP/DDMAT)

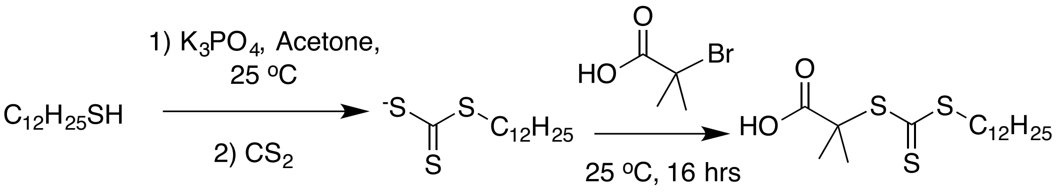

Dodecane thiol (4.75 mL, 19.8 mmol) was added dropwise to a stirred suspension of K_3PO_4 (4.02g, 18.9 mmol) in acetone (60 mL). The reaction vessel was placed in an ice bath. Carbon disulfide (3.20 mL, 53.0 mmol) was added and the solution turned bright yellow, but was still cloudy. After stirring for ten minutes, 2-bromo-2-methylpropionic acid (3.00 g, 18.0 mmol) was added and a precipitation of KBr was noted. The ice bath was removed after 10 minutes and the reaction was left stirring at room temperature for 16 hours. Solvent was removed *in vacuo* and the residue was extracted into DCM (2 x 50 mL) from 1 M HCl (100 mL). The organic extracts were further washed with water (100 mL) and brine (100 mL) and dried over $MgSO_4$. Recrystallisation from n-hexane yielded a bright yellow solid (1.80 g, 27.5%).

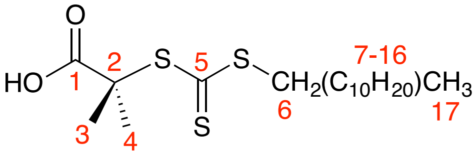

^{1}H NMR (400 MHz, CDCl3) δ_{ppm}: 3.28 (2H, t, J_{HH}=7.5, H6); 1.66 (6H, s, H3/4); 1.10-1.25 (20H, alkyl, H7-16); 0.79 (3H, m, H17).

^{13}C NMR (400 MHz, CDCl3) δ_{ppm}: 220.86 (C5); 178.04 (C1); 55.51 (C2); 37.08 (C7); 31.92 (C6); 29.64, 29.57, 29.46, 29.35, 29.12, 28.98, 27.82 (C8-15); 25.23 (C3/4); 22.70 (C16); 14.13 (C17).

FTIR (solid, ν_{max}/cm^{-1}): 2910 (CH_2); 1710 (C=O); 1440 (C-C); 1305 (C-O); 1070 (S-(C=S)-S).

ESI-MS, positive mode (m/z): 365.2 ($M+H^+$, expected 365.63), 387.1 ($M+Na^+$, expected 387.61).

Synthesis of N-Thiolactone Acrylamide

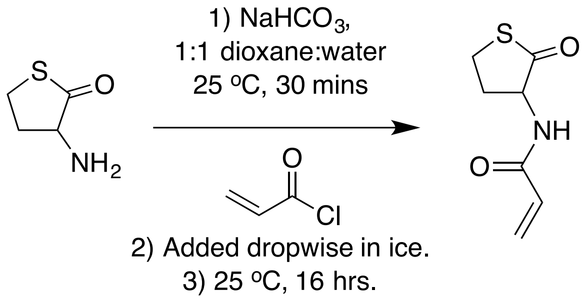

D,L-homocysteine thiolactone hydrochloride (7.04 g, 45.6 mmol) was dissolved in 1:1 dioxane: water (100 mL). The reaction vessel was transferred to an ice bath, and sodium hydrogen carbonate (19.2 g, 228 mmol) was added whilst stirring. After 30 mins stirring, acryloyl chloride (7.45 mL, 91.2 mmol) was added dropwise. The reaction was stirred for 16 hours at room temperature. The reaction was extracted into ethyl acetate (200 mL) from brine (200 mL). The organic layer was dried over Na_2SO_4, filtered and concentrated *in vacuo* to yield a white solid (5.57 g, 71.3%).

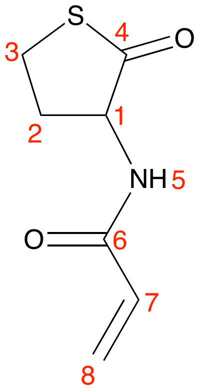

^{1}H NMR (400 MHz, $CDCl_3$) δ_{ppm}: 6.35 (1H, m, H7); 6.17 (1H, m, H8, trans); 5.73 (1H, m, H8, cis); 4.61 (1H, s, H1); 3.41 (1H, m, H3); 3.3 (1H, m, H3); 3.02 (1H, m, H2); 1.99 (1H, qd, J_{HH}=12.5(x3), 6.9, H2).

^{13}C NMR (400 MHz, $CDCl_3$) δ_{ppm}: 165.83 (C), 129.93 (CH, C1), 127.73 (CH_2, C3), 59.59 (CH, C6), 32.07 (CH_2, C7), 27.70 (CH_2, C3).

FTIR (solid, ν_{max}/cm^{-1}): 3290 (N-H); 2900 (CH_2); 1680 (C=O); 1560 (N-H); 1405 (C-C stretch in ring); 1210 (C-N aliphatic); 1005 (=C-H bend); 930 (alkene).

ESI-MS, positive mode (m/z): 194.0 ($M+Na^+$, expected 194.20), 365.0 ($2M+Na^+$, expected 365.41)

Synthesis of b-D-galactose pentaacetate

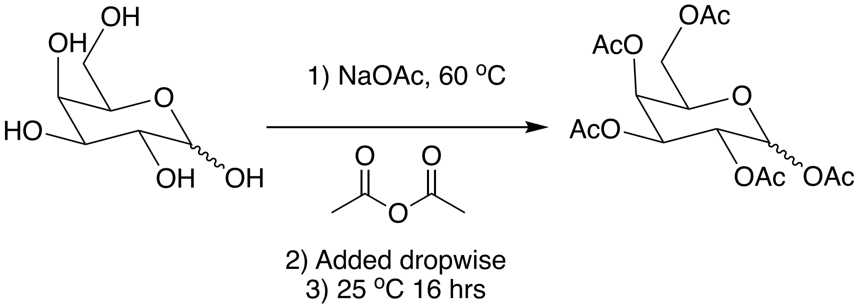

Sodium acetate trihydride (2.06 g, 20.2 mmol) was ground by mortar and pestle and stirred in a 60°C oil bath. D(+)-galactose (2.00 g, 11.1 mmol) was added, and a condenser was attached to the reaction vessel. Acetic anhydride (10 mL, 106 mmol) was added dropwise. The reaction was refluxed for 10 minutes, after which it was cooled to room temperature and left stirring overnight. Ethanol (22 mL) was added to evolve acetic acid. The mixture was concentrated *in vacuo*, extracted into DCM (40 mL) and washed with warm water (2 x 40 mL). The organic layer was dried over $MgSO_4$, filtered and concentrated in vacuo. Ethanol (25 mL) was added, as was a few spatulas of activated charcoal, and the reaction was refluxed for 20 mins, cooled, filtered and recrystallized in ethanol to yield white crystals (1.30 g, 30%).[62]

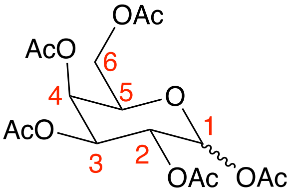

^1H NMR (300 MHz, $CDCl_3$) δ_{ppm}: 5.72 (1H, d, J_{HH}=8.2, H1); 5.45 (1H, br s, H4); 5.36 (1H, t, J_{HH}=9.3 x 2, H2); 5.11 (1H, m, H3); 4.17 (2H, m, H6); 4.07 (1H, m, H5); 2.19, 2.15, 2.07, 2.02 (15H, 4 x s, acetyl groups).

^{13}C NMR (300 MHz, $CDCl_3$) δ_{ppm}: 92.17 (CH, C1), 71.12 (CH, C4), 70.88 (CH, C2), 67.82 (CH, C3), 66.79 (CH, C5), 61.03 (CH_2, C6), 20-21 (CH_3, Acetyls).

FTIR (solid, ν_{max}/cm^{-1}): 2973 (CH_2); 1765 (C=O); 1374 (C-H); 1210 (C-O stretch); 957 (=C-H bend); 900 (C-H “oop” bend).

ESI-MS, positive mode (m/z): 413.1 (M+Na$^+$, expected 413.33)

Synthesis of 1-b-allyl-D-galactose pentaacetate

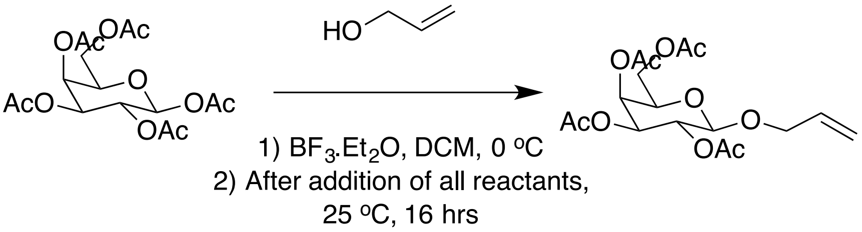

Beta-D-galactose pentaacetate (2.00 g, 5.13 mmol) was dissolved in DCM (40 mL). Allyl alcohol (0.425 mL, 6.25 mmol) was added whilst stirring in an ice bath. Boron trifluoride dietherate (1.35 mL, 7.11 mmol) was added dropwise. 20 minutes later, the reaction was taken out of the ice bath and stirred for 16 hours. Anhydrous potassium carbonate (1.08 g, 7.24 mmol) was added whilst stirring. 30 minutes later, the reaction was filtered and washed with water (2 x 50 mL) and brine (50 mL). The organic layer was dried over $MgSO_4$, filtered and concentrated *in vacuo*. The residue was purified by column chromatography on silica using an eluent comprising 2:3 ethyl acetate: 40 – 60 °C petroleum ether to yield a yellow oil (1.02 g, 51.2%).

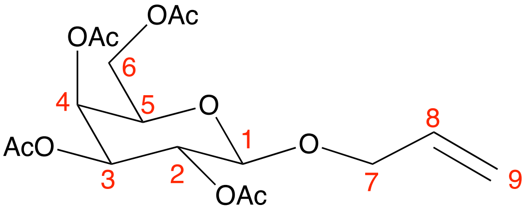

^{1}H NMR (300 MHz, CDCl3) δ_{ppm}: 5.88 (1H, m, H8); 5.41 (1H, d, J_{HH}=3.2, H1); 5.34 (1H, m, H4); 5.28 (1H, m, H2); 5.17 (1H, m, H9); 5.05 (1H, m, H3); 4.5 (2H, m, H6); 4.15 (2H, m, H7); 4.13 (1H, m, H5); 2.15, 2.06, 2.05, 1.99 (15H, 4 x s, acetyl groups)

^{13}C NMR (300 MHz, CDCl3) δ_{ppm}: 117.61 (CH_2, C9), 100.12 (CH, C8), 70.96 (CH, C1), 70.67 (CH, C4), 70.04 (CH_2, C7), 69.01 (CH, C2), 67.07 (CH, C3), 61.30 (CH_2, C6), 30.94 (CH, C5), 20-21 (CH_3, Acetyls).

FTIR (solid, ν_{max}/cm^{-1}): 3027 (O-H); 2920 (CH_2); 1754 (C=O); 1495 (C-H); 1220 (C-O stretch); 705 (C-H).

ESI-MS, positive mode (m/z): 411.1 (M+Na$^+$, expected 411.36)

Synthesis of 1-b-hexyl-D-galactose pentaacetate

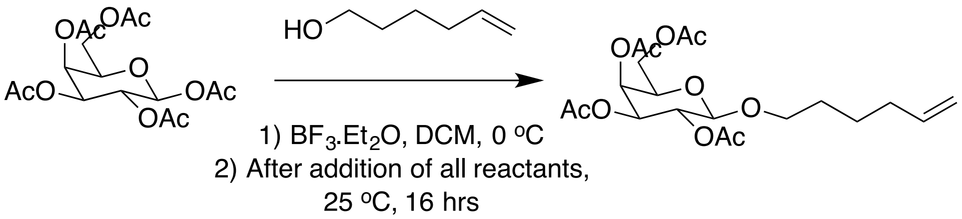

Beta-D-galactose pentaacetate (4.00 g, 10.26 mmol) was dissolved in DCM (60 mL). 5-hexen-1-ol (1.25 mL, 12.5 mmol) was added whilst stirring in an ice bath. Boron trifluoride dietherate (2.70 mL, 14.2 mmol) was added dropwise. 20 minutes later, the reaction was taken out of the ice bath and stirred for 16 hours. Anhydrous potassium carbonate (2.0 g, 14.5 mmol) was added whilst stirring. 30 minutes later, the reaction was filtered and washed with water (2 x 100 mL) and brine (100 mL). The organic layer was dried over $MgSO_4$, filtered and concentrated *in vacuo*. The residue was purified by column chromatography on silica using an eluent comprising 2:3 ethyl acetate: 40 – 60 °C petroleum ether to yield a clear oil (1.45 g, 32.7%)

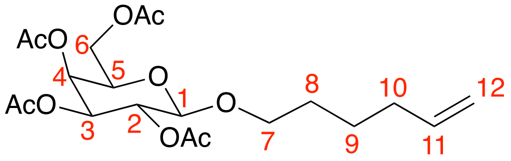

^{1}H NMR (300 MHz, CDCl3) δ_{ppm}: 5.83 (1H, m, H11); 5.41 (1H, m, H1); 5.23 (1H, m, H4); 5.12 (1H, m, H2); 5.00 (3H, m, H12/3); 4.49 (1H, m, H5); 3.92 (2H, m, H6); 3.68 (2H, m, H7); 2.07 (15H, m, acetyl groups); 1.5 (4H, m, H8/9).

^{13}C NMR (300 MHz, CDCl3) δ_{ppm}: 114.69 (CH_2, C12), 101.36 (CH, C11), 70.98 (CH, C1), 70.60 (CH, C4), 70.00 (CH_2,, 7), 68.94 (CH, C2), 67.69 (CH, C3), 67.09 (CH, C5), 61.30 (CH_2, C6), 33.31 (CH_2, C10), 28.82 (CH_2, C8), 25.07 (CH_2, C9), 20.69 (CH_3, Acetyls).

FTIR (solid, ν_{max}/cm^{-1}): 3014-2823 (alkyl/alkenyl CH_2); 1743 (C=O); 1430 (weak, alkyl C-H); 1369 (C-O); 1216 (C-H stretch); 1045 (C-O); 906 (monosubstituted alkene).

ESI-MS, positive mode (m/z): 453.0 (M+Na$^+$, expected 453.4), 883.3 (2M+Na$^+$, expected 883.9).

General Procedure for Polymerisation of N-hydroxyethyl acrylamide (HEA)

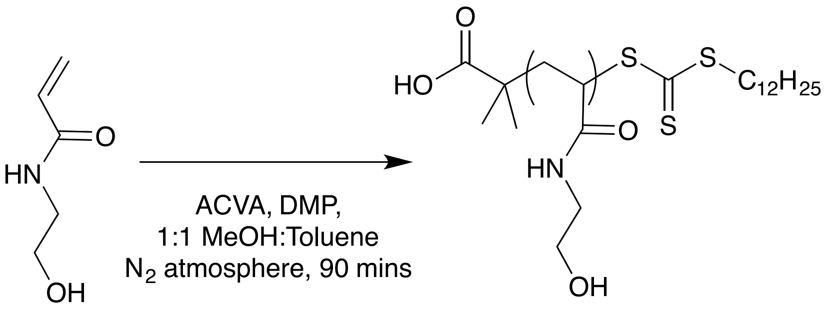

The following procedure describes a reaction with a theoretical degree of polymerisation (DP) of 100 repeat units. 4,4-azobis(4-cyanovaleric acid) (5 mg, 0.018 mmol), 2- (dodecylthiocarbonothioylthio)-2-methylpropanoic acid (CTA, 32 mg, 0.088 mmol) and *N*-hydroxyethyl acrylamide (1 g, 8.8 mmol) were dissolved in 1:1 methanol: toluene (4 mL) in a glass vial with a stirrer bar. Mesitylene (200 µL) was added and a sample was removed for ^{1}H-NMR analysis in $CDCl_3$. The reaction mixture was degassed by N_2 for 30 minutes, sealed and placed in a 70°C oil bath. After 90 minutes, the solution was opened to air and quenched by submerging the flask in $N_{2(l)}$. The polymer (pHEA) was precipitated three times from methanol into diethyl ether to give a light yellow solid.

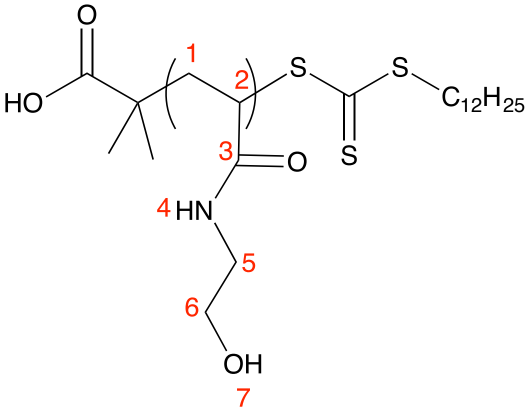

Conversion (NMR): 83.6%; M_n (theoretical): 7051 g.mol^{-1}; M_n (SEC) 13904 g.mol^{-1}; M_w (SEC) 14969 g.mol^{-1}; M_w/M_n (SEC): 1.1.

^{1}H NMR (300 MHz, D_4-MeOH) δ_{ppm}: 4.60-4.90 (br s, H6), 3.55-3.75 and 3.05-3.20 (2 x br s, H5), 2.00-2.20 and 1.50-1.80 (2 x br s, H1/2).

FTIR (solid, ν_{max}/cm^{-1}): 3300 (N-H and O-H stretch), 2854 (alkyl C-H stretch), 1641 (amide C=O stretch), 1555 (N-H bend), 1443 (alkane), 1225 (C-O stretch), 1060 (C-O stretch).

General Procedure for Copolymerisation of N-hydroxyethyl acrylamide (HEA) and N-thiolactone acrylamide (TLAm)

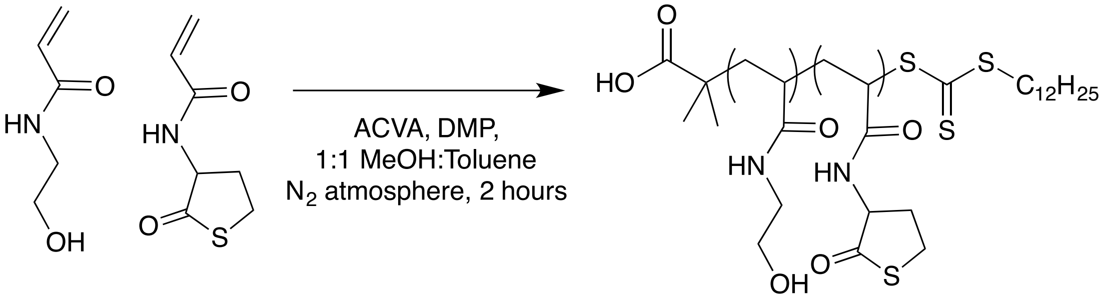

The following procedure describes a reaction with a theoretical degree of polymerisation (DP) of 50 repeat units, with 0.9 equivalents HEA and 0.1 equivalents TLA. 4,4-azobis(4-cyanovaleric acid) (2.5 mg, 0.0089 mmol), 2-(dodecylthiocarbonothioylthio)-2-methylpropanoic acid (CTA, 32 mg, 0.088 mmol), *N*-hydroxyethyl acrylamide (0.458 g, 3.98 mmol) and *N*-thiolactone acrylamide (69 mg, 0.44 mmol) were dissolved in 1:1 methanol: toluene (3 mL) in a glass vial with a stirrer bar. Mesitylene (100 µL) was added and a sample was removed for ^{1}H-NMR analysis in $CDCl_3$. The reaction mixture was degassed by N_2 for 30 minutes, sealed and placed in a 70°C oil bath. After 2 hours, the solution was opened to air and quenched by submerging the flask in $N_{2(l)}$. The polymer (pHEA-*co*-pTLAm) was precipitated three times from methanol into diethyl ether to give a light yellow solid. The characterization below is from a theoretical 20% TLAm copolymer.

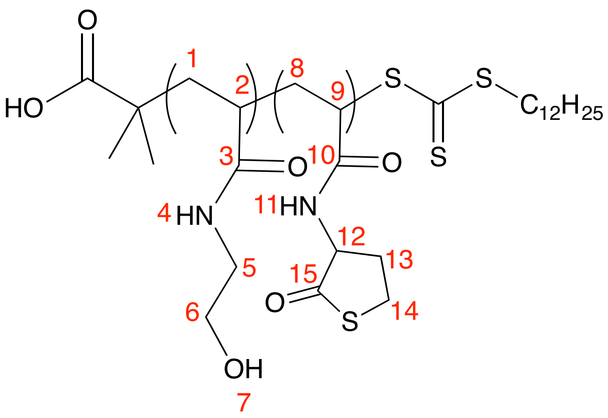

For 5% TLAm: Conversion (NMR): 95.2%; Mn (theoretical): 4402 g.mol-1; Mn (SEC) 8585 g.mol-1; Mw (SEC) 9958 g.mol-1; Mw/Mn (SEC): 1.2. For 10% TLAm: Conversion (NMR): 93.2%; Mn (theoretical): 4540 g.mol-1; Mn (SEC) 8912 g.mol-1; Mw (SEC) 10079 g.mol-1; Mw/Mn (SEC): 1.1.

^{1}H NMR (300 MHz, D4-MeOH) δppm: 7.9-8.15 (br s, N-H (H4/11)); 4.75-4.90 (br s, H6/14); 3.6-3.8 and 3.05-3.20 (2 x br s, H5/13); 2.55-2.7 (br s, H12 (this peak is less visible in 5 or 10% TLAm copolymer)), 2.00-2.40 (the left shoulder of this peak is less visible in 5 or 10% TLAm copolymer) and 1.50-1.85 (2 x br m, H1/2/8/9).

FTIR (solid, ν_{max}/cm^{-1}): 3300 (N-H and O-H stretch); 2854 (alkyl C-H stretch); 1641 (amide C=O stretch); 1555 (N-H bend); 1443 (alkane); 1225 (C-O stretch); 1060 (C-O stretch, peak has a shoulder).

Representative Double Modification of TLAm-containing copolymer: Aminolysis and Thiol-ene "click"

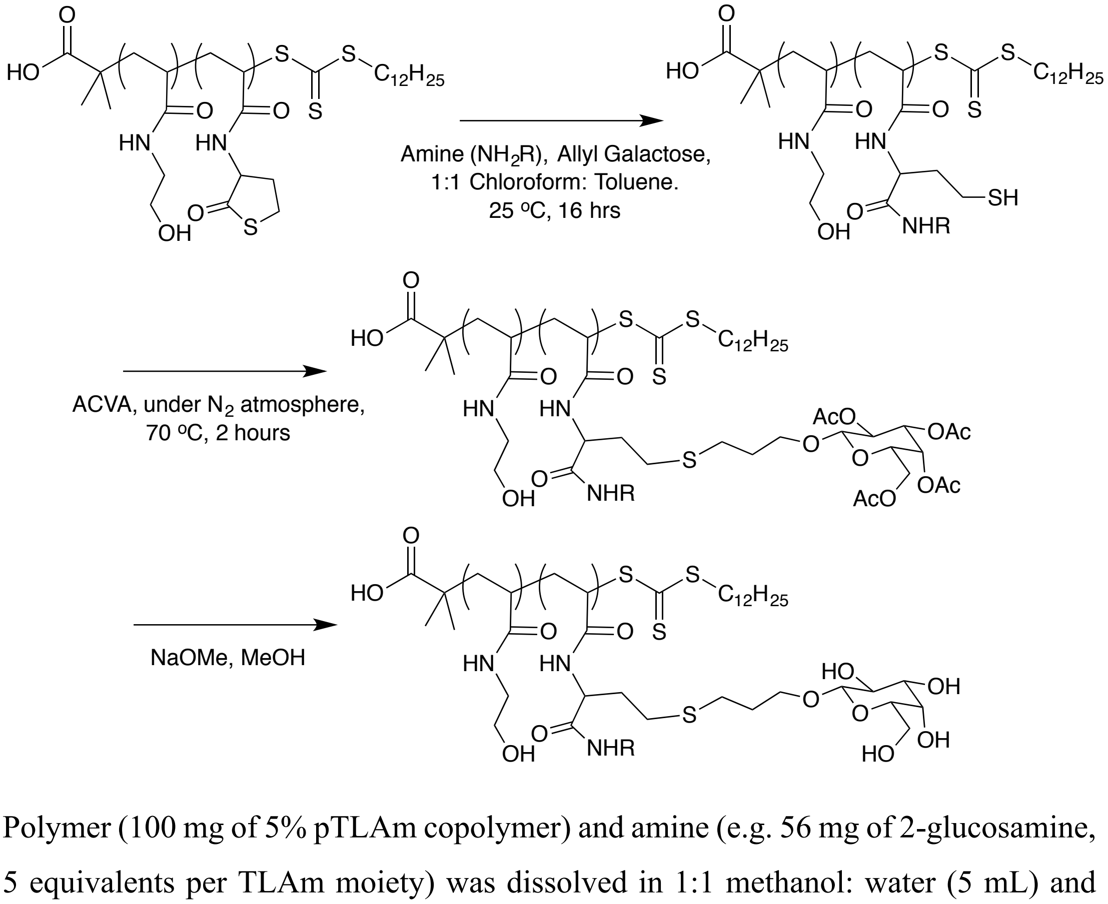

Polymer (100 mg of 5% pTLAm copolymer) and amine (e.g. 56 mg of 2-glucosamine, 5 equivalents per TLAm moiety) was dissolved in 1:1 methanol: water (5 mL) and stirred overnight at room temperature. Alkene-galactose pentaacetate (e.g. 67.4 mg of 1-b-allyl-D-galactose pentaacetate, 5 equivalents per TLAm moiety) and 4,4-azobis(4-cyanovaleric acid) (1.2 mg, 0.0045 mmol) were added. The reaction mixture was degassed by N_2 for 30 minutes, sealed and placed in a 70°C oil bath. After 2 hours, the solution was opened to air and quenched by submerging the flask in $N_{2(l)}$. The reaction mixture was concentrated *in vacuo*, re-dissolved in methanol and filtered. The polymer was then precipitated three times from methanol into diethyl ether to give a light yellow solid. The different precipitation behaviour (all polymers were very difficult to dissolve in solution) was an indication of successful modification. The polymer was subsequently dissolved in methanol (5 mL) and deprotected with sodium methoxide (0.5 μL of 5.4 M solution in methanol) and precipitated three times from methanol into diethyl ether to give a light yellow solid.[52,63]

Fluorescence-linked sorbent assay for polymer inhibitory activity

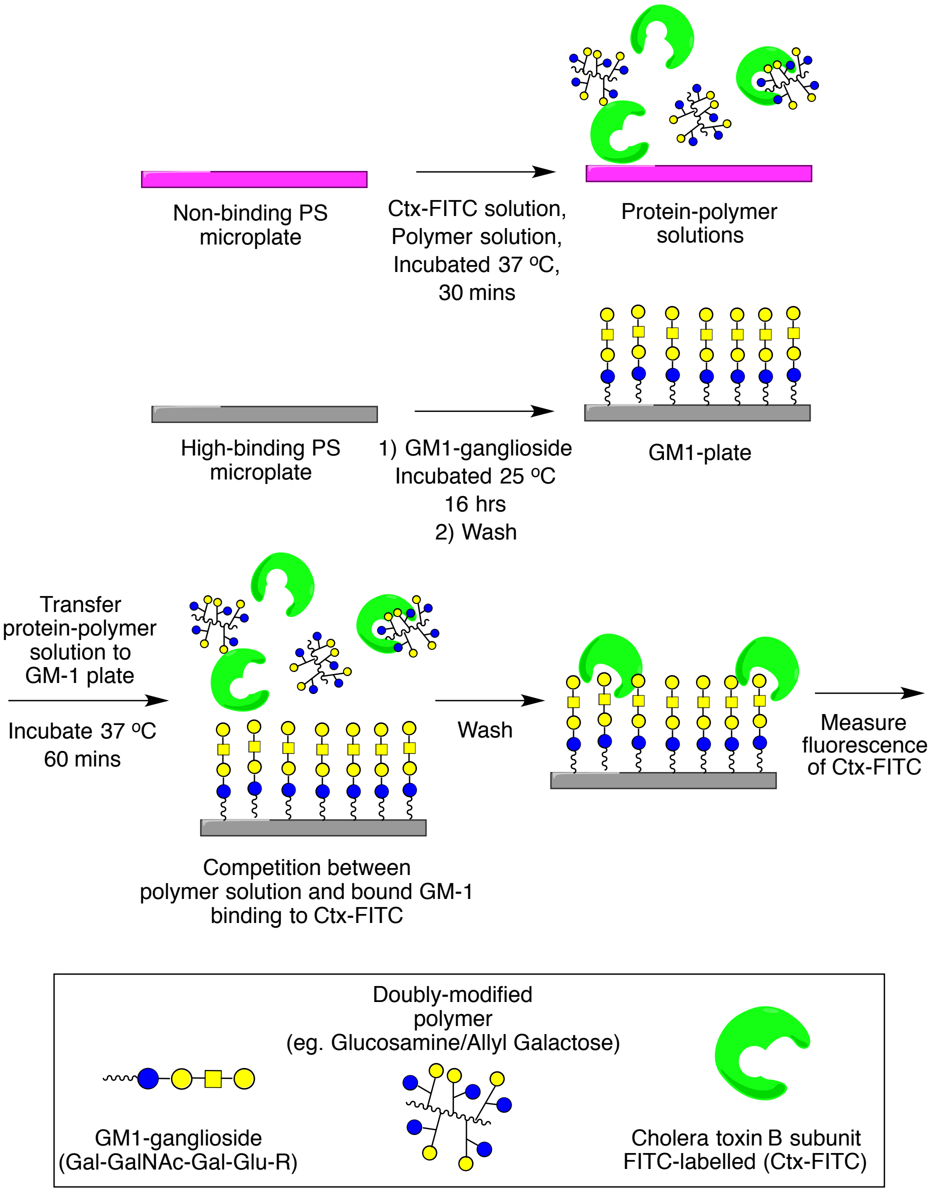

384-well high-binding PS plates were incubated for 16 hours with 50 µL of 100 µg.mL^{-1} GM-1 glycolipid (in PBS). Unbound glycolipid was removed by washing with water (x3). Polymer solutions were made up as serial dilutions (up to 12 dilutions by 2 from 1 mg.mL^{-1} in HEPES). CTx-FITC (4 µL of 100 µg.mL^{-1} in 10mM HEPES buffer with 0.15 M NaCl, 0.1 mM CaCl$_2$ and 0.01 mM Mn^{2+} (pH 7.5)) was added to 36 µL of polymer solution. The CTx/polymer solutions were then transferred to the GM-1-coated plates and incubated at 37°C for 60 minutes. The wells were then washed (x3) with HEPES buffer. Fluorescence of wells was measured at excitation/emission wavelengths of 485/528 nm respectively. All experiments were carried out in triplicate, using pure CTx-FITC wells (with no polymer) as controls. The above protocol is repeated for RCA-FITC to compare polymer inhibitory activity.

Bio-layer interferometry assay for polymer inhibitory activity

The tips of a row of 8 AR2G sensors were soaked in water for 30 minutes before running the assay. Each dipping solution was prepared in an 8-well row of a 96-well plate with 200 µL in each well, as follows. During the assay, these sensor tips were then dipped in water for baseline, dipped in EDC/NHS solution for activation, dipped in toxin (25 µg/mL in HEPES buffer) for loading and ethanolamine (1 M solution in water) for deactivation before being exposed to polymer sample solutions. Polymer solutions were made up as serial dilutions (7 dilutions by 10 from 1 mg.mL^{-1} in HEPES). Association was run for 15 minutes in polymer solution, followed by dissociation in HEPES for 30 minutes. Data was fitted using a heterogeneous sites (2:1) model.

2.7. Appendix

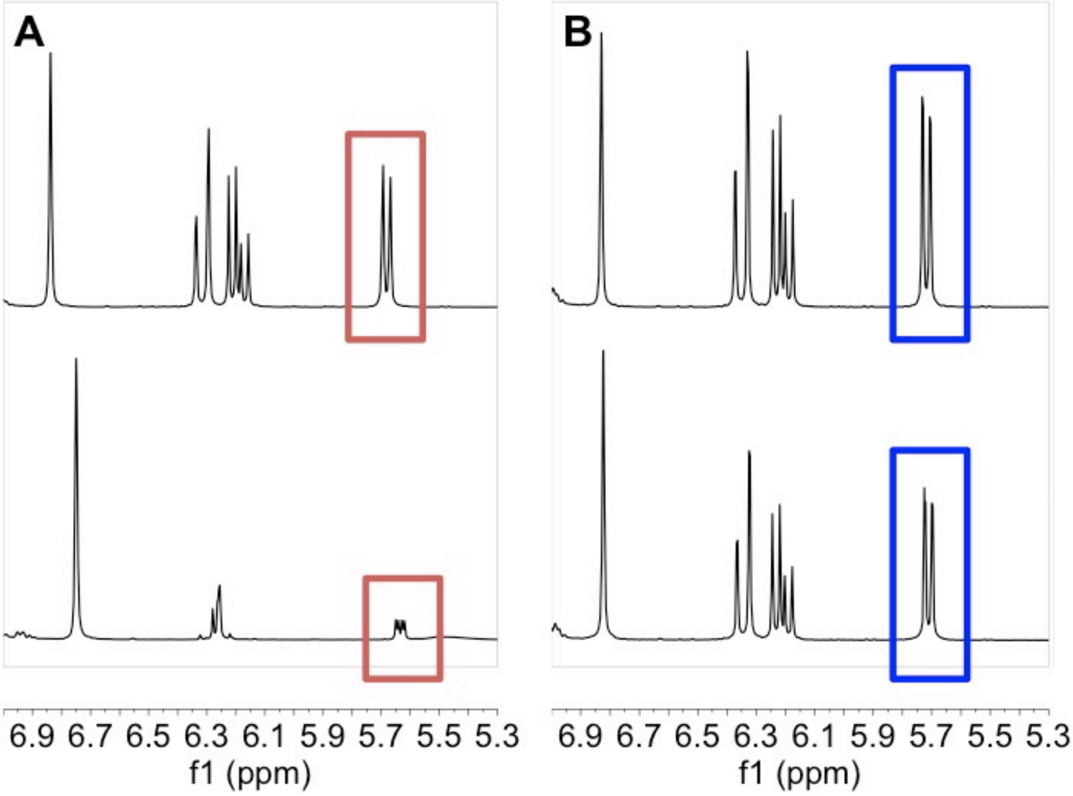

Figure 2-16. ^{1}H-NMR spectra showing depletion of monomer vinyl peaks upon polymerisation. A) Formation of pHEA from HEA monomer. B) Formation of pTLAm from TLAm monomer. The red and blue boxes denote the vinyl peaks in the HEA and TLAm respectively. Here it can be seen that the HEA vinyl peak (~5.6 ppm) can be distinguished from the TLAm vinyl peak (~5.7 ppm).

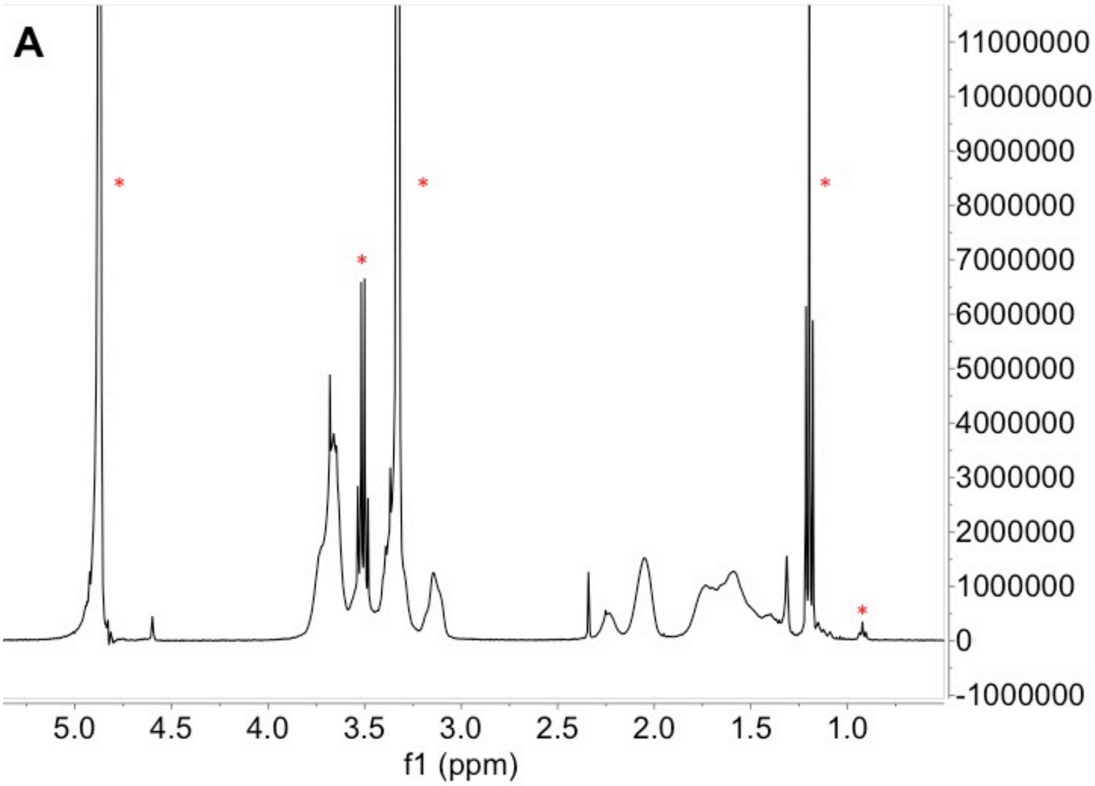

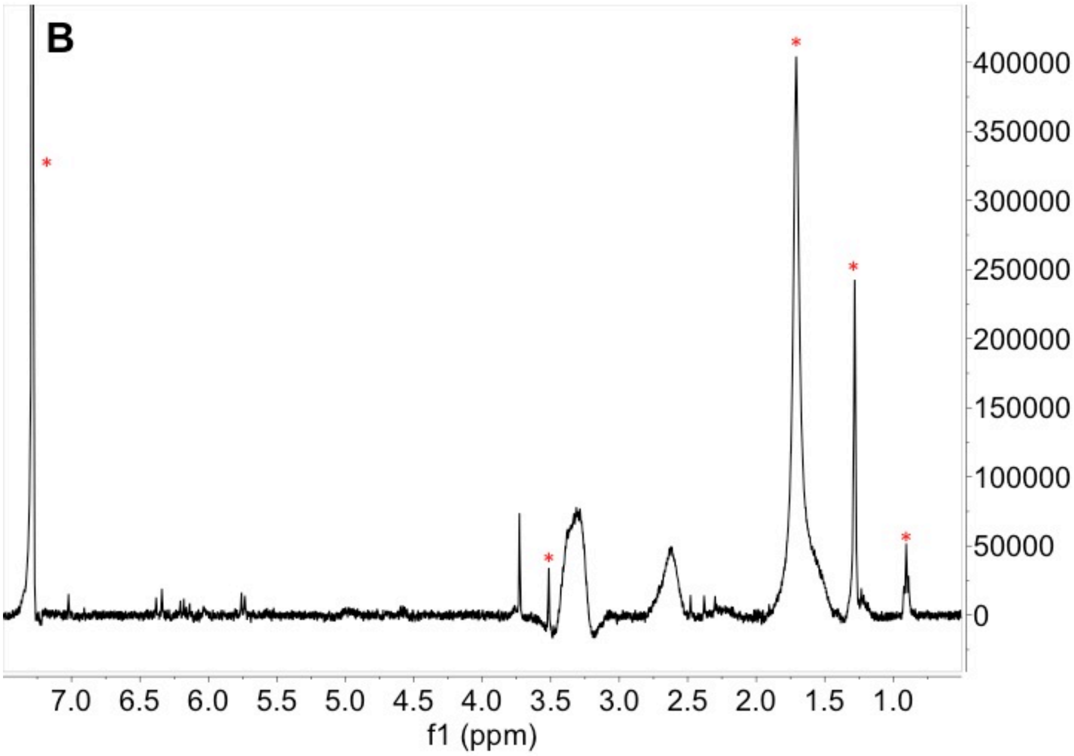

Figure 2-17. ^{1}H-NMR spectra showing difference between polymer peaks from pHEA (soluble in methanol) and pTLAm (soluble in chloroform). 5/10/20 % pTLAm content resulted in polymers still soluble in methanol. A) pHEA. B)

pTLAm. Asterisks denote solvent impurities: chloroform, methanol, water, acetone, grease, diethyl ether (used in purification).

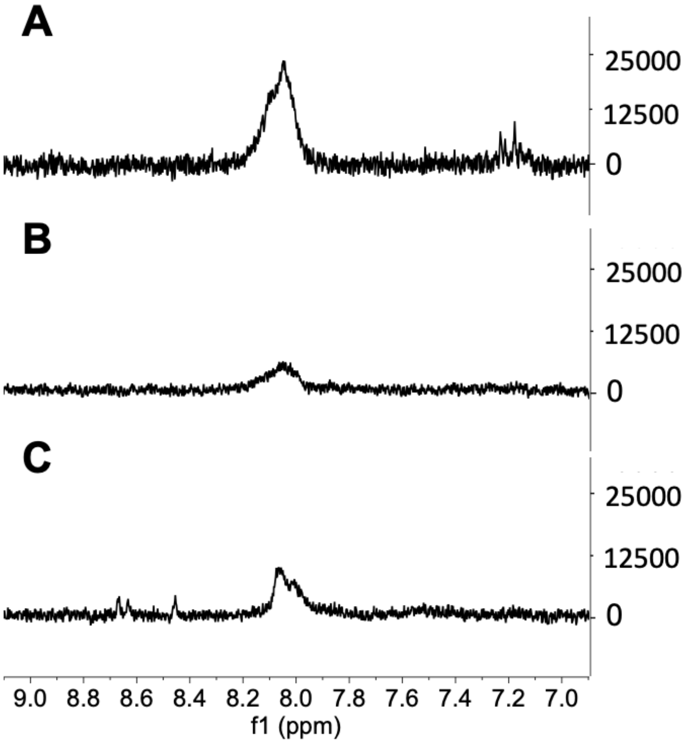

Figure 2-18. ^{1}H-NMR spectra showing change in amide peak. A) pHEA-*co*-TLAm(5 %). B) pHEA-*co*-TLAm(5 %) modified with glucosamine, hexenyl-β-D-galactose. C) pHEA-*co*-TLAm(5 %) modified with glucosamine, allyl-β-D-galactose.

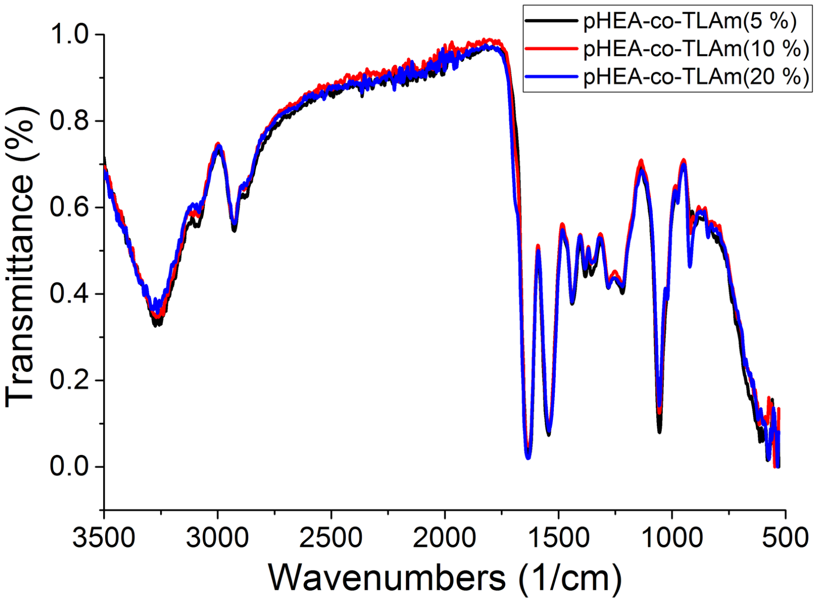

Figure 2-19. Solid-phase FTIR of pHEA-*co*-TLAm.

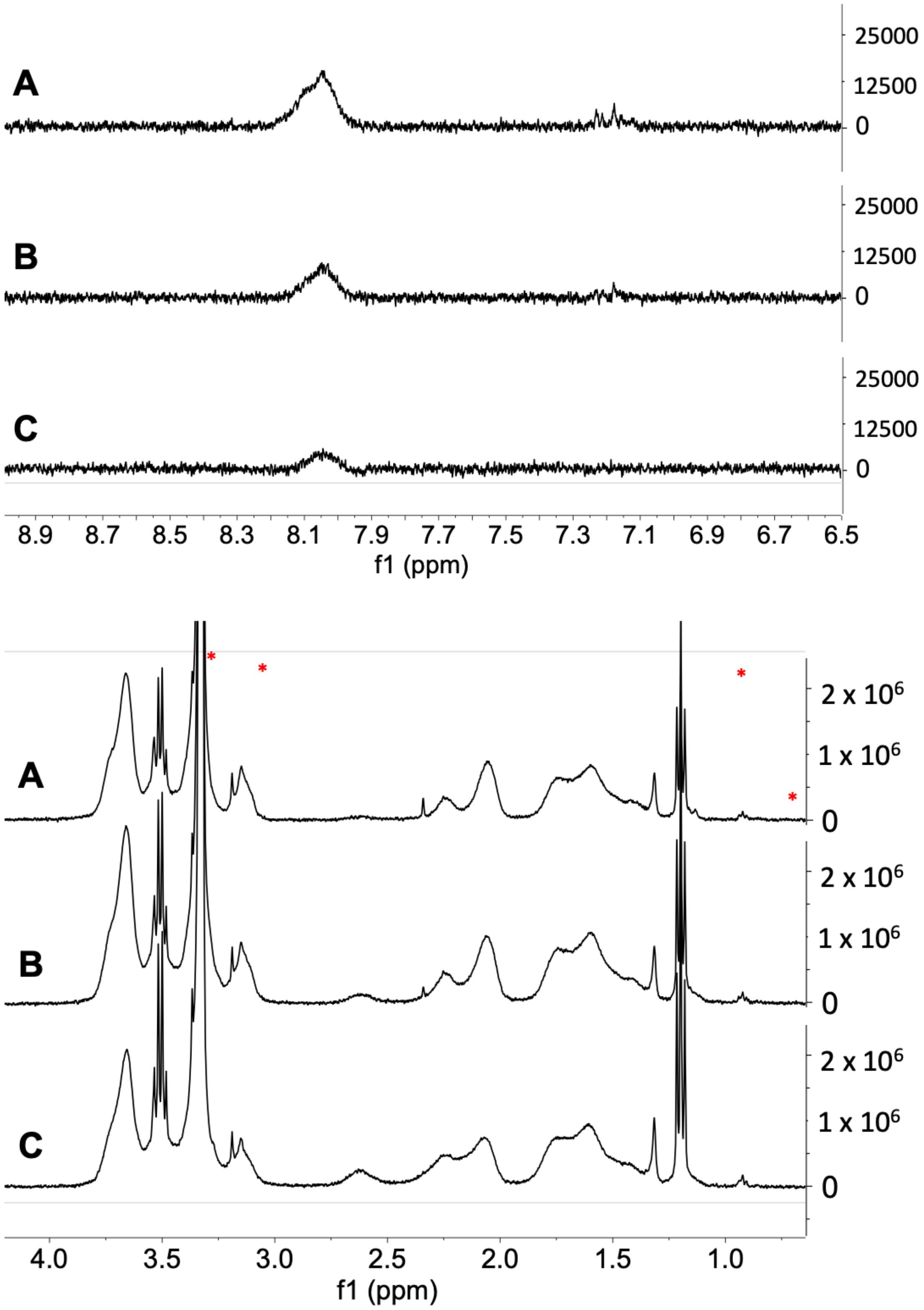

Figure 2-20. ^{1}H-NMR spectra showing difference between polymer peaks from pHEA-*co*-TLAm 5/10/20 % (A/B/C respectively). Top) Heteroatom region showing amide peak. Bottom) Polymer peak region, showing enrichment of ~2.75 ppm peak

with increasing proportion of TLAm. Asterisks denote solvent impurities: methanol, grease, diethyl ether (used in purification).

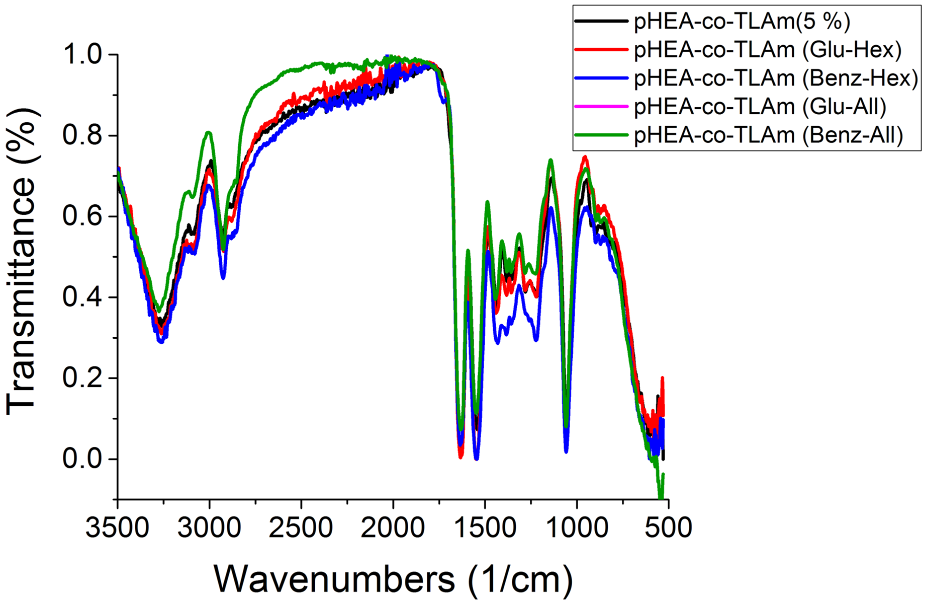

Figure 2-21. Solid-phase FTIR of pHEA-*co*-TLAm(5 %) before and after modification. Brackets after polymer name indicate modification, ie.: secondary modification (glucosamine or benzylamine) – galactose linker (allyl or hexenyl). Of note are potential C-O sugar peaks at ~1000 cm^{-1} and a shoulder on the ~ C=O peak suggesting an additional C=O amide peak in the modified samples.

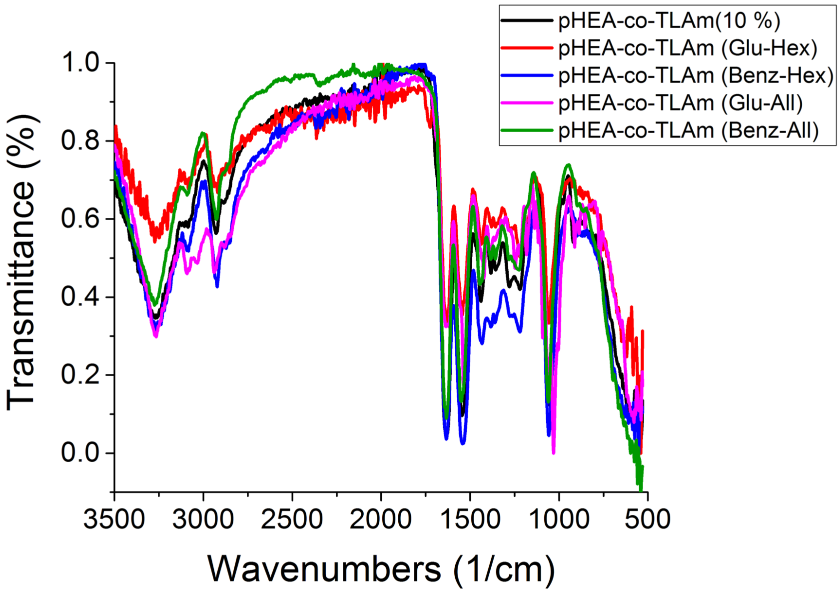

Figure 2-22. Solid-phase FTIR of pHEA-*co*-TLAm(10 %) before and after modification. Brackets after polymer name indicate modification, ie.: secondary modification (glucosamine or benzylamine) – galactose linker (allyl or hexenyl). Of

note are potential C-O sugar peaks at ~1000 cm^{-1} and a shoulder on the ~ C=O peak suggesting an additional C=O amide peak in the modified samples.

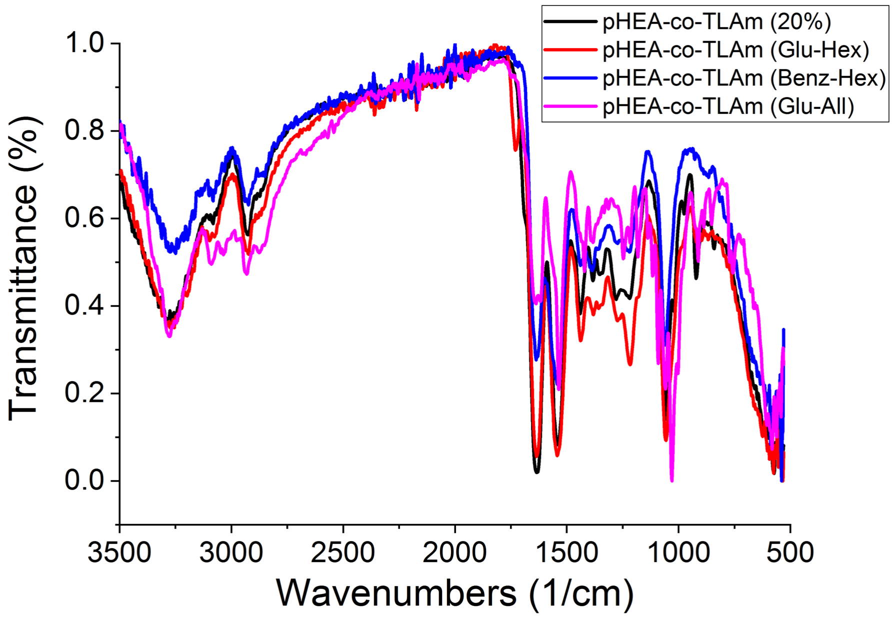

Figure 2-23. Solid-phase FTIR of pHEA-*co*-TLAm(20 %) before and after modification. Brackets after polymer name indicate modification, ie.: secondary modification (glucosamine or benzylamine) – galactose linker (allyl or hexenyl). Of note are potential C-O sugar peaks at ~1000 cm^{-1} and a shoulder on the ~ C=O peak suggesting an additional C=O amide peak in the modified samples.

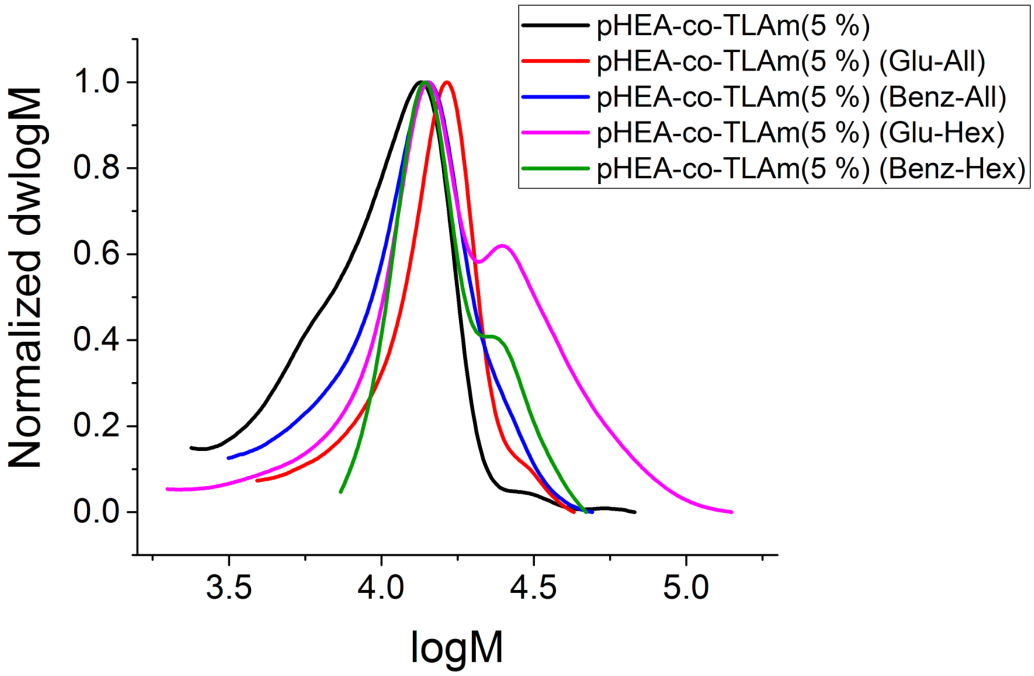

Figure 2-24. DMF SEC molecular weight traces for modification of pHEA-*co*-TLAm(5 %). Several traces are bimodal potentially due to transesterification reactions having taken place.

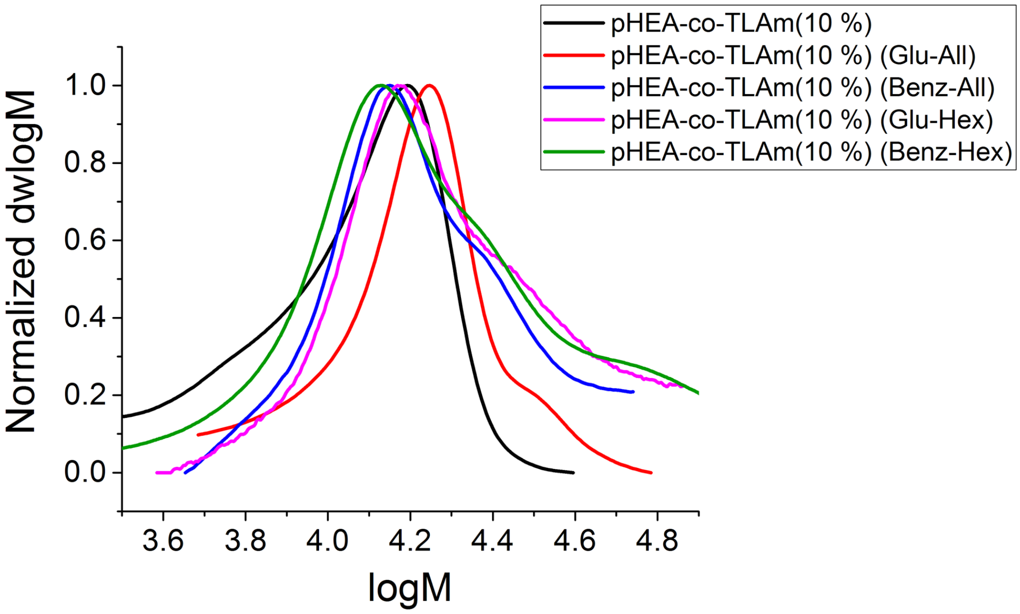

Figure 2-25. DMF SEC molecular weight traces for modification of pHEA-*co*-TLAm(10 %).

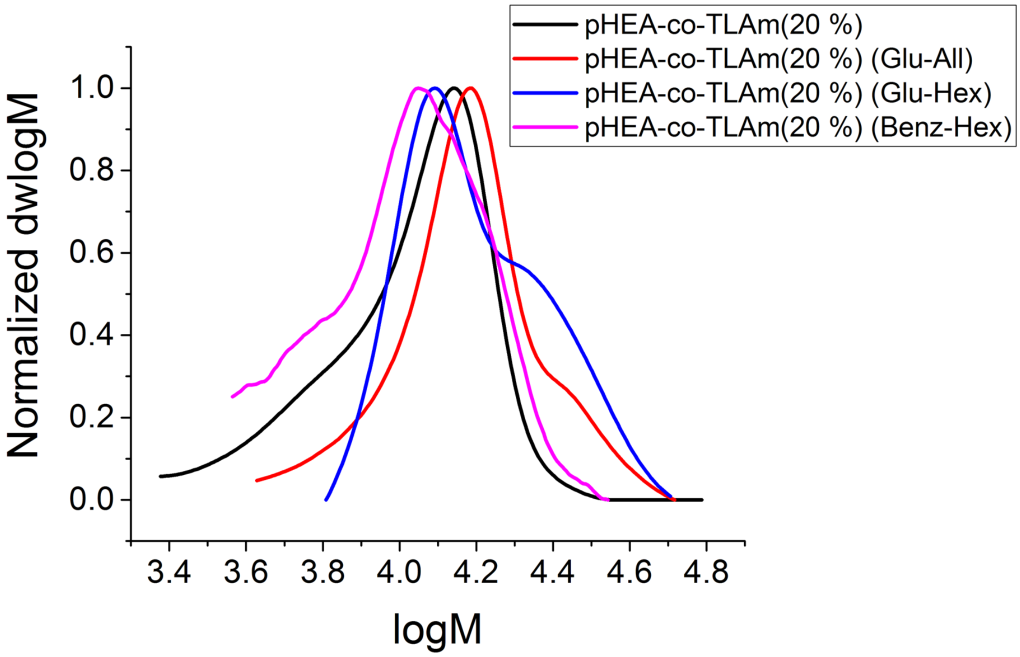

Figure 2-26. DMF SEC molecular weight traces for modification of pHEA-*co*-TLAm(20 %).

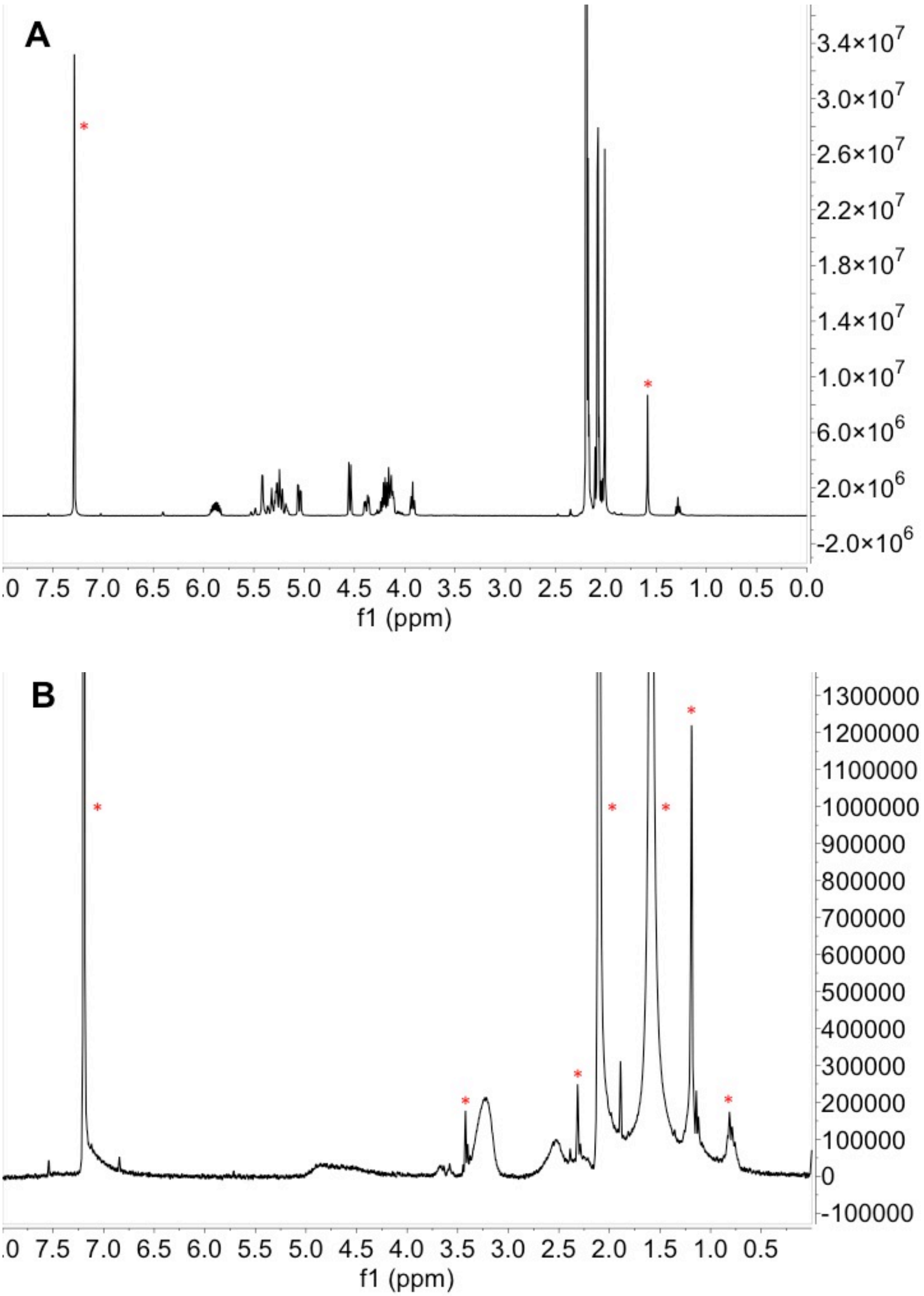

Figure 2-27. ^{1}H-NMR spectra showing difference between allyl-D-galactose precursor (A) and pTLAm homopolymer modified with this compound (B). Key is the loss of the acetate peaks at ~2-2.5 ppm. Asterisks denote solvent impurities: chloroform, water, grease, acetone, diethyl ether (used in purification).

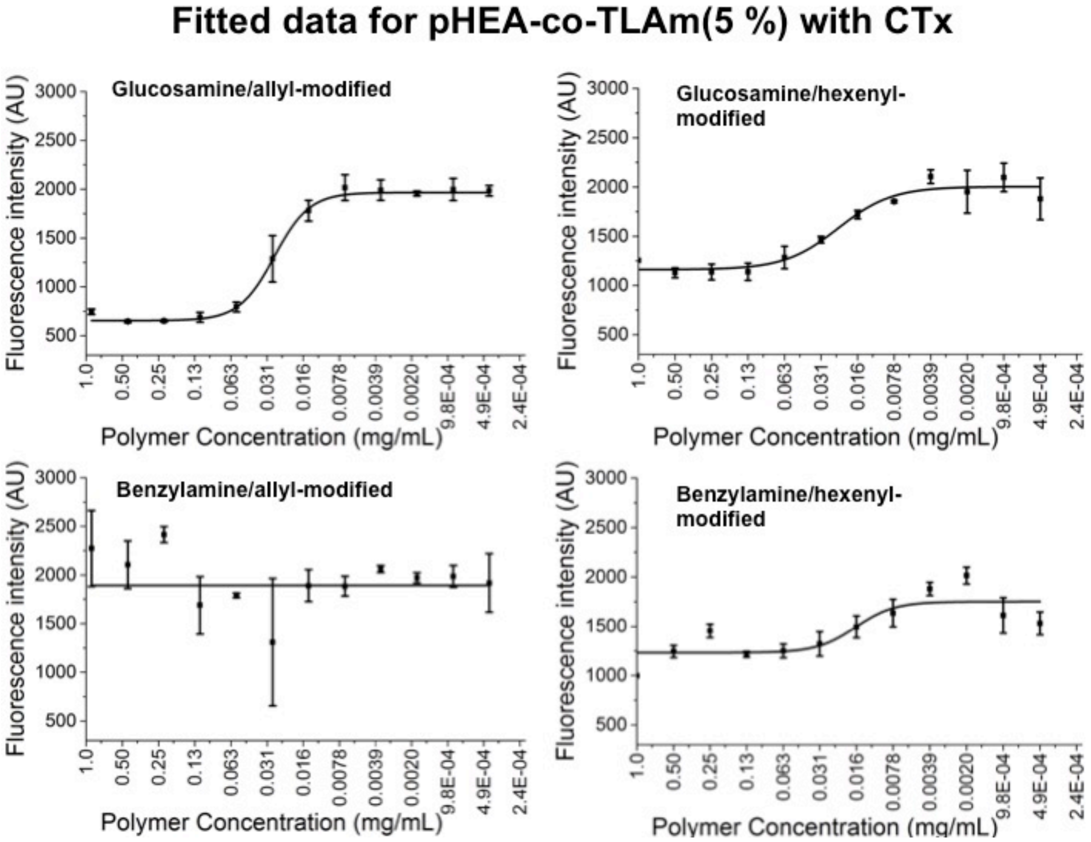

Figure 2-28. Fitted Microplate assay binding curves with CTxB for pHEA-co-TLAm (5 % TLAm) with different galactose linkers and secondary unit modifications. Data was fitted using a heterogeneous sites (2:1) model.

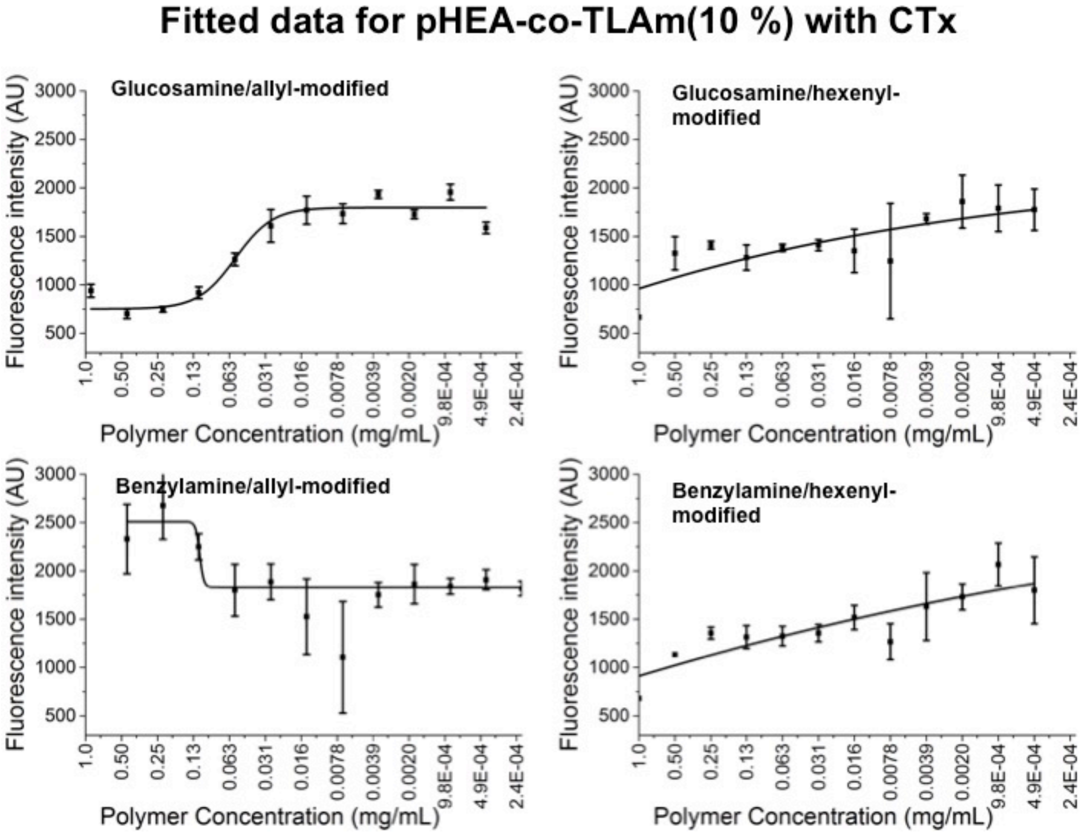

Figure 2-29. Fitted Microplate assay binding curves with CTxB for pHEA-co-TLAm (10 % TLAm) with different galactose linkers and secondary unit modifications. Data was fitted using a heterogeneous sites (2:1) model. It is possible that, excluding the high polymer concentration values in the hexenyl graphs, a sigmoidal fit might have been achieved.

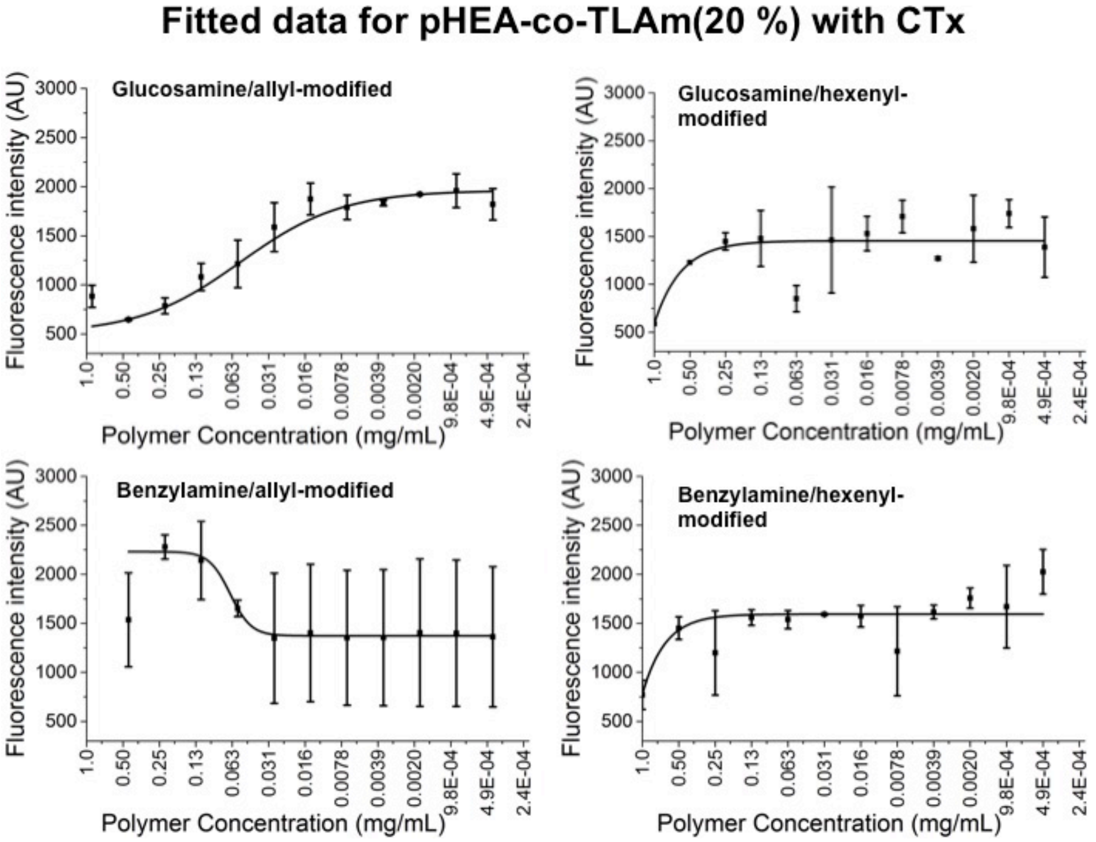

Figure 2-30. Fitted Microplate assay binding curves with CTxB for pHEA-co-TLAm (20 % TLAm) with different galactose linkers and secondary unit modifications. Data was fitted using a heterogeneous sites (2:1) model. It is possible that, excluding the high polymer concentration values in the benzylamine/hexenyl graph, a sigmoidal fit might have been achieved.

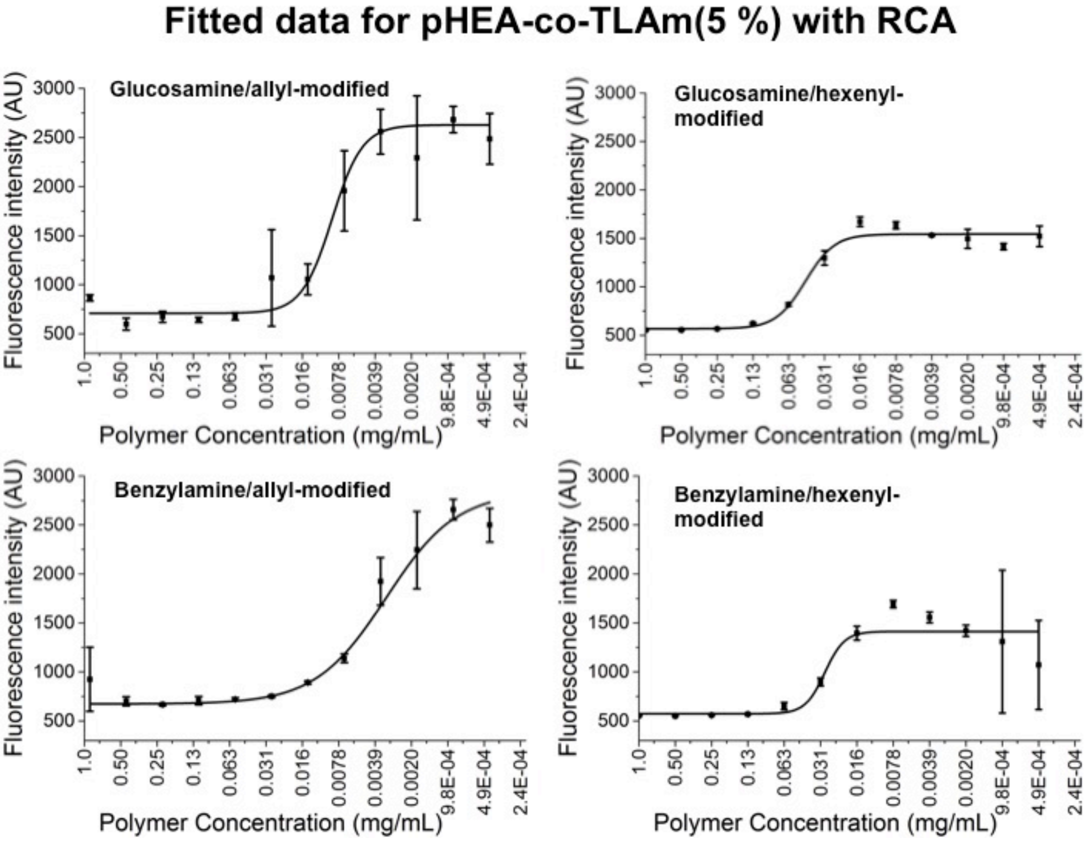

Figure 2-31. Fitted Microplate assay binding curves with RCA_{120} for pHEA-co-TLAm (5 % TLAm) with different galactose linkers and secondary unit modifications. Data was fitted using a heterogeneous sites (2:1) model. Note that a peak is seen in the hexenyl samples at ~0.078 mg/mL polymer, potentially signifying that the fit was not exact.

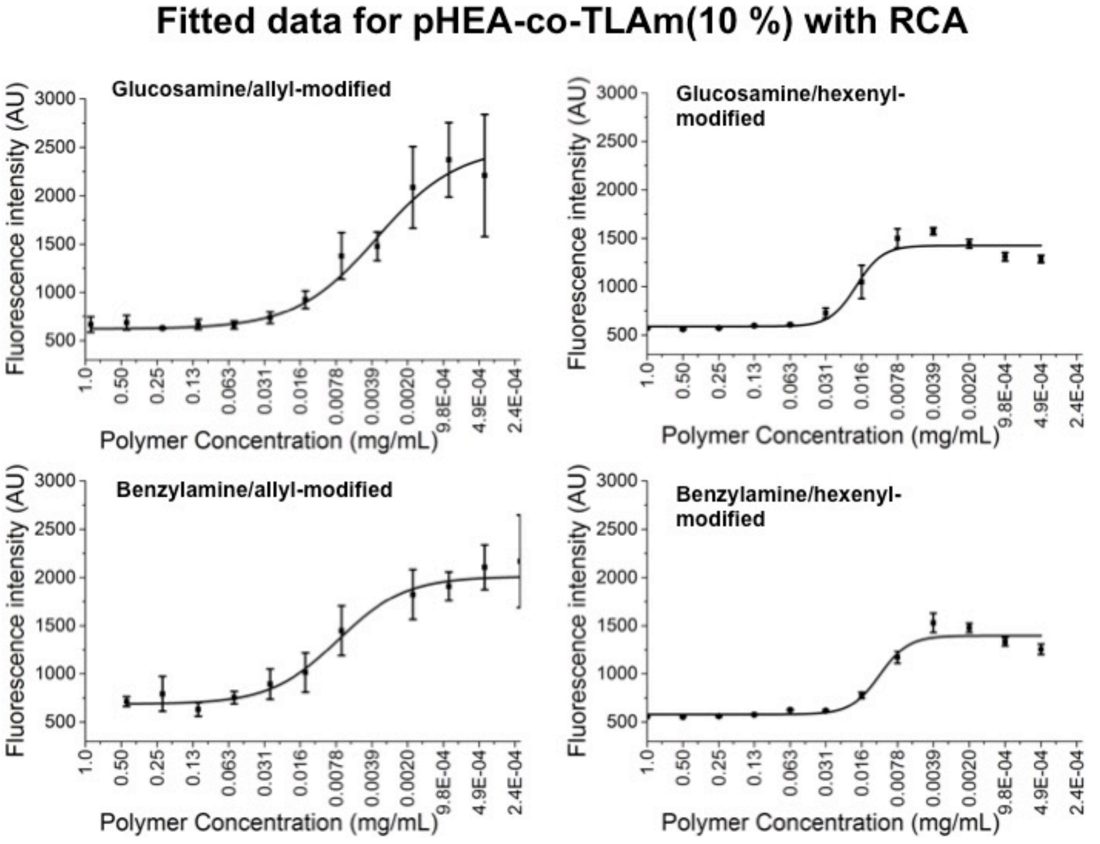

Figure 2-32. Fitted Microplate assay binding curves with RCA_{120} for pHEA-co-TLAm (10 % TLAm) with different galactose linkers and secondary unit modifications. Data was fitted using a heterogeneous sites (2:1) model. Note that a peak is seen in the hexenyl samples at ~0.078 mg/mL polymer, potentially signifying that the fit was not exact.

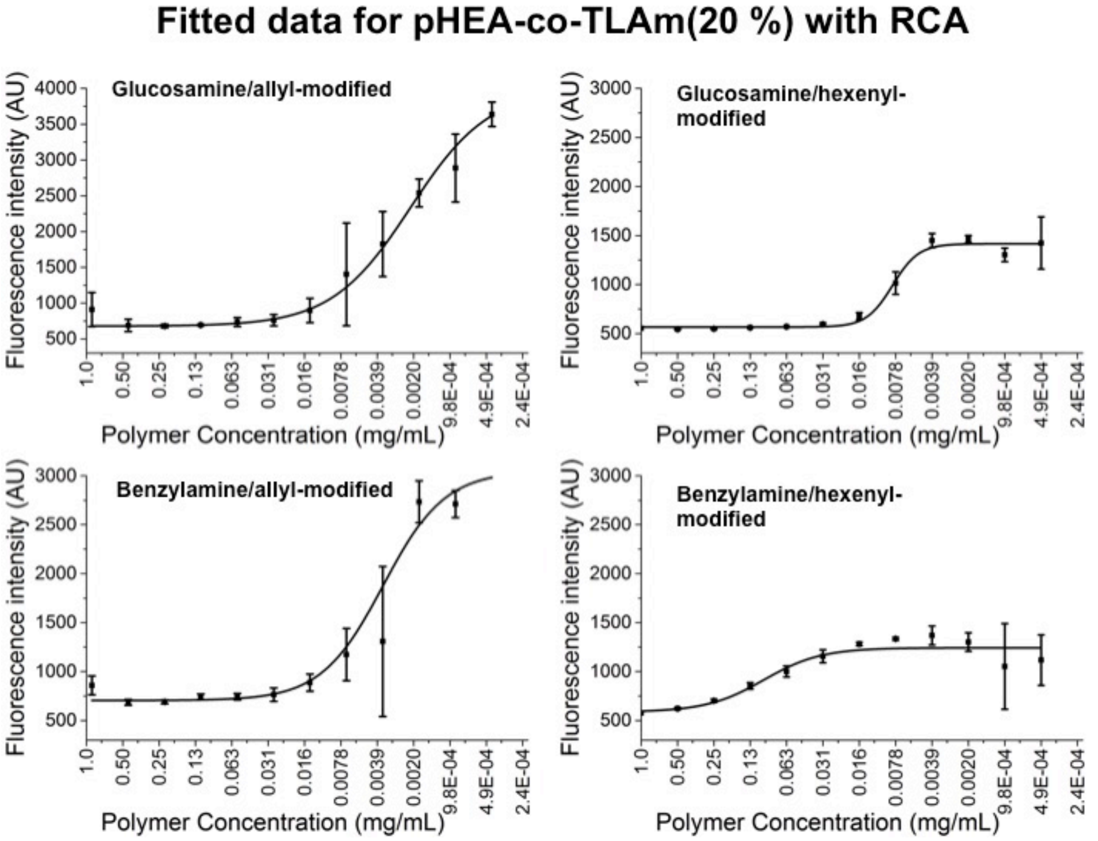

Figure 2-33. Fitted Microplate assay binding curves with RCA_{120} for pHEA-co-TLAm (20 % TLAm) with different galactose linkers and secondary unit modifications. Data was fitted using a heterogeneous sites (2:1) model. Note that a peak is seen in the hexenyl samples at ~0.078 mg/mL polymer, potentially signifying that the fit was not exact.

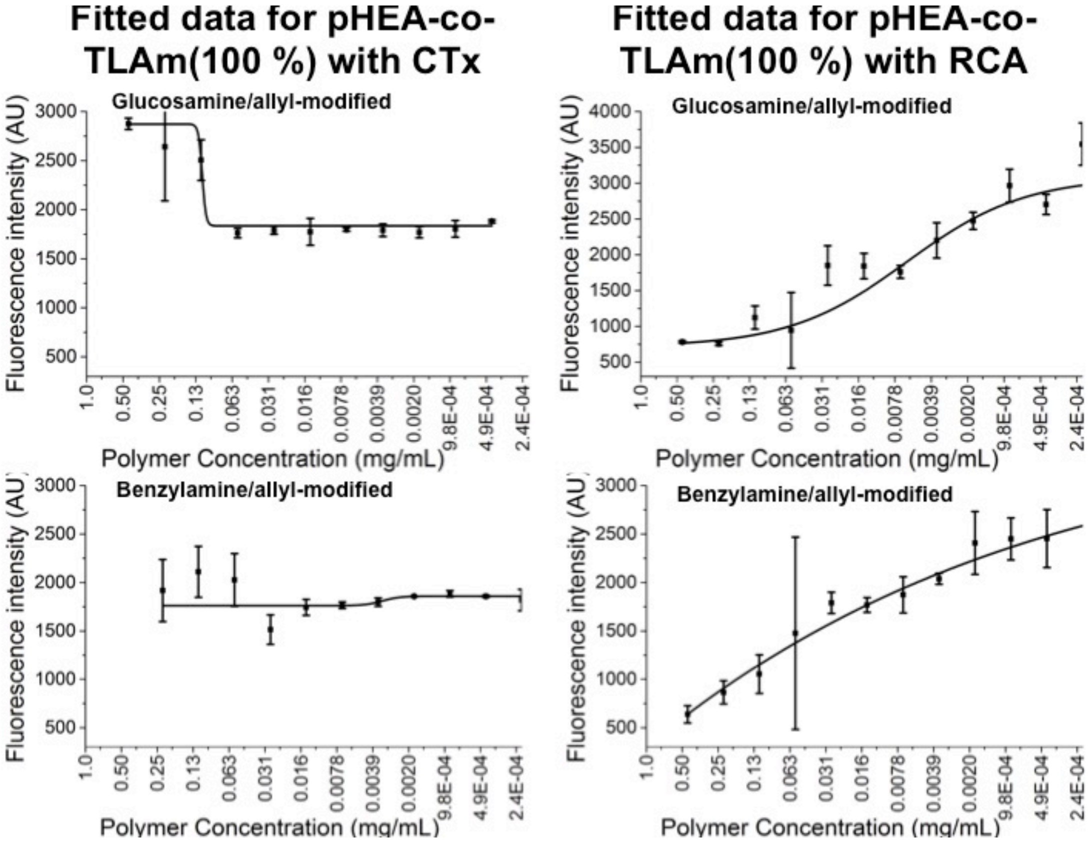

Figure 2-34. Fitted Microplate assay binding curves with CTxB and RCA_{120} for pTLAm homopolymer with allyl-β-D-galactose and different secondary unit modifications. Data was fitted using a heterogeneous sites (2:1) model.

Table 2-3. MIC_{50} values with errors.

Lectin	TLAm density	Galactose linker (alkene)	Amine modification	MIC_{50} values (by polymer concentration) (moles)	< Related error (moles)	MIC_{50} values by galactose concentration (moles)	< Related error (moles)
CTxB	5 %	Allyl-	Gluc	2.02 x 10^{-7}	3.20 x 10^{-7}	5.72 x 10^{-7}	9.08 x 10^{-7}
			Benz	n/a	n/a	n/a	n/a
		Hexenyl-	Gluc	1.64 x 10^{-6}	3.10 x 10^{-7}	5.00 x 10^{-6}	9.45 x 10^{-7}
			Benz	1.19 x 10^{-6}	6.01 x 10^{-7}	3.63 x 10^{-6}	1.83 x 10^{-6}
	10 %	Allyl-	Gluc	3.58 x 10^{-6}	7.21 x 10^{-7}	2.03 x 10^{-5}	4.09 x 10^{-6}
			Benz	n/a	n/a	n/a	n/a
		Hexenyl-	Gluc	n/a	n/a	n/a	n/a
			Benz	n/a	n/a	n/a	n/a
	20 %	Allyl-	Gluc	3.27 x 10^{-6}	1.46 x 10^{-6}	3.12 x 10^{-5}	1.39 x 10^{-5}
			Benz	n/a	n/a	n/a	n/a
		Hexenyl-	Gluc	n/a	n/a	n/a	n/a
			Benz	n/a	n/a	n/a	n/a
RCA_{120}	5 %	Allyl-	Gluc	6.58 x 10^{-7}	2.71 x 10^{-7}	1.87 x 10^{-6}	7.69 x 10^{-7}
			Benz	2.41 x 10^{-7}	4.40 x 10^{-8}	6.83 x 10^{-7}	1.25 x 10^{-7}

	Hexenyl-	Gluc	3.31 x 10^{-6}	3.54 x 10^{-7}	1.01 x 10^{-5}	1.08 x 10^{-6}
		Benz	2.16 x 10^{-6}	4.36 x 10^{-7}	6.59 x 10^{-6}	1.33 x 10^{-6}
10 %	Allyl-	Gluc	2.28 x 10^{-7}	7.65 x 10^{-8}	1.29 x 10^{-6}	4.34 x 10^{-7}
		Benz	5.09 x 10^{-7}	1.39 x 10^{-7}	2.89 x 10^{-6}	7.87 x 10^{-7}
	Hexenyl-	Gluc	1.08 x 10^{-6}	1.40 x 10^{-7}	6.61 x 10^{-6}	8.54 x 10^{-7}
		Benz	7.22 x 10^{-7}	9.77 x 10^{-8}	4.40 x 10^{-6}	5.95 x 10^{-7}
20 %	Allyl-	Gluc	1.27 x 10^{-7}	1.68 x 10^{-8}	1.21 x 10^{-6}	1.60 x 10^{-7}
		Benz	2.31 x 10^{-7}	9.77 x 10^{-8}	2.20 x 10^{-6}	9.30 x 10^{-7}
	Hexenyl-	Gluc	4.85 x 10^{-7}	3.42 x 10^{-8}	4.96 x 10^{-6}	3.50 x 10^{-7}
		Benz	6.09 x 10^{-6}	2.12 x 10^{-6}	6.23 x 10^{-5}	2.17 x 10^{-5}

"n/a" signifies that no MIC_{50} values was obtained as the curve fitting was not sigmoidal.

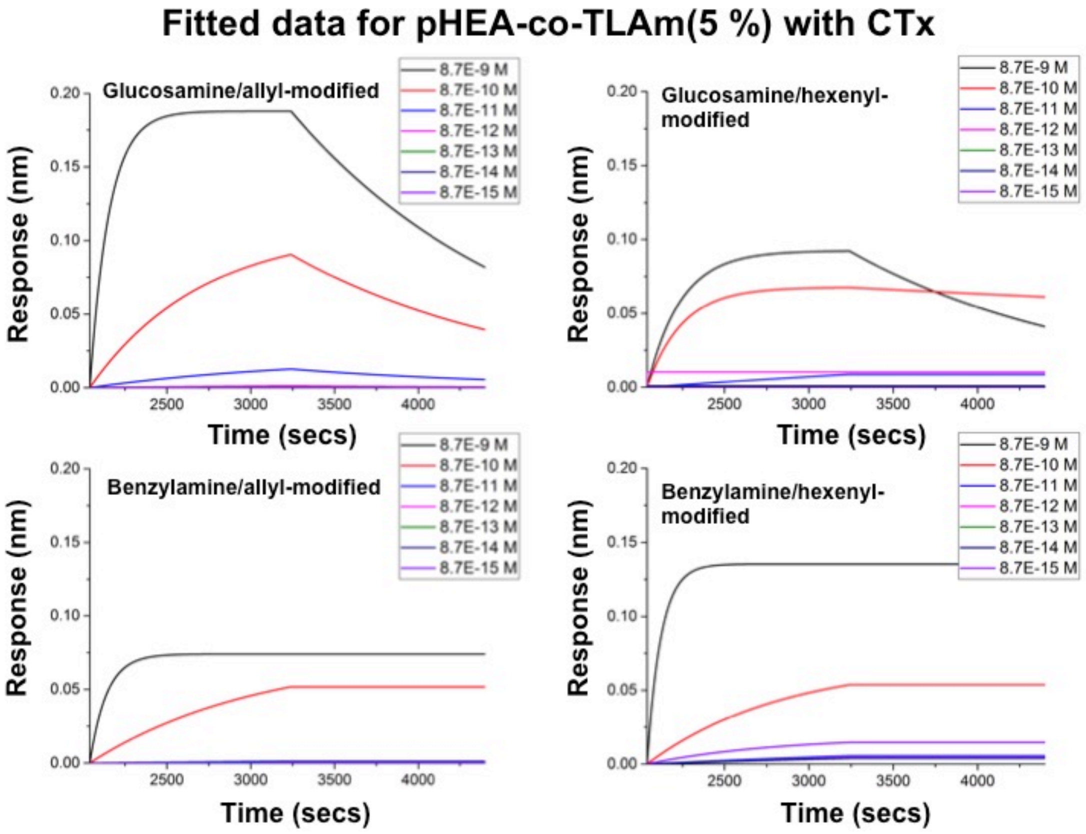

Figure 2-35. BLI fitted curves with CTxB for pHEA-co-TLAm (5 % TLAm) with different galactose linkers and secondary unit modifications.

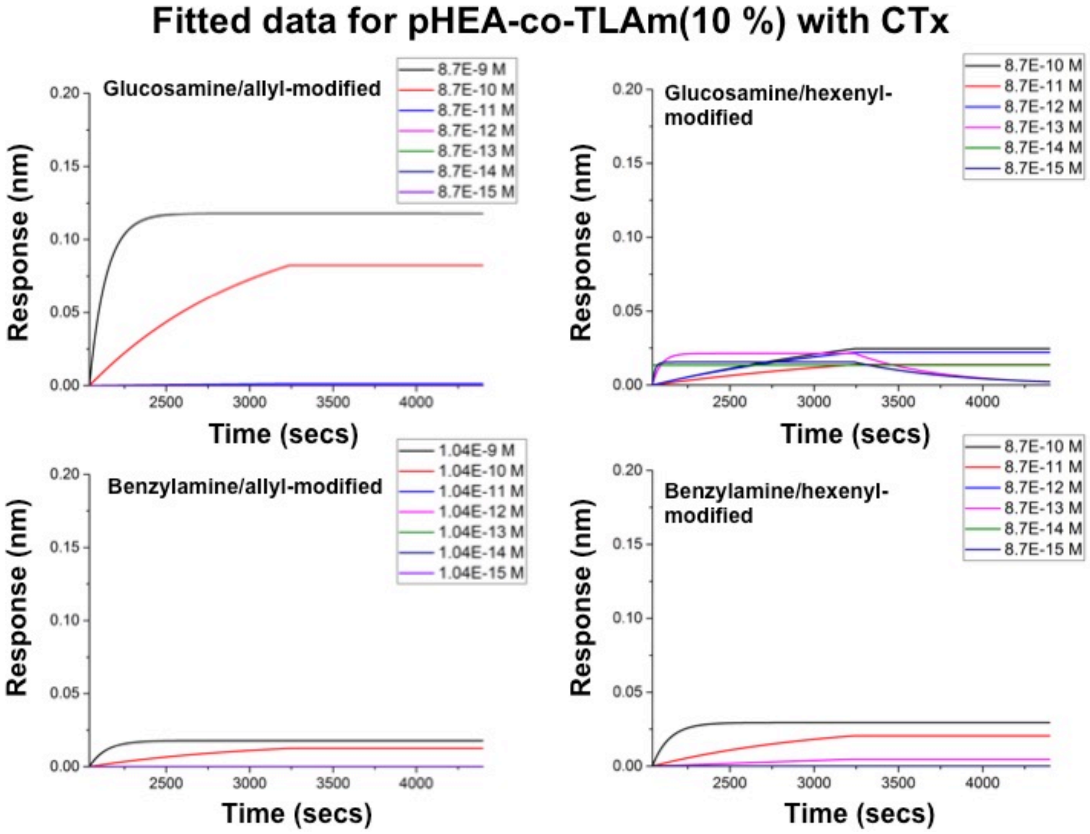

Figure 2-36. BLI fitted curves with CTxB for pHEA-co-TLAm (10 % TLAm) with different galactose linkers and secondary unit modifications.

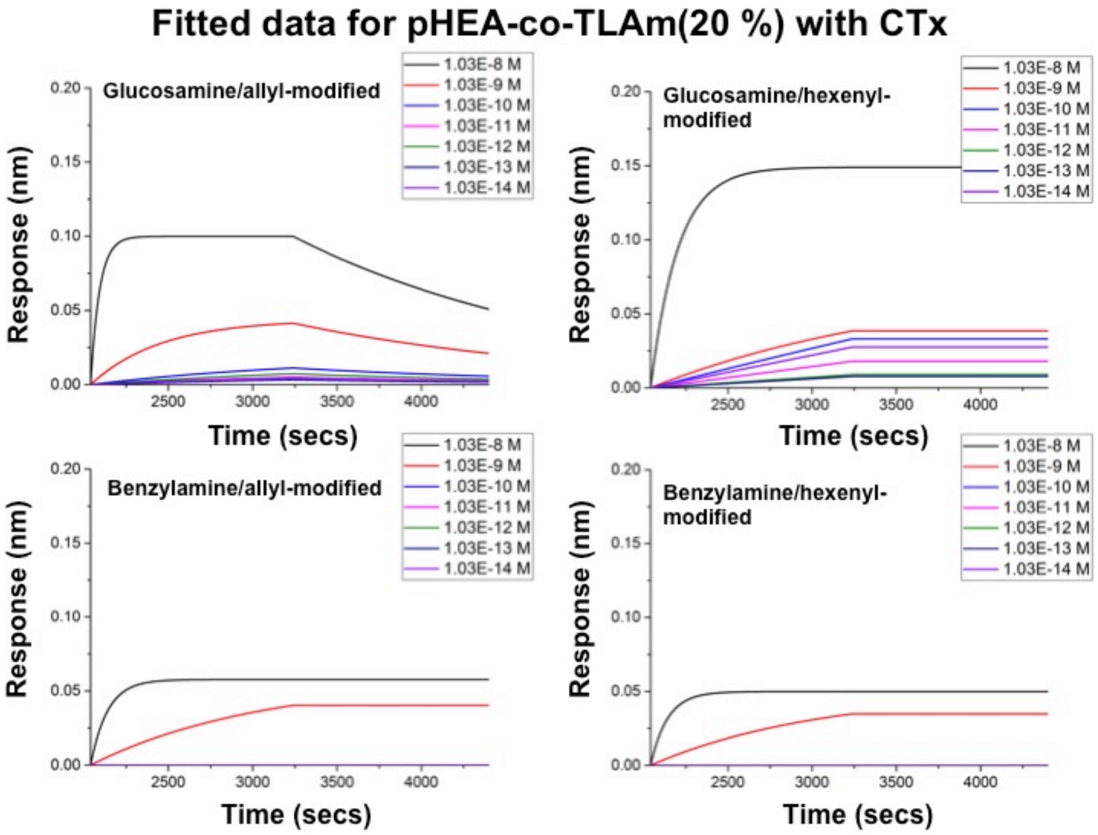

Figure 2-37. BLI fitted curves with CTxB for pHEA-co-TLAm (20 % TLAm) with different galactose linkers and secondary unit modifications.

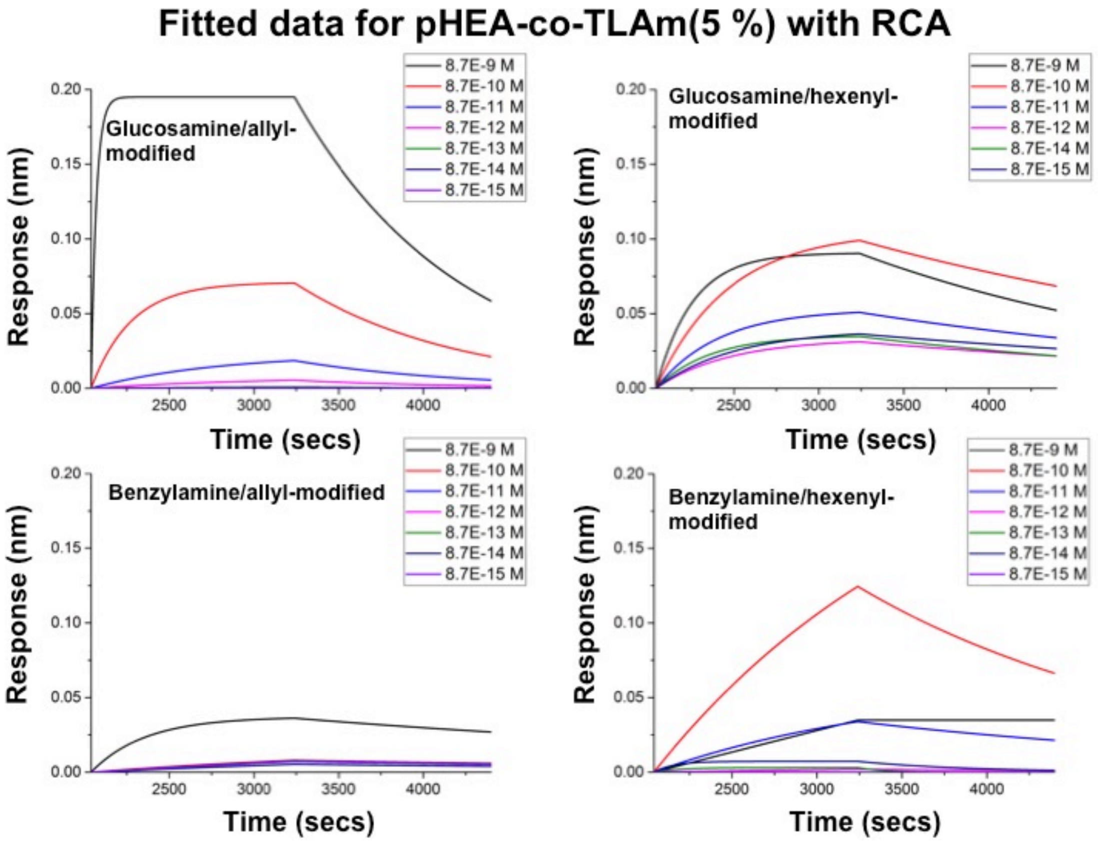

Figure 2-38. BLI fitted curves with RCA_{120} for pHEA-co-TLAm (5 % TLAm) with different galactose linkers and secondary unit modifications.

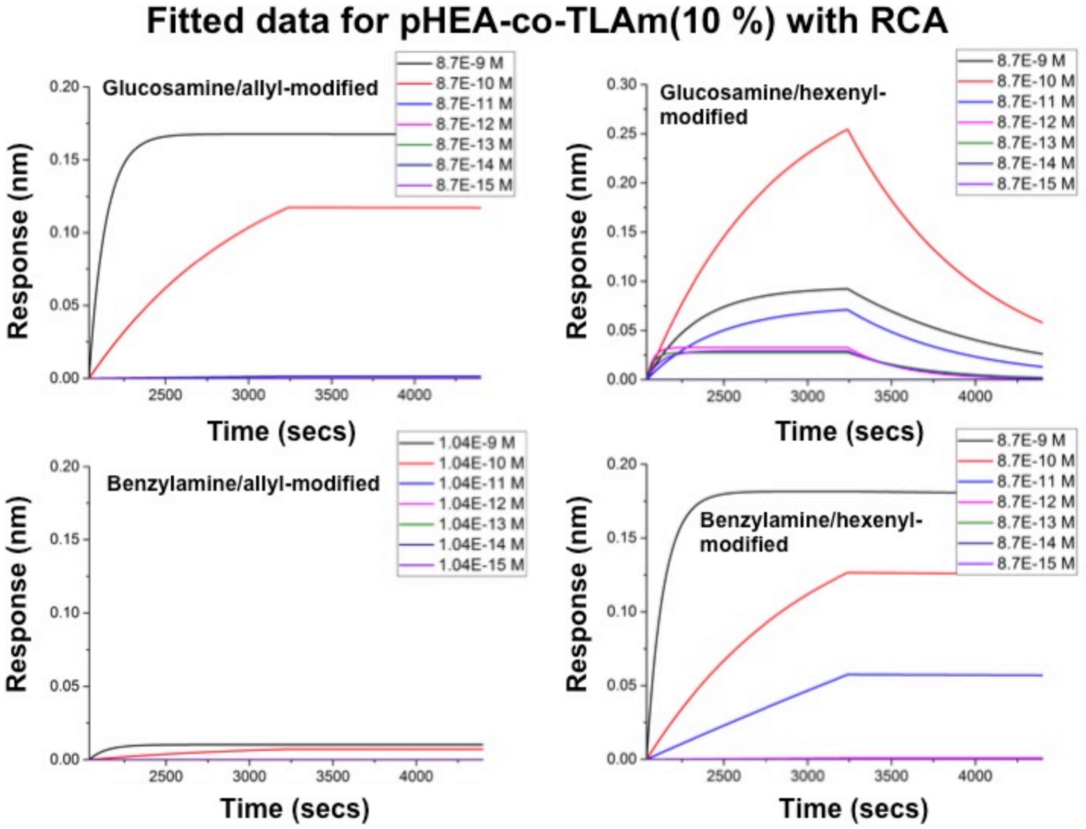

Figure 2-39. BLI fitted curves with RCA$_{120}$ for pHEA-co-TLAm (10 % TLAm) with different galactose linkers and secondary unit modifications.

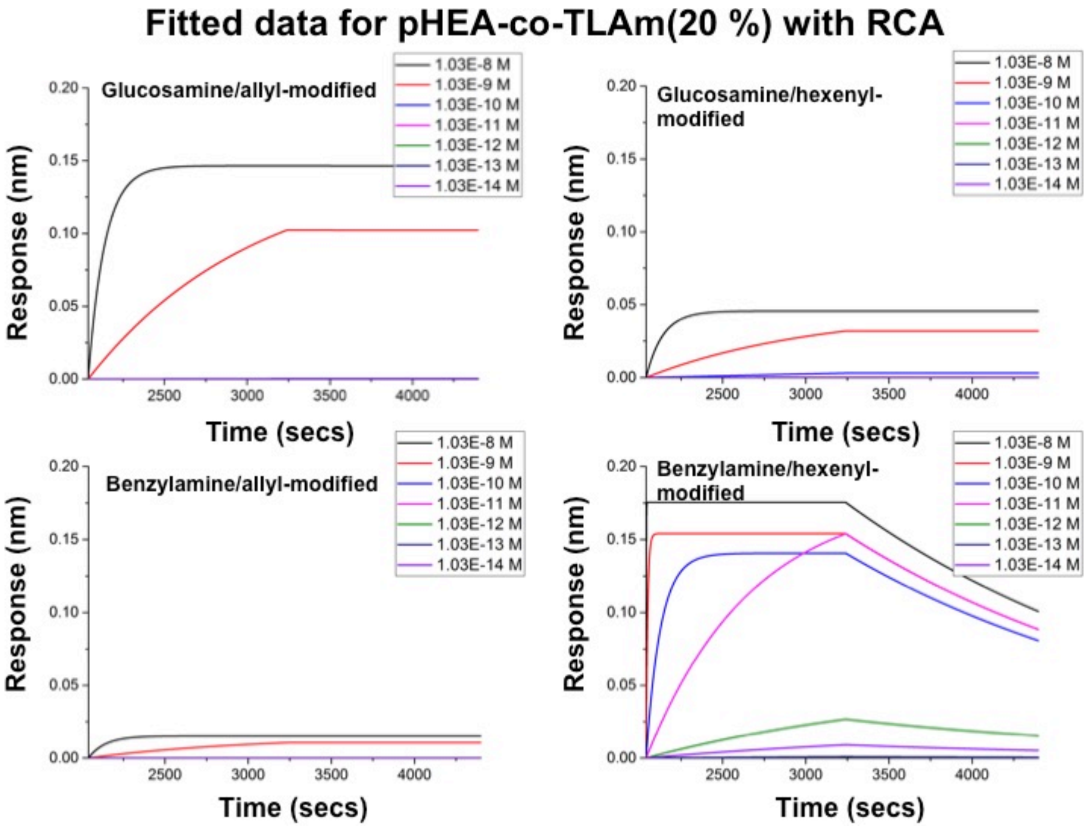

Figure 2-40. BLI fitted curves with RCA$_{120}$ for pHEA-co-TLAm (20 % TLAm) with different galactose linkers and secondary unit modifications.

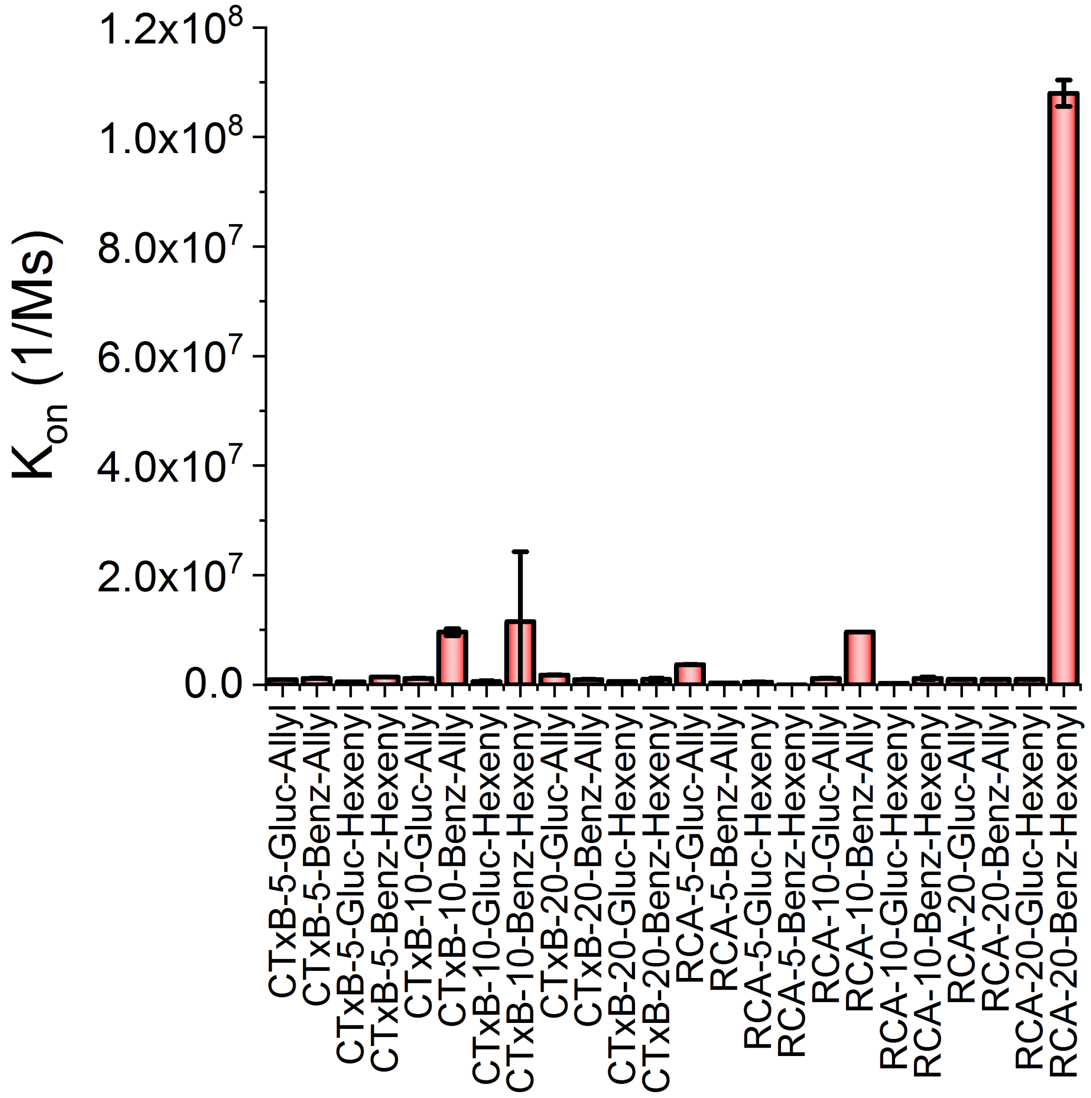

Figure 2-41. k_{on} values by polymer concentration. Axes labels for polymers are in the format TOXIN-TLAmDensity-SecondaryModification-AlkeneGalactoseLinker.

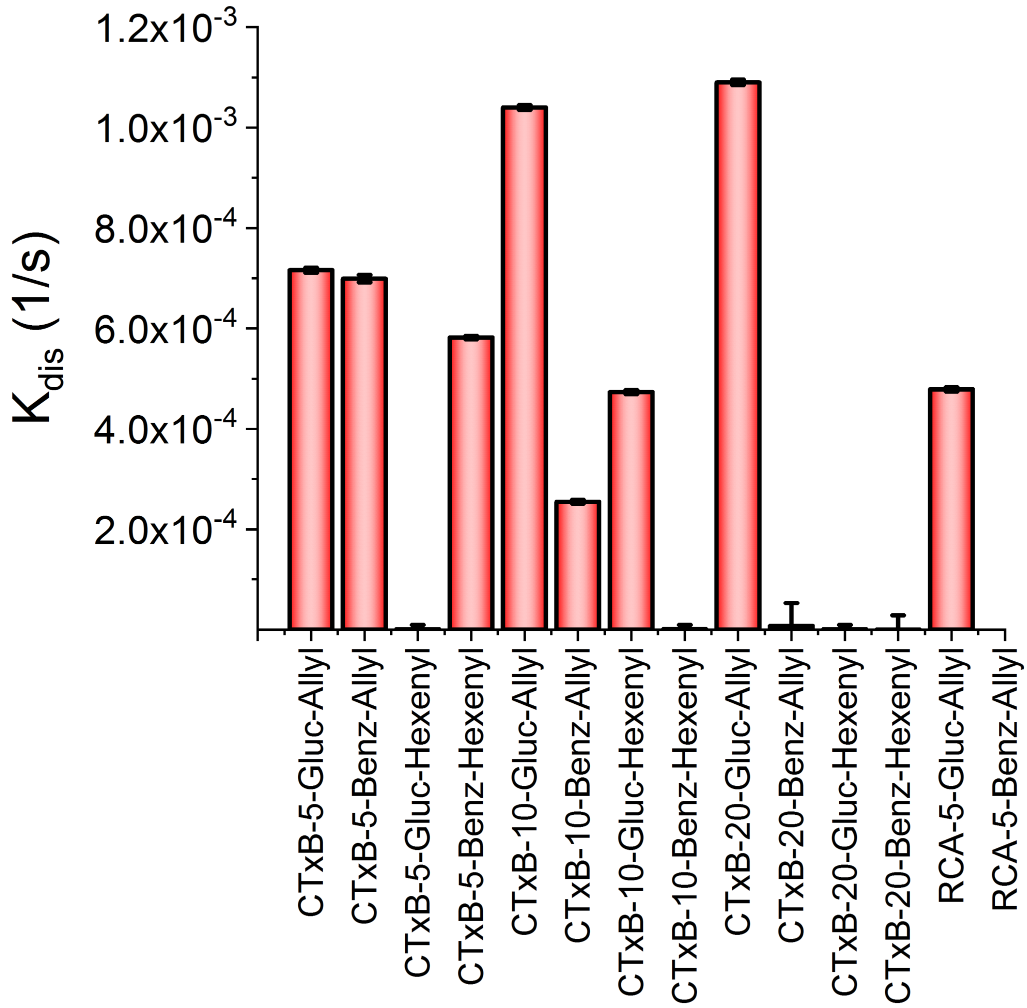

Figure 2-42. k_{dis} values by polymer concentration. Axes labels for polymers are in the format TOXIN-TLAmDensity-SecondaryModification-AlkeneGalactoseLinker. Due to the sensitivity limitations of the instrument, 1 x 10^{-7} is the minimum value (hence the abundance of this value).

2.8. References

(1) Paszek, M. J.; Dufort, C. C.; Rossier, O.; Bainer, R.; Mouw, J. K.; Godula, K.; Hudak, J. E.; Lakins, J. N.; Wijekoon, A. C.; Cassereau, L.; Rubashkin, M. G.; Magbanua, M. J.; Thorn, K. S.; Davidson, M. W.; Rugo, H. S.; Park, J. W.; Hammer, D. A.; Giannone, G.; Bertozzi, C. R.; Weaver, V. M. *Nature* **2014**, *511* (7509), 319.

(2) Woods, E. C.; Yee, N. A.; Shen, J.; Bertozzi, C. R. *Angew. Chem., Int. Ed.* **2015**, *54* (52), 15782.

(3) Rudd, P. M.; Elliott, T.; Cresswell, P.; Wilson, I. A.; Dwek, R. A. *Science (80-.).* **2001**, *291* (5512), 2370.

(4) Lee, Y. C.; Lee, R. T. *Acc. Chem. Res.* **1995**, *28* (8), 321.

(5) Ambrosi, M.; Cameron, N. R.; Davis, B. *Org. Biomol. Chem.* **2005**, *3* (9), 1593.

(6) Rodríguez, E.; Schetters, S. T. T.; Van Kooyk, Y. *Nat. Rev. Immunol.* **2018**, *18* (3), 204.

(7) Reuter, J. D.; Myc, A.; Hayes, M. M.; Gan, Z.; Roy, R.; Qin, D.; Yin, R.; Piehler, L. T.; Esfand, R.; Tomalia, D. A.; Baker, J. R. *Bioconjug. Chem.* **1999**, *10*, 271.

(8) Ofek, I.; Hasty, D. L.; Sharon, N. *FEMS Immunol. Med. Microbiol.* **2003**, *38* (3), 181.

(9) Kobayashi, A.; Kobayashi, K.; Akaike, T. *J. Biomater. Sci. Polym. Ed.* **1992**, *3* (6), 499.

(10) Krachler, A. M.; Orth, K. *Virulence* **2013**, *4* (4), 284.

(11) Raynor, J. E.; Petrie, T. a; Fears, K. P.; Latour, R. a; Garcia, a J.; Collard, D. M. *Biomacromolecules* **2009**, *10*, 748.

(12) Wittmann, V.; Pieters, R. J. *Chem. Soc. Rev.* **2013**, *42* (10), 4492.

(13) Cecioni, S.; Imberty, A.; Vidal, S. *Chem. Rev.* **2015**, *115* (1), 525.

(14) Zheng, R. B.; Jégouzo, S. A. F.; Joe, M.; Bai, Y.; Tran, H. A.; Shen, K.; Saupe,

J.; Xia, L.; Ahmed, M. F.; Liu, Y. H.; Patil, P. S.; Tripathi, A.; Hung, S. C.; Taylor, M. E.; Lowary, T. L.; Drickamer, K. *ACS Chem. Biol.* **2017**, *12* (12), 2990.

(15) Becer, C. R.; Gibson, M. I.; Geng, J.; Ilyas, R.; Wallis, R.; Mitchell, D. A.; Haddleton, D. M. *J. Am. Chem. Soc.* **2010**, *132* (43), 15130.

(16) Das, S.; Angsantikul, P.; Le, C.; Bao, D.; Miyamoto, Y.; Gao, W.; Zhang, L.; Eckmann, L. *PLoS Negl. Trop. Dis.* **2018**, *12* (2), 1.

(17) Jiménez Blanco, J. L.; Ortiz Mellet, C.; García Fernández, J. M. *Chem. Soc. Rev.* **2013**, *42* (11), 4518.

(18) Lundquist, J. J.; Toone, E. J. *Chem. Rev.* **2002**, *102* (2), 555.

(19) Noble, G. T.; Flitsch, S. L.; Liem, K. P.; Webb, S. J. *Org. Biomol. Chem.* **2009**, *7* (24), 5245.

(20) Dimick, S. M.; Powell, S. C.; McMahon, S. A.; Moothoo, D. N.; Naismith, J. H.; Toone, E. J. *J. Am. Chem. Soc.* **1999**, *121* (44), 10286.

(21) Akaike, T.; Goto, M. *J. Biomater. Sci. Polym. Ed.* **1995**, *6* (4), 325.

(22) Ambrosi, M.; Cameron, N. R.; Davis, B. G.; Stolnik, S. *Org. Biomol. Chem.* **2005**, *3* (8), 1476.

(23) Richards, S. J.; Jones, M. W.; Hunaban, M.; Haddleton, D. M.; Gibson, M. I. *Angew. Chem., Int. Ed.* **2012**, *51* (31), 7812.

(24) Spain, S. G.; Cameron, N. R. *Polym. Chem.* **2011**, *2* (7), 1552.

(25) Parry, A. L.; Clemson, N. A.; Ellis, J.; Bernhard, S. S. R.; Davis, B. G.; Cameron, N. R. *J. Am. Chem. Soc.* **2013**, *135* (25), 9362.

(26) Ali, M.; Nelson, A. R.; Lopez, A. L.; Sack, D. A. *PLoS Negl. Trop. Dis.* **2015**, *9* (6).

(27) Silva, A. J.; Benitez, J. A. *PLoS Negl. Trop. Dis.* **2016**, *10* (2), 1.

(28) Baldauf, K. J.; Royal, J. M.; Hamorsky, K. T.; Matoba, N. *Toxins (Basel).* **2015**, *7* (3), 974.

(29) Kumar, V.; Turnbull, W. B. *Beilstein J. Org. Chem.* **2018**, *14*, 484.

(30) Merritt, E. A.; Sarfaty, S.; Akker, F. Van Den; L'Hoir, C.; Martial, J. A.; Hol, W. G. J. *Protein Sci.* **1994**, *3* (2), 166.

(31) Sánchez, J.; Holmgren, J. *Cell. Mol. Life Sci.* **2008**, *65* (9), 1347.

(32) Fishman, P. H. *J. Cell Sci.* **2003**, *116* (3), 431.

(33) De Haan, L.; Hirst, T. R. *Mol. Membr. Biol.* **2004**, *21* (2), 77.

(34) Lencer, W. I.; Hirst, T. R.; Holmes, R. K. *Biochim. Biophys. Acta* **1999**, *1450* (3), 177.

(35) Torgersen, M. L.; Skretting, G.; van Deurs, B.; Sandvig, K. *J. Cell Sci.* **2001**, *114* (Pt 20), 3737.

(36) Strombeck, D. R.; Harrold, D. *Infect. Immun.* **1974**, *10* (6), 1266.

(37) Chinnapen, D. J. F.; Chinnapen, H.; Saslowsky, D. *FEMS Microbiol. Lett.* **2007**, *266* (2), 129.

(38) Galen, J. E.; Ketley, J. M.; Fasano, A.; Richardson, S. H.; Wasserman, S. S.; Kaperl, J. B. *Infect. Immun.* **1992**, *60* (2), 406.

(39) Kuziemko, G. M.; Stroh, M.; Stevens, R. C. *Biochemistry* **1996**, *35* (20), 6375.

(40) Bernardi, A.; Arosio, D.; Sonnino, S. *Neurochem. Res.* **2002**, *27* (7–8), 539.

(41) Bernardi, A.; Carrettoni, L.; Ciponte, A. G.; Monti, D.; Sonnino, S. *Bioorg. Med. Chem. Lett.* **2000**, *10*, 2197.

(42) Bernardi, A.; Checchia, A.; Brocca, P.; Sonnino, S.; Zuccotto, F. *J. Am. Chem. Soc.* **1999**, *121* (10), 2032.

(43) Lanne, B.; Birgitta, Z. *J. Biochem.* **1994**, *116*, 1269.

(44) Wang, Y.; Huang, X.; Zhang, L.-H.; Ye, X.-S. *Org. Lett.* **2004**, *6* (24), 4415.

(45) Mattarella, M.; Garcia-Hartjes, J.; Wennekes, T.; Zuilhof, H.; Siegel, J. S. *Org. Biomol. Chem.* **2013**, *11*, 4333.

(46) Tran, H. A.; Kitov, P. I.; Paszkiewicz, E.; Sadowska, J. M.; Bundle, D. R. *Org.*

Biomol. Chem. **2011**, *9* (10), 3658.

(47) Mahon, C. S.; Fascione, M. A.; Sakonsinsiri, C.; McAllister, T. E.; Bruce Turnbull, W.; Fulton, D. A. *Org. Biomol. Chem.* **2015**, *13* (9), 2756.

(48) Jones, M. W.; Otten, L.; Richards, S. J.; Lowery, R.; Phillips, D. J.; Haddleton, D. M.; Gibson, M. I. *Chem. Sci.* **2014**, *5* (4), 1611.

(49) Reinicke, S.; Espeel, P.; Stamenović, M. M.; Du Prez, F. E. *Polym. Chem.* **2014**, *5* (18), 5461.

(50) Stamenović, M. M.; Espeel, P.; Baba, E.; Yamamoto, T.; Tezuka, Y.; Du Prez, F. E. *Polym. Chem.* **2013**, *4* (1), 184.

(51) Espeel, P.; Goethals, F.; Stamenović, M. M.; Petton, L.; Du Prez, F. E. *Polym. Chem.* **2012**, *3* (4), 1007.

(52) Reinicke, S.; Espeel, P.; Stamenović, M. M.; Du Prez, F. E. *ACS Macro Lett.* **2013**, *2* (6), 539.

(53) Espeel, P.; Du Prez, F. E. *Eur. Polym. J.* **2015**, *62*, 247.

(54) Zhao, Y.; Yang, B.; Zhang, Y.; Wang, S.; Fu, C.; Wei, Y.; Tao, L. *Polym. Chem.* **2014**, *5* (23), 6656.

(55) Espeel, P.; Goethals, F.; Du Prez, F. E. *J. Am. Chem. Soc.* **2011**, *133* (6), 1678.

(56) Belbekhouche, S.; Reinicke, S.; Espeel, P.; Du Prez, F. E.; Eloy, P.; Dupont-Gillain, C.; Jonas, A. M.; Demoustier-Champagne, S.; Glinel, K. *ACS Appl. Mater. Interfaces* **2014**, *6* (24), 22457.

(57) Frank, D.; Espeel, P.; Claessens, S.; Mes, E.; Du Prez, F. E. *Tetrahedron* **2016**, *72* (42), 6616.

(58) Rudolph, T.; Espeel, P.; Du Prez, F. E.; Schacher, F. H. *Polym. Chem.* **2015**, *6* (23), 4240.

(59) Meng, X.; Fang, Y.; Wan, L.; Huang, X.; Xu, Z. *Langmuir* **2012**, *28*, 13616.

(60) Grosdidier, A.; Zoete, V.; Michielin, O. *Nucleic Acids Res.* **2011**, *39* (SUPPL. 2), 270.

(61) Hudson, K. L.; Bartlett, G. J.; Diehl, R. C.; Agirre, J.; Gallagher, T.; Kiessling, L. L.; Woolfson, D. N. *J. Am. Chem. Soc.* **2015**, *137* (48), 15152.

(62) Kadiata, M. M.; Malaisse, W. J. *Life Sci.* **1999**, *64* (9), 751.

(63) Sardzik, R.; Sharma, R.; Kaloo, S.; Voglmeir, J.; Crocker, P. R.; Flitsch, S. L. *Chem. Commun.* **2011**, *47* (19), 5425.

(64) World Health Organization Global Health Observatory, Cholera. http://apps.who.int/gho/data/node.main.174 (accessed June 12, 2018).

3. Multivalent presentation of antifreeze macromolecules, polymers and proteins

3.1. Chapter summary

Understanding the activity and more of action of both antifreeze proteins and synthetic mimics is required to translate them to applications. In particular the impact of architecture is of interest in its capacity for multiple binding to the same ice face, or bridging to other ice crystal faces.

Herein a multivalent AFP type III was conjugated to an AuNP scaffold with various types of linkers. The AFP-SNAP recombinant attached to the AuNP scaffold showed enhanced activity relative to the same number of moles of free AFP, which confirms the assertion that a larger linker length is required to make the entirety of AFP's ice binding face available.

PVA of different lengths was also conjugated to an AuNP scaffold, which was expected to have reduced IRI activity relative to linear PVA of the same molecular weight. This was not the case with larger PVA, however, and it is proposed that this is due to a relatively low grafting density resulting in an increased freedom of movement for the PVA to still utilise its length to interact with the hydroxyls of the ice face.

3.2. Declarations

The work presented herein was carried out by the author except in the case of collaborative research, as outlined below.

- Recombinant AFPs were prepared by Dr Muhammad Hasan at the University of Warwick. Dr Hasan also ran all SDS-PAGE gels used in this chapter.
- All XPS and data analysis was performed by Dr Marc Walker at the University of Warwick.
- All PVA polymers were prepared and characterized by Christopher Stubbs. "Splat" assays and analysis was also performed by Christopher Stubbs. Christopher also performed the SEC analysis of SNAP-AFP attachment to BG-pHEA.
- All sucrose sandwich assays into ice shaping was performed by Alice Fayter.
- All "splat" assays and analysis of AFP-containing samples was performed by Dr Caroline Biggs.
- All thermal hysteresis assays were performed by Dr Peter Davies at Queen's University, Kingston, Ontario, Canada.

3.3. Introduction

Cryopreservation of human tissues and cells remains a major challenge in all health systems and their related industries. Cold storage of material for future use, or for transportation to where it is needed, requires additives to ensure the material is not damaged in the freezing or thawing process. These additives tend to be in the form of osmolytic cryopreservatives that dehydrate cells, and current formulations often include glycerol or DMSO, which can cause damage themselves to the material stored.[1–3] Therefore it stands to reason that cryopreservatives used by cold-surviving organisms in nature can form the basis for developing novel, more suitable, procedures.

Antifreeze proteins are expressed by a variety of cold-dwelling organisms and have a variety of different methods of binding to ice to inhibit its growth: from bacterial ability to bind to ice and form a biofilm, to Arctic fish inhibiting the growth of lethal ice shards in its blood.[4–10] Fish express antifreeze glycoproteins and type I, II and III antifreeze proteins. The AFPs are classified by their general structure and the planes of ice that they bind to. A commonly-used AFP class, type III AFP, are small (~6.5 kDa), globular proteins with a single α-helix turn and several short β-strands. These type III AFPs' mode of action is through a binding site that binds both the secondary and pyramidal planes of ice (shown in Figure 3-1), though how this planar specificity is achieved is unknown. The particular antifreeze activity of interest is ice recrystallization inhibition (IRI) as it is this activity that inhibits the potentially-lethal Ostwald ripening process in nature whereby smaller ice crystals melt whilst the larger crystal grow inside the organism. The antifreeze activity of such macromolecules can also be detected as thermal hysteresis (TH) activity; a depression in the freezing point of a solution upon the addition of antifreeze molecules.

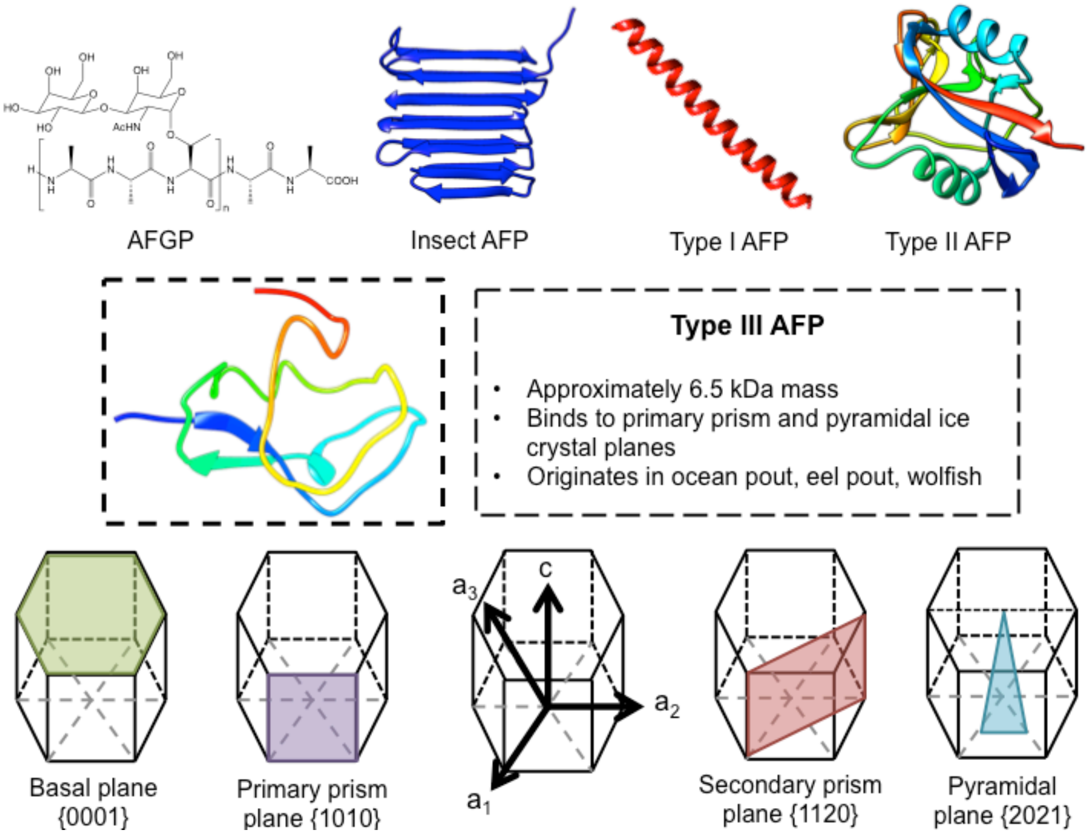

Figure 3-1. The antifreeze protein family, with a focus on the properties of type III AFP. The antifreeze protein family, with a focus on the properties of type III AFP. The following PDB files were used for structures: 1MSI for AFGP; 4DTS for insect AFP; 1WFA for type I; 2PY2 for type II and 1OP2 for type III AFP.

AFP function may be enhanced through its fusion to a larger scaffold; for example, Baardsnes *et al.* in 2003 developed a dimer with two AFP binding sites at opposite ends of the molecule.[11–20] In this study they showed a gain in antifreeze activity (0.8 instead of 0.4 °C thermal hysteresis activity for the dimer rather than the monomer with 1 binding site knocked out) attributed to the simultaneous binding of two ice sites (not just multivalency), and that was only present when the AFP's entire binding site was sterically available. This study was supported by the work of both Can *et al.*[15] and Phippen *et al*[16]., who developed a trimer and an oligomer respectively with several-fold increases in TH activity. It was proposed that this activity results from the capacity to span the interstitial space and bind several ice crystals at once. Stevens *et al.*[12] synthesized a dendrimer-linked AFP that also showed small enhancements to TH activity due to AFP cross-linking multiple ice faces.

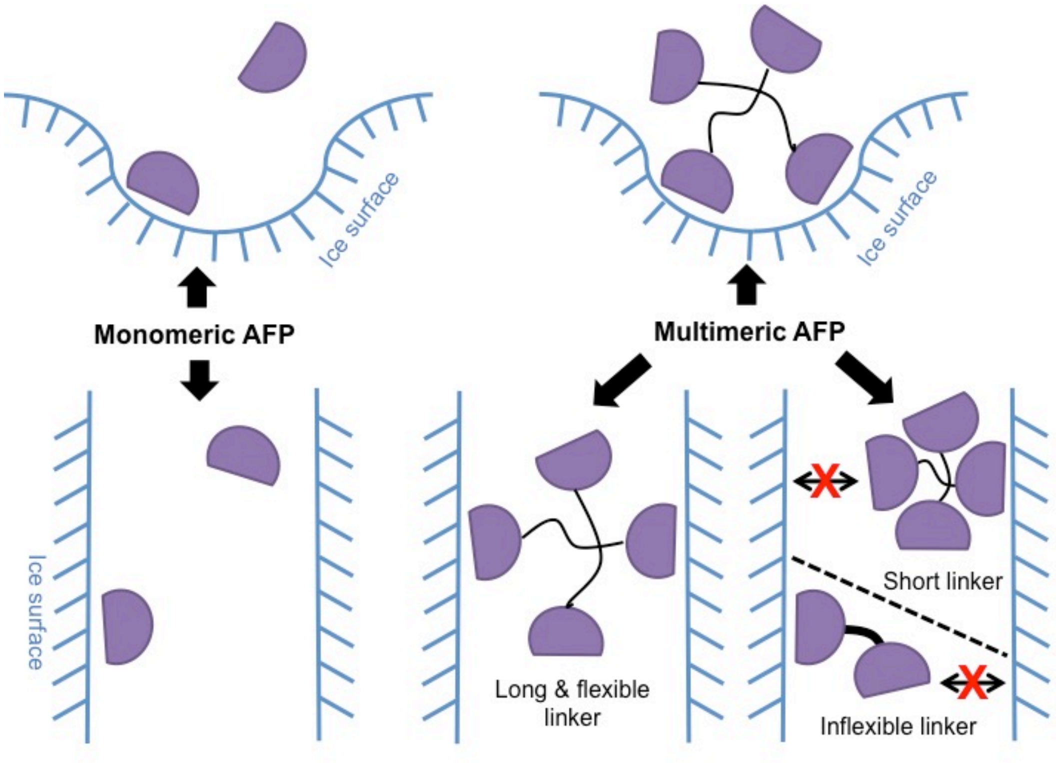

Figure 3-2. Hypotheses for beneficial interactions of antifreeze protein multimer constructs with the ice surface.

Many of these studies suggested a binding model wherein the larger size of the scaffold onto which the AFP is bound, and its orientation, is key due to the necessity of having the entire AFP binding site available to bind several ice sites simultaneously. Moreover, Stevens *et al.* proposed that the size of the AFP on a small scaffold inhibits the capacity for more than a few AFPs bound on the same scaffold to bind to the same surface, but that upon increasing the size of this scaffold more AFPs on the same plane are able to interact with ice.

Other enhancements to the activity of these AFP molecules can be achieved through the synthesis of macromolecular mimics: those that retain their IRI and TH activity but without the need to use recombinant protein, which can have lower yields and be more expensive to manufacture. Polymers are a good choice for these mimics as facile synthesis can afford the large molecule sizes required for mimicking AFP activity. A variety of such materials have been proposed, from metallohelices to self-assembled amphipathic fibres.[1,6,21–24] One particular material of interest is poly(vinyl alcohol)

(PVA), which has molecular weight-dependent antifreeze activity but actually little similarity to the natural AFPs.[25–32]

PVA has both IRI activity, the capacity to shape ice crystals and weak TH activity: several studies have emerged showing its potential for use in cryopreservation due to its biocompatibility.[3,33] Congdon *et al.*[32] found that PVA chain of over ~15 units displayed IRI activity, maintained at concentrations as low as 0.05 mg.mL^{-1}, but that the removal of 20 molar % hydroxyls from the chains resulted in a marked decrease in activity. This suggests that the conformation of the pure PVA chain is essential to its antifreeze activity, or hydrogen bonding to the ice surface. Congdon *et al.* also saw 3-armed PVA stars had equal activity to 2-arm stars, which suggests that branching is unfavourable.[34]

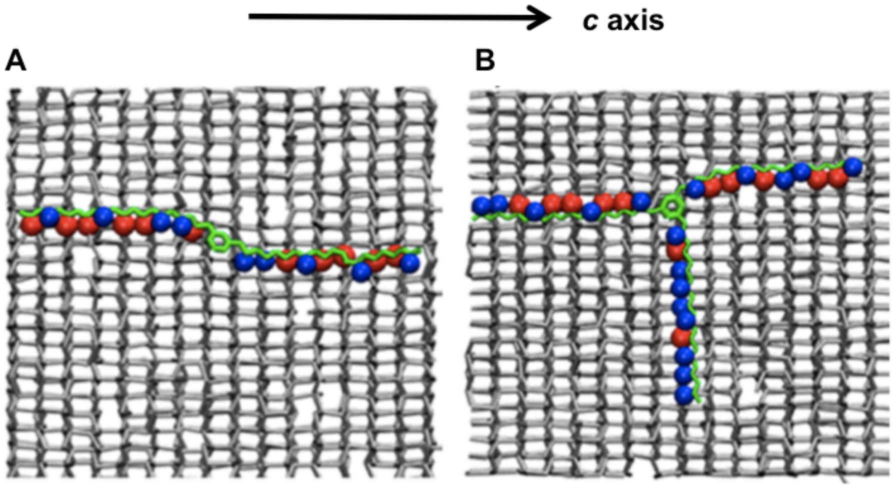

Figure 3-3. The binding of PVA structures to the ice crystal prismatic face from modelling data. Figure from Naullage *et al.*[25] The spacing of the hydroxyl residues allows pattern matching along the c axis. with a 2-arm PVA (a), but this is not possible with the 3-arm structure (b) due to different hydroxyl spacing in this dimension. Red circles indicate binding to the ice hydroxyls, whilst blue circles are residues not bound.

Computational work by Naullage *et al.*[25] elucidated that PVA binding to the prismatic plane of ice through a zipper-like mechanism wherein each residue attaches to the ice surface following its neighbour. It was indicated that this binding is not enhanced through branching of the PVA, as the 3rd arm could not engage in favourable hydrogen bonding due to a lattice mismatch (see Figure 3-3).

3.4. Chapter aims

Understanding the relationship between the valency and the antifreeze activity of both antifreeze proteins and synthetic mimics is key in enhancing this activity. There are currently differing accounts in the literature as to whether multivalent analytes have more activity than the equivalent molar concentration of the monovalent analyte. To this end, the aims of this chapter are as follows:

- To establish synthetic routes to spherical AFP hybrid materials through the use of gold nanoparticle scaffolds.
- To obtain structure-function relationships in branched materials through the use of gold nanoparticle scaffolds.

3.5. Results and Discussion

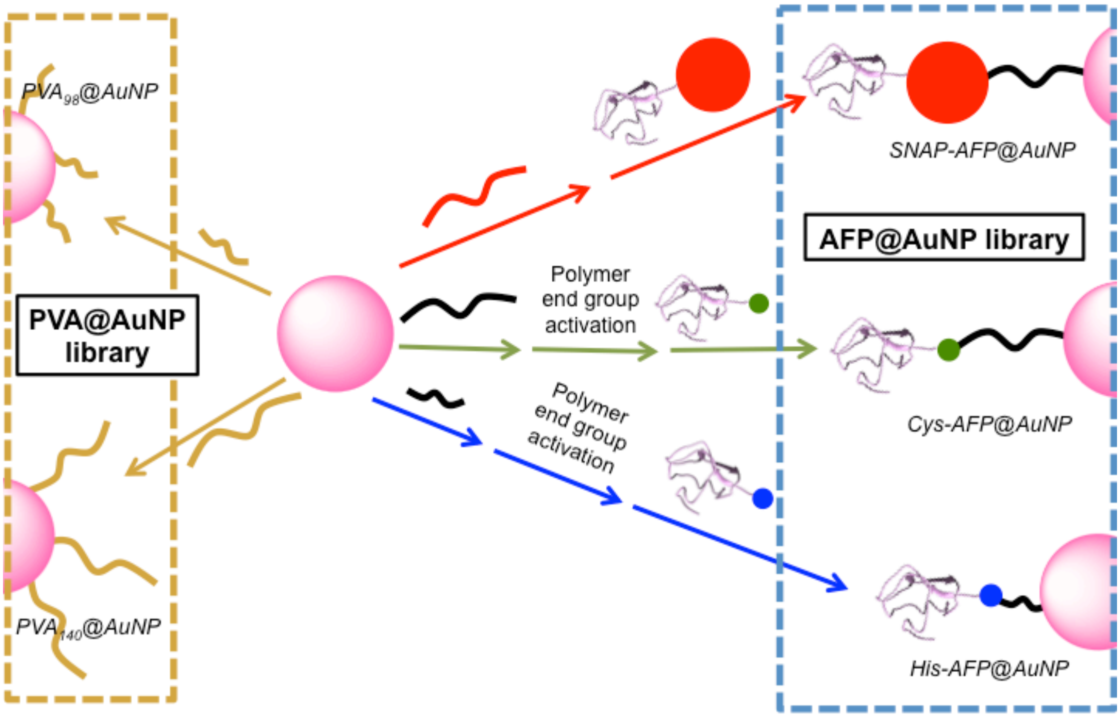

Scheme 3-1. Synthesis of antifreeze/AuNP conjugates.

3.5.1. Synthesis of small gold nanoparticle "templates"

In order to obtain multivalent AFPs, small spherical AuNPs (<5 nm diameter) were synthesized. The small size of these AuNPs allows the development of dendrimer-like structures using an easily conjugated core. Two different methods were used for this synthesis: 1) the citrate reduction method, wherein gold chloride and citrate are mixed, with larger concentrations of citrate employed to "cap" larger AuNP growth; 2) the citrate reduction method, adding ice-cold sodium borohydride as a reducing agent in order to slow the formation of larger nanoparticles by conjugating gold atoms.[35–38]

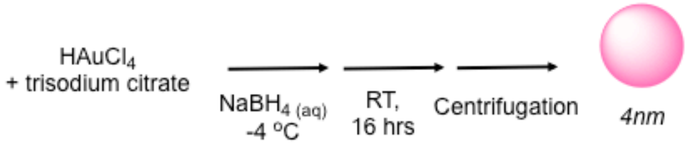

Scheme 3-2. Synthesis of PVA and attachment to AuNPs.

The size of these AuNPs was assessed initially by DLS. DLS is used to determine the distribution of particle sizes in a solution. A monochromatic light source is shone into the sample, and the pattern of diffracted (or scattered) light resulting from the sample is measured. An autocorrelator compares the pattern of scattered light at short time intervals, and measures the decay of the correlation. Smaller particles move more rapidly in solution, resulting in faster decay, and therefore the decay of the autocorrelation function can be determined as a function of particle size in solution. Initial assessment demonstrated that $NaBH_4$ was required for the formation of diameters <5 nm: the standard citrate reduction method resulted in ~15 nm citrate@AuNP diameters, see Figure 3-14 in appendix.

To narrow the distribution of AuNP sizes, the solution was centrifuged and the supernatant taken to remove a low number of larger nanoparticles.[39–41] These solutions are also not stable over longer than several months due to the tendency of these relatively-unstable citrate@AuNPs to aggregate.

3.5.2. Synthesis of thiol-terminated poly(vinyl acetate) and attachment to gold nanoparticles

Various lengths of thiol-terminated PVA were synthesized by RAFT/MADIX polymerization procedure (which varies from RAFT only by the use of a xanthate mediator rather than a dithioester or thiocarbamate), installing a thiol at the ω-terminus via a xanthate chain transfer agent (*S*-benzyl *O*-ethyl carbodithioate). Various ratios of chain transfer agent were employed to produce a panel of poly(vinyl acetate)s (PVAcs), which were then deprotected with hydrazine to produce a library of thiol-terminal PVAs. Successful deprotection was demonstrated by the loss of acetate methyls in ^{1}H-NMR. SEC characterisation demonstrated the removal of acetates and dispersity of the PVAcs, confirming agreement with theoretical M_n values, and the dispersity values suggested a reasonably narrow dispersity with the monomer used, and the loss of acetate carbonyl peaks (1729 cm^{-1}) and hydroxyl peaks (cm^{-1}) by FTIR.

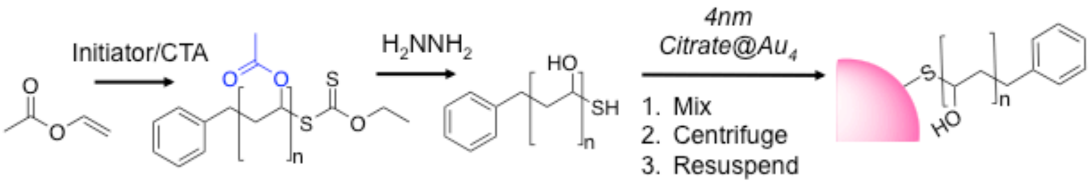

Scheme 3-3. Synthesis of PVA and attachment to AuNPs.

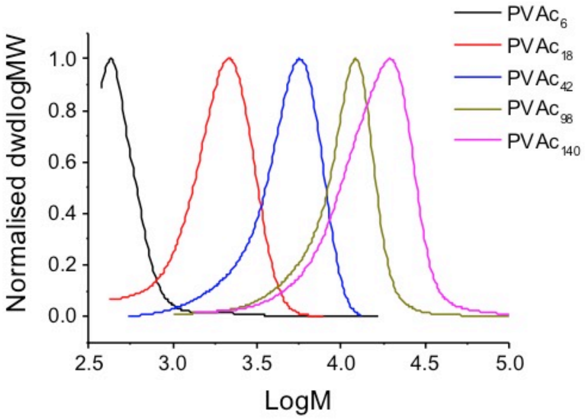

Figure 3-4. SEC molecular weight distributions showing the library of PVA polymers used in this study.

Table 3-1. Poly(vinyl acetate) synthesized in this study.

Polymer	**[M]/[CTA]**[a]	**Conversion (%)**[b]	**$M_{n\,(THEO)}$ (g.mol^{-1})**[b]	**$M_{n\,(SEC)}$ (g.mol^{-1})**[c]	**Đ**[c]
PVAc$_6$	10	72	600	500	1.41
PVAc$_{18}$	40	59	2,000	1,600	1.24
PVAc$_{42}$	60	68	3,500	3,600	1.38
PVAc$_{98}$	100	45	3,900	8,500	1.37
PVAc$_{140}$	250	56	12,000	12,000	1.53

[a] Monomer to RAFT agent molar ratio; [b] Determined by depletion of vinyl peaks in ^{1}H NMR using mesitylene as an internal standard; [c] Determined by SEC.

To form multivalent PVAs, synthesized PVAs were dissolved in citrate@Au_4 solution and incubated on a roller for 1 hour at room temperature before washing 4 times to remove excess polymer in solution. It was immediately apparent that several of the PVA-AuNP samples were unstable due to a red shift in their UV-Vis spectrum, which is indicative of aggregation. Therefore only two of the PVA-AuNP samples were used for further characterisation and analysis: PVA_{98}@Au_4 and PVA_{140}@Au_4.

Table 3-2. Poly(vinyl acetate)/AuNP conjugate characterisation.

Particle	**D_h (DLS) (nm)**[a]	**D_{TEM} (nm)**[b]	**ζ potential (mV)**[c]	**SPR_{max} (nm)**[d]
Citrate@Au_4	4.3 ± 6.8	3.9 ± 0.7	-19.4 ± 2.7 [e]	510
PVA_{98}@Au_4	18.2 ± 5.6	4.4 ± 1.4	-5.5 ± 0.6 [f]	522
PVA_{140}@Au_4	19.4 ± 9.0	3.6 ± 0.9	-4.5 ± 0.4 [f]	521

[a] Hydrodynamic diameter determined by DLS distribution by number of particles, averaged over 3 measurements; [b] Gold core diameter, average of 100 particles by TEM; [c] Averaged over 3 measurements; [d] Maximum of SPR peak determined by UV-Vis spectroscopy; [e] Solution pH 8.93; [f] AuNPs suspended in PBS buffer, pH 7.25.

Changes in size and shape of these conjugates were assessed using DLS and transmission electron microscopy (TEM) measurements. TEM involves firing an electron beam through an ultrathin sample, and measuring the electrons transmitted. AuNPs have high contrast in TEM, and therefore this technique is ideal in visualising the NP core of these samples. In the conjugation of PVA to the citrate@Au_4 samples, the AuNP core did not change significantly in shape or size, with all samples being around 4 nm. In the analysis of the PVA_n@Au_4 samples relative to the citrate@Au_4 precursors, the DLS size distribution did not broaden, but an increase in the hydrodynamic diameter is observed, as expected with the conjugation of ~100/150 DP PVA on a small AuNP core.

Successful conjugation of PVA to the AuNP core was also assessed by X-ray photoelectron spectroscopy (XPS) and zeta potential measurements. XPS entails irradiation of the surface (penetrating up to 10 nm into a sample) of dried samples with an x-ray bean, and measuring the kinetic energy and number of escaped electrons. This data enables determination of the elemental composition of a sample as it changes upon modification (though some contaminants are possible in the modified samples relative to the citrate@Au_4 starting material). Polymer conjugation to the gold surface was detected as a change in the organic character of the sample: such as an increase in the N 1s peak from 0 (citrate@Au_4) to 1.5 % and 0.3 % (PVA_{98}@Au_4 and PVA_{140}@Au_4 respectively), and an increase in the C 1 s peak from 46 % in the precursor to ~65 % in both PVA@AuNP conjugates. Due to the presence of surface coatings, a decrease in Au 4f composition from 0.3 to 0.04 % was also observed.

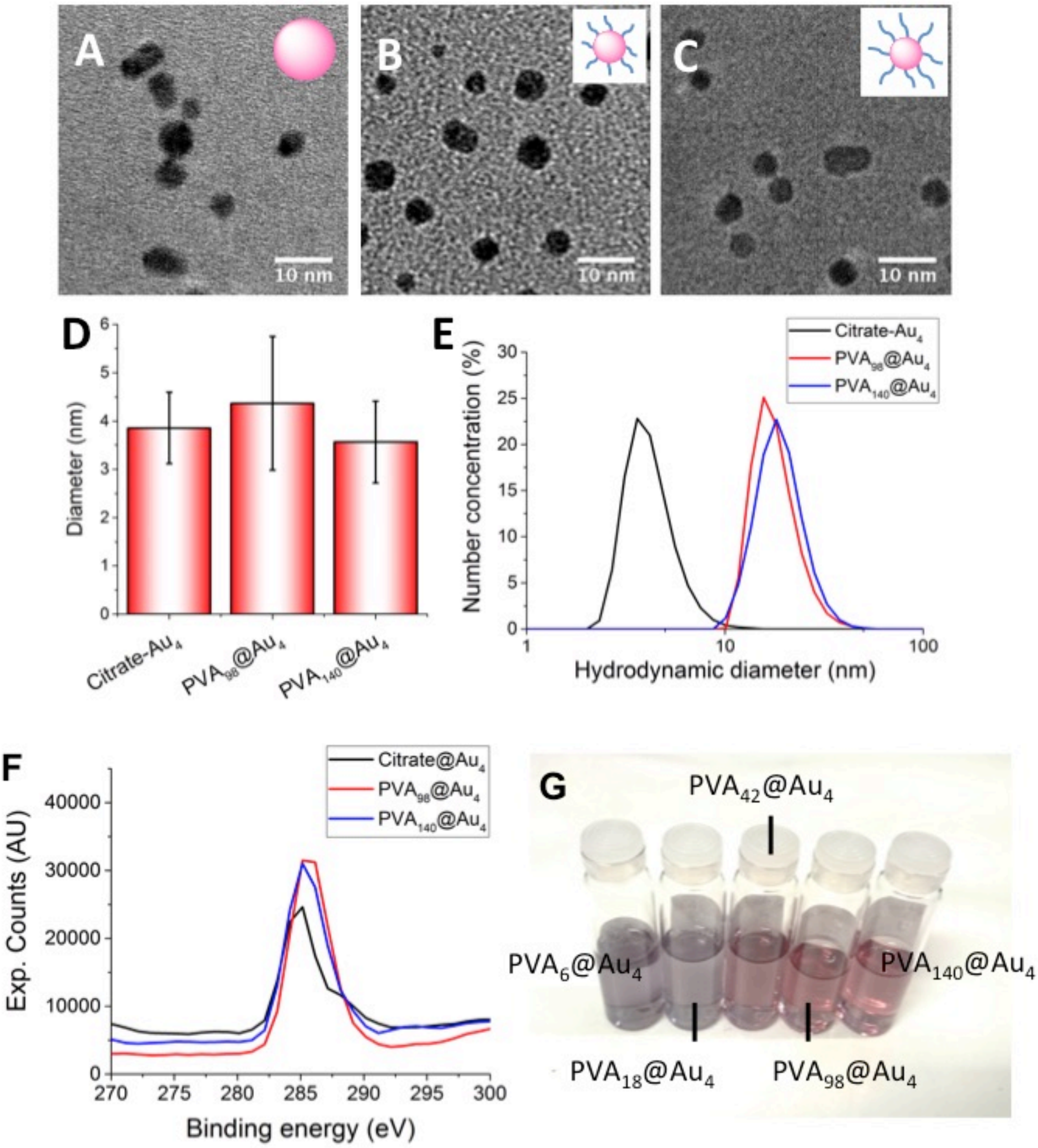

Figure 3-5. Characterisation of PVA@Au4 samples. A-C) TEM micrographs of

citrate@Au4, PVA98@Au4 and PVA140@Au4 respectively. D) Size data from TEM. E) Size distributions by number of particles, from DLS measurements. F) C 1s peak from XPS spectrum showing carbon enrichment upon PVA conjugation. G) Photograph showing the red shift of smaller PVA chains conjugated to Au4: the "more blue" PVA6, PVA18 and PVA42@Au4 samples aggregated.

Zeta potential is a measure of surface charge of particles in a solution, as a difference in charge between the particle surface and bulk solution. The citrate-stabilised gold has a more negative zeta potential, at -19 mV, but this becomes significantly less negative upon polymer conjugation, at -5.5 and -5 mV for the PVA_{98} and $PVA_{140}@Au_4$, as the electrostatically-bound citrate ions are replaced. This change in charge indicates a change in the surface composition of the AuNPs.

To ascertain the mass of polymer coated onto the AuNP scaffold, thermogravimetric analysis (TGA) was used. This is as a simple procedure wherein a dried sample is heated gradually, and the organic components' decomposition can be observed as a mass loss. The mass of polymer attached for a given solution of gold nanoparticles was determined, as 0.24 mg of PVA_{98} and 0.32 mg of PVA_{140} present in 1 mL of undiluted $PVA@Au_4$ solution, and this allows calculation of the density of these polymers on the AuNP surface. The removal of free PVA was confirmed through IRI assays of the washing steps, as detailed in the next section.

3.5.3. IRI activity of PVA@Au4 conjugates

The IRI activity of these $PVA@Au_4$ particles was determined by the "splat" assay, wherein small ice crystals formed at -80 °C were incubated at -8 °C for 30 minutes to observe Oswald ripening to form larger ice crystals. Smaller ice grain sizes relative to a PBS control indicate greater IRI activity. From previous studies of branched PVA structures, we expect branched structures only to show comparable activity to their longest (highest molecular weight) linear chain. This is because the hypothesized binding mode of PVA molecules to ice is via a pattern matching of hydroxyl residues along the c axis of the ice crystal prismatic face, which is not possible with a branched arm.[25]

To ensure free PVA was not present, supernatants were also assayed for IRI. These measurements showed IRI activity in the first wash, demonstrating that free PVA was removed in the washing steps, but not in the two final washes, demonstrating that no more free PVA was present.

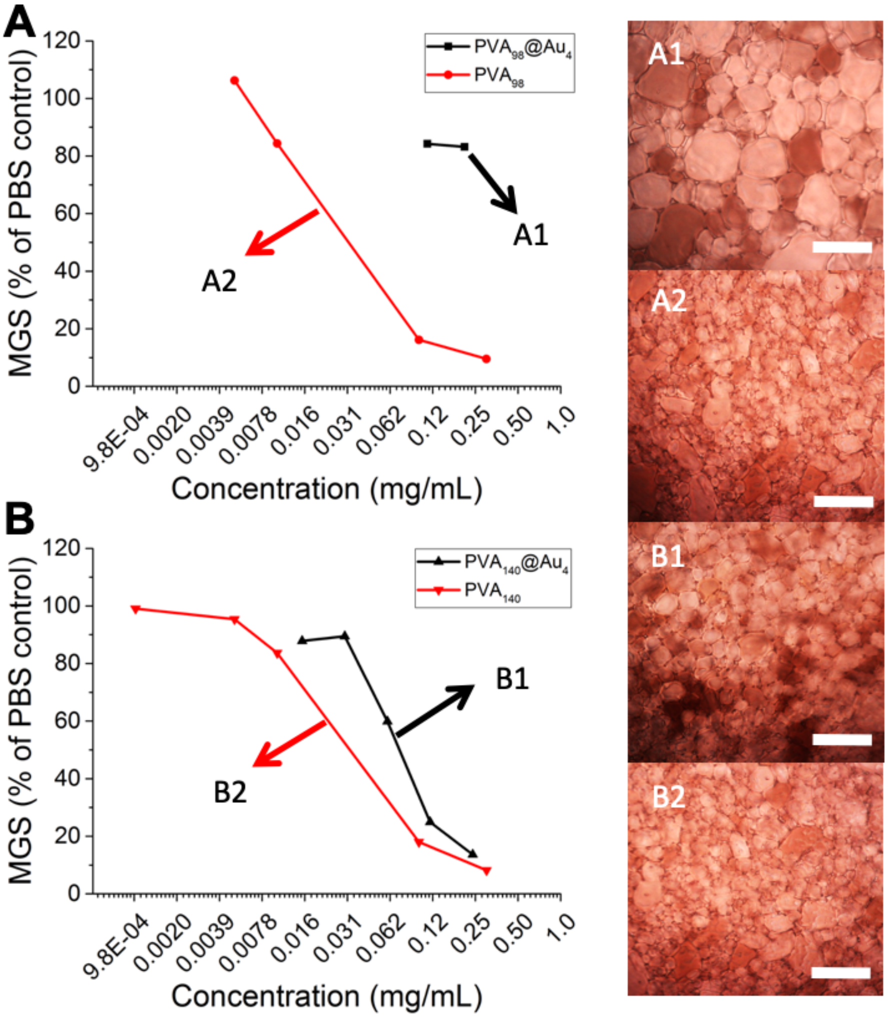

Figure 3-6. Characterisation of IRI activity of PVA@Au$_4$ samples. A-B) Size of ice grains in PVA$_{98}$ and PVA$_{140}$ samples respectively by “splat”. “Splat” optical micrograph scale bars are 10 µm. MGS denotes the mean grain size of all ice grains visible by light microscopy. Note that only 2 measurements of the PVA$_{98}$@Au$_4$ were taken as there was a large grain size at a high concentration, indicating that this analyte did not reduce ice grain size.

Free PVA of both chain lengths gave ice crystals of less than 20 % the size of the PBS control ice crystals at around 0.1 mg.mL^{-1} concentration, demonstrating high IRI activity. At the same concentration of PVA$_{98}$@Au$_4$, ice crystals grew to 80 % of the size of the PBS control, showing that IRI activity of these PVAs is decreased upon tethering to an AuNP scaffold. Conversely, the PVA$_{140}$@Au$_4$ conjugates retained IRI activity within 10 % of the ice crystal size at concentrations above 0.1 mg.mL^{-1}.

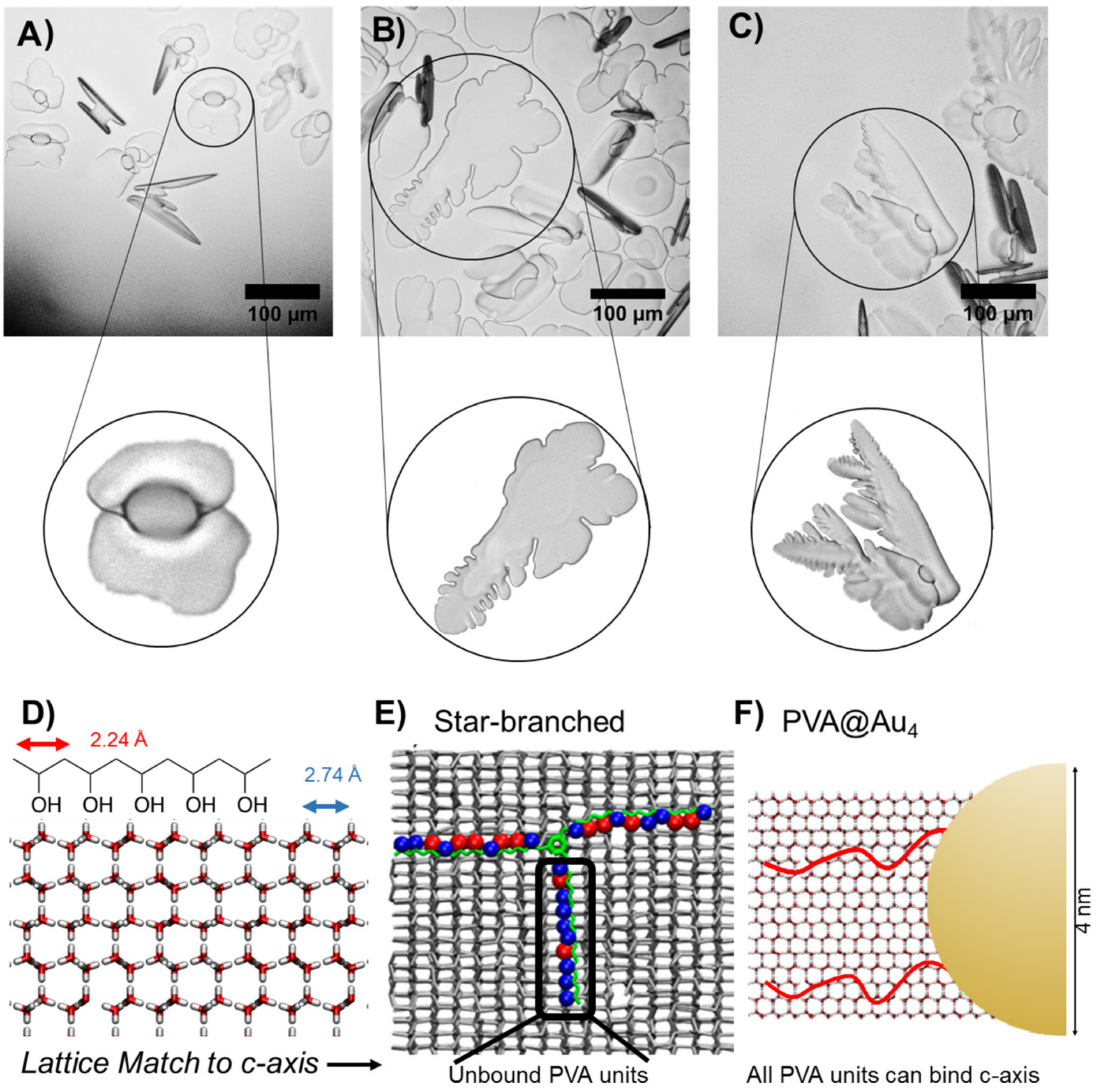

Figure 3-7. Ice shaping and binding images. Full figure taken from Stubbs, C., Wilkins, LE. *et al.*[42] A-C) Cryomicrographs from sucrose "sandwich" ice shaping assays showing ice shapes in H_2O (-6 °C), PVA_{140} (-5.5 °C, 0.2 mg.mL^{-1}) and PVA_{140}@Au_4 (-4.0 °C, 0.2 mg.mL^{-1} of PVA) samples respectively, with zoomed images of crystals of interest. Scale bars = 100 µm. D) Pattern-matching of PVA to ice prismatic face. E) 3-arm PVA star structure binding to ice, with the third arm showing little binding due to a pattern mismatch. Red circles indicate binding to the ice hydroxyls, whilst blue circles are residues not bound. Adapted from Naullage *et al*[25]. F) Schematic of PVA@AuNP binding to ice prismatic face, wherein the low grafting density, with the long PVA chain length, does not constrain the polymer's orientation.

Sucrose "sandwich" assays were also performed to allow visualisation of ice crystal shape, with change relative to a control with no PVA indicating ice-binding (see

Figure 3-7). In these assays, test solution is added to a concentrated sucrose solution (used to reduce the rate of ice growth and nucleation), and placed onto a cryomicroscopy stage, with the temperature gradually lowered until ice crystals are visible. Without a test solution, disc-like ice shapes are observed. Both the free PVA and PVA conjugate samples had different ice shapes to the control, with dendritic ice crystals forming (see Figure 3-7), confirming that these materials are indeed binding to the ice surface.

These IRI and ice shaping assays together suggest that these PVA/AuNP hybrid materials retain the full activity of free PVA polymers despite the immobilisation of the PVA chain end. Previous studies have showed that the longer PVA molecules account for the majority of the polymer solution's IRI activity[26], and that PVA's IRI activity may be attributed to a "zipper mechanism" whereby binding of repeat unit residues in a chain leads to facile binding of the subsequent residues in the chain[25]. It should also be noted that previous studies exploring the activity of branched PVA have not involved branched chains of ~100 chain length. Therefore we could hypothesize that part of the retained activity of our $PVA_{140}@Au_4$ conjugates may stem from the >100 DP length of PVA "branches" applied to the scaffold. With a longer PVA chain, the activity of the residues may be less sterically constrained by the AuNP scaffold (see Figure 3-7), and more able to orientate itself to interact favourably with the ice crystal prismatic face. This enhanced freedom of movement may also be attributed to the low grafting density of PVA on the AuNP scaffold. These data signify that, in the design of such PVA/NP materials, the grafting density and polymer chain length must both be considered to retain the capacity to bind the ice prismatic face, which confirms the previous simulation evidence.

3.5.4. Synthesis of pentafluorophenol-terminated RAFT polymers and post-polymerisation modification of end group

Encouraged by results PVA@AuNP, we wanted to see if similar results are obtained for AFP@AuNP hybrids, which may interact by different mechanisms. Therefore we devised a conjugation method to enable multivalent presentation of AFPs (see Scheme 3-4).

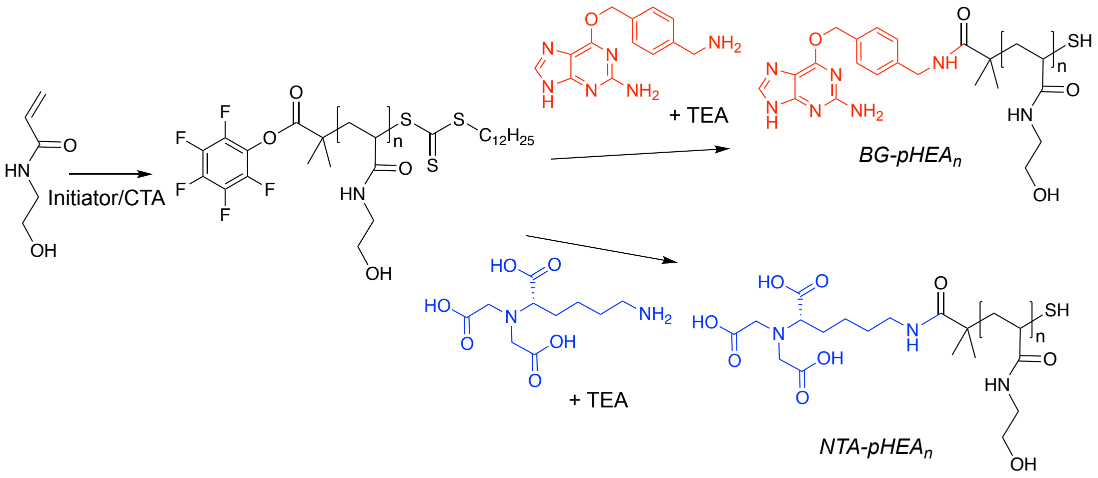

Scheme 3-4. Synthesis of PFP-pHEA polymers and post-polymerisation modification to add functional primary amine group.

RAFT polymerisation was utilised to synthesize pentafluorophenol-terminal poly(hydroxyethyl acrylamide) (PFP-pHEA), with a PFP-ester at the α-terminus and a trithiocarbonate at the ω-terminus. These polymers were synthesised to serve as steric stabilisers on the surface of AuNPs that may be functionalised to capture a tagged protein.

Table 3-3. pHEA Polymers synthesized.

Polymer	**[M]/[CTA]**[a]	**Conversion (%)**[b]	**DP$_n$**	**M$_{n(THEO)}$ (g.mol^{-1})**[b]	**M$_{n\ (SEC)}$ (g.mol^{-1})**[c]	**Đ**[c]
PFP-pHEA$_{17}$ [d]	26	64	17	2,500	3,000	1.1
PFP-pHEA$_{45}$ [e]	47	94	45	5,700	8,300	1.1
PFP-pHEA$_{47}$ [f]	47	94	45	5,700	8,300	1.1
PFP-pHEA$_{95}$	103	93	95	11,000	15,000	1.3

[a] Monomer to RAFT agent molar ratio; [b] Determined by depletion of vinyl peaks in ^{1}H NMR using mesitylene as an internal standard; [c] Determined by SEC; [d] Used in His-AFP-Ni-NTA-pHEA$_{17}$@Au$_4$ conjugates; [e] Used in SNAP-AFP-BG-pHEA$_{45}$@Au$_4$ conjugates; [d] Used in Maleimide-pHEA$_{47}$@Au$_4$ conjugates.

PFP-terminated polymers with three different chain lengths were synthesized: approximately 25, 50 and 100 monomers in length. ^{1}H-NMR was used to determine the theoretical M$_n$, by observing the reduction of the vinyl peak relative to a mesitylene standard peak. SEC, ^{1}H and ^{19}F-NMR were used to confirm the molecular weight, dispersity and structure of the polymers.

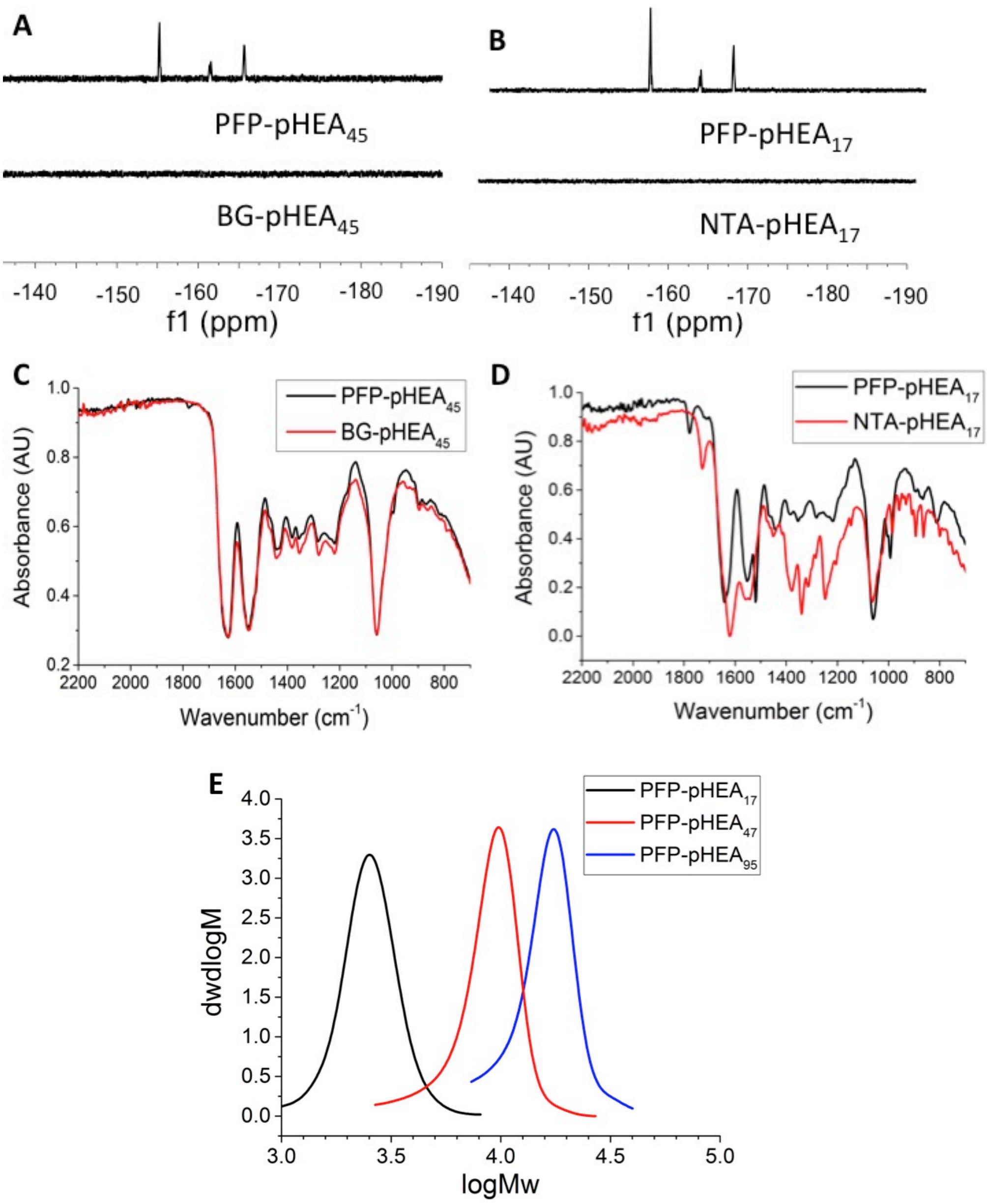

Figure 3-8. Characterisation of PFP-pHEA library, and the removal of the PFP group. A-B) ^{19}F-NMR spectra showing depletion of PFP peaks. C-D) FTIR spectra showing depletion of C-F peaks at 1070 cm^{-1}. E) Molecular weight distributions, by SEC, of PFP-pHEA library.

The α-terminus was functionalised through the replacement of the PFP group with amino-benzylguanine (BG) or Nα,Nα-Bis(carboxymethyl)-L-lysine hydrate (NTA). Successful displacement was confirmed by ^{19}F-NMR, by the removal of the three PFP peaks at ~155-165 ppm, and by the depletion of ~1750 cm^{-1} C-F peaks in FTIR (Figure 3-8). The use of excess primary amine in this reaction is also expected to displace the

RAFT chain transfer agent end group to liberate a ω-terminal thiol: as required for AuNP immobilisation.

3.5.5. Synthesis of AFP@Au4 conjugates

Two different linkers were used to attach AFP to the AuNP scaffold: 1) Ni-NTA-pHEA of relatively short length to interact electrostatically with His-AFP; 2) BG-pHEA of ~50 chain length to interact with the large SNAP tag via covalent attachment of the benzyl group to a cysteine. A maleimide-pHEA of ~50 chain length was also attempted to interact via a bioorthogonal "click" to a recombinant terminal cysteine, but these conjugates were not stable in initial screens, so were discarded.

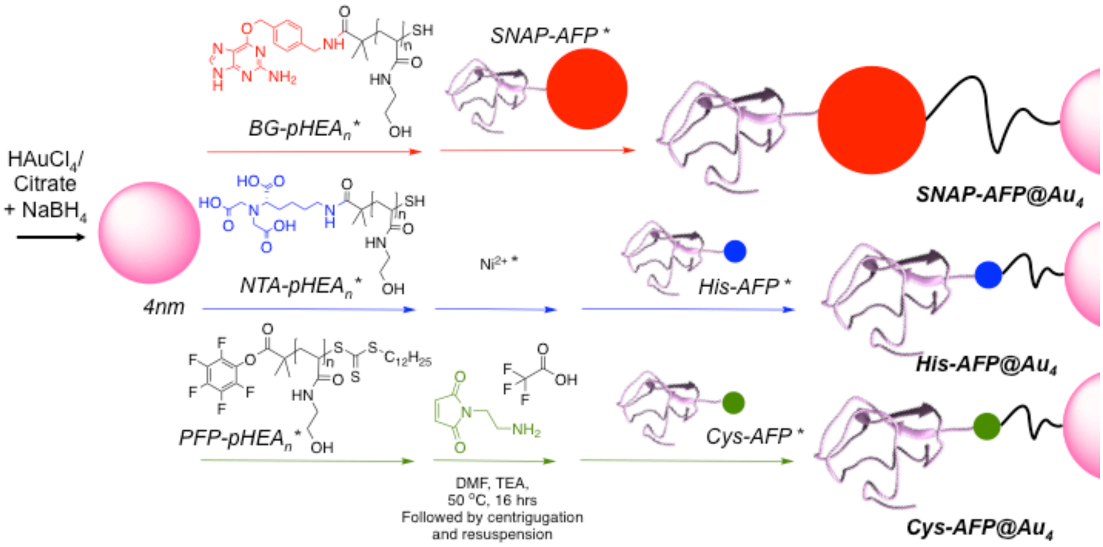

*Upon adding to Au$_4$:
1. Mix
2. Centrifuge
3. Resuspend

Scheme 3-5. Synthesis of AFP@AuNP conjugates.

All NTA-, BG- and PFP-pHEA polymers were dissolved in citrate@Au$_4$ solution and incubated at room temperature for 1 hour on a roller before being washed at least 3 times to remove excess, unattached, polymer. Polymer@Au$_4$ samples were initially assessed by UV-Vis spectroscopy and DLS size measurements to determine the most stable chain length of pHEA polymer. Larger shifts in size or the presence of multiple peaks by DLS size measurements and large shifts in UV-Vis SPR$_{max}$ showed aggregation. From these analyses, the most stable polymer@Au$_4$ samples were selected for further characterisation and protein attachment: NTA-pHEA$_{17}$, BG-pHEA$_{45}$, PFP-pHEA$_{47}$@Au$_4$. Polymer of ~50 chain length were required to stabilise the benzylguanine and pentafluorophenyl terminals conjugated to the AuNP, potentially due to their hydrophobic nature requiring a longer length of hydrophilic polymer. On the other hand, the more hydrophilic NTA end group required only a shorter, ~25, chain length polymer. The NTA-pHEA$_{17}$@Au$_4$ sample was functionalised with Nickel (II), and this sample was shown not to aggregate by analysis by DLS and TEM.

The PFP-pHEA$_{47}$@Au$_4$ sample was subjected to the same conditions as the PFP-pHEA precursor polymers: heated overnight with excess maleimide amine and triethylamine to substitute the PFP group for the desired maleimide. The removal of this PFP end group was performed after AuNP conjugation rather than earlier to avoid forming a cross-linked polymer. Successful modification of the polymer end group was determined by XPS and zeta potential analysis, showing a loss of fluorine and a change in surface charge respectively. This maleimide-pHEA$_{47}$@Au$_4$ began to sediment out of solution when stored in PBS solution in the fridge overnight so was deemed unstable. The sample was thus not fully characterised.

Recombinant AFP type III from ocean pout (*N*-terminally modified His-AFP, SNAP-AFP and Cys-AFP) were produced by Dr. Muhammad Hasan, University of Warwick by recombinant expression in *E. coli* followed by IMAC purification and HPLC. His- and SNAP-AFP were incubated for 2 hours on a roller at room temperature with the prepared AuNP scaffold (Ni-NTA-pHEA$_{17}$@Au$_4$ and BG-pHEA$_{45}$@Au$_4$ respectively). These incubations were then washed at least 4 times to remove excess AFP.

Table 3-4. AFP@Au$_4$ nanoparticle characterization

Particle	**D_h (DLS) (nm)**[a]	**D_{TEM} (nm)**[b]	**ζ potential (mV)**[c]
Citrate@Au$_4$	4.3 ± 6.8	3.9 ± 0.7	-19.4 ± 2.7 [d]
NTA-pHEA$_{17}$@Au$_4$	8.5 ± 8.3	3.7 ± 0.8	-15.9 ± 4.8 [e]
Ni-NTA-pHEA$_{17}$@Au$_4$	7.7 ± 7.2	3.9 ± 0.8	-6.2 ± 1.1 [f]

His-AFP@Au$_4$	8.9 ± 9.7	4.3 ± 0.9	-7.0 ± 1.3 [f]
BG-pHEA$_{45}$@Au$_4$	16.5 ± 10.6	3.9 ± 1.0	-10.2 ± 1.9 [e]
SNAP-AFP@Au$_4$	8.9 ± 10.3	4.0 ± 1.1	-4.4 ± 0.9 [f]

[a] Hydrodynamic diameter determined by DLS distribution by number of particles, averaged over 3 measurements; [b] Gold core diameter, average of 100 particles by TEM; [c] Averaged over 3 measurements; [d] pH 8.93; [e] pH 7.6; [f] AuNPs suspended in PBS buffer, pH 7.25.

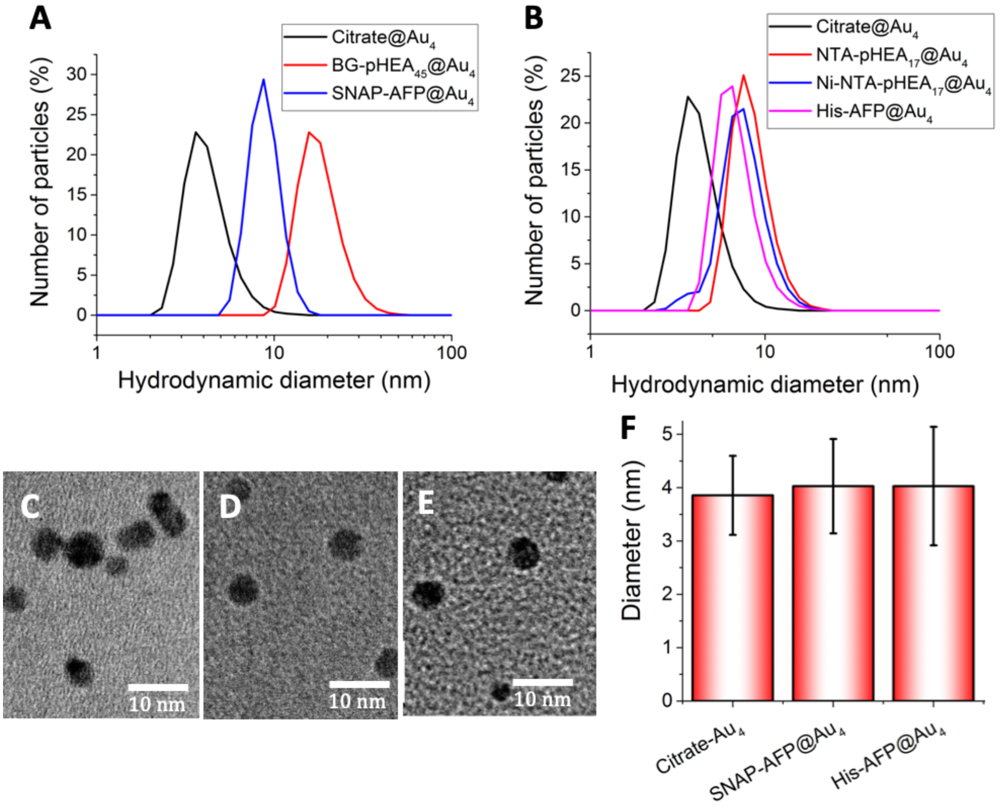

Figure 3-9. Characterisation of AFP@Au$_4$ particles. A-B) Size distributions by number of particles, from DLS measurements, of SNAP-AFP-BG-pHEA$_{45}$@Au$_4$ synthesis and His-AFP-Ni-NTA-pHEA$_{17}$@Au$_4$ respectively. C-E) TEM micrographs of citrate@Au$_4$, SNAP-AFP@Au$_4$ and His-AFP@Au$_4$ respectively. F) Size data from TEM.

DLS and TEM measurements were used to assess the shape and size of all successfully conjugated, stable AuNP samples. TEM showed no significant change in the size and shape of the AuNP core, with a size of 4 nm for all AuNPs. DLS showed an increase in the hydrodynamic volume (an indication of the size of the AuNP and protective shell in solution) of the conjugates relative to the citrate@Au_4 precursors without a significant broadening of the size distributions that would suggest aggregation. The hydrodynamic diameters of the His-AFP and SNAP-AFP@AuNP conjugates were both 4.5 nm greater than the citrate@Au_4 (4.3 nm diameter), which demonstrates that the coatings caused a significant change in AuNP solution behaviour.

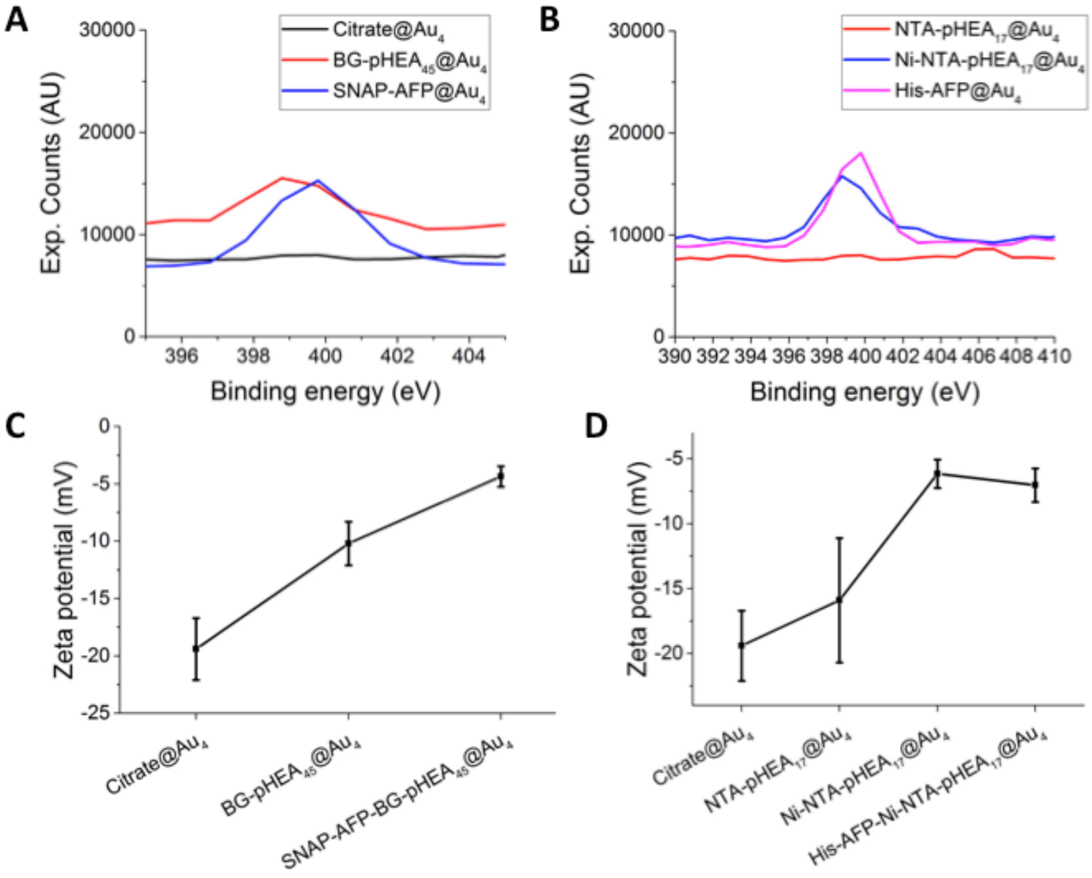

Figure 3-10. Characterisation of AFP@Au_4 AuNP coatings. A-B) N 1s peak from XPS spectra showing change upon conjugation of AFP protein – note that the different samples were not subjected to the same conditions before performing this analysis. C-D) Zeta potential change upon conjugation of AFP protein, from readings in triplicate.

Successful conjugation of polymers, followed by modifications and protein, were assessed by XPS and zeta potential measurements, with the former allowing determination of the elemental composition of a sample (though some contaminants are possible in the modified samples relative to the citrate@Au_4 starting material).

Upon the conjugation of the recombinant AFPs, the organic character of the samples changed. For example, the N 1s proportion increased from 0 % in the citrate@Au_4 to ~12 % in both AFP@AuNP conjugates, whilst the O 1s peak decreased from 53 % to 22 % and 25 % in the His-AFP and SNAP-AFP@AuNP conjugates respectively. The Au 4f peak also decreased from 0.33 % in the citrate@Au_4 to 0.19 and 0.17 in the His-AFP and SNAP-AFP@AuNP conjugates respectively. These changes evidence successful successive coating of the AuNPs, and the conjugation of organic molecules. The analysis also showed the change in specific peaks to evidence a specific change in composition: with a loss of the fluorine 1 s peak upon substituting the maleimide end group for the pentafluorophenol on the PFP-$pHEA_{47}$@Au_4, and a decrease in the Ni 2p peak from 0.15 to 0.12 % when His-AFP is conjugated to the Ni-NTA-$pHEA_{45}$@Au_4.

The zeta potential shows the surface charge of the AuNPs, and changes in this result from a change in surface composition. The zeta potential of the citrate@Au_4 precursors was approximately -19 mV, and conjugation of polymer resulted in a reduction in negativity, due to the replacement of surface citrate ions to around -16 and -10 mV for the NTA-pHEA and BG-pHEA@AuNP conjugates respectively. The conjugation of AFP decreased this negativity again by over 5 mV for both samples, which shows a further change in surface composition.

In order to confirm that all SNAP-AFP present in the SNAP-AFP@Au_4 conjugate solutions was tethered to the AuNP scaffold, the concentration of SNAP-AFP in the post-conjugation washes was determined by nanodrop absorption analysis. These measurements showed that no free SNAP-AFP was present in the third and fourth washes, so no free AFP will be present in the final conjugate solutions. TGA was used to determine the mass of organic matter attached to the inorganic AuNPs in each sample. Upon each successive conjugation, the mass of coating added was determined from the change in mass of the sample, showing there to be approximately 4 μg BG-$pHEA_{45}$ and 0.64 mg SNAP-AFP in 1 mL of undiluted SNAP-AFP@Au_4 conjugate in PBS.

Finally, SEC and SDS-PAGE were used to determine that a covalent linkage occurred between the SNAP-AFP and BG-$pHEA_{45}$. A shift was observed in the SEC sample containing both AFP and polymer, relative to both the free SNAP-AFP and BG-

$pHEA_{45}$ (see Figure 3-11), which suggests that at least some of the molecules have bound to each other. By SDS-PAGE, mixing the BG-$pHEA_{45}$ and SNAP-AFP together resulted in an increase in molecular weight (an shift upwards in the gel, closer to the 35 kDa molecular weight mark).

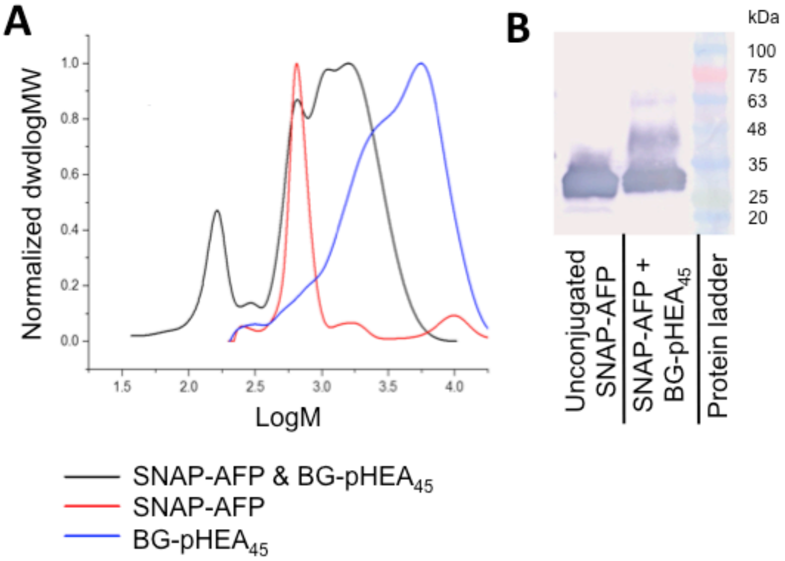

Figure 3-11. BG-$pHEA_{45}$/SNAP-AFP interaction. A) SEC showing peak shift upon polymer conjugation. B) Blot of SDS-PAGE gel showing shift in molecular weight upon conjugation.

3.5.6. IRI activity of AFP@Au4 conjugates

Previous investigations have shown an increase in antifreeze activity upon the development of multimeric AFP structures.[12–14,17,19] In this study we therefore synthesized a multimeric scaffold on which to attach several AFPs. Three different protein tags were employed with the aim of investigating the impact of different linker types and lengths on AFP's antifreeze activity. For the three different protein tags, three different polymer linker structures were proposed to bridge the AFP to the AuNP scaffold: 1) the relatively short Ni-NTA-$pHEA_{17}$ interacts electrostatically with the His tag; 2) the large BG-$pHEA_{45}$ forms a covalent bond to the SNAP tag; 3) maleimide-$pHEA_{47}$ was proposed to attach Cys-AFP to Au_4, but this conjugate was unfortunately not stable in PBS buffer.

It has been shown previously that the entire AFP ice-binding site must be sterically available to see the gain in antifreeze activity with multimeric AFP designs. This suggests that a large scaffold, or longer linker to a scaffold, is preferable to give the attached AFP the freedom of movement to orientate its ice-binding site favourably – and enhanced activity from these constructs would suggest an ice crystal bridging hypothesis of IRI enhancement. Meanwhile, a smaller scaffold, or shorted linker to a scaffold, would result in the AFP molecules spacing closer together, which would support the hypothesis of multiple AFPs binding to the same surface enhancing IRI activity. In this study, it was therefore possible to directly compare the shorter His tag linker directly to the longer SNAP tag linker to see which of these hypotheses was supported in our results.

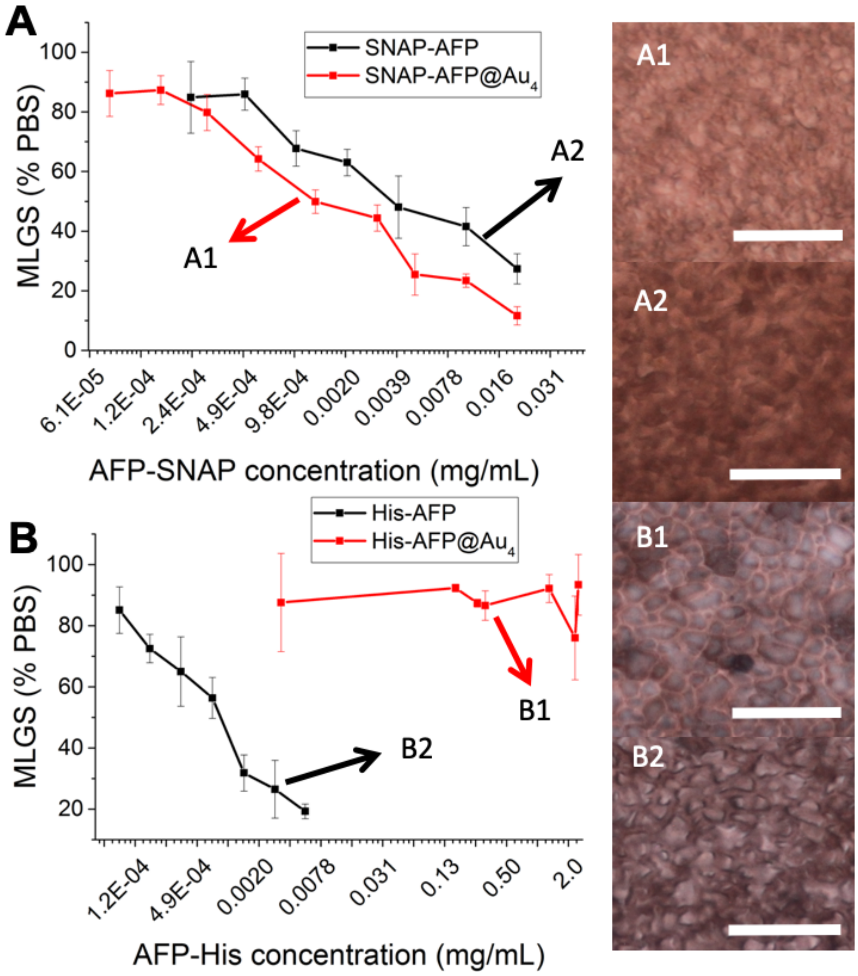

Figure 3-12. Characterisation of IRI activity of AFP and AFP@Au_4 samples. A-B) Size of ice grains in PVA_{98} and PVA_{140} samples respectively by “splat” assay. “Splat” optical micrograph scale bars are 10 µm.

The “splat” assay is used to probe IRI activity by measuring the capacity of an analyte to inhibit the ice nucleating Oswald ripening effect during a 30 minute incubation at -8 °C. Larger ice crystals form in samples with less IRI activity (relative to a PBS control). These assays compared AFP conjugates to the same concentration of free monomeric recombinant AFP to allow a direct comparison in molar concentration. As expected, even at concentrations less than 20 µg.mL^{-1}, the unconjugated recombinant AFPs showed ice crystals at less than 30 % of the size of ice crystals in the PBS control. The His-AFP@Au$_4$ conjugates showed ice crystals at 90% the size of the PBS control up to 2 mg.mL^{-1}, which suggests that the conjugation process inhibits the activity of the AFPs. As the linker used is site-specific, this could be due to the use of a non-covalent linker, or due to the smaller linker length resulting in steric hindrance of the ice-binding site.

Conversely, SNAP-AFP@Au$_4$ showed higher IRI than free monomeric SNAP-AFP, with ice crystals ~10 % smaller in size for the conjugates relative to the equivalent concentration of free SNAP-AFP up to 0.5 µg.mL^{-1}. This enhanced activity could suggest that either a covalent linker is required, or that a lower surface density, longer linker and large fusion protein tag allows freer movement than the His-AFP conjugates with a shorter linker. This may support the hypothesis of enhancement by bridging between ice crystals, but it is unclear, however, how large the scaffold must be to enhance antifreeze activity with this mechanism. We would need to understand the spacing of these ice crystals in nature to know whether this mechanism is viable at all.

In biological systems, AFP results in the formation of shard-like ice crystal shapes, which can damage cells. Ice shaping assays were performed in sucrose solution sandwiched between two glass cover slips to allow visualisation of the ice shapes formed upon the addition of the monomeric and multimeric SNAP-AFP samples. The recombinant His and SNAP-AFP samples resulted in sharp linear shapes, similarly to native AFPs.[4,5] Both conjugates formed branched, feathery structures, which suggests a change in the interaction with ice. It has been hypothesized that the shape of ice that forms upon exposure to AFP occurs due to bulk steric hindrance of ice growth[12], and therefore it stands to reason that AFP molecules forming different shapes in space will form differently shaped ice.

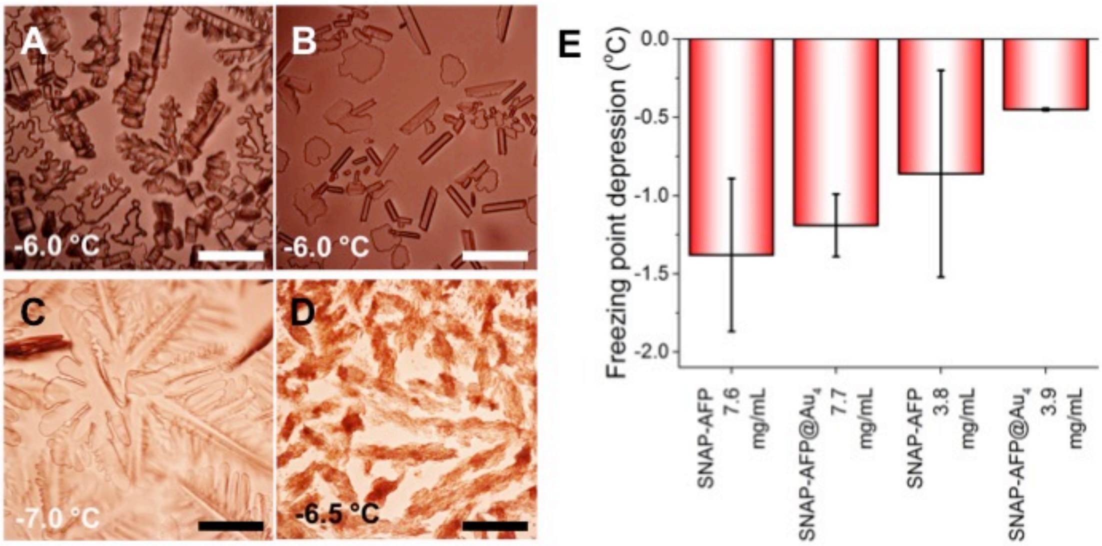

Figure 3-13. Characterisation of antifreeze activity of AFP and AFP@Au_4 samples. A-D) Optical micrographs from sucrose "sandwich" ice shaping assays showing ice shapes in AFP-SNAP-BG-$pHEA_{45}$@Au_4, SNAP-AFP, His-AFP-Ni-NTA-$pHEA_{17}$@Au_4 and His-AFP respectively. E) Freezing point depression in thermal hysteresis assay of SNAP-AFP and SNAP-AFP@Au_4 samples. Scale bars 100 µm.

Another feature of antifreeze activity that AFPs exhibit is thermal hysteresis (TH) – wherein the freezing point of a solution, but not its melting point, is depressed. SNAP-AFP and conjugates were assessed in a TH assay by the Davies group at Queen's University, Canada, and both showed TH temperatures around 1.2 °C for the same concentration of SNAP-AFP. This suggests that the conjugates retain the activity of the free AFP, and that multivalent presentation gives a small increase in activity, by potentially enabling binding to multiple crystal faces.

3.6. Conclusions

This chapter demonstrates the preparation of several antifreeze macromolecules displayed on a multivalent AuNP scaffold: PVA_{98} and PVA_{140}@Au_4, and His-AFP and SNAP-AFP@Au_4.

AuNPs (~4 nm diameter) were coated with a library of PVAs of different chain lengths synthesized by RAFT polymerisation. The longer length PVA-AuNP conjugates were found to have comparable IRI activity to linear PVA architectures of the same molecular weight. This is hypothesized to be due to the long length and low coating density on the AuNP scaffold allowing free orientation of the PVA in space. This free orientation allows the PVA attached to the AuNP scaffold to benefit from the same binding modalities seen in linear PVA.

Separately, terminally functionalised pHEA polymers prepared by RAFT were conjugated onto the Au_4 scaffold, followed by AFP conjugation. Two different types of "multimeric AFP" were prepared: SNAP-AFP-BG-$pHEA_{45}$@Au_4 and His-AFP-Ni-NTA-$pHEA_{17}$@Au_4. These two types of linker and tag allowed us to investigate the affect of linker length on activity, and we found that the longer linker was necessary to afford an enhancement of AFP IRI activity.

Ultimately, these data suggest that AuNPs may be a valuable scaffold for the formation of IRI-active antifreeze materials. In particular, the capacity to coat these AuNPs less densely, with higher molecular weight molecules, allows us to form multimeric molecules with freedom of movement and orientation but without steric hindrance. Incorporation of a metal core may also provide contrast for future cryo-EM studies of AFPs to elucidate their interaction with ice.

3.7. Materials and Methods

3.7.1. Materials

Ultra-pure water with resistance < 18 Ω, was obtained from a Milli-Q© Integral Water Purification System. All chemicals were purchased from Sigma-Aldrich or Thermo Fischer Scientific and used as supplied unless otherwise stated. THF, DMF and ethyl acetate were purchased from Fisher. For washing of AuNPs, Amicon Ultra-0.5 centrifugal filter units with Ultracel-30 or Ultracel-100 membrane were used. The pET20b-AFPIII plasmid encoding for a hexahistidine-tagged AFPIII from ocean pout (*rQAE isoform*, M1.1HISPET20b) was kindly provided by Peter Davies (Queens University, Kingston, Canada). Competent *Escherichia coli* BL21(DE3) cells were sourced from New England Biolabs. IMAC Sepharise 6 Fast Flow columns, HiLoad 16/600 Superdex 75 pg gel filtration columns and PD10 desalting columns were purchased from GE Healthcare and used according to manufacturer's instructions. Thermo Scientific Pierce BCA assay kit was used according to the manufacturer's protocols to determine all protein concentrations. Phusion® High-Fidelity DNA Polymerase and pSNAP-tag® (T7)-2 vector were purchased from New England Biolabs.

3.7.2. Analytical Methods

^{1}H, ^{13}C and ^{19}F-NMR spectra were obtained using a Bruker DPX-400 NMR Spectrometer; all chemical shifts are reported in ppm (δ) relative to residual non-deuterated solvent. Mass spectrometry was carried out in pure methanol or water on the Agilent 6130B ESI-Quad instrument using electrospray in positive mode. FTIR spectroscopy was carried out on a Bruker Vector 22 FTIR spectrometer with a Golden gate diamond attenuated total reflection cell. SEC measurements were carried out on an Agilent 390-LC MDS instrument equipped with a dual angle light scatter (LS), 2 x PLgel Mixed D columns (300 x 7.5 mm) and a PLgel 5 μm guard column. The eluent was DMF with 5 mmol NH_4BF_4 additive. Samples were run at 1ml/min at 50°C. Poly(methyl methacrylate) standards (Agilent EasyVials) were used for calibration between 955,000 – 550 gmol^{-1}. Analyte samples were filtered through a nylon membrane with 0.22 μm pore size before injection. Respectively, experimental molar mass (Mn_{SEC}) and dispersity ($Đ$) values of synthesized polymers were determined by conventional calibration using Agilent SEC software. Nanoparticle size was determined using Dynamic Light Scattering (DLS), performed on a Malvern Instruments Zetasizer Nano- ZS with 4mW HeNe laser 632.8 nm. UV/Vis spectroscopy, optical density and fluorescence plate readings were performed on a BioTek Synergy HT Microplate Reader. UV-vis spectroscopy was used to determine nanoparticle size according to a method developed by Haiss *et al.*[43] Transmission electron microscopy (TEM) was performed on a JEOL 2100 LaB6 high-resolution microscope. X-ray photoelectron spectroscopy (XPS) was carried out on the Kratos Axis Ultra with a delay-line detector. Analysis of the XPS data was performed using CasaXPS software, with mixed Gaussian-Lorentzian lineshapes – only individual measurements were taken, so no errors can be given for this data. Bacterial cell lysis was performed using a STANSTED 'Pressure Cell' FPG12800 homogeniser. Thermal hysteresis measurements were performed using standard procedures.[44] Protein concentration was determined by measuring absorbance at 280 nm on a NanoDrop™ 2000 spectrophotometer.

3.7.3. Synthetic and Experimental Procedures

Synthesis of citrate@Au_4

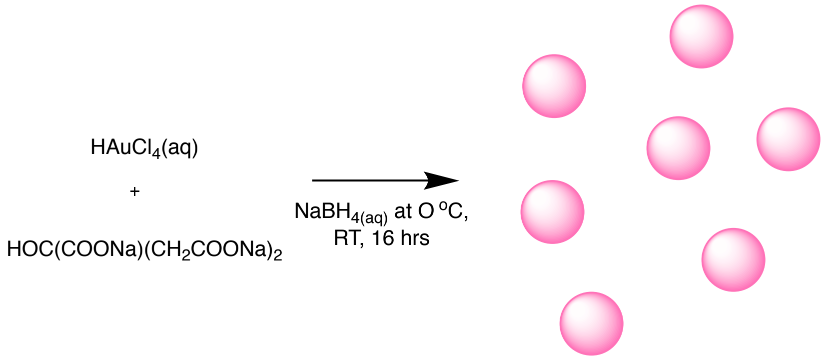

AuNPs were synthesized as follows, based on a method by Ieong *et al.*[35] All glassware was washed with aqua regia prior to commencing the experiment, to reduce nucleation. 240 mL of a 0.21 mmol.L^{-1}, (0.08 mg.mL^{-1}) aqueous solution of $HAuCl_4$ was prepared at room temperature. To this was added 13.8 mg (0.05 mmol) of trisodium citrate to give a final citrate concentration of 0.21 mmol.L^{-1}. 5 mL of an ice-cold 0.1 M (0.5 mmol, 18.5 mg) solution of $NaBH_4$ was added to the gold/citrate solution and stirred at room temperature overnight. Assuming complete reduction of the $HAuCl_4$ to gold particles, the total gold concentration in the final solution was 0.21

mmol.L^{-1} (0.04 mg.mL^{-1}). As these small AuNPs did not pellet upon centrifugation, small AuNPs were isolated by taking the supernatant after centrifugation at 13.2 kRPM for 10 mins at 25 °C. Nanoparticle size and dispersity was measured by TEM, UV-Vis spectroscopy and size and zeta potential measurements by DLS.

Nanoparticle diameter (UV-vis): 3-4 nm; TEM: 3.86 nm (standard deviation 0.74 nm).

Synthesis of 2-(dodecylthiocarbonothioylthio)-2-methylpropionic acid (DMP/DDMAT)

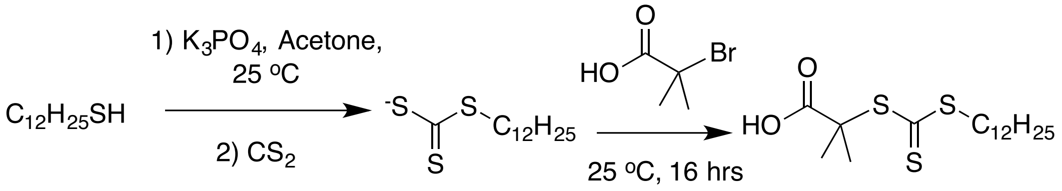

Dodecane thiol (4.75 mL, 19.8 mmol) was added dropwise to a stirred suspension of K_3PO_4 (4.02g, 18.9 mmol) in acetone (60 mL). The reaction vessel was placed in an ice bath. Carbon disulfide (3.20 mL, 53.0 mmol) was added and the solution turned bright yellow, but was still cloudy. After stirring for ten minutes, 2-bromo-2-methylpropionic acid (3.00 g, 18.0 mmol) was added and a precipitation of KBr was noted. The ice bath was removed after 10 minutes and the reaction was left stirring at room temperature for 16 hours. Solvent was removed *in vacuo* and the residue was extracted into DCM (2 x 50 mL) from 1 M HCl (100 mL). The organic extracts were further washed with water (100 mL) and brine (100 mL) and dried over $MgSO_4$. Recrystallisation from n-hexane yielded a bright yellow solid (1.80 g, 27.5%).

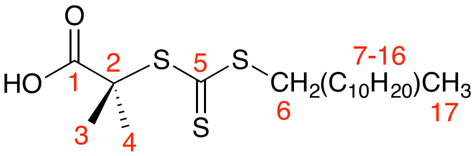

^{1}H NMR (400 MHz, CDCl3) δ_{ppm}: 3.28 (2H, t, J_{HH}=7.5, H6); 1.66 (6H, s, H3/4); 1.10-1.25 (20H, alkyl, H7-16); 0.79 (3H, m, H17).

^{13}C NMR (400 MHz, CDCl3) δ_{ppm}: 220.86 (C5); 178.04 (C1); 55.51 (C2); 37.08 (C7); 31.92 (C6); 29.64, 29.57, 29.46, 29.35, 29.12, 28.98, 27.82 (C8-15); 25.23 (C3/4); 22.70 (C16); 14.13 (C17).

FTIR (solid, ν_{max}/cm^{-1}): 2910 (CH_2); 1710 (C=O); 1440 (C-C); 1305 (C-O); 1070 (S-(C=S)-S).

ESI-MS, positive mode (m/z): 365.2 ($M+H^+$, expected 365.63), 387.1 ($M+Na^+$, expected 387.61).

Synthesis of pentafluorophenyl 2-(dodecylthiocarbonothioylthio)-2-methylpropionic acid (PFP-DMP/PFP-DDMAT)

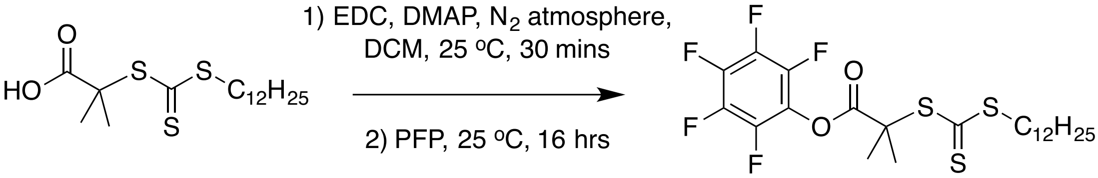

2-(Dodecylthiocarbonothioylthio)-2-methylpropionic acid (DMP) (0.500 g, 1.37 mmol), *N*-(3-dimethylaminopropyl)-*N'*-ethylcarbodiimide hydrochloride (EDC) (0.390 g, 2.05 mmol), and 4-(dimethylamino)pyridine (DMAP) (0.250 g, 2.05 mmol) were dissolved in DCM (50 mL) and stirred for 20 minutes under N_2. Pentafluorophenol (PFP) (0.780 g, 4.24 mmol) in 5 mL DCM was added. The reaction was stirred overnight at room temperature. The reaction was washed with 3 M HCl (100 mL), 1 M $NaHCO_3$ (100 mL) and brine (100 mL), dried over $MgSO_4$, filtered and then concentrated *in vacuo* to evolve a yellow solid with melting point close to room temperature (0.437 g, 60.2%).

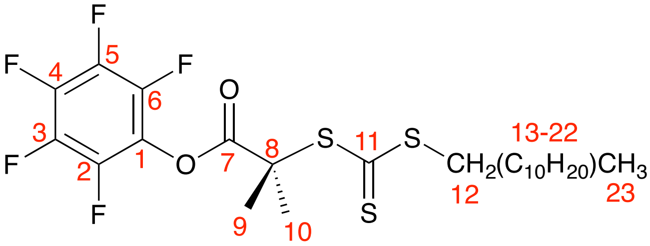

^{1}H NMR (300 MHz, CDCl3) δ_{ppm}: 3.24 (2H, t, J_{HH}=7.4 x 2, H12); 1.62 (6H, m, H9/10); 1.26 (20H, alkyl, H13-22); 0.81 (3H, m, H23).

^{19}F NMR (300 MHz, CDCl3) δ_{ppm}: 151.54 (m, F2/6), 157.74 (m, F3/5), 162.3 (m, F4).

FTIR (solid, ν_{max}/cm^{-1}): 2934 (CH_2); 1705 (C_6F_5C=O); 1439 (C-C); 1260 (C-O); 1080 (S-(C=S)-S).

This species' ESI-MS did not show any of the expected peaks, though the above characterisation was deemed sufficient to prove successful synthesis

General Procedure for Synthesis of pHEA (or PFP-pHEA) polymer

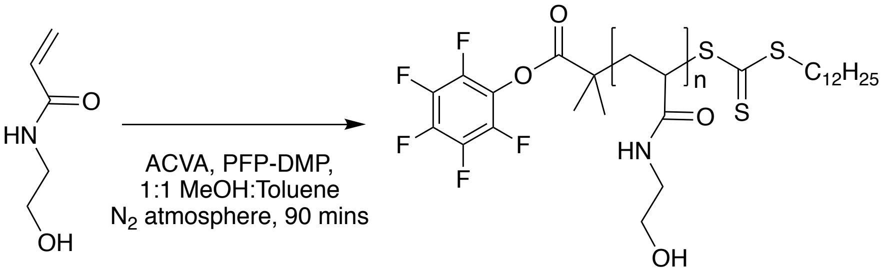

The following procedure describes a reaction with a theoretical degree of polymerisation (DP) of 50 repeat units. 4,4-azobis(4-cyanovaleric acid) (5 mg, 0.018 mmol), pentafluorophenyl 2-(dodecylthiocarbonothioylthio)-2-methylpropionic acid (CTA) (47 mg, 0.088 mmol, for the polymer without a PFP-end group, DMP was used instead of PFP-DMP) and *N*-hydroxyethyl acrylamide (1 g, 8.8 mmol) were dissolved in 1:1 methanol: toluene (4 mL) in a glass vial with a stirrer bar. Mesitylene (200 µL) was added and a sample was removed for ^{1}H-NMR analysis in $CDCl_3$. The reaction mixture was degassed by N_2 for 30 minutes, sealed and placed in a 70°C oil bath. After 90 minutes, the solution was opened to air and quenched by submerging the flask in $N_{2(l)}$. The polymer (pHEA) was precipitated three times from methanol into diethyl ether to give a light yellow solid.

Conversion (NMR): 94.0%; M_n (theoretical): 5664 g.mol-1; M_n (SEC) 8253 g.mol-1; M_w (SEC) 9231 g.mol-1; M_w/M_n (SEC): 1.1.

^{1}H NMR (300 MHz, CDCl3) δ_{ppm}: 8-8.15 (br s, N-H (H4)); 3.4-3.8 and 3.05-3.2 (2 x m, H5); 1.9-2.35 and 1.4-1.8 (2 x m, H1/2).

^{19}F NMR (300 MHz, CDCl3) δ_{ppm}: 155.29, 161.61, 165.67.

FTIR (solid, ν_{max}/cm^{-1}): 3300 (N-H and O-H stretch); 2854 (alkyl C-H stretch); 1641 (amide C=O stretch); 1555 (N-H bend); 1443 (alkane); 1225 (C-O stretch); 1060 (C-O stretch); 950 (C-F peak on shoulder of 1060 peak).

Data are shown for the DP-46 polymer, which was conjugated directly to the AuNPs.

General Procedure for Synthesis of Amine-modified (BG- or NTA-amine) pHEA polymer

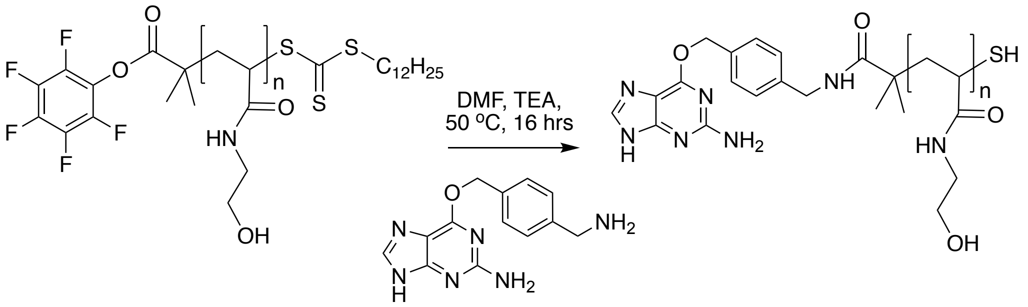

Synthesis of BG-pHEA polymer.

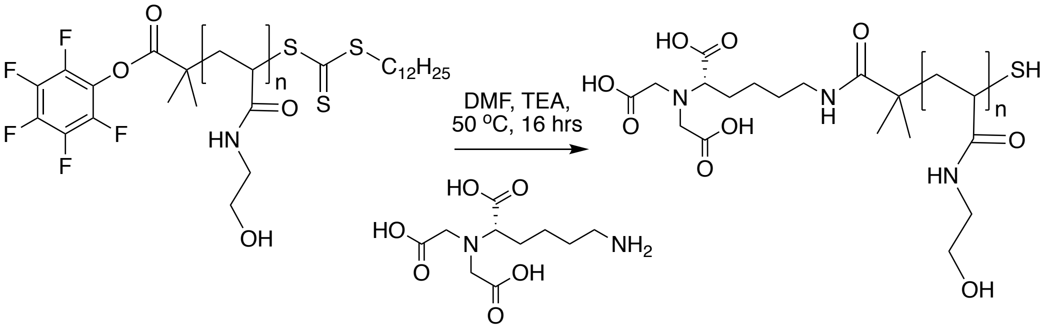

Synthesis of NTA-pHEA polymer.

PFP-pHEA (90.8 mg, 0.018 mmol) and primary amine (6-((4-(aminomethyl)benzyl)oxy)-7H-purin-2-amine (BG) or Nα,Nα-Bis(carboxymethyl)-L-lysine hydrate(NTA)) (0.088 mmol) were dissolved in DMF (5 mL). To the stirred mixture, triethylamine (35 μL) was added, and the reaction was moved to a 50 °C oil bath for 16 hours. The polymer was precipitated three times from methanol into diethyl ether to give a sandy yellow solid.

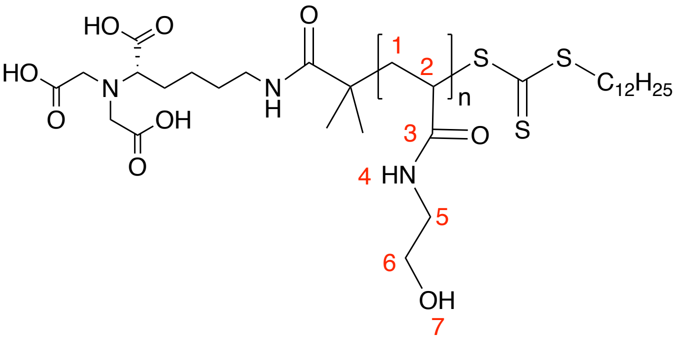

BG-pHEA$_{45}$ polymer

M_n (SEC) 12960 g.mol^{-1}; M_w (SEC) 15977 g.mol^{-1}; M_w/M_n (SEC): 1.2.

^{1}H NMR (300 MHz, D$_4$-MeOH) δ_{ppm}: 4.8-5 (br s, H6), 3.44-3.85 and 3.05-3.22 (2 x br s, H5), 1.94-2.35 and 1.31-1.86 (2 x br s, H1/2).

^{19}F NMR (300 MHz, CDCl3) δ_{ppm}: no peaks visible.

FTIR (solid, ν_{max}/cm^{-1}): 3300 (N-H and O-H stretch); 2854 (alkyl C-H stretch); 1641 (amide C=O stretch); 1555 (N-H bend); 1443 (C-H alkane); 1225 (C-O stretch); 1060 (C-O stretch) (C-F shoulder on 1060 peak is no longer present).

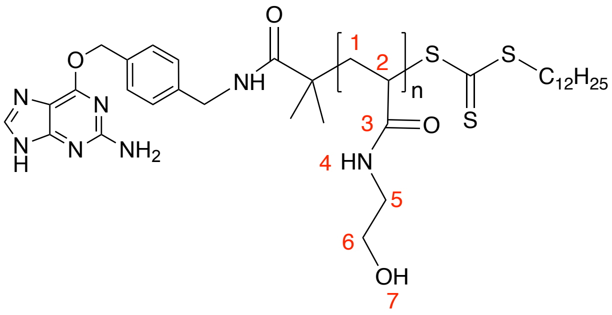

NTA-pHEA$_{17}$ polymer

M_n (SEC) 3040 g.mol^{-1}; M_w (SEC) 3355 g.mol^{-1}; M_w/M_n (SEC): 1.1.

^{1}H NMR (300 MHz, D$_4$-MeOH) δ_{ppm}: 4.8-5 (br s, H6), 3.44-3.85 and 3.05-3.22 (2 x br s, H5), 1.94-2.35 and 1.31-1.86 (2 x br s, H1/2).

^{19}F NMR (300 MHz, CDCl3) δ_{ppm}: no peaks visible.

FTIR (solid, ν_{max}/cm^{-1}): 3300 (N-H and O-H stretch); 2944 (alkyl C-H stretch); 1627 (amide C=O stretch); 1562 (N-H bend); 1390 (C-H alkane); 1060 (C-O stretch) (C-F shoulder on 1060 peak is no longer present).

General Procedure for Synthesis of Polymer-Coated AuNP4 (NTA-pHEA17, PFP-pHEA47 or BG-pHEA45@Au4)

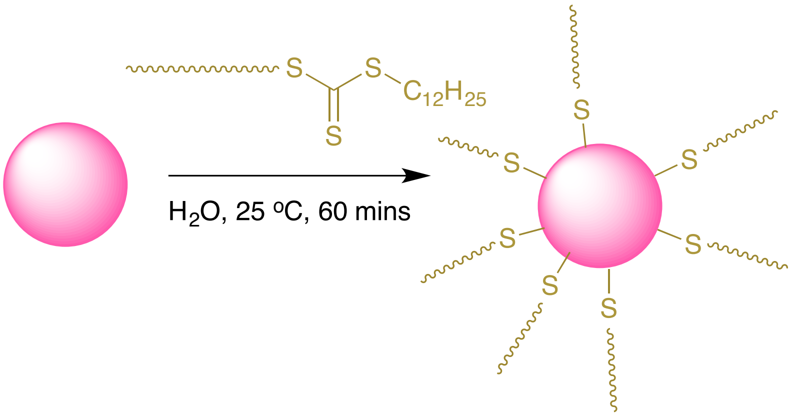

1 mg of polymer (either PFP-pHEA$_{48}$, BG-pHEA$_{45}$ or NTA-pHEA$_{6}$) was added to 1 mL of citrate@Au$_{4}$ in a 1.5 mL Microcentrifuge tube. This was left, agitating, for 60 minutes. The solutions were concentrated by centrifugation in Amicon Ultra-0.5 centrifugal filter units with an Ultracel-30 membrane, before being re-dispersed in the same volume of water. The nanoparticles were washed in this manner a further 3 times before being re-dispersed in the same final volume of distilled water and stored in the fridge until required. Nanoparticle size and dispersity was measured by TEM, UV-Vis spectroscopy and size and zeta potential measurements by DLS.

BG-pHEA$_{45}$@Au$_{4}$: Nanoparticle diameter (UV-vis): 3-4 nm; TEM: 3.87 nm (standard deviation 1.04 nm).

NTA-NTA$_{17}$@Au$_{4}$: Nanoparticle diameter (UV-vis): 3-4 nm; TEM: 3.70 nm (standard deviation 0.74 nm).

PFP-pHEA$_{17}$@Au$_{4}$: Nanoparticle diameter (UV-vis): 3-4 nm; TEM: 4.38 nm (standard deviation 0.68 nm).

3.7.3.1. *Synthesis of Maleimide-pHEA47@Au4*

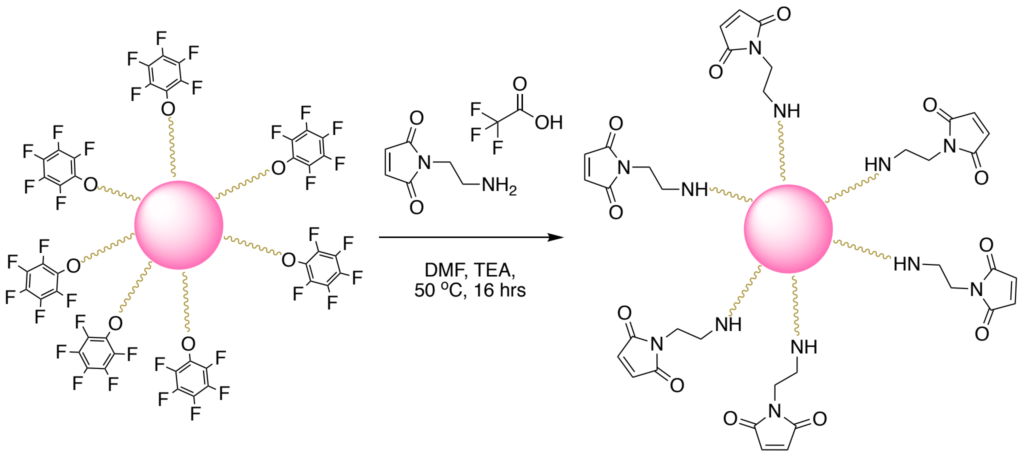

PFP-pHEA$_{47}$@Au$_4$ solution (500 µL) and N-(2-Aminoethyl)maleimide trifluoroacetate salt (0.00088 g, 3.4 µmol) were dissolved in DMF (500 µL) in a 1.5 mL polypropylene microcentrifuge tube and vortexed 30 secs to dissolve. To the stirred mixture, triethylamine (3.5 µL, for 0.5 M solution) was added, and the reaction was moved to a 50 °C oil bath for 16 hours. The solutions were added to 4.5 mL of H_2O before being concentrated by centrifugation in Amicon Ultra-0.5 centrifugal filter units with an Ultracel-30 membrane. The AuNPs were re-dispersed in 500 µL of PBS buffer, pH 7.5. The nanoparticles were washed by concentration and re-dispersion a further 2 times and stored in the fridge until required. Nanoparticle size and dispersity was measured by TEM, UV-Vis spectroscopy and size and zeta potential measurements by DLS.

Nanoparticle diameter (UV-vis): 3-4 nm; TEM: 4.31 nm (standard deviation 0.80 nm).

3.7.3.2. Synthesis of Ni-NTA-pHEA17@Au4

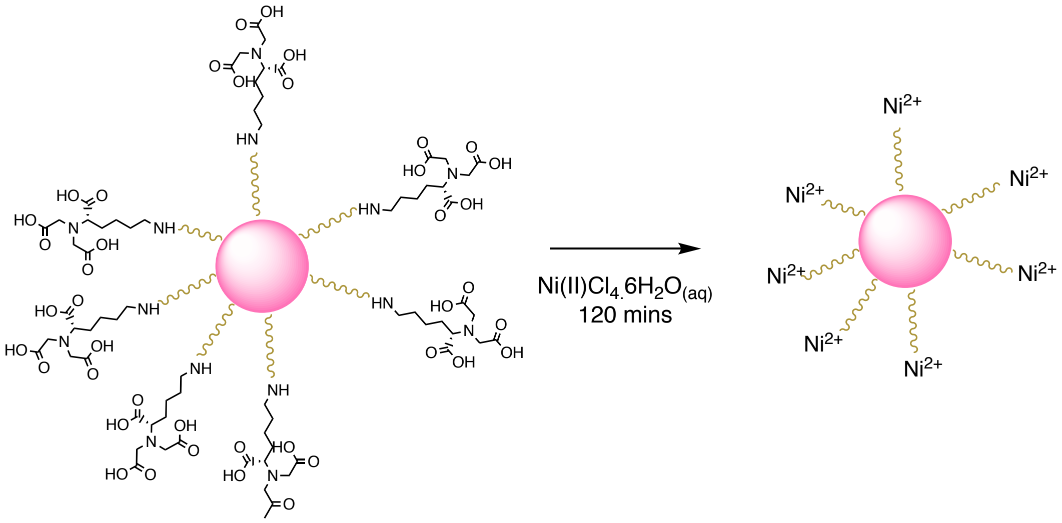

NTA-pHEA$_{17}$@Au$_4$ solution (1 mL) was concentrated by centrifugation in Amicon Ultra-0.5 centrifugal filter units with an Ultracel-30 membrane. To this concentrate was added the same volume Nickel(II) Chloride Hexahydrate (1 mL of 500 µM solution at pH 8 in 10 mM HEPES, 100 mM NaCl buffer). This was left, agitating, for 120 minutes. The solutions were concentrated by centrifugation in Amicon Ultra-0.5 centrifugal filter units with an Ultracel-30 membrane, before being re-dispersed in the same volume of pH 7.5 HEPES/NaCl buffer. The nanoparticles were washed in this manner a further 3 times before being re-dispersed in the same final volume of buffer and stored in the fridge until required. Nanoparticle size and dispersity was measured by TEM, UV-Vis spectroscopy and size and zeta potential measurements by DLS.

Nanoparticle diameter (UV-vis): 3-4 nm; TEM: 3.89 nm (standard deviation 0.75 nm).

3.7.3.3. General Synthesis of protein-conjugated Au4 (SNAP-AFP, His-AFP, Cys-AFP)

Polymer@Au$_4$ solution (500 µL) was concentrated by centrifugation in Amicon Ultra-0.5 centrifugal filter units with an Ultracel-30 membrane. SNAP-tagged AFP was conjugated to the BG-pHEA$_{45}$-AuNP4; Cys-AFP was conjugated to Mal-pHEA$_{47}$-AuNP4; and His-tagged AFP was conjugated to Ni-NTA-pHEA$_{17}$-AuNP4. To this concentrate was added the same volume of protein solution as desired. This was left, agitating, for 120 minutes at room temperature. The solutions were concentrated by centrifugation in Amicon Ultra-0.5 centrifugal filter units with an Ultracel-100 membrane, before being re-dispersed in the same volume of pH 7.5 PBS buffer. The nanoparticles were washed in this manner a further 2 times before being re-dispersed in the same final volume of PBS and stored in the fridge until required. Protein concentration in the washes was determined by measuring absorbance at 280 nm. Nanoparticle size and dispersity was measured by TEM, UV-Vis spectroscopy and size and zeta potential measurements by DLS.

3.7.3.4. Synthesis of S-benzyl O-ethyl carbondithioate.

PERFORMED BY CHRISTOPHER STUBBS. Acetone (40 mL) was added to a round bottom flask equipped with a stirrer bar. Potassium ethyl xanthogenate (2 g, 0.0124 mol, 1 eq.) was added and left to dissolve for 30 minutes. Benzyl bromide (2.13 g, 0.0124 mol, 1eq.) was added and stirred for 24 hours at 50 °C. The solution was filtered and the filtrate concentrated in vacuo. The resulting yellow oil was purified on a column of silica with DCM as eluent. Yield 1.26 g 48 %.

^{1}H NMR (300 MHz, $CDCl_3$): δppm = 1.3 ($CH_3CH_2OC(S)S$, t, 3H), 4.3 ($OC(S)SCH_2$, s, 2H), 4.6 ($CH_3CH_2OC(S)S$, q, 2H), 7.2 ($C(S)SCH_2C_6H_5$, br, 5H).

^{13}C NMR (400 MHz, $CDCl_3$): δppm = 14 (CH_3CH_2), 40 ($C(S)SCH_2$), 70 (CH_3CH_2), 127 (para CH), 128 (meta CH), 129 (ortho CH), 213 (OC(S)S).

3.7.3.5. General procedure for synthesis of poly(vinyl acetate).

PERFORMED BY CHRISTOPHER STUBBS. As a representative example, vinyl acetate (3 g, 3.21 mL, 34 mmol, 1000 eq), S-benzyl O-ethyl carbondithioate (0.074 g, 0.34 mmol, 10 eq.), 4,4'azobis(4-cyanovaleric acid) (0.0098 g, 0.034 mmol, 1 eq.) and mesitylene (0.1 g, 0.086 mL) were added to a 10ml vial and sealed with a subaseal. The solution was left to degas under nitrogen for 15 minutes, before being placed into an oil bath at 68 °C. The reaction was left for 24 hours before being plunged into liquid nitrogen. Poly(vinyl acetate) was recovered as a sticky yellow oil after precipitation into diethyl ether.

^{1}H NMR (400 MHz, $CDCl_3$) δppm = 4.90 – 4.70 ($CH_2CH(OOCH_3)$, br, 1H), 2.07 ($CH_2CH(OOCH_3)$, br, 3H), 1.90-1.60 ($CH_2CH(OOCH_3)$, br, 2H).

FTIR (solid, ν_{max}/cm^{-1}): C-H 2954 cm^{-1}, C=O 1729 cm^{-1}, C-O 1407 cm^{-1}.

Mn (SEC, THF) = 8500 Da, Mw/Mn = 1.4.

Data are shown for poly(vinyl acetate)$_{98}$.

3.7.3.6. General procedure for synthesis of poly(vinyl alcohol).

PERFORMED BY CHRISTOPHER STUBBS. As a representative example, poly(vinyl acetate) (1 g) was dissolved in methanol (5 mL) in a round bottom flask and stirred until dissolved. Hydrazine hydrate solution (15 mL, 78-82 % in water) was added and the reaction heated to 50 °C in an oil bath for 24 hours. The solution was cooled and diluted with water (50ml) before being purified by dialysis (100-500 MWCO) followed by lyophilization to form a white powder. Representative characterization data for poly(vinyl alcohol)98:

^{1}H NMR (400 MHz, D_2O) δ = 4.00 – 3.80 ($CH_2CH(OH)$, br, 1H), 1.80 – 1.30 ($CH_2CH(OH)$, br, 2H).

FTIR (solid, ν_{max}/cm^{-1}) = O-H 3000-3400 cm^{-1}, C-H 2917 cm^{-1}, C-O 1411 cm^{-1}. Data are shown for poly(vinyl alcohol)$_{98}$.

3.7.3.7. Recombinant expression of AFPIII-His

PERFORMED BY DR. MUHAMMAD HASAN. A pET20b-AFPIII plasmid encoding for a hexahistidine-tagged AFPIII from ocean pout (*rQAE isoform*, M1.1HISPET20b) was kindly provided by Peter Davies (Queens University, Kingston, Canada). The plasmid was transformed into competent Escherichia coli BL21(DE3) cells (New England Biolabs). A colony was selected to inoculate 50 mL of LB-medium containing 100 µg/mL ampicillin and was grown overnight at 37 °C under continuous shaking of 180 rpm. The following day, 5 mL of the preculture was added to 500 mL of LB-medium in a 2 L Erlenmeyer flask and grown at 37 °C with a shaking speed of 180 rpm till an OD600 of 0.6 was reached. The temperature was then reduced to 16 °C and IPTG was added to a final concentration of 0.4 mM. The overexpression of the protein was allowed to take place overnight following which the cells were centrifuged at 4000 g for 30 minutes at 4 °C.

Pelleted cells were resuspended in PBS supplemented with Pierce protease inhibitor mini-tablets. The suspension was passed through a STANSTED 'Pressure Cell' FPG12800 homogeniser in order to lyse the cells. The cell lysate was centrifuged at

14,000 g and the supernatant was passed through a 0.45 nm filter and applied to an IMAC Sepharose 6 Fast Flow (GE Healthcare) column charged with Ni(II) ions and pre-equilibrated with PBS. The column was washed with 20 column volumes of 20 mM imidazole in PBS. Bound AFPIII was eluted using 300 mM Imidazole in PBS. The AFPIII was further purified using a HiLoad 16/600 Superdex 75 pg gel filtration column (GE Healthcare) with PBS as the running buffer. Fractions exclusively containing the AFPIII were pooled and concentrated to 5 $mg.mL^{-1}$. Purity was estimated using SDS-PAGE and protein concentration determined using Thermo Scientific Pierce BCA assay kit. This was verified by measuring absorbance at 280 nm and obtaining protein's extinction coefficient [as predicted by ProtParam (http://web.expasy.org/protparam/)] for use in Beer-Lambert law.

3.7.3.8. Recombinant expression of AFPIII-Cys

PERFORMED BY DR. MUHAMMAD HASAN. The terminal Ala in the pET20b-AFPIII plasmid was mutated to Cys by site-directed mutagenesis using the primer sequence 5'-GTTAAAGGTTACGCTTGTCTCGAGCACCAC-3' and employing Phusion® High-Fidelity DNA Polymerase (New England Biolabs) according to the manufacturer;s protocol. The expression and purification was performed as detailed for AFPIII with the exception that 2 mM β-mercaptoethanol was added to all buffers when performing IMAC and gel filtration to prevent the formation of disulfide bonds. The β-mercaptoethanol was removed prior to use by buffer exchanging using PD10 desalting columns (GE Healthcare).

3.7.3.9. Recombinant expression of AFPIII-SNAP

PERFORMED BY DR. MUHAMMAD HASAN. A genetic fragment encoding for AFPIII fused to a hexahistidine tag was amplified from the pET20b-AFPIII plasmid using 5'-GTACGGATCCAACCAGGCTAGCGTTGTG-3' (BamHI site underlined) as the forward primer and 5'-ATTAGCGGCCGCAGCCGGATCTCAGTG-3' (NotI site underlined) as the reverse primer. The BamHI/NotI digested products were ligated into a pSNAP-tag® (T7)-2 vector (New England Biolabs). The plasmid was then transformed into competent Escherichia coli BL21(DE3) cells (New England Biolabs). The subsequent expression and purification was performed as detailed for AFPIII.

3.7.3.10. Ice Recrystallisation Inhibitory activity "SPLAT" assay

PERFORMED BY DR. CAROLINE BIGGS AND CHRISTOPHER STUBBS. The sample was prepared in PBS solution, and a 10 μL was dropped onto a glass microscope coverslip atop an aluminium plate cooled to -78 °C with dry ice. The thin wafer of ice that forms upon contact with the coverslip was transferred to a cryostage held at -8 °C using liquid nitrogen, and left to anneal for 30 minutes at this temperature. Three images were taken at different locations on this wafer at 20 x zoom under cross polarizers. Using ImageJ, the number of crystals in the images were counted and the average crystal size per wafer was calculated as mean grain area (MGA).

3.7.3.11. Modified Sucrose Sandwich Ice Shaping Assay

PERFORMED BY ALICE FAYTER. Samples dissolved in PBS buffer containing 45% sucrose were sandwiched between two glass coverslips and sealed with immersion oil. Samples were cooled to −50 °C on a Linkam Biological Cryostage BCS196 with T95-Linkpad system controller equipped with a LNP95-Liquid nitrogen cooling pump, using liquid nitrogen as the coolant (Linkam Scientific Instruments UK, Surrey, U.K.). The temperature was then increased to −8 °C and held for 1 hour to anneal. The samples were then heated at 0.5 °C.min^{-1} until few ice crystals remained and then cooled at 0.05 °C.min^{-1} and the shape of ice crystals observed. Micrographs were obtained every 0.1 °C using an Olympus CX41 microscope equipped with a UIS-2 20x/0.45/∞/0−2/FN22 lens (Olympus Ltd., Southend on sea, U.K.) and a Canon EOS 500D SLR digital. Image processing was conducted using ImageJ.

3.8. Appendix

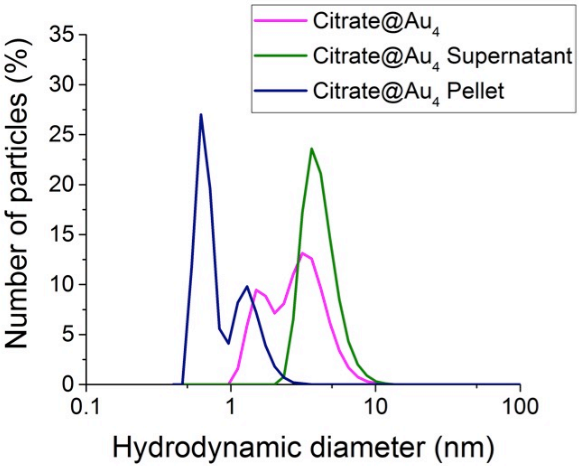

Figure 3-14. Size distribution of AuNPs of 4 nm size before and after purification by centrifugation, from DLS measurements of distribution by number.

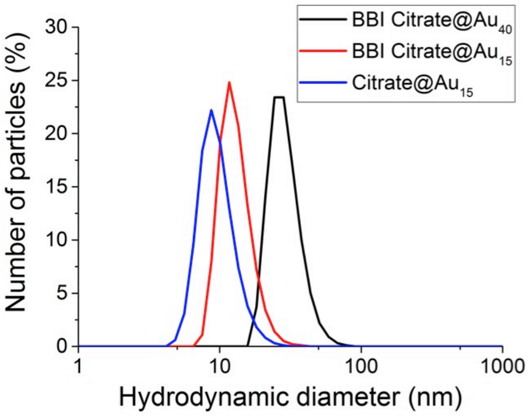

Figure 3-15. Size distributions by number of particles, from DLS measurements of distribution by number. Shows size of commercial samples (from BBI) and the first-synthesized “small” 15 nm AuNPs.

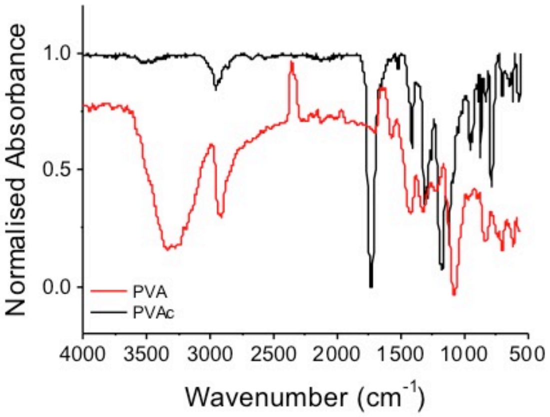

Figure 3-16. Representative FTIR of PVAc converted to PVA.

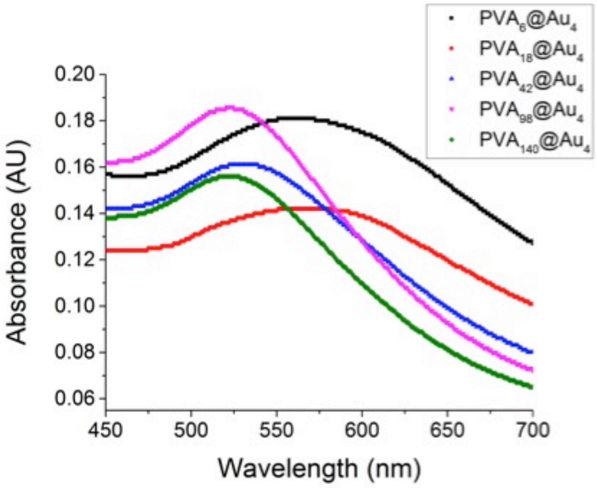

Figure 3-17. UV-Vis spectra showing red shift in PVA@Au$_4$ samples.

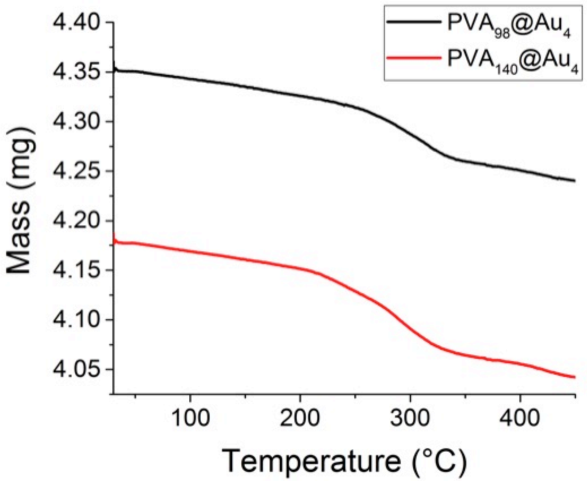

Figure 3-18. Thermogravimetric analysis of PVA@Au$_4$ showing decomposition of samples over increasing temperature. PVA$_{98}$@Au$_4$ contains 0.24 mg.mL^{-1} and PVA$_{140}$@Au$_4$ 0.32 mg.mL^{-1} of PVA.

Table 3-5. PVA@Au_4 elemental composition determined by XPS.

Particle	**C** [a]	**O** [a]	**N** [a]	**S** [b]	**Au** [c]
Citrate@Au_4	46.4	52.8	0.00	0.43	0.33
PVA_{98}@Au_4	65.5	29.0	1.45	0.24	0.04
PVA_{140}@Au_4	65.1	30.3	0.28	0.25	0.04

[a] 1s peak; [b] 2s peak; [c] 4f peak.

Note that not all elements are included in the above table, only those relevant to our analysis.

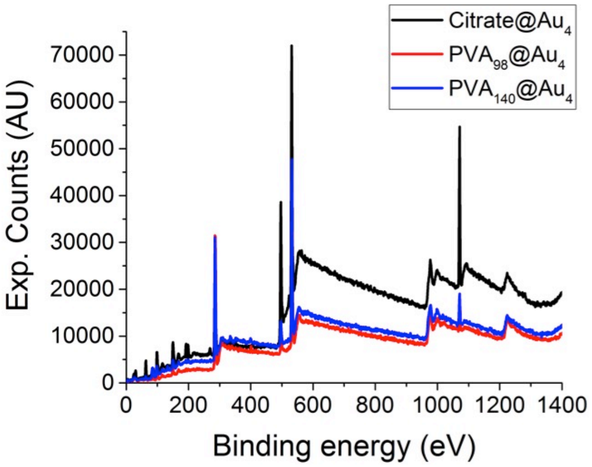

Figure 3-19. XPS survey scan of citrate and PVA@Au_4 samples.

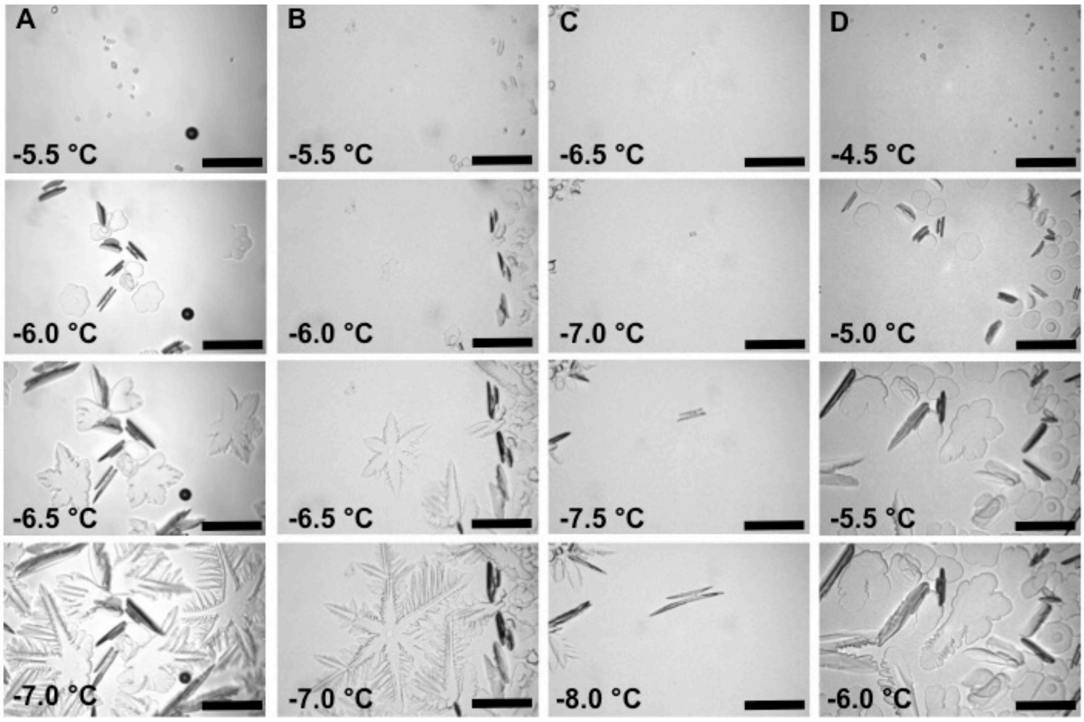

Figure 3-20. Sucrose sandwich assay optical micrographs showing ice formation over decreasing temperature. A) PVA_{98} 0.24 mg.mL^{-1}; B) $PVA_{98}@Au_4$ 0.24 mg.mL^{-1} PVA; C) $PVA_{140}@Au_4$ 0.32 mg.mL^{-1} PVA; D) PVA_{140} 0.32 mg.mL^{-1}. All scale bars 100 μm.

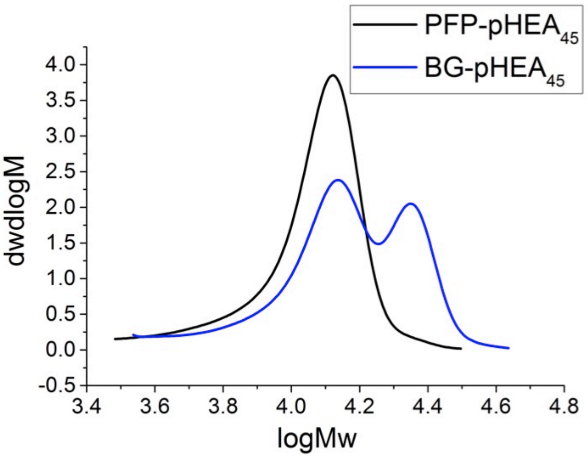

Figure 3-21. Molecular weight distributions, by SEC, of BG-pHEA.

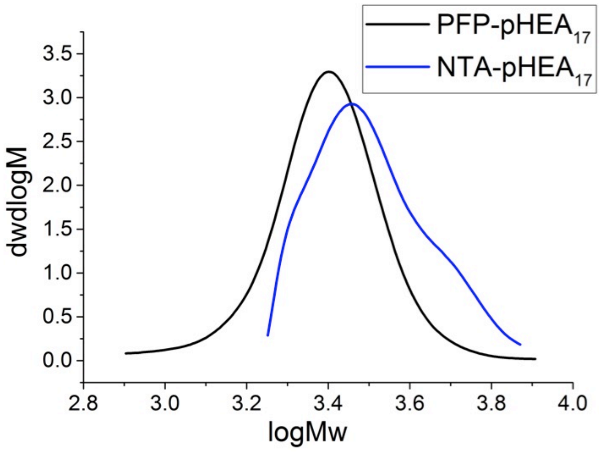

Figure 3-22. Molecular weight distributions, by SEC, of NTA-pHEA derived from PFP-pHEA.

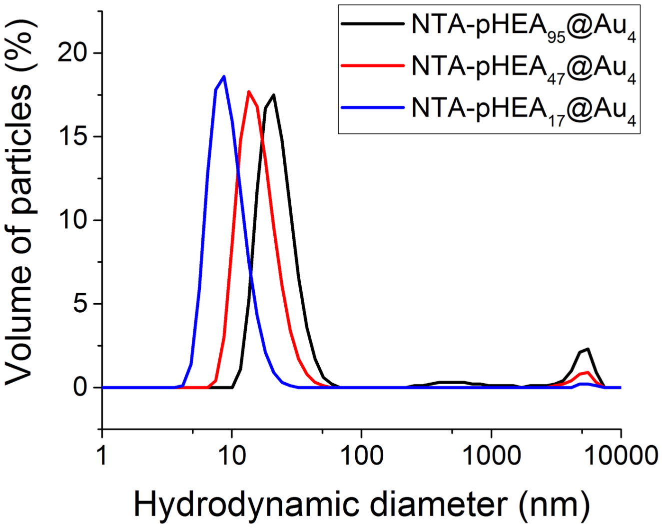

Figure 3-23. Size distributions by volume of particles, from DLS measurements. Shows change in size upon conjugation of different lengths of NTA-pHEA$_n$ polymer. In this case, the number distribution showed no aggregation, but the volume distribution shows more aggregates forming with the longer pHEA chain lengths.

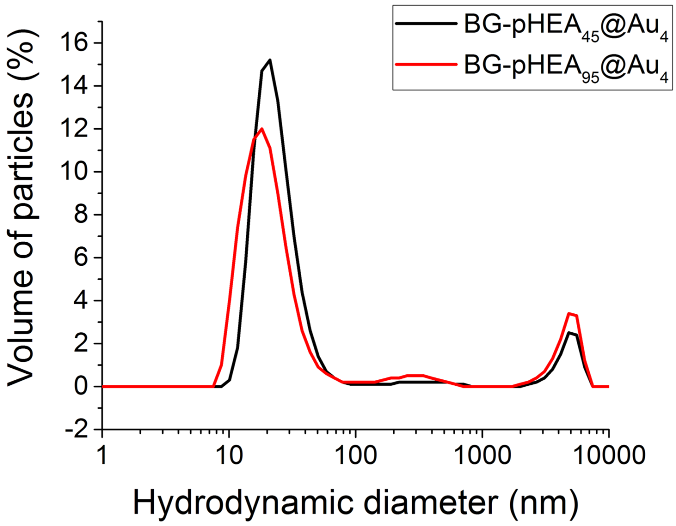

Figure 3-24. Size distributions by volume of particles, from DLS measurements. Shows change in size upon conjugation of different lengths of BG-pHEA$_n$ polymer. In this case, the number distribution showed no aggregation, but the volume distribution shows more large aggregates forming with the longer pHEA chain length. The BG-pHEA$_{17}$@Au$_4$ conjugate was not stable at all, precipitating out during the washing stage.

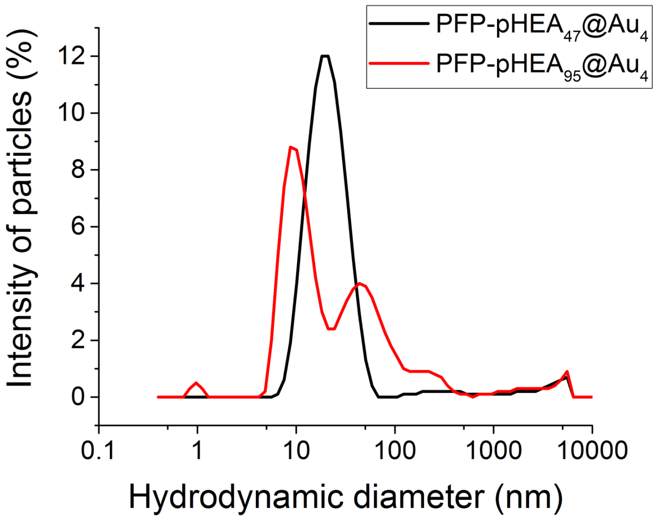

Figure 3-25. Size distributions by volume of particles, from DLS measurements. Shows change in size upon conjugation of different lengths of PFP-pHEA$_n$ polymer. In this case, the number and volume distributions showed no aggregation, but the intensity distribution shows more large aggregates forming with the longer pHEA

chain length. The PFP-pHEA$_{17}$@Au$_4$ conjugate was not stable at all, precipitating out during the washing stage.

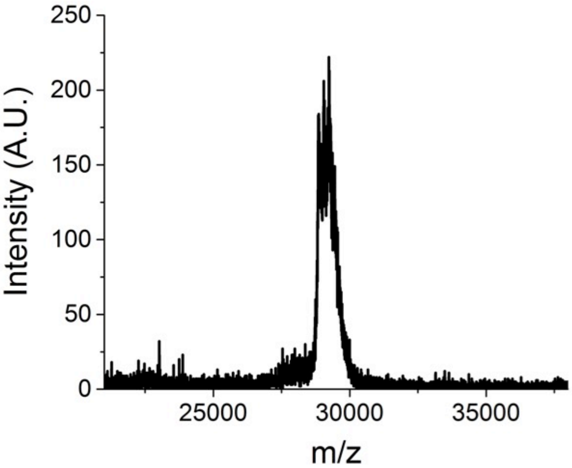

Figure 3-26. MALDI spectrum of SNAP-AFP recombinant protein. Peak at 29100 Da (Mw is 29107 Da)

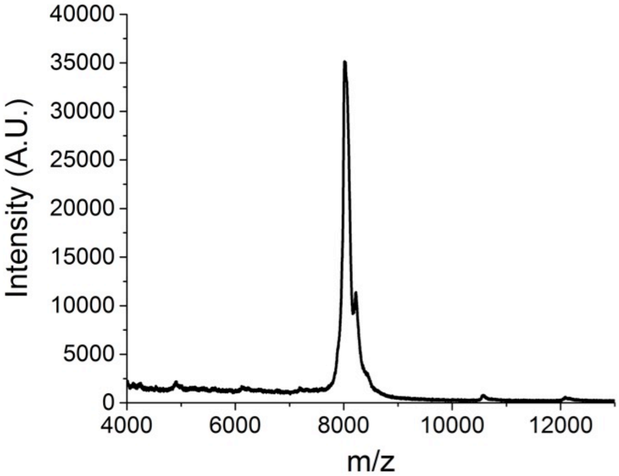

Figure 3-27. MALDI spectrum of His-AFP recombinant protein. Peak at 8010 Da (Mw is 7463 Da).

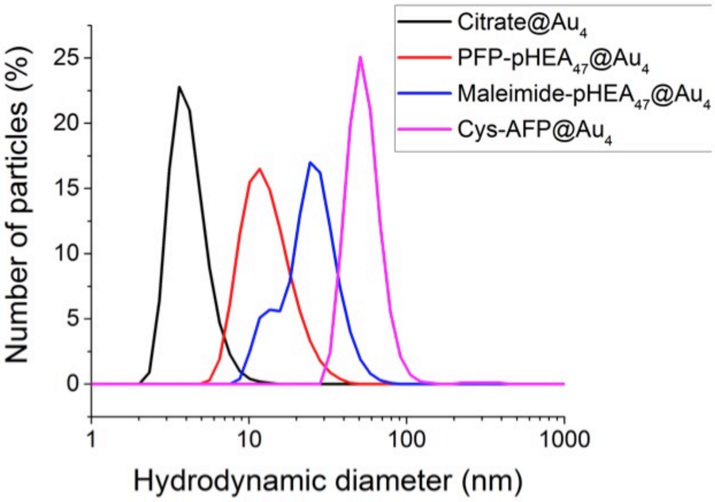

Figure 3-28. Size distributions by number of particles, from DLS measurements. Shows change in size upon successive conjugation leading to Cys-AFP@Au$_4$ conjugate.

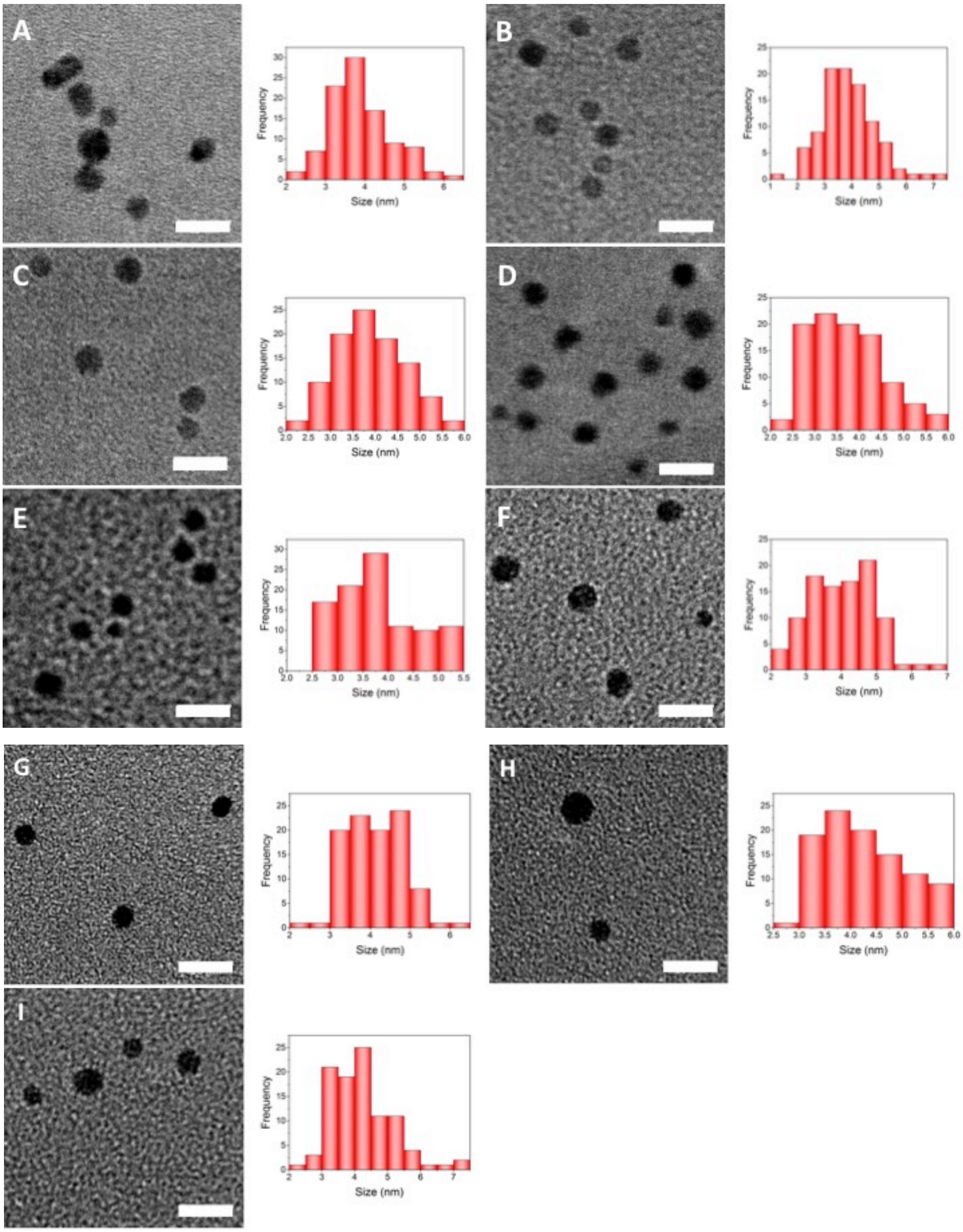

Figure 3-29. TEM micrographs and size distributions (from 100 particles analysed by TEM) or Au_4 samples. A) citrate@Au_4; B) BG-pHEA$_{45}$@Au_4; C) SNAP-AFP-BG-pHEA$_{45}$@Au_4; D) NTA-pHEA$_{17}$@Au_4; E) Ni-NTA-pHEA$_{17}$@Au_4; F) His-AFP-Ni-NTA-pHEA$_{17}$@Au_4; G) PFP-pHEA$_{47}$@Au_4; H) Maleimide-pHEA$_{47}$@Au_4; I) Cys-AFP-Maleimide-pHEA$_{47}$@Au_4. All scale bars 10 nm.

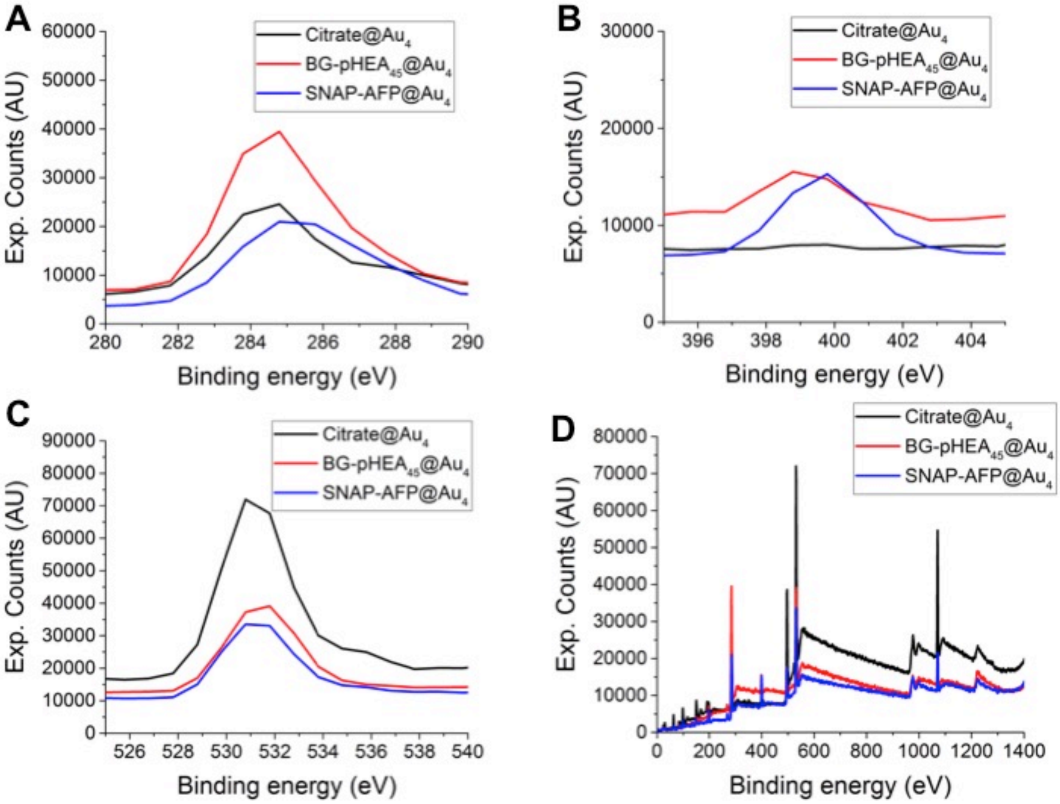

Figure 3-30. XPS survey scan data of SNAP-AFP@Au$_4$ sample and precursor AuNP conjugates. A) C 1s peak; B) N 1s peak; C) O 1s peak; D) full survey scan.

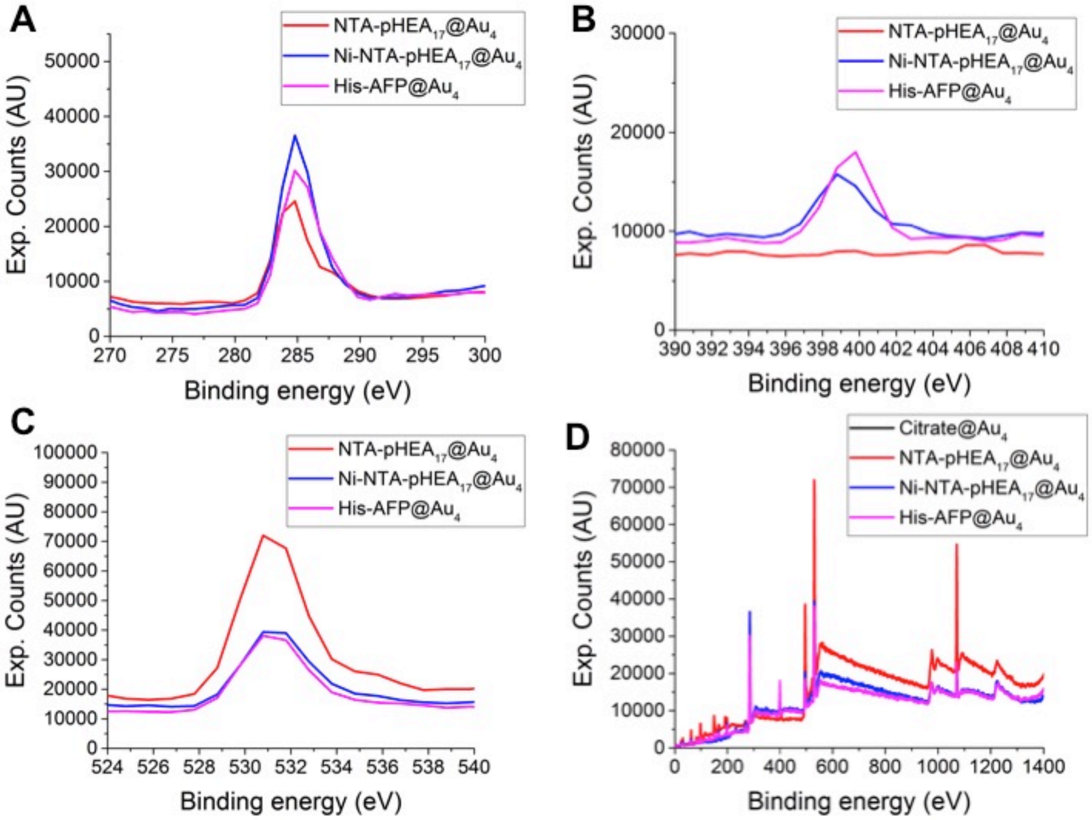

Figure 3-31. XPS survey scan data of His-AFP@Au4 sample and precursor AuNP conjugates. A) C 1s peak; B) N 1s peak; C) O 1s peak; D) full survey scan.

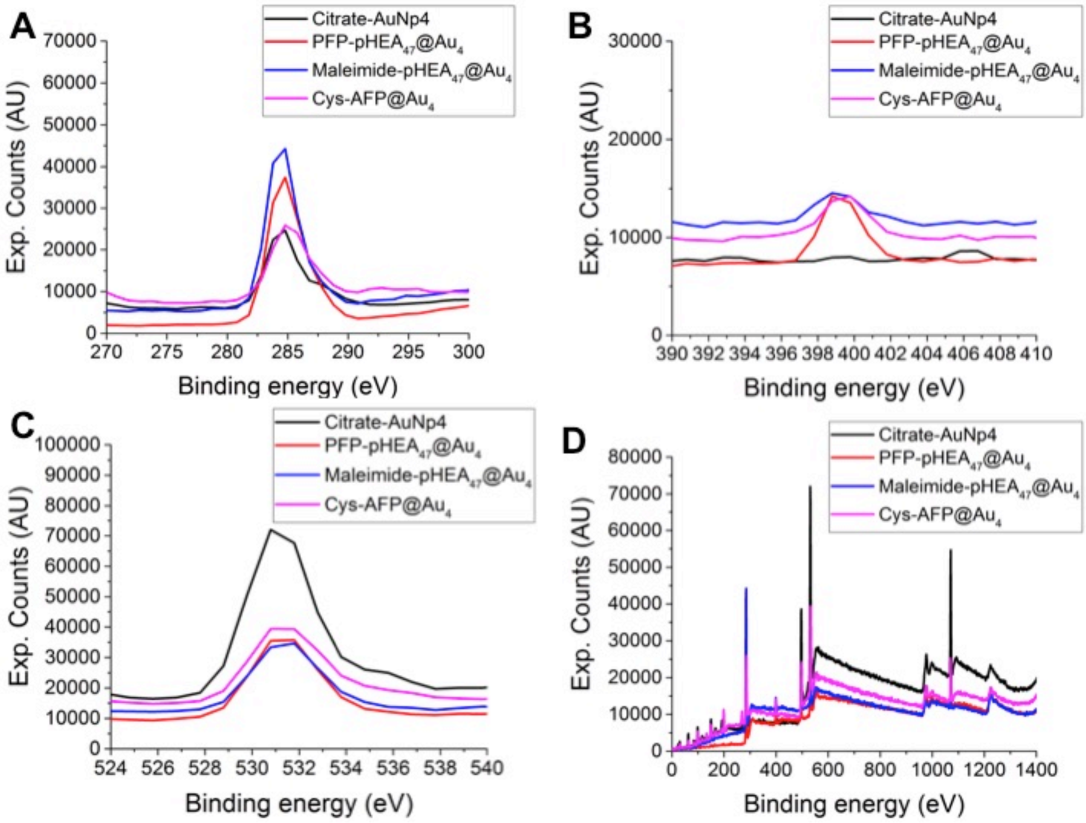

Figure 3-32. XPS survey scan data of Cys-AFP@Au$_4$ sample and precursor AuNP conjugates. A) C 1s peak; B) N 1s peak; C) O 1s peak; D) full survey scan.

Table 3-6. AFP@Au_4 elemental composition determined by XPS.

Particle	C [a]	O [a]	N [a]	F [a]	S [b]	Au [c]	Ni [d]
Citrate@Au_4	46.41	52.82	0.00	-	0.43	0.33	-
NTA-$pHEA_{17}$@Au_4	66.06	23.10	9.21	-	1.51	0.12	-
Ni-NTA-$pHEA_{17}$@Au_4	67.40	19.45	9.62	-	3.30	0.06	0.15
His-AFP-Ni-NTA-$pHEA_{17}$@Au_4	63.93	21.98	12.42	-	1.36	0.19	0.12
BG-$pHEA_{45}$@Au_4	68.40	23.65	7.37	-	0.35	0.23	-
SNAP-AFP-BG-$pHEA_{45}$@Au_4	58.48	24.74	12.27	0.30	0.22	0.17	-
PFP-$pHEA_{47}$@Au_4	72.85	19.80	6.59	0.29	0.42	0.05	-
Maleimide-$pHEA_{47}$@Au_4	73.28	21.05	4.89	0.00	0.48	0.30	-
Cys-AFP-Maleimide-$pHEA_{47}$@Au_4	52.68	32.98	7.17	0.32	0.18	0.33	-

[a] 1s peak; [b] 2s peak; [c] 4f peak; [d] 2p peak.

Note that not all elements are included in the above table, only those relevant to our analysis.

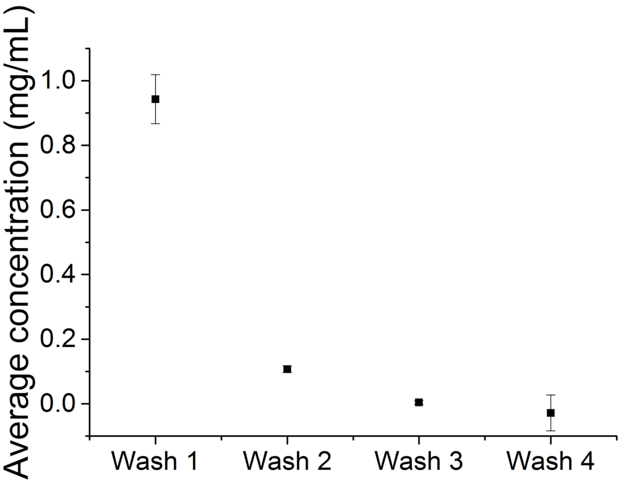

Figure 3-33. Nanodrop measurements of washes after SNAP-AFP conjugation to BG-pHEA$_{45}$@Au$_4$.

Table 3-7. Masses of organic substances present in AFP@Au$_4$ samples determined by TGA.

Particle	Mass present in sample (mg.mL^{-1}) [a]
NTA-pHEA$_{17}$ onAu$_4$	0.048
His-AFP on Au$_4$[b]	2.32
BG-pHEA$_{45}$ on Au$_4$	0.042
SNAP-AFP on Au$_4$[b]	0.64

[a] All calculations were taken as the mass difference between 150 and 600, and all AuNP samples were determined to be the same concentration of gold by UV-Vis spectroscopy; [b] All protein-containing sample calculations were blanked relative to PBS solution, and where then calculated relative to the known organic weight of a protein standard.

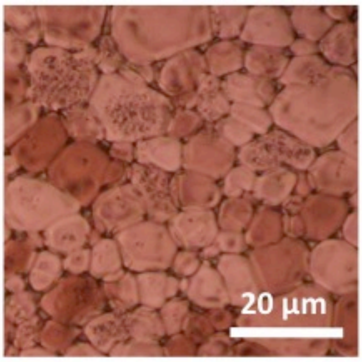

Figure 3-34. “Splat” optical micrograph of PBS control. This was used to give test sample solutions percentage ice grain sizes relative to a control.

3.9. References

(1) Deller, R. C.; Vatish, M.; Mitchell, D. A.; Gibson, M. I. *ACS Biomater. Sci. Eng.* **2015**, *1* (9), 789.

(2) Capicciotti, C. J.; Kurach, J. D. R.; Turner, T. R.; Mancini, R. S.; Acker, J. P.; Ben, R. N. *Sci. Rep.* **2015**, *5*, 1.

(3) Deller, R. C.; Pessin, J. E.; Vatish, M.; Mitchell, D. A.; Gibson, M. I. *Biomater. Sci.* **2016**, *4* (7), 1079.

(4) Voets, I. K. *Soft Matter* **2017**, *13* (28), 4808.

(5) Davies, P. L. *Trends Biochem. Sci.* **2014**, *39* (11), 548.

(6) Gibson, M. I. *Polym. Chem.* **2010**, *1* (8), 1141.

(7) Bar Dovel, M.; Braslavsky, I.; Davies, P. L. *Annu. Rev. Biochem.* **2016**, *85*, 515.

(8) Yeh, Y.; Feeney, R. E. *Chem. Rev.* **1996**, *96* (2), 601.

(9) Graether, S. P.; Sykes, B. D. *Eur. J. Biochem.* **2004**, *271* (16), 3285.

(10) Kim, H. J.; Lee, J. H.; Hur, Y. B.; Lee, C. W.; Park, S. H.; Koo, B. W. *Mar. Drugs* **2017**, *15* (2).

(11) Baardsnes, J.; Kuiper, M. J.; Davies, P. L. *J. Biol. Chem.* **2003**, *278* (40), 38942.

(12) Stevens, C. A.; Drori, R.; Zalis, S.; Braslavsky, I.; Davies, P. L. *Bioconjug. Chem.* **2015**, *26* (9), 1908.

(13) Nishimiya, Y.; Ohgiya, S.; Tsuda, S. *J. Biol. Chem.* **2003**, *278* (34), 32307.

(14) DeLuca, C. I.; Chao, H.; Sönnichsen, F. D.; Sykes, B. D.; Davies, P. L. *Biophys. J.* **1996**, *71* (5), 2346.

(15) Can, Ö.; Holland, N. B. *Biochemistry* **2013**, *52* (48), 8745.

(16) Phippen, S. W.; Stevens, C. A.; Vance, T. D. R.; King, N. P.; Baker, D.; Davies, P. L. *Biochemistry* **2016**, *55* (49), 6811.

(17) Drori, R.; Li, C.; Hu, C.; Raiteri, P.; Rohl, A. L.; Ward, M. D.; Kahr, B. *J. Am. Chem. Soc.* **2016**, *138* (40), 13396.

(18) Garnham, C. P.; Natarajan, A.; Middleton, A. J.; Kuiper, M. J.; Braslavsky, I.; Davies, P. L. *Biochemistry* **2010**, *49* (42), 9063.

(19) Marshall, C. B.; Daley, M. E.; Sykes, B. D.; Davies, P. L. *Biochemistry* **2004**, *43* (37), 11637.

(20) Leinala, E. K.; Davies, P. L.; Doucet, D.; Tyshenko, M. G.; Walker, V. K.; Jia, Z. *J. Biol. Chem.* **2002**, *277* (36), 33349.

(21) Biggs, C. I.; Bailey, T. L.; Ben Graham; Stubbs, C.; Fayter, A.; Gibson, M. I. *Nat. Commun.* **2017**, *8* (1), 1.

(22) Mitchell, D. E.; Cameron, N. R.; Gibson, M. I. *Chem. Commun.* **2015**, *51* (65), 12977.

(23) Mitchell, D. E.; Lilliman, M.; Spain, S. G.; Gibson, M. I. *Biomater. Sci.* **2014**, *2* (12), 1787.

(24) Gibson, M. I.; Barker, C. A.; Spain, S. G.; Albertin, L.; Cameron, N. R. *Biomacromolecules* **2009**, *10* (2), 328.

(25) Naullage, P. M.; Lupi, L.; Molinero, V. *J. Phys. Chem. C* **2017**, *121* (48), 26949.

(26) Vail, N. S.; Stubbs, C.; Biggs, C. I.; Gibson, M. I. *ACS Macro Lett.* **2017**, *6* (9), 1001.

(27) Deller, R. C.; Congdon, T.; Sahid, M. A.; Morgan, M.; Vatish, M.; Mitchell, D. A.; Notman, R.; Gibson, M. I. *Biomater. Sci.* **2013**, *1* (5), 478.

(28) Wang, H. Y.; Inada, T.; Funakoshi, K.; Lu, S. S. *Cryobiology* **2009**, *59* (1), 83.

(29) Phillips, D. J.; Congdon, T. R.; Gibson, M. I. *Polym. Chem.* **2016**, *7* (9), 1701.

(30) Congdon, T. R.; Notman, R.; Gibson, M. I. *Biomacromolecules* **2016**, *17* (9), 3033.

(31) Congdon, T.; Dean, B. T.; Kasperczak-Wright, J.; Biggs, C. I.; Notman, R.; Gibson, M. I. *Biomacromolecules* **2015**, *16* (9), 2820.

(32) Congdon, T.; Notman, R.; Gibson, M. I. *Biomacromolecules* **2013**, *14* (5), 1578.

(33) Deller, R. C.; Vatish, M.; Mitchell, D. A.; Gibson, M. I. *Nat. Commun.* **2014**, *5*, 1.

(34) Congdon, T. R.; Notman, R.; Gibson, M. I. *Eur. Polym. J.* **2017**, *88*, 320.

(35) Ieong, N. S.; Brebis, K.; Daniel, L. E.; Reilly, R. K. O.; Matthew, I. *Chem. Commun.* **2011**, *47* (42), 11627.

(36) Daniel, M. C. M.; Astruc, D. *Chem. Rev.* **2004**, *104*, 293.

(37) Low, A.; Bansal, V. *Biomed. Imaging Interv. J.* **2010**, *6* (1), 3.

(38) Richards, S. J.; Gibson, M. I. *ACS Macro Lett.* **2014**, *3* (10), 1004.

(39) Bonaccorso, F.; Zerbetto, M.; Ferrari, A. C.; Amendola, V. *J. Phys. Chem. C* **2013**, *117* (25), 13217.

(40) Sweeney, S. F.; Woehrle, G. H.; Hutchison, J. E. *J. Am. Chem. Soc.* **2006**, *128* (10), 3190.

(41) Robertson, J. D.; Rizzello, L.; Avila-Olias, M.; Gaitzsch, J.; Contini, C.; MagoÅ, M. S.; Renshaw, S. A.; Battaglia, G. *Sci. Rep.* **2016**, *6*, 1.

(42) Stubbs, C.; Wilkins, L. E.; Fayter, A. E. R.; Walker, M.; Gibson, M. I. *Langmuir* **2018**, acs. langmuir.8b01952.

(43) Haiss, W.; Thanh, N. T. K.; Aveyard, J.; Fernig, D. G. *Anal. Chem.* **2007**, *79* (11), 4215.

(44) Tyshenko, M. G.; Doucet, D.; Davies, P. L.; Walker, V. K. *Nat. Biotechnol.* **1997**, *15* (9), 887.

4. Investigations into the binding activity of the adenovirus tail fibre-like protein of a novel Photorhabdus virulence cassette “nanosyringe” construct

4.1. Chapter summary

The *Photorhabdus* bacteria contain highly conserved gene loci for nanosyringe-like constructs, termed *Photorhabdus* virulence cassettes (PVCs). These PVCs are multi-protein macromolecular structures, used by the bacteria for the delivery of protein toxins into host cells. Several recent clinical infection cases of *Photorhabdus asymbiotica* have resulted in interest in understanding the mechanisms by which these bacteria infect mammalian cells, and whether these PVCs might be a key infection mechanism. Nothing is currently known in terms of molecular targets for PVCs (to the best of our knowledge), although each PVC operon is seen to encode a protein structurally similar to adenovirus host binding proteins, called Pvc13. Each *Photorhabdus* genome can be seen to encode between 5 and 6 different PVC operons, with these Pvc13 binding fibre-like proteins exhibiting the greatest sequence diversity.

Herein we develop a method of attaching these Pvc13 proteins (for example, from the PVC*lumt* operon homologue) to gold nanoparticles (LUMT@AuNP) in order to develop assays to assess binding to the A549 cell line. Unfortunately, ICP-OES following incubation with both the A549 and SW480 human cell lines demonstrated no binding of these LUMT@AuNP constructs. Further experiments were, however, undertaken with recombinant Pvc13 tail fibre proteins, which resulted in a range of glycan or eukaryotic protein candidates being proposed as binding partners.

These data suggest that eukaryotic, and even human, targets for these PVCs do exist, and that further work in this area could be exciting in leading to a nanosyringe-like delivery system to specifically inject a payload into target cells.

4.2. Declarations

The work herein was carried out by the author except in the case of collaborative research, as outlined below.

- Recombinant PVC*lumt*_Pvc13 and PVC*pnf*_Pvc13 tail fibre proteins were prepared by Joseph Healey of the Waterfield group.
- All XPS and data analysis was performed by Dr Marc Walker at the University of Warwick.
- Orbitrap mass spectrometry was performed in the University of Warwick Proteomics RTP by Cleidi Zampronio. Perseus and Scaffold analysis was performed by me.
- All A549 and SW480 cells were prepared in the Gibson cell lab, passaged and cultured by Trisha Bailey, but I undertook all assays.
- CACO2 cells were provided ready for lysis by Blessing Anonye of the Unnikrishnan group, but lysed and used by me.
- Recombinant PVC*unit4*_Pvc13 tail fibre protein was prepared by Dr Alexia Hapeshi of the Waterfield group. THP1 and S2 cells were also provided ready for lysis by Dr Alexia Hapeshi, but lysed and used by me. *Caenorhabditis elegans* were provided by the Waterfield lab, and lysate preparation was performed jointly with Alexia Hapeshi.
- CryoEM reconstructions of PVCs were performed by Franziska Leidreiter at the Max Planck Institute of Molecular Physiology, Dortmund, Germany.

4.3. Introduction

Photorhabdus is a genus of motile, Gram negative, bioluminescent insect pathogenic bacteria belonging to the family *Enterobacteriacae.*[1–11] They exist in an obligate symbiosis with insect pathogenic *Heterorhabditis* nematodes.[1] The genus contains three species insect host restricted *P. luminescens* and *P. temperata* and the dual insect/human pathogens *P. asymbiotica*

Photorhabdus luminescens' symbiotic nematode partner is *Heterhorhabditis bacteriophora*. The highly-motile bacteria colonise the intestine of an infective juvenile (IJ) nematode.[1,12] New IJs hatch from eggs retained inside the maternal nematode's body cavities, causing an effect known as *endotokia matricida*, a phenomenon that is apparently vital to the symbiotic re-association and transmission of the bacteria.[13] These new IJ worms disperse from the previous insect cadaver and hunt down and invade other soil-dwelling insect larvae, entering via natural openings or directly through the cuticle. Once in the hemocoel (the insect's open blood system), the nematode regurgitates the bacteria. *P. luminescens* are able to overcome the insect immune system and divide unrestricted, producing a variety of toxic compounds such as exozymes to kill the insect host by lethal septicaemia. After host insect death, the nematode begins to replicate as a hermaphrodite, eating the *Photorhabdus* bacteria. Both the bacteria and nematode are able to undergo several rounds of replication within the cadaver before again emerging into the soil as an IJ carrying *Photorhabdus*, looking for the next host insect. In the case of *P. asymbiotica*, nematodes are believed to burrow into human skin and release the bacteria, causing a serious human infection. The natural life cycle of these mammalian pathogenic strains also includes insect hosts and it is not known if there is a natural (non-human) mammalian reservoir host for these in nature.

Only 10-100 bacterial cells are sufficient to overcome the insect's immune system, and the IJs actually show little specificity in infection, suggesting that the bacteria are well-adapted to be highly pathogenic in a wide variety of (at least) insect immune systems.[1,6,7,10]

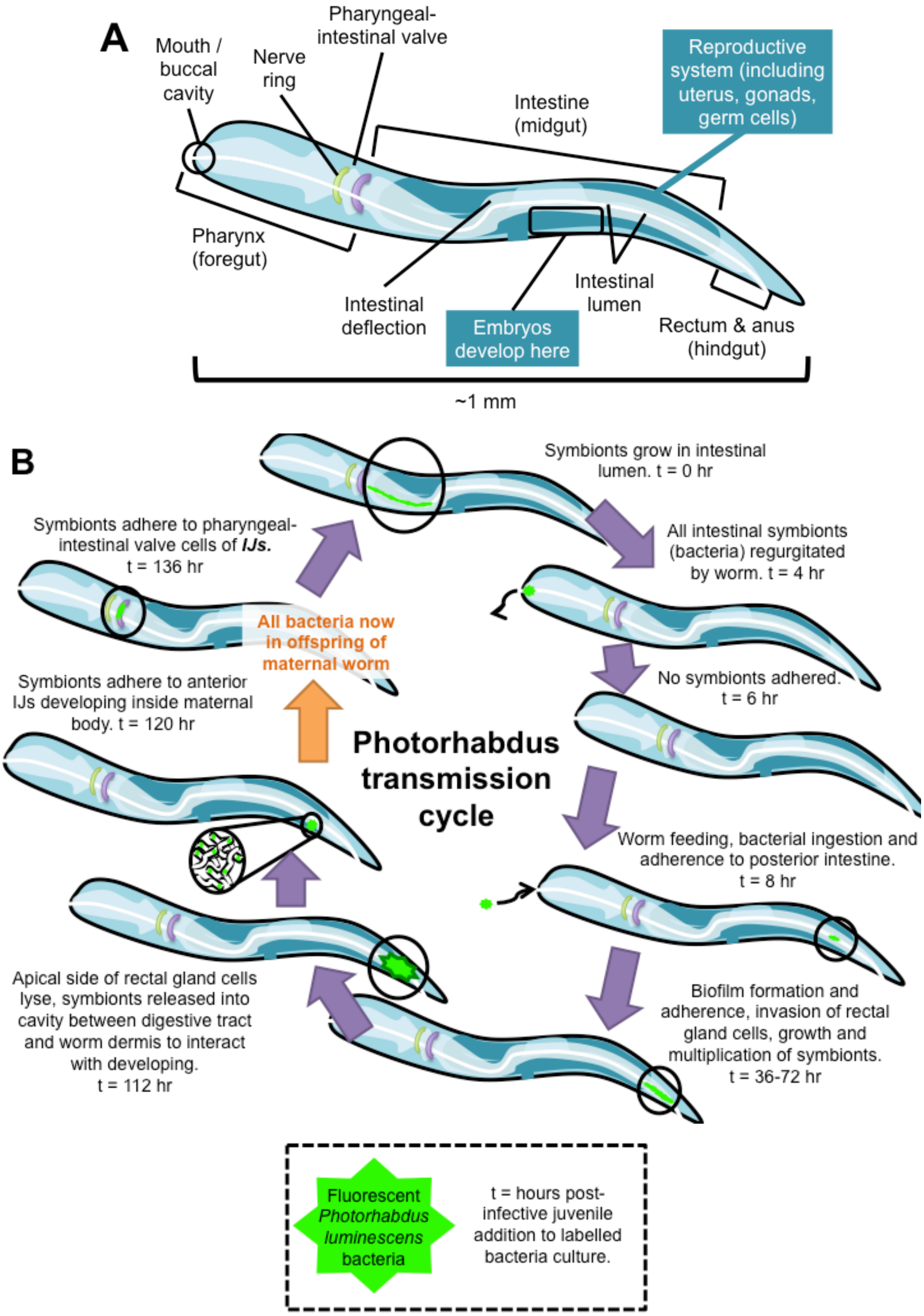

Figure 4-1. Transmission cycle of *P. luminescens* in symbiosis with *Heterhorhabditis bacteriophora* nematode. A) Worm anatomy. B) Cartoon of transmission cycle. Adapted from Waterfield et al.[1]

P. luminescens contains four major groups of toxins: toxin complexes, *Photorhabdus* insect-related proteins, "make caterpillars floppy" toxins and *Photorhabdus* virulence cassettes (PVCs).[1,9,14,15] The genetic loci that encode PVCs consist of 16 conserved structural genes, several of which are similar to bacteriophage tail and base plate assembly proteins, similar in many respects, generically and visually under the electron microscope, to regions of operons encoding anti-bacterial "R-type pyocins".[1,9,11,14,16] Importantly, each unique PVC operon encodes specific protein toxins similar to type III secretion system delivered effectors at there 3' end, the so called "payload region" of the operon. The current hypothesis is that these PVCs act as secreted molecular syringe constructs that inject their toxic payloads directly into a host cell, in a presumed similar fashion to *Serratia entomophila*'s antifeeding prophage (these "Afp" constructs show similarity to PVCs in 16 of their 18 gene clusters).[1,17–19]

Despite some superficial similarity to R-type pyocins, which are produced by several other Gram-negative bacteria to give them a competitive advantage over related strains, the PVC needle complexes show no antibacterial activity.[1] However certain PVCs have been shown to be highly toxic to insects, causing rapid killing of the immune cells, macrophage equivalents known as hemocytes.[1,9,20] Although these constructs are bacteriocin-like, they have somehow modified to exclusively attack eukaryotes. There are also multiple PVCs present in all *Photorhabdus* species' genomes, suggesting their acquisition by horizontal gene transfer.[1] The bacteria are readily culturable away from their nematode symbiont hosts.

Yang *et al.*[11] demonstrated the injectable insecticidal activity of recombinant *E. coli* expressing various PVC operons using *Photorhabdus* cosmids and the larvae of the wax moth (*Galleria mellonella*). Bleeding the larvae also demonstrated that hemocytes were destroyed within 30 mins of injection, which suggests that successful pathogenicity occurs through compromising the host's immune cells. Heat treatment prior to injection eliminated toxicity, and the *P. asymbiotica* PVCs also showed the greatest insecticidal activity.

Investigations have shown PVCs effector payload toxins transiently expressed inside tissue culture cells rearranged the actin cytoskeleton, targeting actin condensation in particular.[1,11,14] What is not understood, however, is whether hemocytes are their primary target, or if they are less specific. The delivery mechanism of their toxic payload, and whether this is truly syringe-like, is also unknown.

Invertebrates constitute both more extant species and individual “infectable” animals than the better-studied mammalian diseases, and have been exposed to pathogens for a longer period of evolutionary time. As invertebrates also serve as hosts of vectors for many vertebrates pathogens (for example, flea vectors for bubonic plague), it makes sense that pathogens commonly target invertebrates.[5] As PVCs are regurgitated directly into the insect blood system, they are evidently well adapted to the dealing with the immediate phagocytic challenge of the innate immune system. Phagocytosis uses free radicals and killer proteases to degrade foreign agents and is a crucial response in both insect and mammalian innate immune systems.[1]

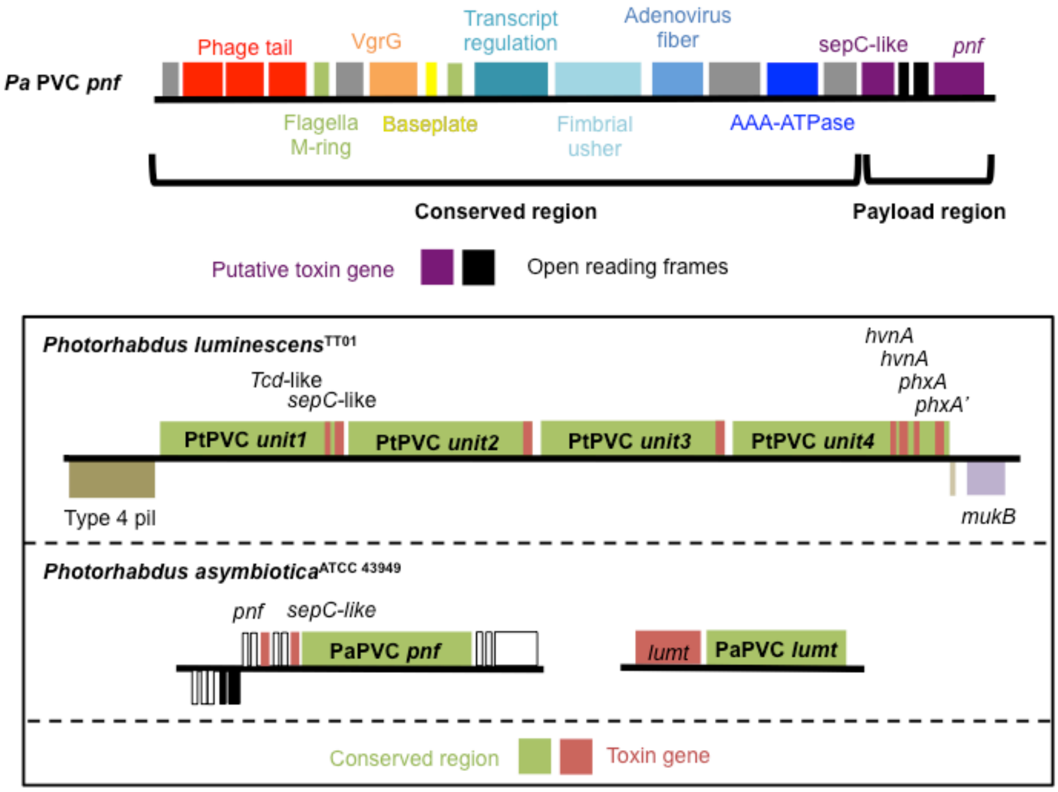

Figure 4-2. PVC products in *Photorhabdus luminescens* and *asymbiotica*. **Not to scale**. Adapted from Waterfield et al.[1]

As previously mentioned, there are three species of *Photorhabdus*, each with their own variety of PVC products. *P. luminescens* has been studied and used for agricultural purposes as a biological pest control agent, but *P. asymbiotica* is of interest due to its survival at 37°C, and its capacity to infect mammals.[1,8]

P. asymbiotica also exists in symbiosis with a nematode, and has been isolated from human infections in North America and Australia.[1,8,12,20–26] The bacteria has the capacity to infect otherwise healthy humans as a primary pathogen rather than opportunistically, with incidence likely higher than reported due to the bacteria not being present on standard clinical bacteriology databases.[1,27] Clinical cases of infection are correlated only with outdoor activity, with limb infection related to contact with soil, with the symbiont nematode (*Heterorhabditis gerradii*) presumably serving as an inoculation vector.[1] The bacteria locally invade soft tissue to form a painful necrotic ulcer, but often, remote soft tissue infections are observed, suggesting bacteremic spread (bacteria present in the blood, which is abnormal). This is evidenced through bacteria being isolated from blood and even sputum as well as pus.

Macrophage cultures infected with *P. asymbiotica* showed replication inside both murine and human immune cells, and both *P. asymbiotica* and *P. luminescens* have shown resistance to human serum, which suggests that these bacteria could survive the blood stream through compromising the host immune system.[1,28] In contrast to *P. luminescens*, *P. asymbiotica* seems to be able to invade cells as an intracellular infection.[28] It seems reasonable to hypothesise that that invaded macrophages act as vehicles for dissemination of bacterial cells in humans.

PVC products may be important in the adaptation of *Photorhabdus* to different insect species and even human infection, with all species showing a variety of them in their genomes (see Figure 4-2).[1,29] Due to their capacity to invade hemocytes, it could be that these PVCs have a central role in invasion of the host immune system, which is key in infecting a variety of species.[11] Of particular interest are the "tail fibres" near the baseplate-like region of the PVC construct, which are hypothesized to attach directly to the target cell, as these may have a role in specificity (see Figure 4-3).[18]

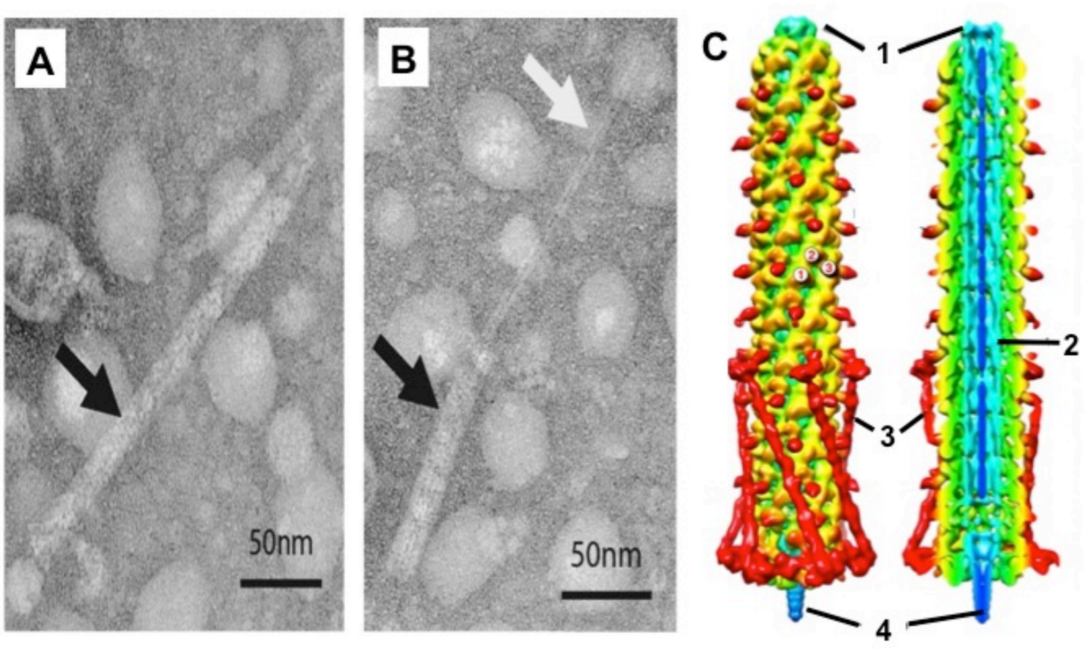

Figure 4-3. Structure of PVC and AFP needle complexes. A) Transmission electron micrograph of relaxed PNF PVC product, showing outer sheath. B) Micrograph of contracted PNF PVC product with outer sheath (black arrow) and inner “needle” (white arrow). A-B taken from Yang et al.[11] C) Reconstructed structure of AFP from *Serratia entomophila*, taken from Heymann et al.[18]: 1. Cap; 2. Tube containing toxic payload; 3. Phage baseplate-like fibres; 4. Needle. The similarity of this structure to PVCs is is supported by reconstructions of PVC structure by CryoEM as seen in the appendix, Figure 4-17.

4.4. Chapter aims

PVC*lumt*_Pvc13 is a protein produced by the *Photorhabdus asymbiotica* bacterium suspected to be involved in pathogenesis, but its mammalian binding target is entirely unknown. To this end, the aims of this chapter are as follows:

- To synthesis and characterise AuNP conjugates of recombinant PVC*lumt*_Pvc13 (a PVC operon known to be expressed in simulated human infection environment) followed by assays in human cell lines to determine binding activity.
- To assess glycan, lipid and protein binding of the recombinant PVC*lumt*_Pvc13 tail fibre protein through glycan microarrays, lipid arrays and pull-down assays with whole cell lysates.
- To assess protein binding of the alternative recombinant Pvc13 tail fibre proteins, encoded by PVC*pnf_pvc13* and PVCunit4*_pvc13* operon genes via pull-down assays with whole cell lysates.

4.5. Results and Discussion

4.5.1. Synthesis of PVC*lumt*_Pvc13 protein conjugated to AuNPs

Previous studies have indicated that *Photorhabdus asymbiotica* is pathogenic in humans.[3,21,28,30–32] The gene sequences and synteny of PVC operons are generally well-conserved. We hypothesised that the adenovirus fibre like Pvc13 proteins represent the needle complex subunits responsible for host cell binding. To test this we immobilised heterologously expressed (in E. coli) *P. asymbiotica* Pvc13 proteins from the PVC*lumt* operon onto an AuNP scaffold, in order to use these to help us understand a possible role for PVCs in the *Photorhabdus asymbiotica* infection mechanism. Briefly, recombinant His-tagged PVC*lumt*_Pvc13 tail fibre protein (simply referred to as "LUMT" below) was conjugated to AuNPs *via* a sterically stabilising polymer linker, in order to allow the AuNP scaffold to serve as a marker for Pvc13 protein adhesion to cells and function.

Pentafluorophenol-terminated (at the α-terminus) poly(hydroxyethyl acrylamide)s (PFP-pHEAs) were synthesized by controlled RAFT polymerisation to act as steric stabilisers when conjugated to AuNP, especially upon exposure to the buffer solution required in the use of proteins. pHEA of DP ~50 was also synthesized without a PFP-containing chain transfer agent. Three different chain lengths of PFP-pHEA were synthesized (approximately 25, 50 and 100 DP). Conversion and theoretical molecular weight was determined by ^{1}H-NMR vinyl peak reduction relative to a mesitylene standard peak (see Table 4-1). ^{19}F-NMR, SEC and FTIR were used to further confirm the structure, molecular weight and dispersity of all the polymers.

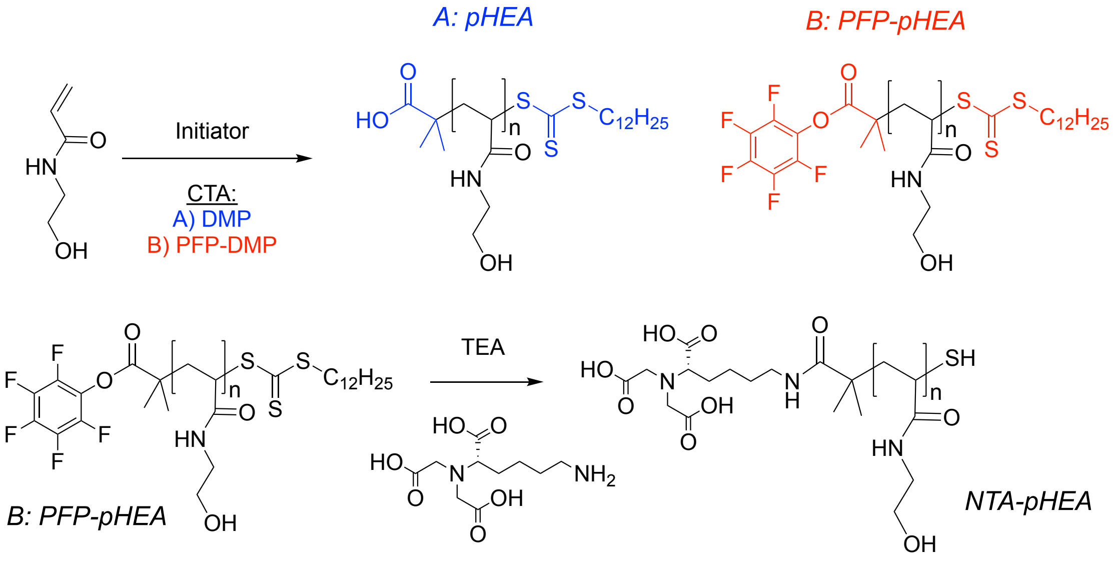

Scheme 4.1. Synthesis of NTA-pHEA polymers and control pHEA.

Table 4-1. pHEA Polymers synthesized.

Polymer	**[M]/[CTA]**[a]	**Conversion (%)**[b]	**DP$_n$**	**M$_{n(THEO)}$ (g.mol^{-1})**[b]	**M$_{n\ (SEC)}$ (g.mol^{-1})**[c]	**Đ**[c]
pHEA$_{46}$	56	82	46	5,600	8,500	1.2
PFP-pHEA$_{17}$	26	64	17	2,500	3,000	1.1
PFP-pHEA$_{45}$ [d]	47	94	45	5,700	8,300	1.1
PFP-pHEA$_{95}$	103	93	95	11,000	15,000	1.3

[a] Monomer to RAFT agent molar ratio; [b] Determined by depletion of vinyl peaks in ^{1}H NMR using mesitylene as an internal standard; [c] Determined by SEC; [d] Used in His-LUMT-Ni-NTA-pHEA$_{45}$@Au$_{40}$ conjugates.

The PFP α-terminal group was functionalised by substitution with excess Nα,Nα-Bis(carboxymethyl)-L-lysine hydrate (NTA) in DMF overnight, with triethylamine as a base. This amine terminal was selected to allow subsequent capture of His-tagged protein. PFP elimination was confirmed by the loss of three PFP peaks by ^{19}F-NMR (between -150 and -170 ppm) and C-F peaks by FTIR (~1750 cm^{-1}), as shown in

Figure 4-4. Excess primary amine also liberates a ω-terminal thiol, conveniently for AuNP conjugation.

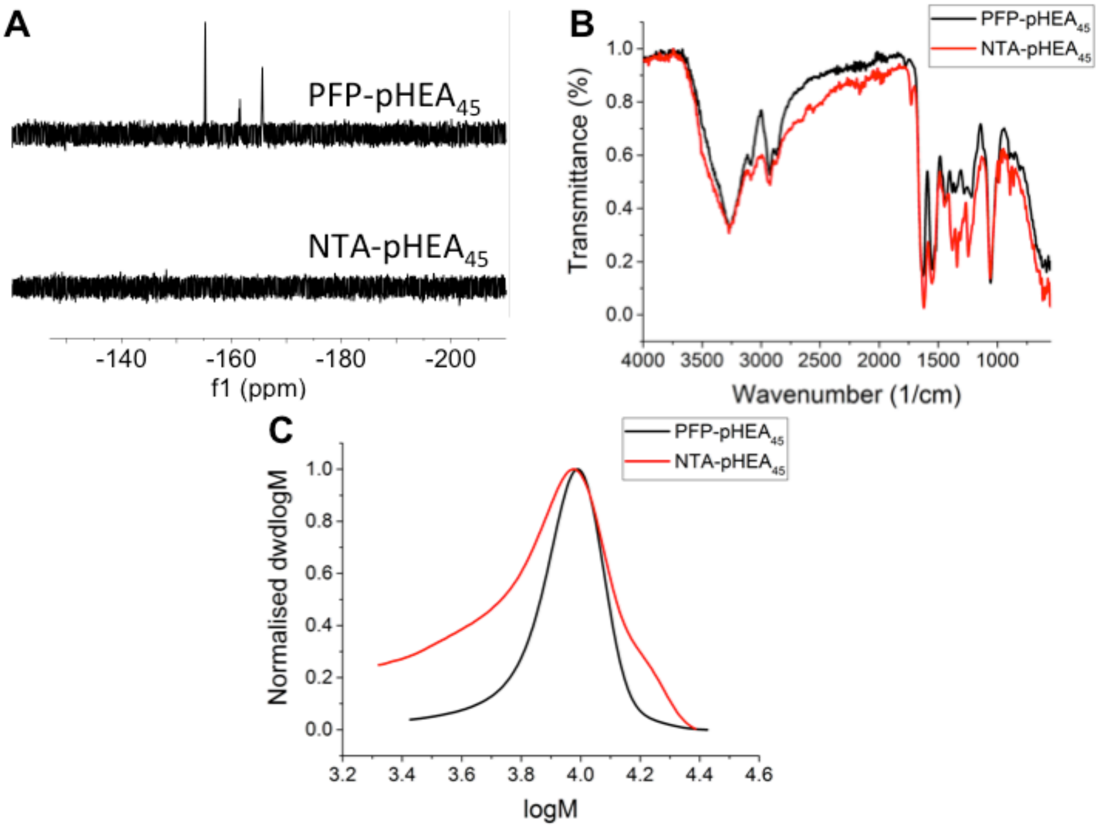

Figure 4-4. Characterisation of pHEA polymers, and the removal of the PFP group. A) ^{19}F-NMR spectra showing depletion of PFP peaks (~1750 cm^{-1}). B) FTIR spectra showing depletion of C-F peaks and thus PFP removal. C) Molecular weight distributions, by SEC, of PFP- and NTA-pHEA polymers used. A shoulder is visible in the NTA-pHEA trace, possibly due to transamination reactions.

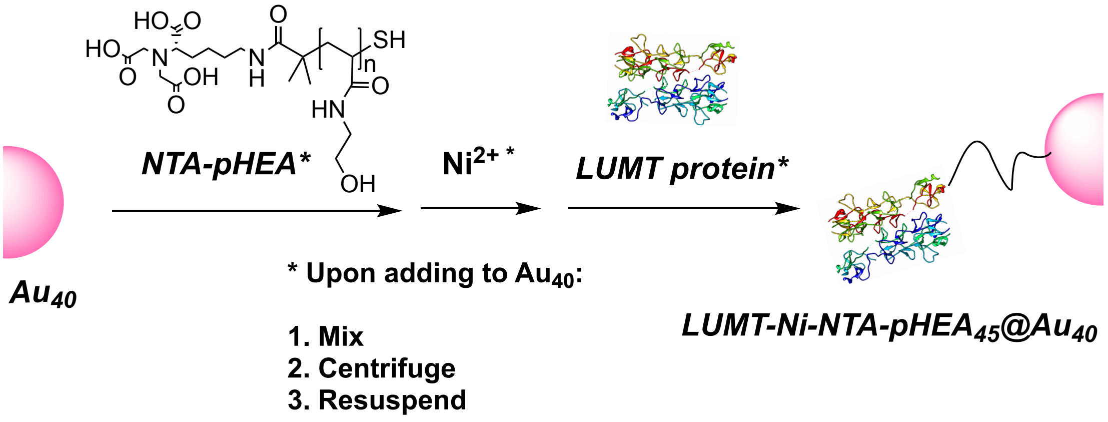

Scheme 4.2. Synthesis of LUMT-Ni-NTA-pHEA$_{45}$@Au$_{40}$.

The pHEA polymers were dissolved in 40 nm citrate stabilised gold nanoparticles, citrate@Au_{40} (purchased from BBI solutions), and incubated on a roller at room temperature for an hour, then washed 4 times to remove excess free polymer from solution. The three PFP-$pHEA_n$@Au_{40} solutions were initially assessed by DLS to observe any instability (evidenced as large aggregate formation), and the NTA-$pHEA_{45}$@Au_{40} was selected as being the most stable, with other chain lengths leading to aggregation.

This sample was functionalised with $NiCl_2$ in HEPES buffer, washed, and again shown to be stable by DLS. Finally, the Ni-NTA-$pHEA_{45}$@Au_{40} solution was incubated with His-tagged protein, in order to capture the protein via the surface Ni^{2+} atoms, and washed to remove excess free protein in solution. The use of Ni-NTA groups immobilised on NP surfaces have been used extensively in His-tag protein capture, and is routine for protein purification.[33] *N*-terminal His-tagged recombinant protein of the LUMT PVC tail fibre segment, from *Photorhabdus asymbiotica*, was expressed from *E. coli* by Joseph Healey at the University of Warwick and purified by immobilised metal affinity chromatography (IMAC). To optimise protein conjugation, a dilution series was used to determine which applied protein concentrations were stable, and 5 $\mu g.mL^{-1}$ was determined to be the highest concentration at which these conjugates were stable: the addition of higher protein concentration resulted in AuNP precipitation.

DLS, UV-Vis and TEM measurements were used to assess the stability, shape and size of all AuNP samples. The hydrodynamic diameter of the protein conjugates increased with each successive conjugation step without the presence of higher diameter aggregates (indicative of instability), showing a ~20 nm increase in diameter from the citrate to protein conjugates, and a ~10 nm increase in diameter from the citrate to $pHEA_{46}$@Au_{40} conjugates. Indeed, >8000 $g.mol^{-1}$ polymers, and proteins, on an Au_{40} surface would be expected to cause an increase in size in solution relative to citrate ions.

Table 4-2. AFP@Au_4 nanoparticle characterization

Particle	D_h (DLS) (nm)[a]	D_{TEM} (nm)[b]	ζ potential (mV)[c]	SPR_{max} (nm)[d]
Citrate@Au_4	42.7 ± 21.7	38.3 ± 3.7	-37.8 ± 0.2 [e]	525
$pHEA_{46}$@Au_{40}	53.6 ± 27.5	41.5 ± 4.7	1.3 ± 7.27 [f]	528
NTA-$pHEA_{45}$@Au_{40}	56.5 ± 32.4	37.1 ± 4.1	-4.8 ± 20.1 [f]	529
Ni-NTA-$pHEA_{45}$@Au_{40}	57.3 ±30.1	36.4 ± 3.4	-3.9 ± 16.5 [g]	528
LUMT-Ni-NTA-$pHEA_{45}$@Au_{40}	63.3 ± 28.5	30.3 ± 3.8	-6.2 ± 19.4 [g]	520

[a] Hydrodynamic diameter determined by DLS distribution by intensity of particles, averaged over 3 measurements; [b] Gold core diameter, average of 100 particles by TEM; [c] Averaged over 3 measurements; [d] From UV-Vis measurements; [e] commercial AuNP solution, pH 4.88; [f] pH 7.6; [g] AuNPs suspended in HEPES buffer, pH 7.9.

Electrons on the surface of AuNPs oscillate collectively at a specific wavelength of visible light, and this is termed surface plasmon resonance (SPR), and this SPR alters with changes in AuNP size, shape, surface functionality and aggregation. By UV-Vis spectroscopy, a change in the peak of maximum SPR absorbance may be measured, as an indication of a change in surface functionality or AuNP aggregation. An increase in the SPR_{max} by 3 nm was observed between the citrate@Au_{40} precursors and the $pHEA_{46}$ and Ni-NTA-$pHEA_{45}$@Au_{40} conjugates, but no change >10 nm were observed, suggesting that no aggregation occurred with the conjugations. TEM was used to determine the size and shape of the AuNP core. These measurements showed no change in shape, and no significant changes in size: all changes between successive conjugation steps were <10 nm, with errors of ~4 nm suggesting these changes were not significant.

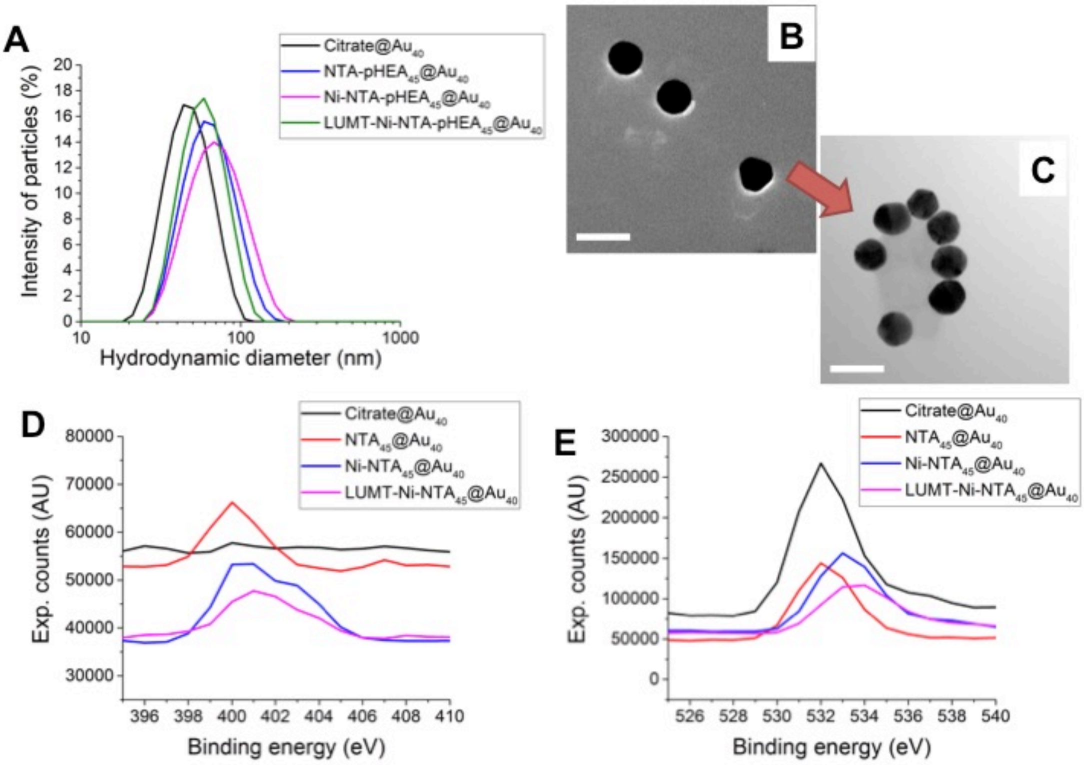

Figure 4-5. Characterisation of LUMT@Au$_{40}$ samples. A) Size distributions by intensity of particles, from DLS measurements. B-C) TEM micrographs of citrate@Au$_{4}$ and LUMT-Ni-NTA-pHEA$_{45}$@Au$_{40}$ respectively. D-E) N 1s and O 1s peaks respectively from XPS spectra showing change upon conjugation of AFP protein.

XPS and zeta potential measurements demonstrated conjugation of the citrate@Au$_{40}$ precursors with polymer and protein. XPS allows determination of the elemental composition of the AuNPs, and showed a relative decrease in the Au 4f peak upon polymer coating, from 0.96 % to 0.51 % and 0.31 % for the pHEA$_{46}$ and NTA-pHEA$_{45}$ conjugates respectively. A relative increase in the Ni 2p peak from NTA-pHEA$_{45}$@Au$_{40}$ after Nickel (II) conjugation (from 0 to 0.82 %), followed by a decrease upon LUMT PVC tail fibre conjugation (back to 0 %), evidenced the presence of Ni on the AuNP surface, and its obscuring by protein conjugation. In particular the organic character of the samples (the percentage of C, O and N 1s character) changed with each conjugation step. For example, the N 1s content increased upon pHEA$_{46}$ and NTA-pHEA$_{45}$ conjugation by ~1 and 4 % respectively, and the C 1s content increase by 7 % upon LUMT protein conjugation to Ni-NTA-

$pHEA_{45}@Au_{40}$. These changes support the success of the conjugation of polymer and protein to the AuNPs.

Zeta potential is a measure of AuNP surface charge, resulting from changes in surface composition. The conjugation of polymers reduced the negativity relative to the $citrate@Au_{40}$ precursor, from -38 mV to 1 mV and -5 mV for the $pHEA_{46}$ and NTA-$pHEA_{45}$ conjugates respectively. This is indicative of the displacement of negatively charged citrate ions on the AuNP surface. The protein conjugates (LUMT-Ni-NTA-$pHEA_{45}@Au_{40}$) did not show a large change in zeta potential relative to the NTA-$pHEA_{45}@Au_{40}$ conjugates, as this change was less than 2 mV and the values showed large standard deviation errors (19 mV for the LUMT conjugate).

TGA was used to determine the mass of the polymer and protein conjugated to the AuNPs. The mass of NTA-$pHEA_{45}$ was determined to be ~0.2 mg and the mass of $pHEA_{46}$ ~0.4 mg in 1 mL of solution. The TGA data also suggests that *all* applied LUMT PVC tail fibre protein is captured by the Ni-NTA-$pHEA_{45}@Au_{4}$ conjugates, with 5 μg present per mL of solution, which could be the reason for the instability of the AuNPs when more protein was applied. As the LUMT PVC tail fibre does not pellet at the centrifuge speed used in the washing steps, there is expected to be no free protein present in the LUMT-Ni-NTA-$pHEA_{45}@Au_{40}$ solution.

4.5.2. Cytotoxicity assays with LUMT/AuNP conjugations

Incubations with typical human epithelial cells, using A549 lung adenocarcinoma cells, serves as a test of whether or not the protein/AuNP conjugates interact with mammalian cells. Stability experiments were first performed to ensure that the final $LUMT@Au_{40}$ conjugates were stable in cell medium (necessary for subsequent experiments). In these experiments, the Au_{40} samples were transferred to cell media and incubated at 37 °C over a weekend. DLS measurements after incubation showed no change in size or dispersity of conjugates in media instead of buffer (showing a mean diameter of 66.6 and 61.6 nm before and after incubation respectively), though slight changes are expected due to the change in suspension medium.

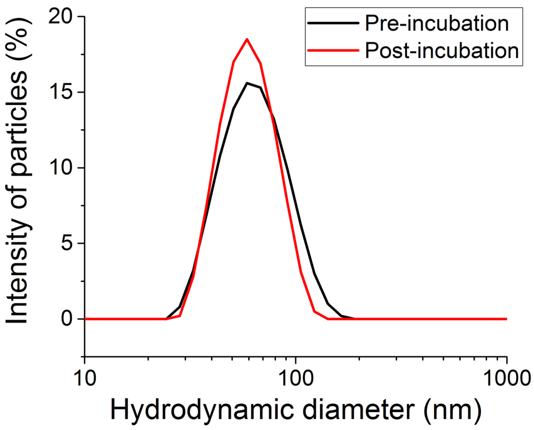

Figure 4-6. DLS measurements for stability tests. LUMT-Ni-NTA-pHEA$_{45}$@Au$_{40}$ pre- and post-incubation for 48 hrs at 37 °C.

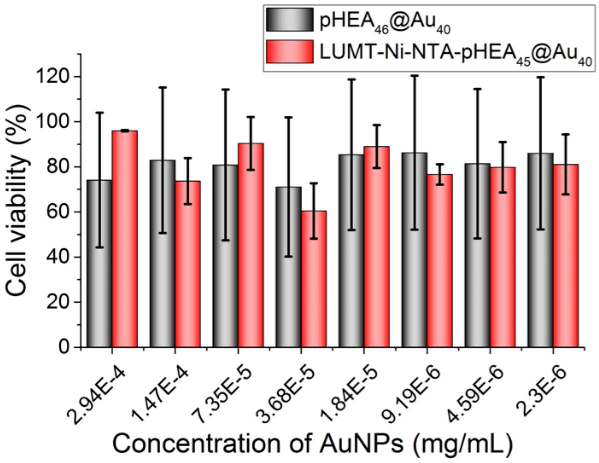

Figure 4-7. MTT assay data showing cell viability. Experiments performed in triplicate, with 24 hrs of culture.

The MTT assay determines the metabolic activity of a cell population by assessing the cells' capacity to metabolise the MTT (3-(4,5-dimethylthiazol-2-yl)-2,5-diphenyltetrazolium bromide) dye to an insoluble formazan, to enable viability to be probed. The transformation of the yellow MTT to purple formazan is indicative of the viability of the cells after incubation with an analyte. A549 cells were incubated in a Microplate for 2 hours to allow adhesion, before 24-hour incubation with a serial dilution of LUMT-Ni-NTA-pHEA$_{45}$@Au$_{40}$ or pHEA$_{46}$@Au$_{40}$ control solution (to determine non-specific polymer/AuNP activity). Cells were then washed, incubated with MTT for 3 hours, and solution was added to solubilise any insoluble formazan that had formed. The transformation of MTT to formazan was determined by UV-Vis absorbance readings, and % viability determined relative to control wells of cells incubated in cell medium alone. The LUMT-Ni-NTA-pHEA$_{45}$@Au$_{40}$ conjugates caused a loss of 10 to 30 % cell viability, with no obvious concentration dependence. The pHEA$_{46}$@Au$_{40}$ control conjugates showed just slightly lower viability, with 70-85 % cell viability in all dilutions, but with greater deviations between replicates. The assay suggested there might be no significant difference in cell viability between the LUMT conjugates and pHEA$_{46}$@Au$_{40}$ control solutions (see Table 4-11 in appendix for statistical test showing no significant difference).

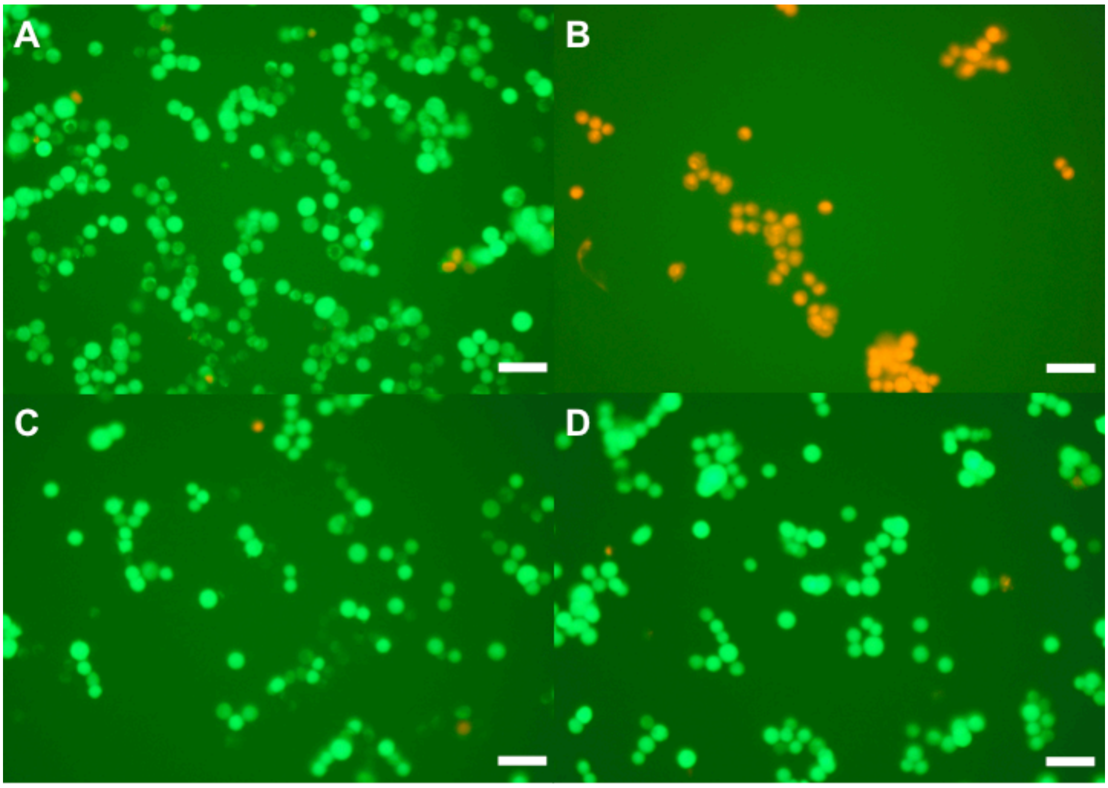

Figure 4-8. Live/dead cell survival assay microscopy images showing (A) live control in PBS, (B) dead control in methanol, (C) LUMT-Ni-NTA-pHEA$_{45}$@Au$_{40}$ and (D) pHEA$_{46}$@Au$_{40}$ at 0.3 ng/mL AuNP concentration respectively. All scale bars 100 µm. Experiments performed with 24 hrs of culture.

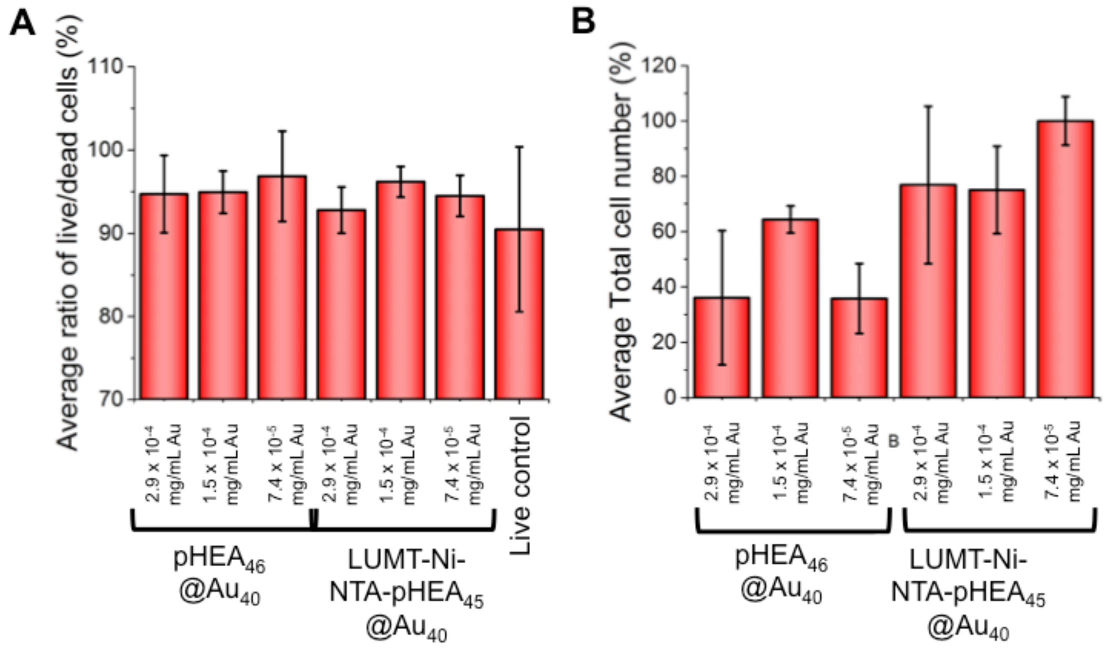

Figure 4-9. Live/dead cell survival assay data. A) Ratio of live cells in samples. B) Total number of cells as a percentage of cells present in the live control. Experiments performed in triplicate, with 24 hrs of culture.

However, the MTT assay measures only the metabolic activity of a cell population, and not if the cells are alive or dead. Therefore the live/dead membrane integrity assay was also used, in which calcein AM and ethidium homodimer-1 (EthD-1) were applied to cells incubated with an analyte solution. Calcein AM is transported through the membranes of live cells, thereby staining them fluorescent green. EthD-1 is not membrane permeable, but it is able to move through the compromised cell membranes of dead cells and bind to their DNA, staining them red. In this assay, cells were prepared as above, before the MTT assay, then incubated with calcein AM and EthD-1 for 30 minutes, then washed. The ratio of green-stained to red-stained cells indicates the ratio of live to dead cells, and this can be compared to live (incubated in cell media) and dead (incubated in ethanol) cell controls.

Although this live/dead assay was performed qualitatively rather than quantitatively, counting the cells in the images produced allowed crude quantitation of the ratio of live cells in each sample (the number of live cells divided by the total number of cells). Both the images and this data showed no significant change in the ratio of live cells in each sample, with the live control and all test samples all having over 90 % live cells (see Table 4-11 in appendix for statistical test showing no significant difference between the samples). There was a visible difference, however, with the number of cells in each image (see Figure 4-8, C in particular). The data bore out this change in total number of cells, with the pHEA/AuNP conjugates showing less than 40 % of the cell numbers visible in the live control, though the LUMT/AuNP conjugates showed over 80 % at even the undiluted concentration (~0.3 ng/mL Au concentration). This change in total cell numbers of the pHEA conjugates could signify that the adherence of the A549 cells to the microplate is affected by the presence of the nanoparticles, suggesting that the live cell ratios may be overly high due to the loss of an unknown quantity of non-adhering dead cells. That there is less change in both the live cell ratio and total cell number with the LUMT/AuNP conjugates is promising, however, as it suggests that these effects may potentially be due to the structure of the AuNP construct rather than the surface protein.

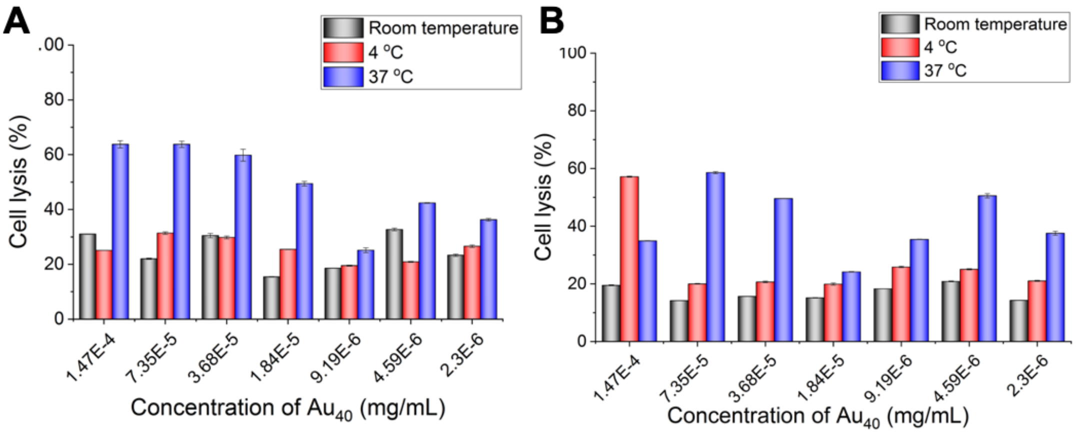

Figure 4-10. Cell lysis from hemolysis assay of ovine erythrocytes. A-B) Assay with LUMT-Ni-NTA-pHEA$_{45}$@Au$_{40}$ and pHEA$_{46}$@Au$_{40}$ respectively. Experiments performed in triplicate, with 24 hrs of culture.

As previous studies have shown PVCs to bind to insect hemocytes, it is possible that these constructs may interact specifically with circulating cells.[1,9,11,14] Hemolysis assays, with ovine erythrocytes, were therefore undertaken to determine if these specific Pvc13 subunit proteins could themselves be haemolytic. Ovine erythrocytes were washed and incubated with AuNP solutions for 16 hours at 4 °C, 25 °C and 37 °C. The intensity of hemoglobin present in the cells' supernatant was used to assess hemolysis as % cell recovery relative to incubation with a PBS control. This assay showed LUMT-Ni-NTA-pHEA$_{45}$@Au$_{40}$ to be lytic, causing approximately 65 % hemolysis at 37 °C, which reduced to ~30 % at 64X dilution. Incubations at room temperature and 4 °C were only ~30 % haemolytic, reducing by 5 % with 64X dilution. The $pHEA_{46}@Au_{40}$ control conjugates, to test non-specific polymer/AuNP binding, showed slightly less hemolysis than the protein/AuNP conjugates at 37 °C and room temperature, with around 80 % for all room temperature incubations. Conversely, the $pHEA_{45}@Au_{40}$ conjugates showed more hemolysis at 4 °C, with 40 % recovery rising to ~80 % recovery upon 64X dilution. These data suggests that both the protein and polymer/AuNP conjugates are haemolytic, and there are no significant differences between the samples (see Table 4-11 in appendix for statistics). That there is a decrease in lysis between the protein and polymer conjugates at room temperature and 37 °C suggests that part of this hemolysis may be specifically caused due to the presence of protein on the AuNP surface.

From these assays we can therefore conclude that there is no significant change in cell viability or the ratio of live cells (by the MTT and live/dead assays) between the pHEA/AuNP control and protein/AuNP samples when looking at human epithelial cells. Hemolysis assays, however, showed an increase in hemolysis with the protein conjugates over the $pHEA_{46}@Au_{4}$ controls, which suggests that, as suspected, the LUMT protein may indeed have more activity with circulating cells (previous studies showing interaction with eukaryotic hemocytes) than internal endothelial cells, which indicates a possible route to pathogenicity.

4.5.3. ICP-OES investigations into A549 and SW480 cell interactions with LUMT/AuNP conjugates

Following the synthesis of protein@AuNP conjugates, cytotoxicity and haemolysis assays, inductively-coupled plasma optical emission spectroscopy (ICP-OES) was used to determine AuNP attachment to cells over a 24 hour incubation period. As previously documented clinical cases of *Photorhabdus asymbiotica* are linked only by outdoor activity, it stands to reason that pathogenic targets might be present in those cells either on the body surface, or present upon the inhalation or ingestion of pathogens present in soil (ie. either the lungs or gastrointestinal cells, though this is unlikely).[1] In these experiments, therefore A549 cells were used here as a model lung epithelial cell, to provide a full cell study data set in combination with previous cytotoxicity studies (see section 4.5.2). SW480 colorectal cells were also being cultured in the laboratory, so these were used here as a model gastrointestinal epithelial cell for these studies. Alternatively many surface proteins will be common to most cell types so it was considered reasonable to test these as representatives of typical human cells.

In ICP-OES, samples are excited using inductively coupled plasma to produce excited atoms that emit electromagnetic radiation. The spectrum emitted is characteristic of the elements present (such as an Au peak at 268 nm), and the intensity at an element's characteristic wavelength is a measure of its quantity in the analyte. In this experiment the intensity of the Au elemental peak relative to a calibration curve was used to determine the amount of AuNPs attached to the cells, and is particularly appealing as no additional labels, such a fluorophores, are required.

A549 cells were incubated in a microplate for 2 hours to allow adhesion, before 24-hour incubation with a serial dilution of LUMT-Ni-NTA-$pHEA_{45}@Au_{40}$ or $pHEA_{46}@Au_{40}$ control solution. Cells were washed and removed from their well by trypsin digestion. These solutions were then digested by aqua regia to atomise AuNPs present before being diluted and analysed by ICP-OES. Incubation with increasing concentrations of $pHEA_{45}@Au_{40}$ showed an increase in gold concentration, suggesting non-specific adhesion. This was not observed, however, in the LUMT conjugates, where it appeared that negligible quantities of AuNPs were attaching to the A549 cells.

A key consideration should be the quantity of AuNP present per cell in these experiments, but unfortunately this was not possible here. The live/dead experiments suggested a lower cell count in those experiments with LUMT@AuNP incubations. This could mean that, rather than free AuNPs (not cell-bound) being lost, the washing step of this procedure could have removed unattached cells with *or* without AuNPs bound. Cell counting during the washing steps after incubation would have made it possible to calculate the number of AuNPs present per cell, which would be a better metric for ascertaining whether these constructs bind to mammalian cells.

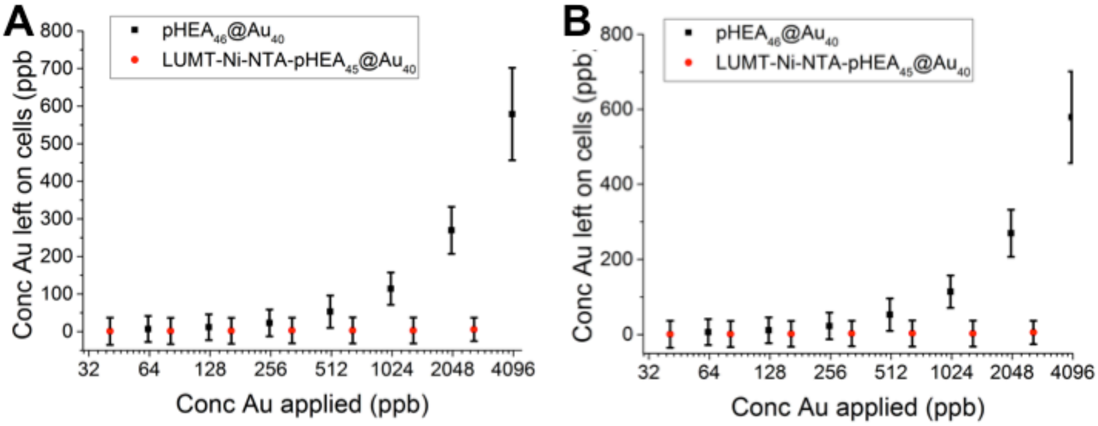

Figure 4-11. ICP-OES data showing quantity of AuNP adhered to cells upon incubation, indirectly through [Au]. A) Experiment with A549 cells. B) Experiment with SW480 cells. Experiments performed in triplicate, with 24 hrs of culture.

Following these data with A549 cells, incubation and ICP-OES was undertaken with SW480 cells. These experiments were performed at concentrations guided by A549 results, and they showed the same results as incubation with A549. This suggests that the protein conjugates did not adhere to these two human cell lines. This could be due to there not being sufficient protein present on the AuNP surface, a steric effect resulting in the protein being unable to interact with its cell surface target, or due to the protein simply not interacting with the cell surface moieties that are expressed on these cell lines to a significant extent. It is also possible that, because *Photorhabdus asymbiotica* has been proposed to be an intracellular pathogen, it is not well-adapted to interact with the mammalian cell surface.[28]

4.5.4. Lipid-binding assays to determine LUMT interaction

Previous results in this chapter showed no cell binding, but in our investigation we wanted to look at isolated targets as well. Arrays can be used as a high-throughput method to determine the binding of a tagged protein to a library of targets.[34–38] Lipids are a class of biomolecules that have functions in membranes, the storage of energy and a variety of signalling pathways.[36,37,39] Their presence in the plasma membrane is of particular interest in uncovering the membrane-binding partners for *Photorhabdus asymbiotica*'s PVC*lumt*_Pvc13 construct. His-tagged recombinant tail fibre protein was incubated with a library of lipids pre-spotted and dried on nitrocellulose membranes. This was followed by washing, incubation with anti-his antibodies and development to visualise any Pvc13 protein bound to the lipid array. This assay showed no binding of the analyte protein to any of the target lipid spots (see Figure 4-12). This suggests that the LUMT PVC protein may not bind to any of the 15 lipids included in this assay.

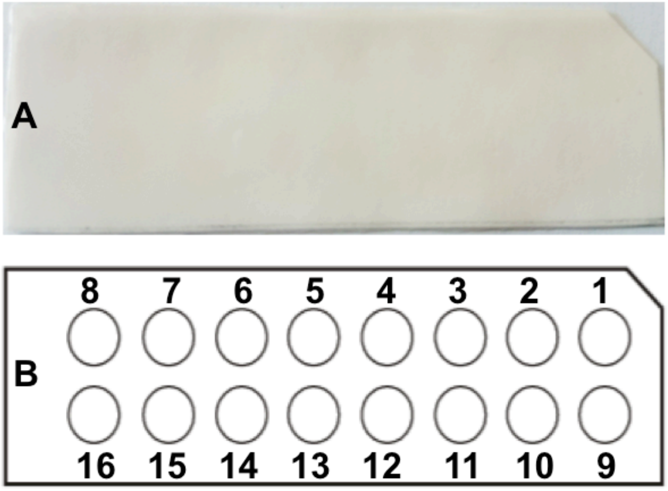

Figure 4-12. PIP strips^{TM} experiment to assess protein binding to lipid array. A) Experiment with His-tagged LUMT PVC tail fibre protein. B) Schematic showing lipid spots on array purchased from Molecular Probes (MP 23748).

Table 4-3. Legend for Figure 4-10.

Spot #	Lipid	Spot #	Lipid
1	Lysophosphatidic acid	9	Sphingosine 1-phosphate
2	Lysophosphatidylcholine	10	PtdIns(3,4)P_2
3	Phosphatidylinositol (PtdIns)	11	PtdIns(3,5)P_2
4	PtdIns(3)P	12	PtdIns(4,5)P_2
5	PtdIns(4)P	13	PtdIns(3,4,5)P_3
6	PtdIns(5)P	14	Phosphatidic acid
7	Phosphatidylethanolamine	15	Phosphatidylserine
8	Phosphatidylcholine	16	Blank

4.5.5. Glycan microarray assay to determine LUMT binding

Glycan microarrays are a valuable tool for assessing the binding of adhesive proteins to their glycan targets, especially as glycoproteins serve as the keystone of immune cell recognition, and all mammalian cells are covered in a thick glycocalyx, which is a primary site for pathogen adhesion.[40–46] This is particularly important in understanding the interaction of the PVC construct to immune cells such as macrophage-like cells, which has been proposed as a possible mechanism of action.[1,28] In addition to this, a recent study found a novel galactose-binding lectin in the *Photorhabdus luminescens* genome suggesting a role in specific glycan binding in this bacteria's attachment to its nematode host or insect host targets.[47]

His-tagged PVC*lumt*_Pvc13 protein was pre-incubated with fluorescent anti-His_6 dye (mouse monoclonal antibody fused to Alexa Fluor 488) before being incubated with an array of glycans attached to a glass slide. This slide was then washed to remove excess protein or dye, and read using a fluorescence array scanner to determine binding to glycan targets. Glycan "hits" were determined as having at least a 1-fold increase in fluorescence relative to fluorescence with the control array (incubated with dye but not protein), with increase in more than one spot in each set of six replicate spots, in more than one array.

Table 4-4. Glycan-binding "hits"

Structure	**Glycan**	**Structure**	**Glycan**
1	Heparin disaccharide III-S (ΔUA→2S-GlucNS)	**8**	α1-3-Mannobiose
2	Heparin unsaturated disaccharide I-H	**9**	α1-6-Mannobiose
3	Heparin unsaturated disaccharide IV-H	**10**	Galβ1-6Gal
4	Lacto-*N*-difucohexaose I	**11**	Galβ1-3GalNAcβ1-4Galβ1-4Glc
5	Asialo galactosylated, fucosylated biantennary (NA2F)	**12**	3'-Sialyllactosamine
6	Asialo, galactosylated, biantennary (NA2)	**13**	LS-Tetrasaccharide c (LSTc)
7	Asialo, galactosylated, tetranatennary, N-linked glycan (NA4)	**14**	Neocarratetraose-$4^{1,3}$-di-O-sulphate (Na+)

There were a variety of saccharides with which the PVC*lumt*_Pvc13 interacted (see Table 4-4). In particular, there were several sialyl, galactose and heparin glycan hits, but these are too varied to make any specific conclusions about the glycan binding of these proteins. Sialic acids or sialyllactoses have been proposed as cellular receptors for adenoviruses with structures closely related to the PVC construct.[48] However, further glycan arrays, with greater diversity, would be beneficial to unpack what lies behind these glycan hits and observe any significant trends.

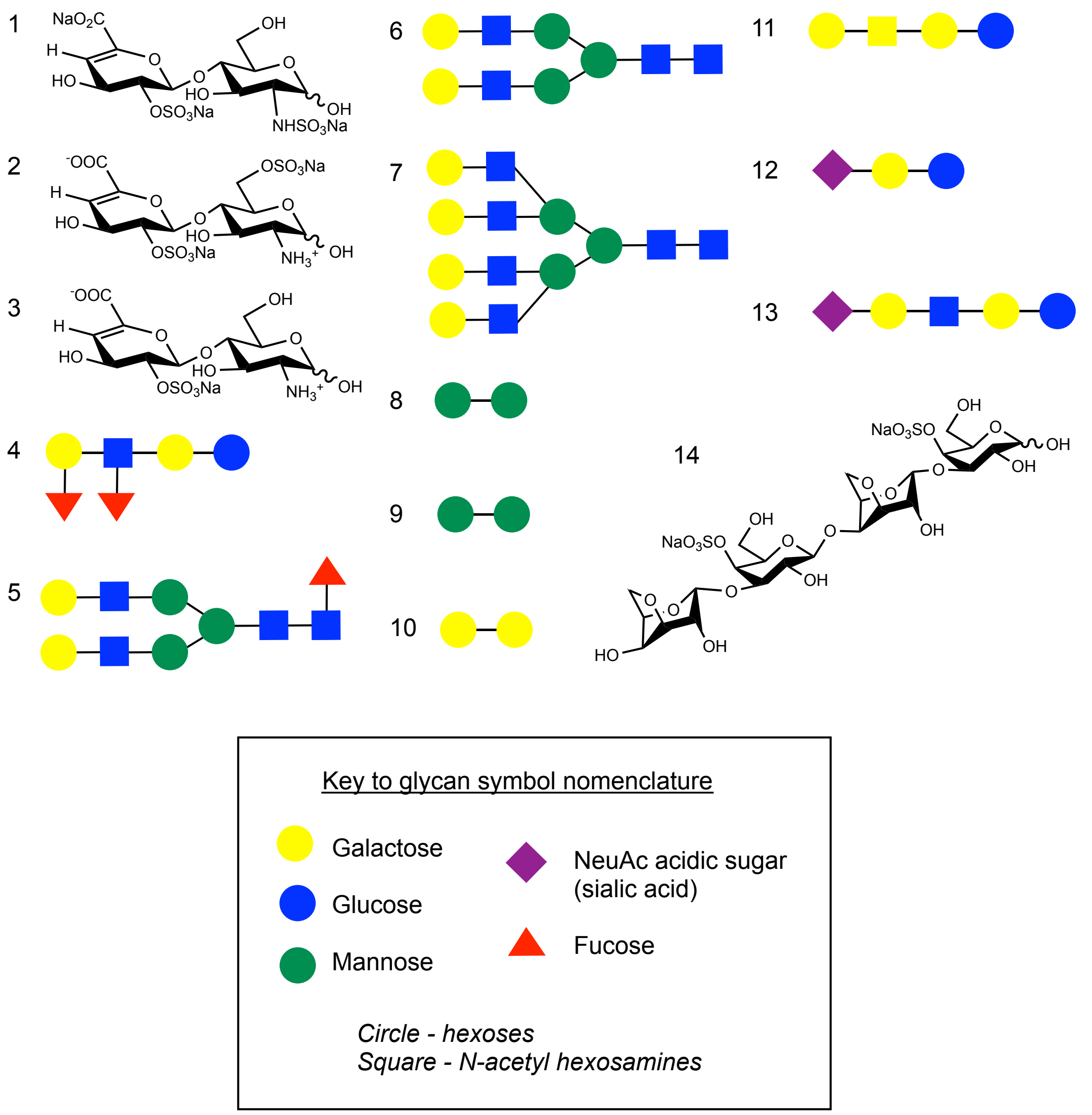

Figure 4-13. Structures of glycan array "hits".

4.5.6. PVC*lumt*_Pvc13 pull-down experiments with mammalian cell lysates

Photorhabdus PVC operons are reasonably well conserved, although their precise roles, if any, in human infection by *P. asymbiotica* remains un-investigated. Indeed it is not known which, if any, of the specific PVC operons encoded by *P. asymbiotica* could elaborate needle complexes capable of binding to mammalian cells.[8,21] However due to strong mammalian environment specific expression of the PVC*lumt* operon, its Pvc13 binding fibres remain the most likely candidate for mammalian specific cell type binding.

Following the lipid and glycan assays, only a small number of small molecule targets were identified (see sections 4.5.4 and 4.5.5). Proteomics analyses of whole cell lysates were therefore performed to look at a larger pool of potential binding candidates. In these experiments, the recombinant PVC*lumt*_Pvc13 construct was used as “bait” in mammalian cell extract “pull-down” experiments. Pull-down experiments with cellular lysates allow the determination of any protein targets present in the lysate solution with which the “bait” can bind.

Herein, protein/FeNP conjugates were produced, using His-Ni-NTA technology to immobilise His-tagged PVC*lumt*_Pvc13 recombinant tail fibre protein (“bait”) to a Ni-NTA-coated FeNP, and exposed to cellular lysates. Multiple washes were performed by pulling the magnetic FeNPs from solution magnetically before being re-suspended. Cellular proteins bound to PVC*lumt*_Pvc13, still attached after the washes, were subsequently eluted with imidazole solution (similarly to the IMAC protocol). Eluted protein samples were assessed by SDS-PAGE gel to ascertain that the “bait” was still present, before being prepared and run through Orbitrap mass spectrometry to identify any bound cellular proteins enriched relative to control experiments that had no Pvc13 “bait” present. Orbitrap mass spectrometry and data acquisition was performed in the University of Warwick Proteomics RTP by Cleidi Zampronio. Perseus software was used to statistically screen candidate binding partner proteins (see section 4.8.3.20) seen in replicate experiments. Where candidates were identifiable by both Perseus and Scaffold analysis, they may be considered more significant: but for this study, all candidates are shown regardless of significance.

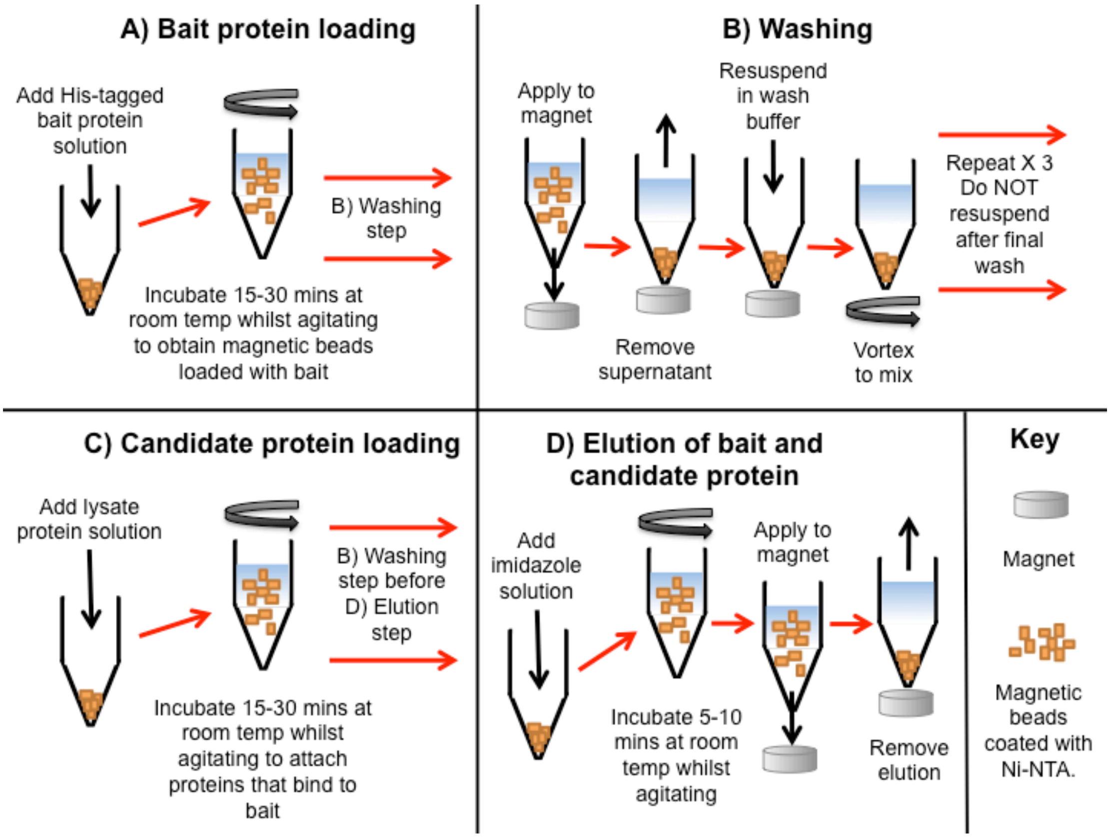

Figure 4-14. Cartoon of pull-down experiment procedure.

Protein candidates from pull-down experiments with PVC*lumt*_Pvc13 tail fibre "bait" interacting with mammalian lysates are shown in Table 4-5 and Table 4-11 in appendix. The mammalian lysates used in these studies were chosen due to being readily available in the laboratory; therefore, protein candidates that were identified in multiple lysates are highlighted here. The use of multiple lysates allows the ruling out of candidates being chosen purely due to overexpression in the cell line lysate used.

Proteins that were not known to localise to the plasma membrane (using the Uniprot database) were also filtered out from analysis. Known contaminants (such as skin debris) were also excluded from the analysis by use of the Perseus software. This software was also used to statistically screen potential candidates, resulting in "volcano" plots to visualise these candidates overrepresented in the pull down experiments relative to the controls (see Figures 4-15 and Figures 4-33 and 4-34 in appendix). As those clinical cases previously observed are linked only by outdoor activity, and the nematode symbiont with which *Photorhabdus* associates dwells in soil, it makes sense that the pathogen's targets would be present in cells exposed to the outside. The Human Protein Atlas was used to determine the protein expression levels in skin, the immune system and the gastrointestinal system.

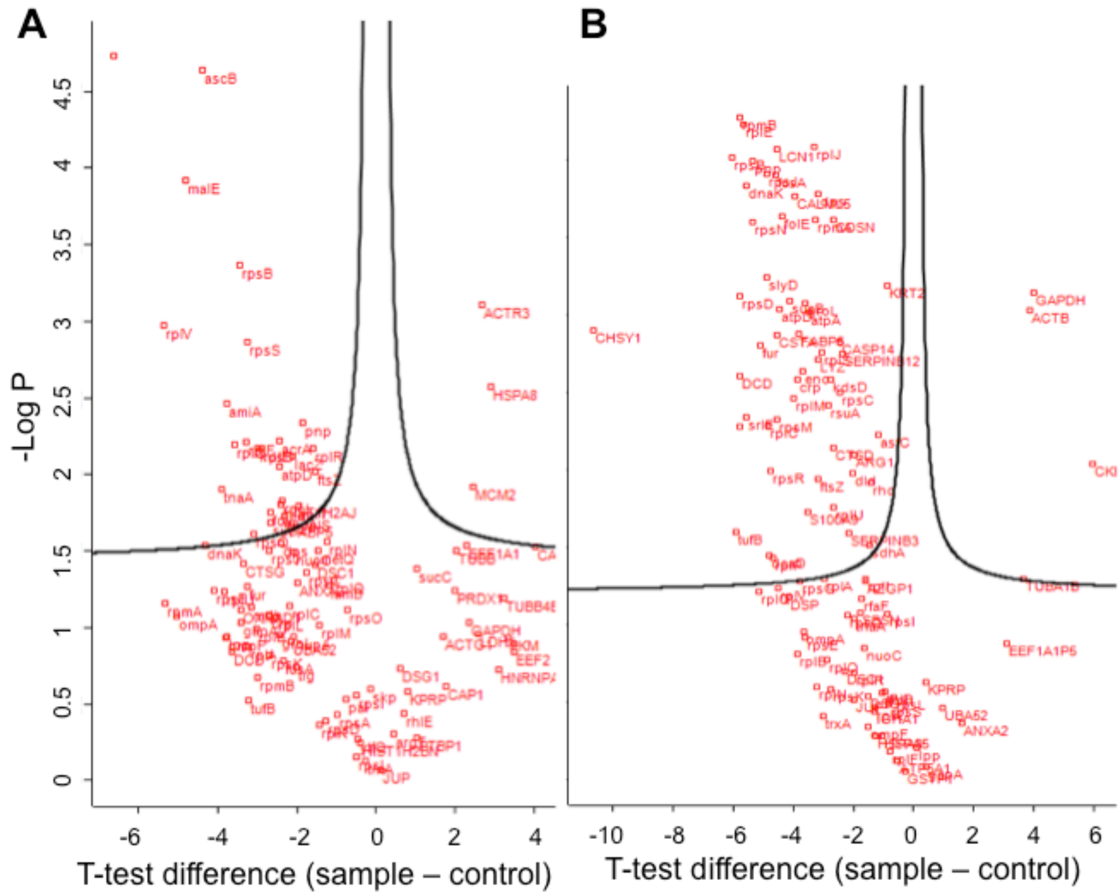

Figure 4-15. Volcano plots from pull-down experiments with His-tagged recombinant PVC*lumt*_Pvc13 tail fibres. A) THP-1 human monocytic cell line. B) Caco-2 human epithelial colorectal adenocarcinoma cell line. See section 4.8.3.20 for full details on the analysis of this data and generation of this plot.

These data suggest that membrane-bound protein targets for the PVC*lumt*_Pvc13 protein derived from *Photorhabdus asymbiotica* do exist, which is promising if the pathogen requires these adhesive toxins to bind the outside of host cells and facilitate bacterial internalisation. In particular, these assays suggest that *P. asymbiotica*'s PVC*lumt*_Pvc13 tail fibre construct has the capacity to bind to a range of mammalian cell surface proteins. A large number of the protein candidates identified also showed expression in skin, immune system or gastrointestinal tissue. It is not clear at this point if this represents a real range of binding partner protein targets, or if this could represent a general property to bind a common epitope on different cellular proteins, such a sugar group, or general “stickiness” of Pvc13 (or the host proteins).

Several cadherin-related proteins appear in this candidate list, namely: desmocollin, desmoglein and desmoplakin, These proteins are involved in the desmosome, a protein structure linking together the keratin in two adjacent cells. The filaggrin and hornerin candidate proteins are also known to interact with keratin fibres in their function. In addition, several membrane channel candidates are present in the list (gene IDs CLIC1, SLC12A2 and SLC3A2).

Looking specifically at what would correlate with previous studies, PVCs exposed to hemocyte cell cultures have the capacity to rearrange the actin cytoskeleton.[1,11] Therefore it is of interest that several candidate proteins, such as ezrin and the SLC9A3R2, connect to the actin skeleton and the plasma membrane. In particular, contactin is related to the cellular periphery and the rearrangement of the actin cytoskeleton. It is unclear, however, whether these proteins have extracellular motifs with which a pathogen protein such as Pvc13 might interact. Two tight junction proteins (TJP1 and 2) were also identified as candidates. These proteins are known to connect the actin cytoskeletons of adjacent cells, and are therefore confirmed to present on the cellular surface.

As previous studies have also shown that PVCs interact with eukaryotic immune cells, it is of note that there are also several protein candidates involved in the immune response: an immunoglobin, and proteins S100A8 and 9, which are involved in inflammation in cystic fibrosis.[1] These various protein candidates may provide us with potential routes to pathogenicity in mammals.

Table 4-5. Candidates identified from LUMT pulled down with more than one mammalian lysate

Gene ID	Protein	Lysates with which candidate was identified	Protein expression in human			-Log (p-value) [b]	T-test differ-
			Skin	Bone marrow	Gastro-intestinal		
ANXA1	Annexin A1	CACO2. A549	✓✓	✓✓✓	✓✓✓	1.55 [c]	1.31 [c]

DSC1, DSC3	Desmocollin-1 and 3	A549, THP-1, CACO2, SW480	✓✓✓	✗	✓✓✓	DSC1: 8.00 ^{*c} 2.67 ^{*d} 8.67 ^{*e} 4.00 ^{*f}	DSC1: 3.67 $^{+c}$ 1.00 $^{+d}$ 3.00 $^{+e}$ 1.00 $^{+f}$
DSG1	Desmoglein-1	A549, THP-1, CACO2, SW480	✓✓✓	✓✓✓	✓	4.00 ^{*c} 7.67 ^{*d} 27.0 ^{*e} 11.3 ^{*f}	2.00 $^{+c}$ 4.00 $^{+d}$ 9.00 $^{+e}$ 5.33 $^{+f}$
DSP	Desmoplakin	A549, THP-1, CACO2, SW480	✓✓✓	✓✓	✓✓	26.3 ^{*c} 1.67 ^{*d} 17.0 ^{*e} 7.00 ^{*f}	18.3 $^{+c}$ 1.67 $^{+d}$ 13.3 $^{+e}$ 5.67 $^{+f}$
ENO1	Enolase	A549, SW480	✓✓	✓✓	✓✓	2.42 ^{c} 0.67 ^{*f}	2.31 ^{c} 0.67 $^{+f}$
FLG, FLG2	Filaggrin and filaggrin-2	A549, THP-1, CACO2, SW480	✓✓✓	✓✓	✓✓	FLG: 0.67 ^{*c} 2.00 ^{*d} 23.7 ^{*e} FLG2: 6.00 ^{*d} 15.7 ^{*e} 3.67 ^{*f}	FLG: 0.67 $^{+c}$ 2.00 $^{+d}$ 10.7 $^{+e}$ FLG2: 3.33 $^{+d}$ 5.67 $^{+e}$ 2.33 $^{+f}$
HRNR	Hornerin	A549, THP-1, CACO2, SW480	n/a	n/a	n/a	25.7 ^{*c} 22.3 ^{*d} 29.3 ^{*e}	6.00 $^{+c}$ 10.3 $^{+d}$ 10.3 $^{+e}$
IGHA1	Immunoglobulin heavy constant alpha 1	THP-1, CACO2, SW480	n/a	n/a	n/a	0.33 ^{*d} 1.00 ^{*e} 0.67 ^{*f}	0.33 $^{+d}$ 0.67 $^{+e}$ 0.67 $^{+f}$

S100A6, S100A8	Protein S100 A6 and 8	A549, CACO2	✓✓✓	✓✓✓	✓✓✓	S100A6: 1.87 [c] S100A8: 2.00 [*e]	S100A6: 2.03 [c] S100A8: 1.33 [+e]
TJP1, TJP2	Tight junction protein ZO-1 and 2	A549, THP-1, SW480	✓	✓✓	✓✓	TJP1: 3.68 [c] 6.67 [*f] TJP2: 0.67 [*d] 2.33 [*f]	TJP1: 6.11 [c] 5.00 [+f] TJP2: 0.67[+d] 1.67 [+f]

[a] The Human Protein Atlas was used to obtain this information, [b] From Perseus software, student's t-test between Sample and Control. [c]/[d]/[e]/[f] Values from experiments with A549/THP-1/CACO2/SW480 respectively. ✓✓✓ = high. ✓✓ = medium. ✓ = low. ✗ = not detected. n/a = protein either not in database, or is not annotated with protein expression. [*]/[+] Identified by Scaffold software analysis, difference in average (over 3 samples and controls) total unique spectra or total unique peptides respectively.

4.5.7. Pvc13 tail fibre pull-down experiments with Drosophila cell lysate to determine protein binding

Both *P. luminescens* and *P. asymbiotica* interact pathogenically with the cells of their insect hosts after being regurgitated within the blood by their nematode symbionts. Members of this genus conserve serval the PVC gene loci, which produces syringe-like constructs shown to be toxic to insects.[11] The His-tagged versions of heterologously produced Pvc13 tail fibre proteins from three different PVC operons; PVC*lumt* and PVC*pnf*, from *P. asymbiotica* and PVC*unit4* from *P. luminescens*, were conjugated to magna beads as described above and used as bait in insect cell pull down experiments. *Drosophila menanogaster* S2 whole cell lysates were used as a convenient source of insect cells as the line was readily available in the laboratory.

Herein, tail fibres were bound to magnetic FeNP beads, washed and exposed to the S2 lysate. These beads were washed several times before the “bait” and any proteins from the lysate were eluted with imidazole solution from the beads. The elusions were assessed by SDS-PAGE gel to confirm the presence of the “bait” before being analysed by Orbitrap mass spectrometry to identify any protein candidates enriched in the pull-down samples with “bait” present versus controls without any “bait” attached to the beads. Orbitrap mass spectrometry and data acquisition was performed in the University of Warwick Proteomics RTP by Cleidi Zampronio. Perseus software was used to statistically screen candidates (see section 4.8.3.20), as well as produce “volcano” plots to visualise the data (see Figure 4-16 and Figure 4-35 in appendix). Where candidates were identifiable by both Perseus and Scaffold analysis, they may be considered more significant; but for this study, all candidates are shown regardless of significance.

A very short list was produced of candidates pulled down by more than one of the candidate proteins various, though it is likely that the fibres will bind to different cellular receptors (for reference, all proteins are shown here (Table 4-6) regardless of cellular localisation). This is because it is possible that the bait could pull down whole cellular protein complexes, binding surface proteins, but pulling down intracellular proteins by association in a complex. Protein candidates where several family members were identified (Table 4-7) and single protein candidates localised to the plasma membrane or cell projections are also shown (Tables 4-12 and 4-13 in appendix). Flybase was used to determine the cellular localisation and molecular function of the various protein candidates identified, such that proteins expressed in the plasma membrane or cellular projections could be highlighted. Proteins without a gene ID, or not present on the Flybase database, were also excluded from analysis. No contaminants should be present in this candidates list due to the use of a *Drosophila* cell line as opposed to a human one.

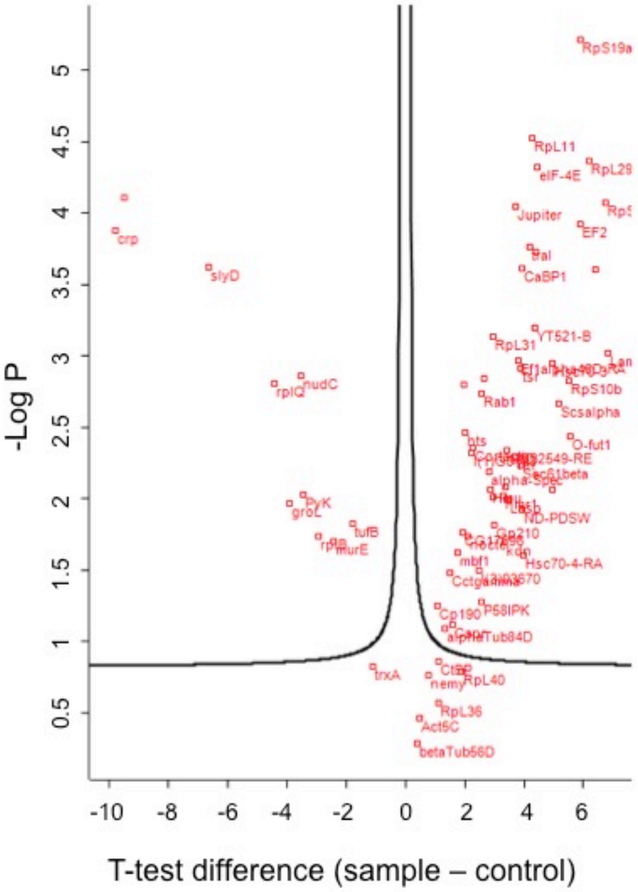

Figure 4-16. Volcano plots from pull-down experiments with His-tagged recombinant Pvc13 tail fibres from the PVC*pnf* construct and Schneider 2 (S2) *Drosophila melanogaster* macrophage-like cell line.

It is clear that PVC*unit4*_Pvc13 showed a larger number of protein candidates than the other lysates, potentially suggesting that these PVCs show some species specificity, and that this Pvc13 fibre is better adapted to interacting with cells of *Drosophila menanogaster* than LUMT or PNF. This fits with PVC*unit4*_Pvc13 being derived from an insect host restricted strain, *P. luminescens* TT01.

Several proteins related to the glycosylphosphatidylinosityl (GPI) lipid cell surface anchoring mechanism are implicated in the candidate list (gene IDs PIG-S, PIG-T, Cont and Nrx-IV). This GPI anchor is involved in cell-cell adhesion, such as in septate junctions present in epithelia. Other miscellaneous protein candidates present in the S2 plasma membrane include various receptors and channels (kuzbanian, and gene IDs pvr, stim), proteins involved in notch cell-cell communication (gp150), a lectin-like protein domain (ergic53, similar to ConA's glycan-binding domain, which suggests galactose-binding is possible), various proteins involved in vesicle trafficking (rab1, 5 and 11) and various proteins involved in fatty acid trafficking and metabolism (spectrin and desaturase 1).

PVC*pnf* expressed in *E. coli* and injected into *Galleria mellonella* larva caused extensive actin cytoskeleton rearrangements in the hemocytes *in vivo*.[1,11] Therefore it is of particular interest that a large number of proteins that bind to actin or microtubules were presented as candidates in these assays. For example, the actin-related proteins, hu-li tai shao, lasp, cheerio, profiling, shibire, kinesin and Rho1are all involved in modulating the actin cytoskeleton or the crosslinking of f-actin. LanA and rap1 GTPase are proteins involved in cell migration and organisation. While the cognate Pnf toxin (responsible for actual re-arrangement) is not being "delivered" in these pull downs, its possible that the PVCpnf_Pvc13 binding fibre is "pulling down" entire complexes involved with the cytoskeleton. For example; the karst and zipper proteins involved in cell adhesion and movement respectively, serve as key connections between the external cell-surface and the cytoskeleton.

It is believed that, at least some, PVCs may selectively interact with eukaryotic immune cells in order to manipulate the host immune system. Therefore the presence of down syndrome cell adhesion molecule 1 (DSCAM1) and TER94 (see Table 4-12 in appendix), which are an insect immunoglobin-like molecule and a protein involved in various other organismal responses, is of note.[1] In particular, DSCAM1, which has been proposed to be the insect equivalent of the mammalian hyper-variable immunoglobin antibody.

Table 4-6. Candidates identified from S2 lysate pulled down by more than one recombinant PVC tail fibre

Gene ID	Protein	Lysates with which candidate was identified	-Log (p-value) [b]	T-test difference [b]
alpha-Spec	Spectrin α chain	PNF, Unit 4	2.19 [d] 31.3 [*e]	2.83 [d] 25.3 [+e]
CCT3 [a]	T-complex	PNF, Unit 4	1.43 [d] 3.33 [*e]	1.52 [d] 3.00 [+e]
Hsc70-3 and 4 [a]	Heat shock 70-kDa protein cognate 3 and 4, isoform E	LUMT, PNF, Unit 4	HSC70-3: 2.95 [d] 2.67 [*c] 34.7 [*e] HSC70-4: 1.61 [d] 0.67 [*c] 22.7 [*e]	HSC70-3: 4.96 [d] 5.00 [+c] 17.0 [+e] HSC70-4: 4.00 [d] 1.00 [+c] 12.3 [+e]
hts	Protein hu-li tai shao	PNF, Unit 4	2.46 [d] 5.00 [*e]	2.00 [e] 4.00 [+e]
Lam [a]	Lamin	LUMT, PNF, Unit 4	1.33 [*c] 3.02 [d] 23.7 [*c]	1.67 [+c] 6.81 [d] 16.0 [+e]
Lasp	LIM and SH3 domain protein Lasp	PNF, Unit 4	2.00 [d] 9.33 [*c]	3.46 [d] 7.00 [+e]
Nocte [a]	No circadian temperature entrainment, isoform D	LUMT, Unit 4	0.67 [*c] 5.00 [*c]	0.67 [+c] 4.67 [+e]
Ref1 [a]	LD24793p	LUMT, Unit 4	0.67 [*c] 4.33 [*c]	0.67 [+c] 3.00 [+e]
SsRbeta [a]	Translocon-associated protein subunit beta	LUMT, Unit 4	0.67 [*c] 5.33 [*c]	1.00 [+c] 4.00 [+e]

Tsr [a]	Cofilin/actin-depolymeri-zing factor homolog	PNF, Unit 4	2.91 [d] 3.00 [*e]	3.91 [d] 2.00 [+e]

[a] Not known to localise to the plasma membrane or cell projection, [b] From Perseus software, student's t-test between Sample and Control. [c]/[d]/[e] Values from experiments with LUMT/PNF/Unit 4 respectively. [*]/[+] Identified by Scaffold software analysis, difference in average (over 3 samples and controls) total unique spectra or total unique peptides respectively.

Table 4-7. Candidates identified from S2 lysate pulled down by recombinant PVC tail fibre, where more than one protein family member candidate was identified.

Protein family	**Gene ID**	**Protein name**	**Lysate with which candidate was identified**	**-Log (p-value)** [b]	**T-test differ-ence** [b]
14-3-3 proteins	**14-3-3epsilon**	14-3-3 protein ε	Unit 4	1.67 [*e]	1.33 [+e]
	14-3-3zeta	14-3-3 protein ζ		5.67 [*e]	4.67 [+e]
Actin-related proteins	**Arp3**	Actin-related protein 3	Unit 4	1.33 [*e]	1.33 [+e]
	Arpc4 [a]	Actin-related protein 2/3 complex subunit 4		0.67 [*e]	0.67 [+e]
Heat shock protein 70 chaperones	**Hsc70-3** [a]	Heat shock 70-kDa protein cognate 3, isoform E	LUMT, PNF, Unit 4	2.95 [d] 2.67 [*c] 34.7 [*e]	4.96 [d] 5.00 [+c] 17.0 [+e]
	Hsc70-4 [a]	Heat shock protein cognate 4, isoform G	LUMT, PNF, Unit 4	1.61 [d] 0.67 [*c] 22.7 [*e]	4.00 [d] 1.00 [+c] 12.3 [+e]
	Hsc70-5 [a]	Heat shock protein cognate 5, isoform B	Unit 4	1.00 [*e]	1.00 [+e]
	Hsc70Cb [a]	Hsc70Cb, isoform G		1.67 [*e]	1.67 [+e]
Heat shock protein Hsp90 family	**Gp93**	Glycoprotein 93	Unit 4	7.00 [*e]	6.00 [+e]
	Hsp83	Heat shock protein 83		11.7 [*e]	8.33 [+e]
	LanA	Laminin subunit α	Unit 4	4.67 [*e]	4.00 [+e]

Laminin protein subunits	**LanB1**	Laminin subunit β-1		8.33 *^{e}	5.67 $^{+e}$
	LanB2	Laminin subunit γ-1		6.33 *^{e}	4.67 $^{+e}$
Mitochondrial complex I - NADH:ubiquionine oxidoreductase complex subunits	**ND-B15**	NADH dehydrogenase (Ubiquinone) B15 subunit	Unit 4	0.67 *^{e}	0.67 $^{+e}$
	ND-B17	GM23292p		0.67 *^{e}	0.67 $^{+e}$
	ND-PDSW	CG8844 protein		1.00 *^{e}	0.67 $^{+e}$
Oligosaccharyltransferase	**Ost48**	Dolichyl-diphosphooligosaccharide--protein glycosyltransferase 48 kDa subunit	Unit 4	10.7 *^{e}	7.00 $^{+e}$
	OstDelta	Oligosaccharide transferase δ subunit, isoform B		4.67 *^{e}	2.67 $^{+e}$
	Ostgamma	GH11935p		2.00 *^{e}	1.00 $^{+e}$
Phosphatidylinositol glycan anchor biosynthesis complexes	**PIG-S**	Phosphatidylinositol glycan anchor biosynthesis, class S ortholog	Unit 4	2.67 *^{e}	2.33 $^{+e}$
	PIG-T	RE52151p		1.67 *^{e}	1.33 $^{+e}$
RAB GTPases	**Rab1**	FI01544p	Unit 4	4.00 *^{e}	3..3 $^{+e}$
	Rab11	Drab11		0.67 *^{e}	0.67 $^{+e}$
	Rab5	Drab5		0.67 *^{e}	0.67 $^{+e}$
Spectrin protein complex	**alpha-Spec**	Spectrin α chain	PNF, Unit 4	2.19 ^{d} 31.3 *^{e}	2.83 ^{d} 25.3 $^{+e}$
	beta-Spec	Spectrin β chain	Unit 4	1.00 *^{e}	1.00 $^{+e}$

[a] Not known to localise to the plasma membrane or cell projection, [b] From Perseus software, student's t-test between Sample and Control. ^{c}/^{d}/^{e} Values from experiments with LUMT/PNF/Unit 4 respectively. */$^{+}$ Identified by Scaffold software analysis, difference in average (over 3 samples and controls) total unique spectra or total unique peptides respectively.

4.5.8. PVCunit4_Pvc13 tail fibre pull-down experiments with *Caenorhabditis elegans* lysate to determine cell protein binding partner(s)

Photorhabdus luminescens exists in an obligate symbiosis with *Heterhorhabditis bacteriophora* nematode worm vector in order to gain access to their insect host.[5,11,15] Therefore there are hypothesised to be specific genes and/or operons required for symbiosis.

The PVC*unit4* operon is the single variant found in all strain genomes so far examined, and furthermore experiments with over-expressed Unit4 needle complex showed a very strong phenotype (induced *endotokia matricida*) in *Caenorhabditis elegans* nematode worms (Addison, M., Hapeshi, A. and Waterfield, N., unpublished data). Herein a pull-down experiment was performed between the recombinant PVC*unit4*_Pvc13 tail fibre and *C. elegans* proteins to attempt to determine the potential nematode binding protein partner.

As with the previous pull-down experiments, PVC*unit4*_Pvc13 tail fibre "bait" was bound to magnetic FeNP beads, washed and exposed to the *C. elegans* lysate. The beads were washed to remove unattached proteins before both bait and candidate proteins were eluted with imidazole solution. SDS-PAGE was used to determine the presence of bait, before analysis by Orbitrap mass spectrometry to identify proteins enriched in the pull-down samples with bait present versus controls without any bait attached to the beads. Orbitrap mass spectrometry and data acquisition was performed in the University of Warwick Proteomics RTP by Cleidi Zampronio. Candidates were screened for significance by Perseus software, as well as produce "volcano" plots to visualise the resultant candidates (see Figure 4-36 in appendix). Where candidates were identifiable by both Perseus and Scaffold analysis they may be considered more significant; but for this study, all candidates are shown regardless of significance.

A shortlist of candidates for PVC*unit4*_Pvc13 tail fibre binding, with significantly more protein present in the samples versus controls with no Pvc13 present, as determined by Perseus and/or Scaffold analysis, was identified (Table 4-8), and unknown proteins or proteins not known to localise to the plasma membrane are shown in the appendix (Table 4-14).

The PVC*unit4*_Pvc13 tail fibre showed binding to myosin-4, intermediate filament protein ifb-1 and tropomyosin isoforms a/b/d/f, all of which are actin-binding proteins. Myosins are a superfamily of ATP-dependent proteins that regulate cell movement via actin-binding.[49,50] Tropomyosins are integral components of the actin filaments, and in some forms are essential in the regulation of actin/myosin interactions.[51] This is potentially significant as the *endotokia matricida* phenotype is believed to require paralysis of the nematode vulva muscle, preventing egg laying and causing the eggs to be retained and hatch with the body of the hermaphrodite adult.

A novel fucose-binding lectin has been identified from *Photorhabdus luminescens*, suggesting that glycan-binding may be an adhesive mechanism for this bacteria.[52] Two carbohydrate binding proteins, protein irg-7 and probable galaptin (implicated in regulating cell-cell adhesion) lec-8, are in the candidate list. Membrane transporters, vacuolar H ATPase and anion exchange protein, and two V-type proton ATPases, probable V-type proton ATPase subunits B and G, are also in the candidate list.

It should be noted that, from what is known of the *P. luminescens*/*H. bacteriophora* symbiotic life cycle, it is expected that bacteria are transferred from maternal to infective juvenile nematodes developing in the maternal body cavities, and therefore attachment of *P. luminescens* to their nematode host is expected to occur at this stage.[1,13] As the function of many proteins, such as tropomyosins, is dependent on the organism's developmental stage, understanding at which development stage the PVCs bind to *C. elegans* would be very useful.

Table 4-8. Candidates identified from *Caenorhabditis elegans* lysate pulled down by Unit 4 recombinant PVC tail fibre, where cellular localisation is at least suggested to plasma membrane.

Accession Number [a]	**-Log (p-value)** [b]	**T-test difference** [b]	**Protein name** [a]	**Function** [c]
A0A131MBU3-2|IRG7	2.11 6.33 *	4.44 5.67 $^{+}$	Protein irg-7	Possible extracellular/secreted protein. Carbohydrate binding, involved in innate immune response

A0A2C9C2Z1	2.79 5.33 *	6.10 5.33 $^{+}$	Uncharacterised protein	Localised to membrane. Unknown function, but integral component of membrane, possible chaperone
B3WFV9	0.33 *	0.33 $^{+}$	Anion exchange protein	Plasma membrane anion/anion antiporter.
G5ECR0	5.58 1.00 *	4.63 1.00 $^{+}$	Uncharacterised protein	Integral component of plasma membrane
LEC8	0.33 *	0.33 $^{+}$	Probable galaptin lec-8	Carbohydrate, glycolipid binding. Involved in defense response to gram positive bacterium/toxic substances
MYO4	2.77 5.00 *	1.81 4.67 $^{+}$	Myosin-4	Binds actin filaments and microtubules
Q19853	2.98 0.33 *	2.95 0.33 $^{+}$	Uncharacterised protein	Integral component of plasma membrane, involved in motor neuron axon guidance
Q95X44	1.00 *	1.00 $^{+}$	Vacuolar H ATPase	Localised to plasma membrane. Proton-transporting ATPase activity, rotational mechanism
Q19289-2|IFB1	0.33 *	0.33 $^{+}$	Intermediate filament protein ifb-1	Potentially cytoplasmic. Provides mechanical strength to cells. Essential protein involved in attachment structures in epidermal cells that connect muscles to external cuticle.
TPM1	3.80 11.3 *	7.15 9.33 $^{+}$	Tropomyosin isoforms a/b/d/f	Potentially cytoplasmic. In association with troponin complex, which has a central role in Ca-dependent striated muscle contraction. Muscle actin filament organization, muscle arm extension and morphology. Binds to F-actin.
VATB	2.30 3.00 *	1.63 2.33 $^{+}$	Probable V-type proton ATPase subunit B	Localised to plasma membrane and cytosol. Subunit of V1 complex of vacuolar ATPase, which acidifies various intracellular compartments
VATG	2.45 0.33 *	2.22 0.33 $^{+}$	Probable V-type proton ATPase subunit G	Catalytic subunit of V1 complex of vacuolar ATPase, which acidifies various intracellular compartments

[a] For Uniprot database (note that those from *Caenorhabditis elegans* also have “CAEEL” after their accession number, [b] From Perseus software, student’s t-test between Sample and Control, [c] According to Uniprot database (including data from

Wormbase database). $*/^{+}$ Identified by Scaffold software analysis, difference in average (over 3 samples and controls) total unique spectra or total unique peptides respectively. In this table, where samples were only identified by scaffold, no protein was found in the controls.

4.6. Conclusions

In this chapter we developed an entirely new method using nanoparticles to probe complex protein function, enabling us to determine a large number of potential candidate binding targets for the Pvc13 tail fibre proteins from three different PVC operons from two different *Photorhabdus* species.

The potentially mammalian-active PVC*lumt*_Pvc13 recombinant tail fibre protein from the *Photorhabdus asymbiotica* was attached to a Ni-NTA@AuNP scaffold and characterised by a battery of analytical techniques (including TEM, DLS, XPS and TGA) to ensure uniformity, stability and successful protein conjugation to the AuNP scaffold. This use of the His-tag to attach a protein of unknown function to AuNPs could be a useful technique for elemental analysis of cell line incubations. Both cytotoxicity and ICP-OES assays performed after 24 hours incubation with human A549 lung adenocarcinoma cells exhibited no binding to this cell line. Subsequent ICP-OES of human SW480 colorectal cells also showed no binding, which suggests that these cell types may not express (or may not express highly) PVC*lumt*_Pvc13 protein binding partners.

This PVC*lumt*_Pvc13 tail fibre recombinant protein was then exposed to lipid and glycan arrays, which showed no significant affinity for the lipids tested, but potential candidates in sialated or heparin-related targets. These are in fact typical targets of host interaction factors from diverse pathogens, such a viral binding fibres and bacterial toxins.

Finally, assessment of pull-down assays in a range of human whole cell lysates uncovered various candidates such as actin-binding or immunity proteins. Separately, the Pvc13 tail fibre recombinant proteins were tested in pull down experiments with *Drosophila menanogaster* S2 whole cell lysate, and the PVC*unit4*_Pvc13 specifically with *C. elegans* whole lysate. In these assays, various keratin or actin-binding protein candidates, as well as several proteins linked to the immune response, were identified, which may indicate a potential route to mammalian pathogenicity.

These data suggest that protein targets for PVC Pvc13 tail fibre protein do exist, as do possible human extracellular targets (both proteins and glycans). This is promising in considering future application of these constructs in specific drug delivery.

4.7. Further Work

The work presented in this chapter may be considered as on going: therefore there are a variety of avenues that future investigations may follow. As the number of candidates assessed by the PIP strips assay and the glycan array is limited, further microarray assays might yield more hits to be further analysed (particularly if informed by the glycan hits identified here).

The development of the ICP-OES and pull-down systems as detailed herein could be used in more human cell lines to develop a greater understanding of candidate binding proteins for PVC constructs. Namely, skin cells (due to previous clinical cases showing skin lesions), immune cells (due to previous hematocyte invasion studies) or gastrointestinal cells (as many candidates identified here were found to be expressed highly in this system). Analysis of a variety of relevant cell lines would also allow us to determine the significance of the identification of certain candidate proteins in context.

Additional insect cell line experiments would also be useful as the presence of few protein binding candidates with the PVC*pnf* and PVC*lumt* recombinant Pvc13 tail fibre proteins suggests a specificity in efficacy with different insect targets of these PVCs.

4.8. Materials and Methods

4.8.1. Materials

Ultra-pure water with resistance < 18 Ω, was obtained from a Milli-Q© Integral Water Purification System. All chemicals were purchased from Sigma-Aldrich and used as supplied unless otherwise stated. 6-((4-(aminomethyl)benzyl)oxy)-7H-purin-2-amine was purchased from Carbosynth.. Goat anti-rabbit IgG antibody, Halt^{TM} phosphatase inhibitor cocktail, Micrococcal Nuclease Solution (100 U/L), THF, DMF, ethyl acetate and 6x-His Tag, Alexa Fluor 488, clone: 4E3D10H2/E3 (by Invitrogen^{TM}) were purchased from Fisher. For washing of AuNPs, Amicon Ultra-0.5 centrifugal filter units with Ultracel-30 membrane were used. 40 nm citrate-stabilised gold colloid solution was purchased from BBI solutions.

All cell cultures reagents were sourced from either Thermo Fisher Scientific at the highest attainable quality and stored at 4 °C or -20 °C as instructed when not in use. Complete medium consisted of Ham's F-12K (Kaighn's) medium (with phenol red) containing 10 % (v/v) FBS plus 100 U/mL Penicillin and 100 µg/mL Streptomycin (unless otherwise specified) and all cells were incubated at 37 °C in a 5 % CO_2(g) humidified atmosphere. PBS was sourced from Thermo Fisher Scientific. All cell culture plastic ware was obtained from Greiner Bio-One Ltd, Gloucestershire, UK and all cell culture experiments were performed in a class II biosafety cabinet to ensure sterility with cells regularly assessed for bacterial and, fungal and yeast contamination. Defibrinated sheep blood was purchased from TCS Biosciences and used within 5 days of delivery. Lysis buffer was prepared as follows, containing no EDTA, ionic detergents, DTT or DTE to be compatible with subsequent dynabeads pull-down assays: 1 mL of 150 mM NaCl, 1% Triton X-100, 50 mM Tris, pH 8.0. Buffers used for PIP strip assay, Glycan microarray and Dynabead^{TM} pulldown experiments were prepared as detailed in their respective manuals. Other buffers (PBS, TBS, TS-T) were prepared in house by the University of Warwick Life Sciences technicians. PIP Strips^{TM}, glycan microarray and Dynabeads^{TM} were all used as described by Molecular Probes, Dextra UK and Invitrogen respectively. A549 and SW480 cells used for lysis were prepared in house as described in 4.5.3.9 below. CACO2 cells used for lysis were provided in 100 mm plates as provided by Dr Blessing Anonye. THP1 and S2 cells were provided in suspension as provided by Dr Alexia Hapeshi of the Waterfield group. LUMT and PNF His-tagged proteins were supplied by Joe Healey of the Waterfield Group, and Unit4 His-tagged protein was supplied by Dr Alexia Hapeshi of the Waterfield group. Reagents used for preparation of proteins for mass spectrometry analysis were provided in house at the University of Warwick Proteomics Research Technology Platform.

4.8.2. Analytical Methods

^{1}H, ^{13}C and ^{19}F-NMR spectra were obtained using a Bruker DPX-400 NMR Spectrometer; all chemical shifts are reported in ppm (δ) relative to residual non-deuterated solvent. Mass spectrometry was carried out in pure methanol or water on the Agilent 6130B ESI-Quad instrument using electrospray in positive mode. FTIR spectroscopy was carried out on a Bruker Vector 22 FTIR spectrometer with a Golden gate diamond attenuated total reflection cell. SEC (GPC) measurements were carried out on an Agilent 390-LC MDS instrument equipped with a dual angle light scatter (LS), 2 x PLgel Mixed D columns (300 x 7.5 mm) and a PLgel 5 μm guard column. The eluent was DMF with 5 mmol NH_4BF_4 additive. Samples were run at 1ml/min at 50°C. Poly(methyl methacrylate) standards (Agilent EasyVials) were used for calibration between 955,000 – 550 gmol^{-1}. Analyte samples were filtered through a nylon membrane with 0.22 μm pore size before injection. Respectively, experimental molar mass ($Mn_{,SEC}$) and dispersity ($Đ$) values of synthesized polymers were determined by conventional calibration and universal calibration using Agilent GPC/SEC software. Nanoparticle size was determined using Dynamic Light Scattering (DLS), performed on a Malvern Instruments Zetasizer Nano- ZS with 4mW HeNe laser 632.8 nm. UV/Vis spectroscopy and fluorescence plate readings were performed on a BioTek Synergy HT Microplate Reader. UV-vis spectroscopy was used to determine nanoparticle size according to a method developed by Haiss et al.[53] Transmission electron microscopy (TEM) was performed on a JEOL 2100 LaB6 high-resolution microscope. X-ray photoelectron spectroscopy (XPS) was carried out on the Kratos Axis Ultra with a delay-line detector. Mass spectrometry of the pulldown experiment elution samples was performed in the University of Warwick Proteomics Research Technology Platform using the in-house in-gel trypsin digest protocol. Glycan microarrays were scanned using an Agilent Technologies 2 Colour Array Scanner with a 50 sample auto chamber.

4.8.3. Synthetic Methods

4.8.3.1. Synthesis of 2-(dodecylthiocarbonothioylthio)-2-methylpropionic acid (DMP/DDMAT)

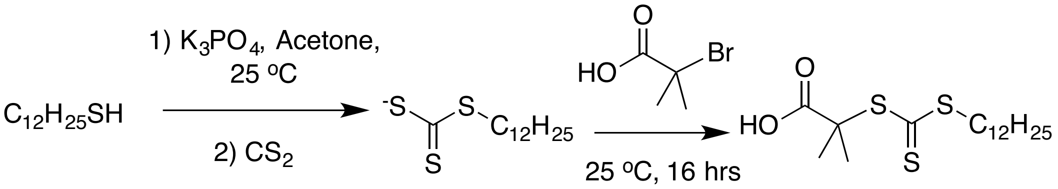

Dodecane thiol (4.75 mL, 19.8 mmol) was added dropwise to a stirred suspension of K_3PO_4 (4.02g, 18.9 mmol) in acetone (60 mL). The reaction vessel was placed in an ice bath. Carbon disulfide (3.20 mL, 53.0 mmol) was added and the solution turned bright yellow, but was still cloudy. After stirring for ten minutes, 2-bromo-2-methylpropionic acid (3.00 g, 18.0 mmol) was added and a precipitation of KBr was noted. The ice bath was removed after 10 minutes and the reaction was left stirring at room temperature for 16 hours. Solvent was removed *in vacuo* and the residue was extracted into DCM (2 x 50 mL) from 1 M HCl (100 mL). The organic extracts were further washed with water (100 mL) and brine (100 mL) and dried over $MgSO_4$. Recrystallisation from n-hexane yielded a bright yellow solid (1.80 g, 27.5%).

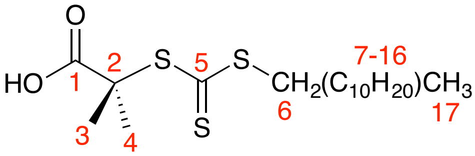

^{1}H NMR (400 MHz, CDCl3) δ_{ppm}: 3.28 (2H, t, J_{HH}=7.5, H6); 1.66 (6H, s, H3/4); 1.10-1.25 (20H, alkyl, H7-16); 0.79 (3H, m, H17).

^{13}C NMR (400 MHz, CDCl3) δ_{ppm}: 220.86 (C5); 178.04 (C1); 55.51 (C2); 37.08 (C7); 31.92 (C6); 29.64, 29.57, 29.46, 29.35, 29.12, 28.98, 27.82 (C8-15); 25.23 (C3/4); 22.70 (C16); 14.13 (C17).

FTIR (solid, ν_{max}/cm^{-1}): 2910 (CH_2); 1710 (C=O); 1440 (C-C); 1305 (C-O); 1070 (S-(C=S)-S).

ESI-MS, positive mode (m/z): 365.2 (M+H$^+$, expected 365.63), 387.1 (M+Na$^+$, expected 387.61).

4.8.3.2. Synthesis of pentafluorophenyl 2-(dodecylthiocarbonothioylthio)-2-methylpropionic acid (PFP-DMP/PFP-DDMAT)

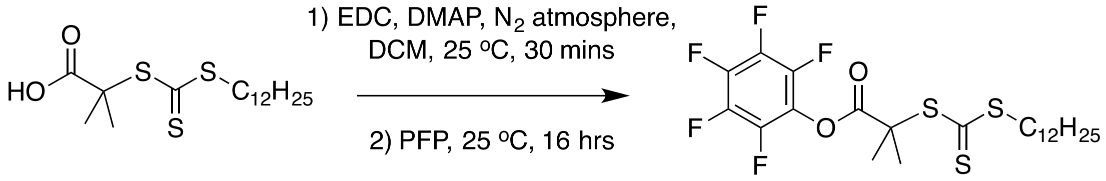

2-(Dodecylthiocarbonothioylthio)-2-methylpropionic acid (DMP) (0.500 g, 1.37 mmol), *N*-(3-dimethylaminopropyl)-*N'*-ethylcarbodiimide hydrochloride (EDC) (0.390 g, 2.05 mmol), and 4-(dimethylamino)pyridine (DMAP) (0.250 g, 2.05 mmol) were dissolved in DCM (50 mL) and stirred for 20 minutes under N_2. Pentafluorophenol (PFP) (0.780 g, 4.24 mmol) in 5 mL DCM was added. The reaction was stirred overnight at room temperature. The reaction was washed with 3 M HCl (100 mL), 1 M $NaHCO_3$ (100 mL) and brine (100 mL), dried over $MgSO_4$, filtered and then concentrated *in vacuo* to evolve a yellow solid with melting point close to room temperature (0.437 g, 60.2%).

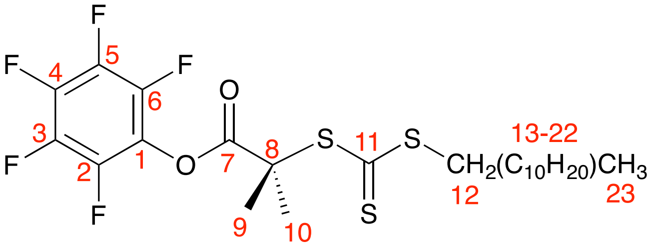

^{1}H NMR (300 MHz, CDCl3) δ_{ppm}: 3.24 (2H, t, J_{HH}=7.4 x 2, H12); 1.62 (6H, m, H9/10); 1.26 (20H, alkyl, H13-22); 0.81 (3H, m, H23).

^{19}F NMR (300 MHz, CDCl3) δ_{ppm}: 151.54 (m, F2/6), 157.74 (m, F3/5), 162.3 (m, F4).

FTIR (solid, ν_{max}/cm^{-1}): 2934 (CH_2); 1705 (C_6F_5C=O); 1439 (C-C); 1260 (C-O); 1080 (S-(C=S)-S).

This species' ESI-MS did not show any of the expected peaks, though the above characterisation was deemed sufficient to prove successful synthesis.

4.8.3.3. General Procedure for Synthesis of pHEA (or PFP-pHEA) polymer

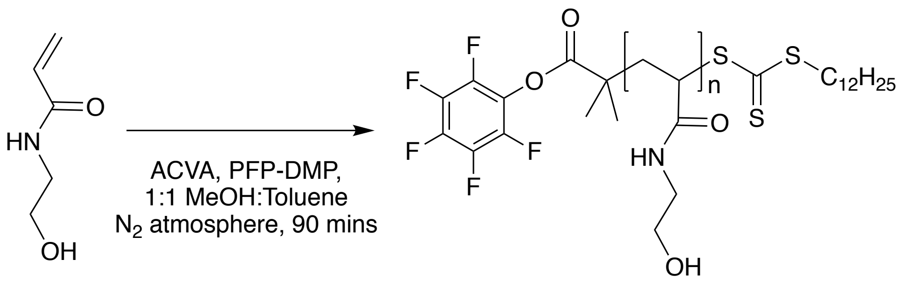

The following procedure describes a reaction with a theoretical degree of polymerisation (DP) of 50 repeat units. 4,4-azobis(4-cyanovaleric acid) (5 mg, 0.018 mmol), pentafluorophenyl 2-(dodecylthiocarbonothioylthio)-2-methylpropionic acid (CTA) (47 mg, 0.088 mmol, for the polymer without a PFP-end group, DMP was used instead of PFP-DMP) and *N*-hydroxyethyl acrylamide (1 g, 8.8 mmol) were dissolved in 1:1 methanol: toluene (4 mL) in a glass vial with a stirrer bar. Mesitylene (200 µL) was added and a sample was removed for ^{1}H-NMR analysis in $CDCl_3$. The reaction mixture was degassed by N_2 for 30 minutes, sealed and placed in a 70°C oil bath. After 90 minutes, the solution was opened to air and quenched by submerging the flask in $N_{2(l)}$. The polymer (pHEA) was precipitated three times from methanol into diethyl ether to give a light yellow solid.

Conversion (NMR): 94.0%; Mn (theoretical): 5664 g.mol-1; Mn (SEC) 8253 g.mol-1; Mw (SEC) 9231 g.mol-1; Mw/Mn (SEC): 1.1.

^{1}H NMR (300 MHz, CDCl3) δ_{ppm}: 8-8.15 (br s, N-H (H4)); 3.4-3.8 and 3.05-3.2 (2 x m, H5); 1.9-2.35 and 1.4-1.8 (2 x m, H1/2).

^{19}F NMR (300 MHz, CDCl3) δ_{ppm}: 155.29, 161.61, 165.67.

FTIR (solid, ν_{max}/cm^{-1}): 3300 (N-H and O-H stretch); 2854 (alkyl C-H stretch); 1641 (amide C=O stretch); 1555 (N-H bend); 1443 (alkane); 1225 (C-O stretch); 1060 (C-O stretch); 950 (C-F peak on shoulder of 1060 peak).

Data are shown for the PFP-$pHEA_{45}$ polymer, which was conjugated to the AuNPs.

4.8.3.4. General Procedure for Synthesis of NTA-amine-modified pHEA polymer

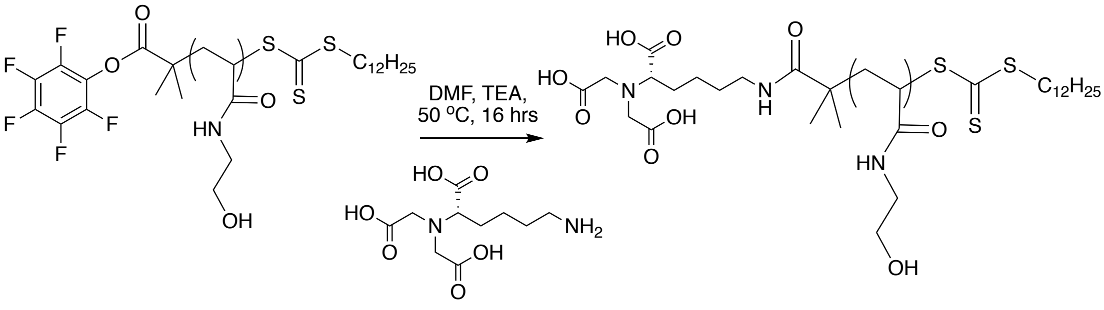

PFP-pHEA$_{45}$ (90.8 mg, 0.018 mmol) and primary amine (6-((4-(aminomethyl)benzyl)oxy)-7H-purin-2-amine (BG) or Nα,Nα-Bis(carboxymethyl)-L-lysine hydrate(NTA)) (0.088 mmol) were dissolved in DMF (5 mL). To the stirred mixture, triethylamine (35 μL) was added, and the reaction was moved to a 50 °C oil bath for 16 hours. The polymer was precipitated three times from methanol into diethyl ether to give a sandy yellow solid.

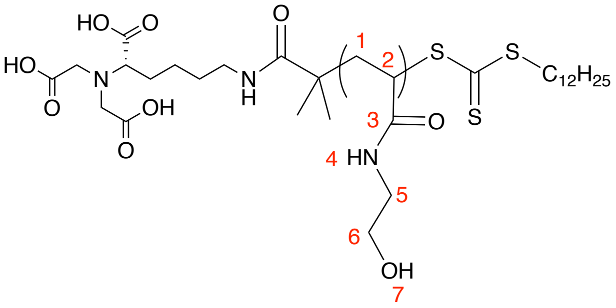

M_n (SEC) 6101 g.mol^{-1}; M_w (SEC) 8205 g.mol^{-1}; M_w/M_n (SEC): 1.3 (an increase in dispersity is observed post-modification).

^{1}H NMR (300 MHz, D$_4$-MeOH) δ_{ppm}: 4.8-5 (br s, H6), 3.44-3.85 and 3.05-3.22 (2 x br s, H5), 1.94-2.35 and 1.31-1.86 (2 x br s, H1/2).

^{19}F NMR (300 MHz, CDCl3) δ_{ppm}: no peaks visible.

FTIR (solid, ν_{max}/cm^{-1}): 3300 (N-H and O-H stretch); 2944 (alkyl C-H stretch); 1627 (amide C=O stretch); 1562 (N-H bend); 1390 (C-H alkane); 1060 (C-O stretch) (C-F shoulder on 1060 peak is no longer present).

4.8.3.5. Synthesis of NTA-pHEA45@Au40

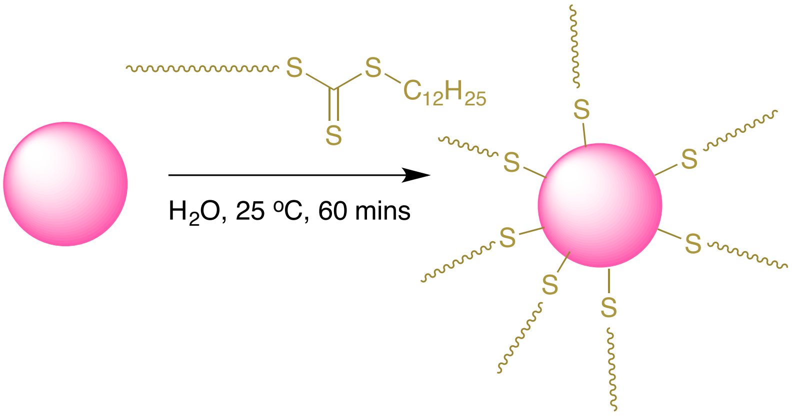

1 mg of NTA-pHEA$_{45}$ polymer was added to 1 mL of Au$_{40}$ in a 1.5 mL microcentrifuge tube. This was left, covered with foil, for 60 minutes. The solution was centrifuged at 13,200 rpm, for 5 minutes, supernatant removed, and the pellet re- dispersed in 1 mL water. The nanoparticles were washed in this manner a further 3 times before being re-dispersed in a final volume of 1 mL distilled water and stored in the fridge until required. Nanoparticle size and dispersity was measured by TEM, UV-Vis spectroscopy and size and zeta potential measurements by DLS.

Nanoparticle diameter (TEM): 37.1 nm (standard deviation 4.1 nm).

4.8.3.6. Synthesis of pHEA46@Au40

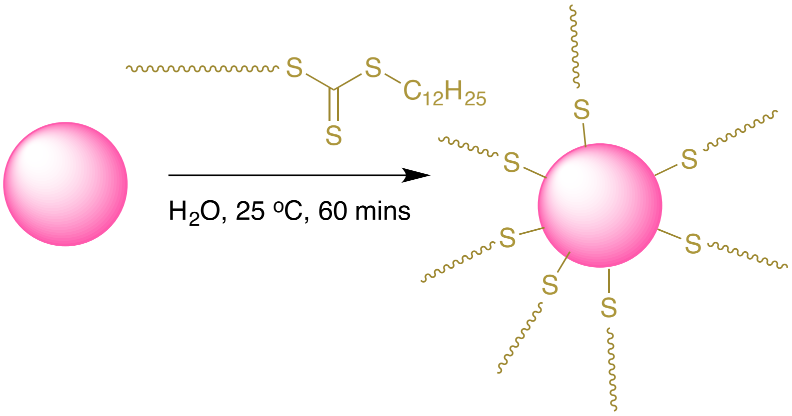

1 mg of pHEA$_{46}$ polymer was added to 1 mL of gold nanoparticles in a 1.5 mL microcentrifuge tube. This was left, covered with foil, for 60 minutes. The solution was centrifuged at 13,200 rpm, for 5 minutes, supernatant removed, and the pellet re-dispersed in 1 mL water. The nanoparticles were washed in this manner a further 3 times before being re-dispersed in a final volume of 1 mL distilled water and stored in

the fridge until required. Nanoparticle size and dispersity was measured by TEM, UV-Vis spectroscopy and size and zeta potential measurements by DLS.

Nanoparticle diameter (TEM): 41.5 nm (standard deviation 4.7 nm).

4.8.3.7. Ni-NTA-pHEA45@Au40

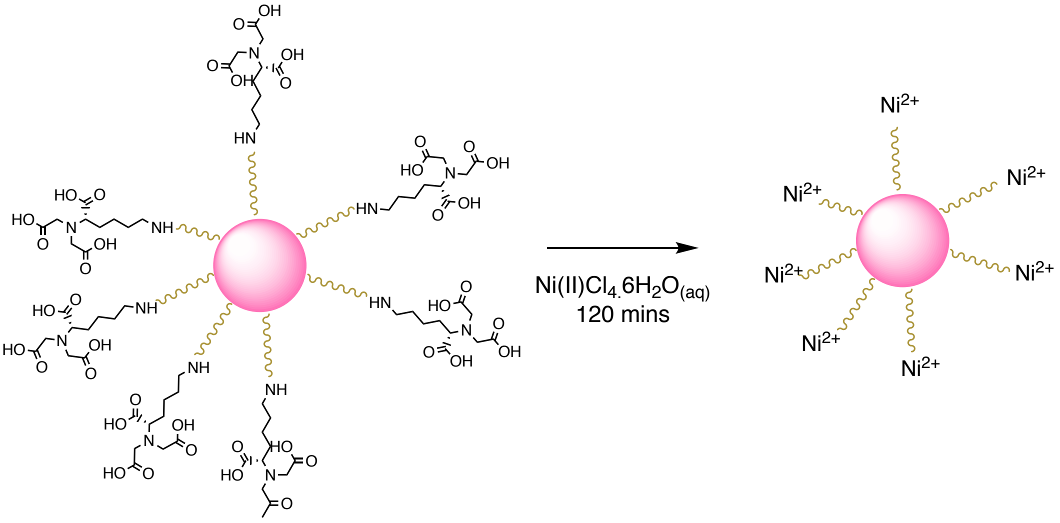

1 mL of NTA-pHEA$_{45}$@Au$_{40}$ solution was centrifuged at 13,200 rpm, for 5 minutes, supernatant removed and Nickel(II) Chloride Hexahydrate (1 mL of 500 µM solution at pH 8 in 10 mM HEPES, 100 mM NaCl buffer) was added to the pellet. This was left, covered with foil, for 60 minutes. The solution was centrifuged at 13,200 rpm, for 6 minutes, supernatant removed, and the pellet re- dispersed in 1 mL water. The nanoparticles were washed in this manner a further 3 times before being re-dispersed in a final volume of 1 mL distilled water and stored in the fridge until required. Nanoparticle size and dispersity was measured by TEM, UV-Vis spectroscopy and size and zeta potential measurements by DLS.

Nanoparticle diameter (TEM): 36.4 nm (standard deviation 3.4 nm).

4.8.3.8. Synthesis of LUMT-Ni-NTA-pHEA45@Au40

Recombinant LUMT PVC tail fibre protein with a hexa-histidine tag was provided by Joseph Healey of the Waterfield Group, University of Warwick. 1 mL of Ni-NTA-pHEA$_{45}$@Au$_{40}$ solution was centrifuged at 13,200 rpm, for 6 minutes, supernatant removed and LUMT protein in HEPES buffer (4.6 µg/mL protein in 10 mM HEPES, 100 mM NaCl) was added to the pellet. This was left, covered with foil, for 120 minutes. The solution was centrifuged at 13,200 rpm, for 6 minutes, supernatant removed, and the pellet re- dispersed in 1 mL water. The nanoparticles were washed in this manner a further 3 times before being re-dispersed in a final volume of 1 mL distilled water and stored in the fridge until required. Nanoparticle size and dispersity was measured by TEM, UV-Vis spectroscopy and size and zeta potential measurements by DLS.

Nanoparticle diameter (TEM): 30.3 nm (standard deviation 3.8 nm).

4.8.3.9. Rejuvenation and passage of cultured A549 cells

A single 1 mL cryopreserved aliquot (10 % (v/v) DMSO in complete medium) in a 1.8 mL cryovials of cells was removed from cryostorage ($N_{2(l)}$) and immediately thawed rapidly in a 37 °C water bath. Thawed cells were then immediately placed in a 75 cm^3 flask containing 20 mL of pre-warmed medium and incubated overnight. Phase-contrast light microscopy (Nikon UK Limited, Surrey, UK) was used to confirm the presence of adherent cells and the medium aspirated and cells washed with 10 mL of PBS to remove any non-adherent cells, debris and residual DMSO. 20 mL of pre-warmed medium was added and cells incubated until confluency.

The following quantities are based on transfer from/to a 175 cm^3 flask, and should be adjusted according to these volumes for different-sized flasks. Confluence is defined as 70-80 % of the total surface area consisting of cultured cells according to light microscopy. All cells were incubated at 37 °C in a 5 % $CO_{2(g)}$ humidified atmosphere. Medium from confluent cells was removed and the cells were washed with 25 mL PBS and replaced with 3.5 mL 0.25 % (w/v) trypsin solution. The flask was incubated for 5 minutes to ensure all cells were detached but not allowed to aggregate. The trypsin solution was neutralized by the addition of 3.5 mL of media, and the cells pelleted and resuspended in 1 mL media. Trypan blue was used, along with a hemocytometer, to determine cell concentration by light microscopy. 1 ml was removed and transferred into a 175 cm^3 flask containing 25 mL of pre-warmed (37 °C) media. The flask was then replaced in the incubator and cells allowed to adhere and proliferate to 70-80 % confluency

4.8.3.10. MTT Reduction assay

The following details a MTT reduction assay for cells seeded in a 96-well plate format. A549 cells (1 x 10^4 cells/well) were seeded in phenol-free (otherwise complete) medium in a 96-well plate and incubated for 3 hours at 37 °C in a 5 % $CO_{2(g)}$ humidified atmosphere. Medium was removed and replaced with 100 μL analyte in pre-warmed (37 °C) phenol-free (otherwise complete) medium. Cells were incubated for 24 hours. After incubation, medium was removed, cells washed with 100 μL PBS and replaced with 100 μL phenol-free (otherwise complete) medium. 10 μL of MTT (10 mg/mL) was added in each well and the plate was incubated for 3 hours. After incubation, 100 μL DMSO was added to solubilize insoluble formazan, and the plate was agitated in a plate shaker for 30 minutes at room temperature to give a uniform distribution of product. Absorbance was measured by plate-reader at $\lambda1 = 570$ nm and $\lambda2 = 630$ nm to show the mitochondrial reduction of yellow MTT to purple/blue formazan. This assay was repeated three times, with duplicates of each analyte in each assay. Results were analysed as the average of viability (% of the untreated control in medium) +/- standard deviation. This allowed a calculation of percentage cell recovery after treatment with analytes. A single-factor ANOVA test was used to assess whether the LUMT@AuNP incubation data were significantly dissimilar from the pHEA@AuNP incubation data.

4.8.3.11. Live/Dead assay

The following details a Live/Dead assay for cells seeded in a 96-well plate format. A549 cells (1 x 10^4 cells/well) were seeded in phenol-free (otherwise complete) medium in a 96-well plate and incubated for 3 hours at 37 °C in a 5 % $CO_{2(g)}$ humidified atmosphere. For visualization assays, black clear-bottomed plates were used, whilst for plate-reader assays black plates were used. Medium was removed and replaced with 100 μL analyte in pre-warmed (37 °C) phenol-free (otherwise complete) medium. Controls (live and dead) were incubated in phenol-free (otherwise complete) medium. Cells were incubated for 24 hours. After incubation, medium was removed, cells washed twice with 100 μL PBS and replaced with 100 PBS (except for dead control, which was replaced with 100 μL methanol). 2 x Live/Dead solution was made up as 4 μL EthD-1, 1 μL Calcein AM and 2 ml PBS and vortexed to ensure dissolution. 100 μL of this solution was added to each well, and the plate was incubated for 30 minutes at 37 °C in a 5 % $CO_{2(g)}$ humidified atmosphere. For the visualization assay, fluorescence microscopy was performed with red and green filters taken for each image. For the plate reader assay, the plate was read at excitation/emission of 485/530 nm and 530/645 nm for Calcein AM and EthD-1 respectively. Viable cells fluoresce green (with Calcein AM uptake) and dead cells fluoresce red (with EthD-1) due to membranolysis. A single-factor ANOVA test was used to assess whether the LUMT@AuNP incubation data were significantly dissimilar from the pHEA@AuNP incubation data.

4.8.3.12. Haemolysis assay

Fresh ovine RBCs as supplied were centrifuged (23 °C, 10 minutes, 1950 g) and the top layer containing residual plasma was removed. The RBCs were resuspended to a volume of 6.25 mL in PBS and mixed thoroughly. 20 µL of RBCs was added to each microcentrifuge, along with 60 µL of analyte, followed by vortexing to mix. For each analyte at temperatures of 4 °C, 25 °C and 37 °C, triplicate samples were prepared to allow averaging. Samples were incubated overnight in darkness at the specified temperature. The next day, 320 µL PBS was added for a 5 x dilution of the RBCs. Samples were centrifuged (23 °C, 10 minutes, 1950 g) and three aliquots of 100 µL were removed to a clear, flat-bottomed 96-well polystyrene plate. Absorbance at 415 nm was measured to give an average and standard deviation for each analyte at each temperature relative to a PBS control. This allowed the calculation of % cell recovery and hemolysis using the following equations. A 100% hemolysis control was calculated as samples suspended in 540 µL H_2O for 5 minutes (induce 100 % hemolysis) before adding 60 µL of 10 x PBS solution. A single-factor ANOVA test was used to assess whether the LUMT@AuNP incubation data were significantly dissimilar from the pHEA@AuNP incubation data.

$$\% \, Hemolysis = \frac{[Abs_{415nm}(sample) - Abs_{415nm}(0\% \, control)]}{[Abs_{415nm}(100\%) - Abs_{415nm}(0\% \, control)]}$$

$$\% \, Cell \, Recovery = \, 100 \, \% - (\%) Hemolysis$$

Equation 1. Calculation of % cell recovery of red blood cells

4.8.3.13. ICP-OES experiments

The following details an ICP-OES experiment assay for A549 cells seeded in a 96-well plate format. The same procedure was used for SW480 cells. This assay was performed in triplicate. A549 cells (1 x 10^4 cells/well) were seeded in medium in a 96-well plate and incubated for 3 hours at 37 °C in a 5 % $CO_{2(g)}$ humidified atmosphere. Medium was removed and replaced with 100 µL analyte in pre-warmed (37 °C) phenol-free (otherwise complete) medium. Cells were incubated for 24 hours. After incubation, medium was removed, cells washed with 100 µL PBS and replaced with 50 µL 0.25 % (w/v) trypsin solution. The microplate was incubated for 5 minutes to ensure all cells were detached but not allowed to aggregate. The trypsin solution was neutralized by the addition of 50 µL of media, and the cells transferred to labeled glass vials. Incubation with aqua regia for 30 minutes was used to atomise the AuNP samples, with the same quantities of aqua regia, media and trypsin present in all samples and calibration controls. All samples were subsequently diluted with distilled water to final nitric acid content of 2 %.

4.8.3.14. General procedure for lysis of adherent mammalian cells

Lysates were prepared according to standard procedures such as recommended by Bio-Rad and Thermo-fisher manuals. This procedure was utilised for the preparation of lysates of A549, CACO2 and SW480 cells. Briefly, cells were washed twice in a 100 mm dish with ice-cold PBS and gently rocked. Ice-cold lysis buffer (1 mL) was added and the dish was tilted in ice for 20 minutes, gently agitating every few minutes. Cells were scraped from the surface using a rubber spatula and the solution was transferred to a microcentrifuge tube. This was centrifuged down for 10 minutes at 4 °C, 12 kRPM and the supernatant removed to a fresh tube. Lysates were stored at -20 °C before use.

4.8.3.15. General procedure for lysis of cells in suspension

Lysates were prepared according to standard procedures such as recommended by Bio-Rad and Thermo-fisher manuals. This procedure was utilised for the preparation of THP1 (mammalian) and S2 (drosophila) cell lysates. Briefly, cells were pelleted at low speed in a 15 mL centrifuge tube and media was removed. Ice-cold PBS was added and the tube inverted to wash the cells. Cells were again pelleted and liquid removed. This washing procedure was repeated. Ice-cold lysis buffer (1 mL) was added and the tube was placed in ice for 20 minutes, gently agitating every few minutes. This was centrifuged for 10 minutes at 4 ºC, 12 kRPM and the supernatant removed to a fresh tube. Lysates were stored at -20 ºC before use.

4.8.3.16. Lysis of *C. elegans* nematode worms

The protocol used was based on a protocol by Walhout, A. J. M. and Boulton, S. J..[54] Cultured *C. elegans* worms were prepared and provided by Dr Alexia Hapeshi of the Waterfield Lab. Worms were washed thrice in cold saline solution (0.1 M NaCl) and centrifuged (2500 G, 4 minutes, 25 °C) to remove residual bacteria and dead worms in the supernatant. The pellet was resuspended in modified CSK lysis buffer (100mM Pipes (pH 6.0), 100mM NaCl, 3mM $MgCl_2$, 1mM PMSF, 0.3M sucrose, 0.5% triton X 100, complete (Roche) protease inhibitor tablets, and Halt^{TM} phosphatase inhibitor cocktail: 2mM β-glycerophosphate, 5mM NaF, 1mM Na_3VO_4, 0.1 μM okadaic acid). The worm solution was twice frozen on dry ice and thawed in a 37 °C water bath. This lysate was dounced in a dounce homogenizer 6 times, followed by centrifugation to collect the soluble lysate supernatant (5000 G, 5 minutes, 25 °C).The pellet was resuspended in half its volume of modified CSK buffer, and micrococcal nuclease solution was added to a final concentration of 3U/μl. The suspension was incubated for 30 minutes, shaking at 37 °C, and the chromatin lysate supernatant collected by centrifugation (5000 G, 5 minutes, 25 °C). The chromatin and soluble lysates were combined to give a *C. elegans* whole lysate.

4.8.3.17. PIP strips fat-binding assay

The PIP Strips^{TM} standard experimental protocol as published by Molecular Probes (MP 23748, 100 pmoles of lipid present in each array spot) was followed, using the manual's recommended buffer preparations. Briefly, the membrane was blocked with blocking buffer (Tris-buffered saline pH 7.5 + 0.1 % Tween (TBS-T) + 3% fatty acid-free BSA) for one hour at room temperature on a rocker. Buffer was removed and the membrane incubated overnight in solution containing recombinant LUMT PVC tail fibre protein with a hexa-histidine tag (provided by Joseph Healey of the Waterfield Group, University of Warwick) (0.5 μg/mL in blocking buffer) at 4 ºC. Following this, the membrane was washed 6 times, incubating 10 mins each time in blocking buffer. The membrane was then incubated in primary antibody (Rabbit IgG diluted in blocking buffer) for 90 minutes and washed. The membrane was then incubated in secondary antibody (Goat anti-rabbit IgG Secondary antibody with HRP, in blocking buffer) for 1 hour and washed. Antibodies were diluted as described by the manufacturer. Finally the membrane was incubated in developing solution (Pierce ECL substrate) or 2 hours and a photo was taken.

4.8.3.18. Glycan array glycan-binding assay

The glycan array kit user manual's standard procedure as published by Dextra (Dextra Glycan Array Kit User Manual v6) was followed, using the manual's recommended buffer preparations. Briefly, 1 μg of protein (recombinant LUMT PVC tail fibre protein with a hexa-histidine tag provided by Joseph Healey of the Waterfield Group, University of Warwick) was prepared in array PBS (62.5 μL) and this was pre-complexed with alexa fluor 488 His-tag antibody (2.5 μL) for 10 minutes at 4 ^{o}C in the dark. A control was also prepared with the same concentration antibody in array PBS. The slide was pre-blocked with 0.5% BSA in array PBS for 5 minutes, followed by two 2 minute washes in just array PBS. Gene frames were applied to the slide and protein or control solution (65 μL for each array) was applied to each array, and these were incubated 30 minutes at room temperature in the dark. The slide was then submerged in 0.5% BSA in array PBS to facilitate gene frame removal, and agitated for 2 minutes, followed by two washes in 0.5% BSA in array PBS. The slide was dried by centrifugation (200 g) for 10 minutes in an empty 50 mL centrifuge tube prior to scanning.

4.8.3.19. General procedure for DynabeadsTM pull-down assay

The Dynabeads^{TM} His-tag isolation and pulldown standard procedure as published by Invitrogen (MAN0017121) was followed, using the manual's recommended buffer preparations. Briefly, lysates were buffer-exchanged into pull-down buffer and histidine-tagged bait protein was exchanged into binding/wash buffer prior to starting the assay. Recombinant LUMT or PNF PVC tail fibre protein was provided by Joseph Healey, whilst recombinant Unit 4 PVC tail fibre protein was provided by Dr Alexia Hapeshi, both of the Waterfield Group, University of Warwick. The dynabeads vial was vortexed to mix the particles, and 50 μL beads were transferred to a microcentrifuge tube. The tube was placed on a magnet for 2 mins to pellet and supernatant was removed. The bait protein sample (<700 μL) was added to the tube and incubated on a roller for 15 minutes at room temperature. The beads were pelleted by applying to a magnet for 2 minutes, supernatant was removed and the beads were washed 4 times by resuspending in bind/wash buffer (300 µL), vortexing, pelleting and removing the supernatant. Lysate sample (<700 µL) was added at this point, the tube was vortexed and incubated on a roller for 30 minutes at room temperature. The beads were pelleted, supernatant was removed and the beads were washed 4 times by resuspending in bind/wash buffer (300 µL), vortexing, pelleting and removing the supernatant. His-elution buffer (50 µL) was added, the tube was vortexed and incubated on a roller for 5 minutes at room temperature. The beads were pelleted and supernatant was removed to a fresh tube. The presence of the bait sample in this elution was determined using SDS-PAGE gel.

4.8.3.20. General procedure for Perseus and Scaffold statistical analysis of Proteomics data

In the Perseus software, a paired t-test (assuming equal variance) was utilised. An s0 value of 2 was selected, to give a greater relative importance on the difference between the means of the sample and control datasets relative to the p value. Proteins with a –logP of greater than 1, and a t-test difference of greater than 0, were selected as candidates. Known contaminants (such as skin debris), and proteins with identification by site alone, were removed from analysis. Throughout processing, the data was assessed visually to determine it was acceptable.

Scaffold analysis was also utilised to identify certain protein hits. Processed Scaffold files were provided by the University of Warwick Proteomics RTP team, and total spectrum and peptide count were used as measures for protein enrichment in the samples relative to the controls. In order to identify a protein as being significantly enriched, the average and total count over the 3 samples had to be higher than the average and total counts for the 3 controls, for both total spectrum count and total unique peptide count.

Data from both Perseus and Scaffold are shown in the accompanying data tables.

4.9. Appendix

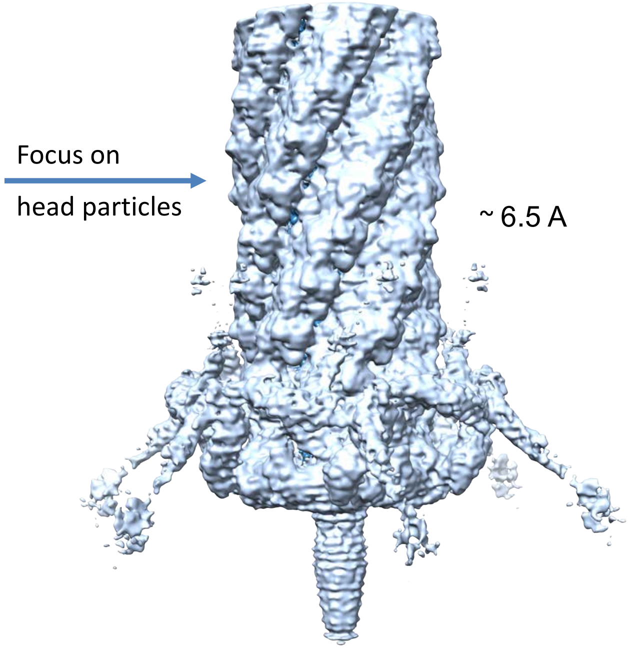

Figure 4-17. Reconstruction of PVC head particle structure from CryoEM. Unpublished results, performed in collaboration with Franziska Leidreiter at the Max Planck Institute of Molecular Physiology, Dortmund, Germany. The presumed Pvc13 binding fibres can be see projecting in 6 fold symmetry from the baseplate region.

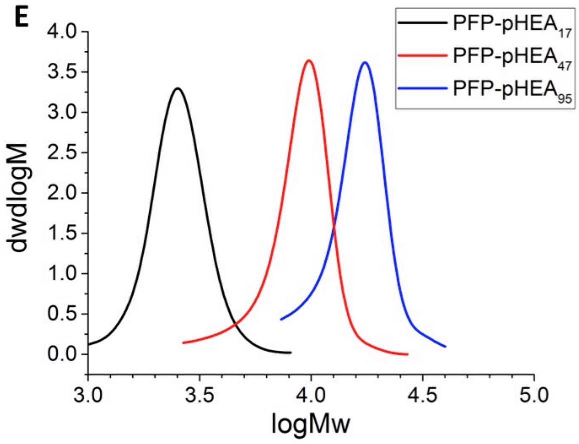

Figure 4-18. Molecular weight distributions, by SEC, of PFP-pHEA library.

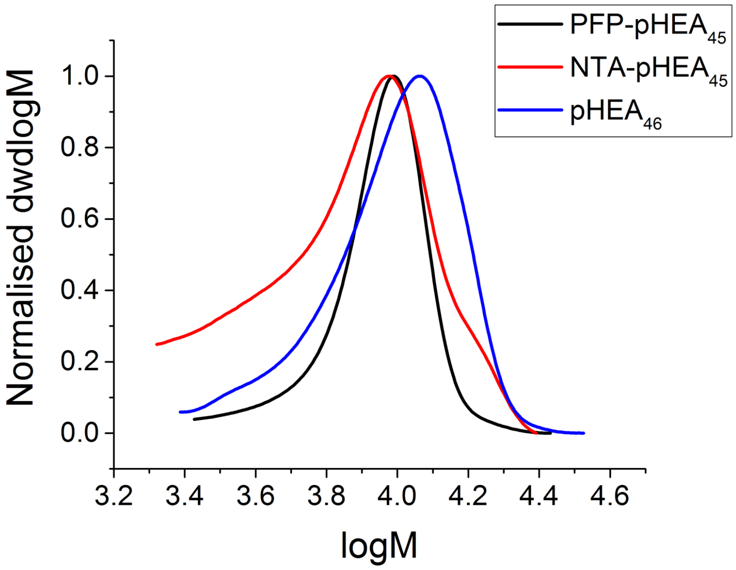

Figure 4-19. Molecular weight distributions, by SEC, of all polymers used in this investigation.

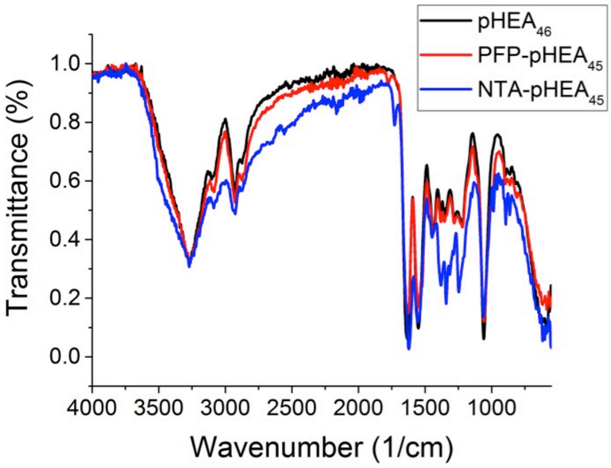

Figure 4-20. FTIR of polymers utilised in this investigation.

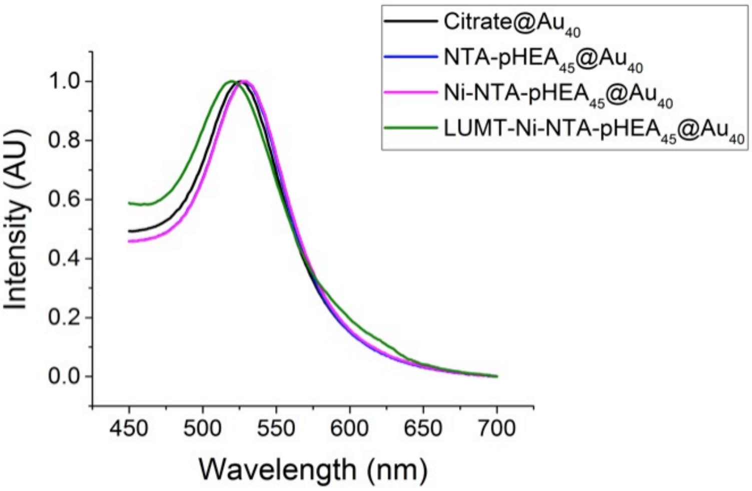

Figure 4-21. UV-Vis spectra for stages of synthesis of LUMT-Ni-NTA-pHEA$_{45}$@Au$_{40}$.

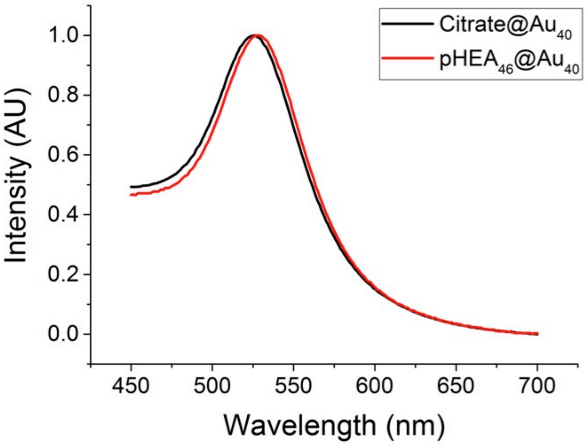

Figure 4-22. UV-Vis spectra for stages of synthesis of pHEA$_{46}$@Au$_{40}$.

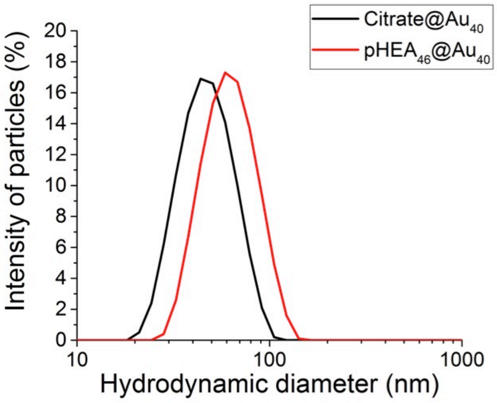

Figure 4-23. DLS data showing distribution of particle sizes by intensity, for stages of synthesis of pHEA$_{46}$@Au$_{40}$.

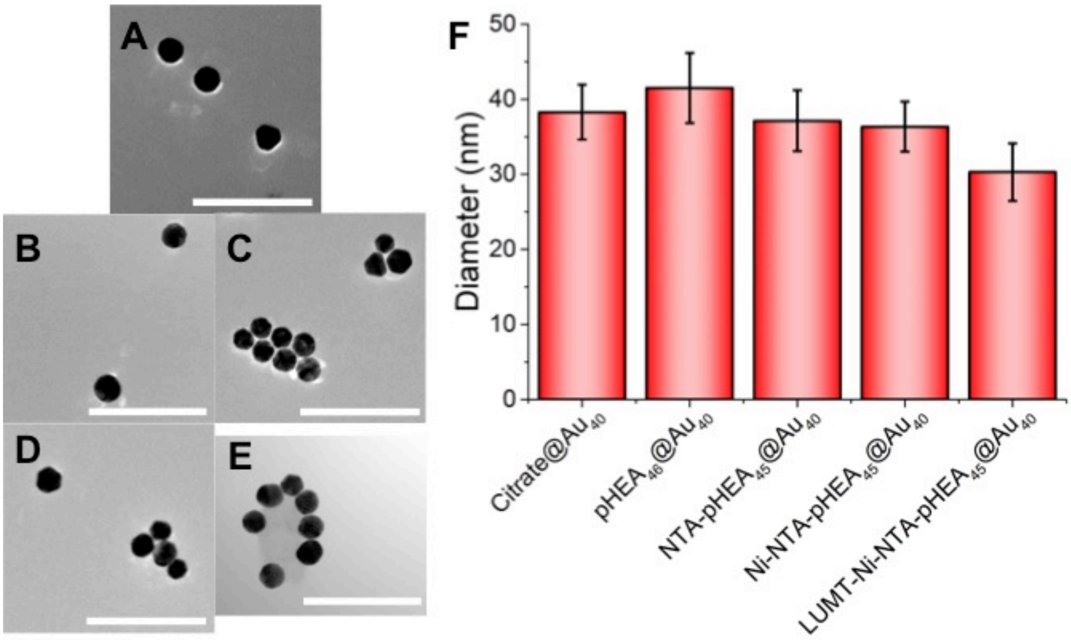

Figure 4-24. TEM datafor all AuNPs used in this study. A) Citrate@Au$_{40}$. B) pHEA$_{46}$@Au$_{40}$. C) NTA-pHEA$_{45}$@Au$_{40}$. D) Ni-NTA-pHEA$_{45}$@Au$_{40}$. E) LUMT-Ni-NTA-pHEA$_{45}$@Au$_{40}$. F) Distribution of particle sizes by TEM, from an average of 30 particles. All scale bars 100 nm.

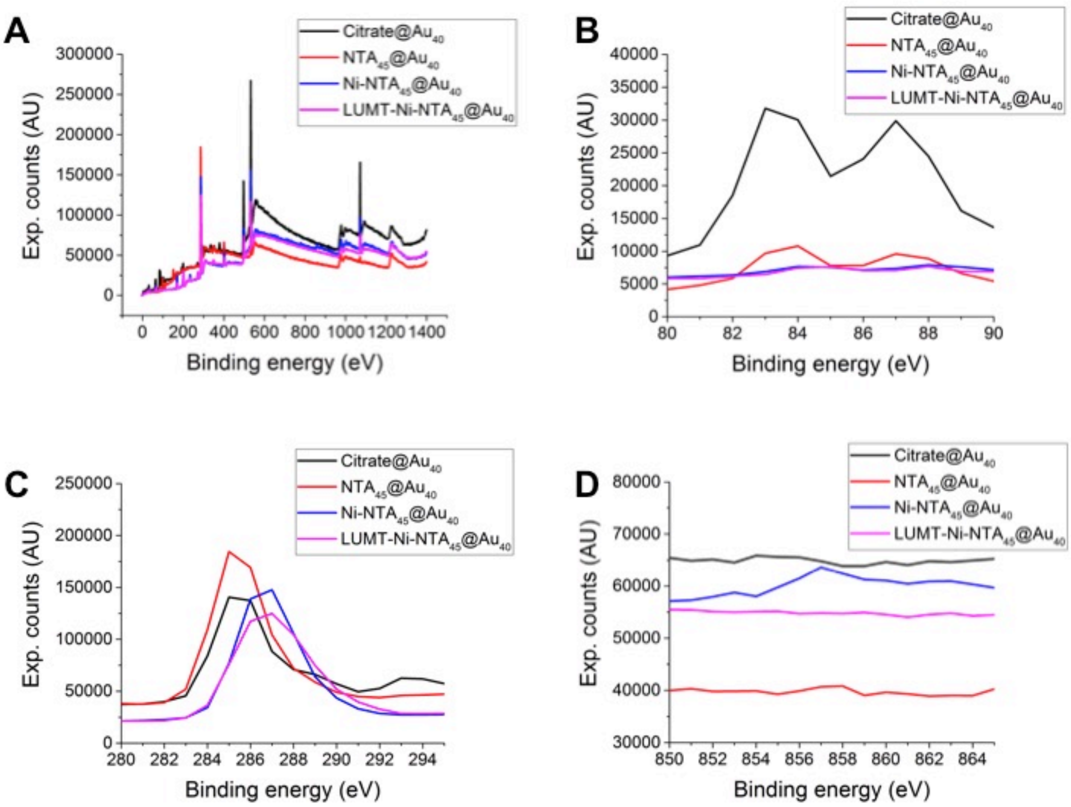

Figure 4-25. XPS data for TEM data for stages of synthesis of LUMT-Ni-NTA-pHEA$_{45}$@Au$_{40}$. A) Survey scans. B) Au 4f peak. C) C 1s peak. D) Ni 2p peak.

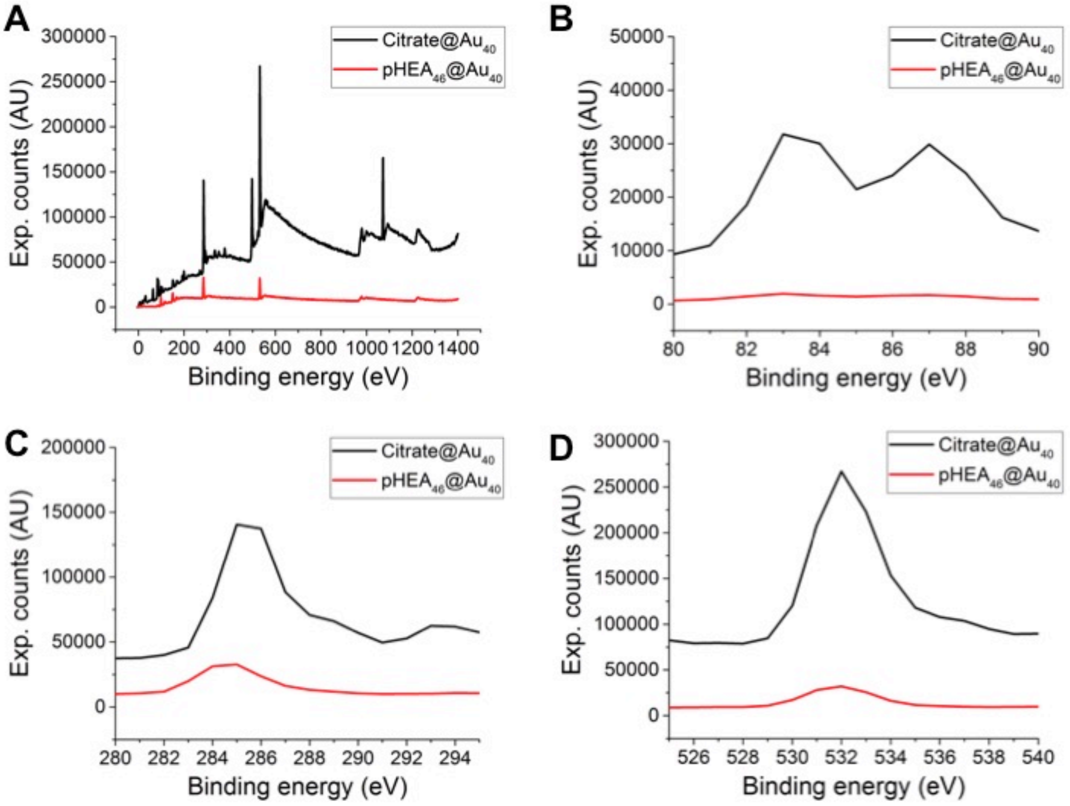

Figure 4-26. XPS data for TEM data for stages of synthesis of pHEA$_{46}$@Au$_{40}$. A) Survey scans. B) Au 4f double peak at 82-88 eV. C) C 1s peak at 284-287 eV. D) O 1s peak at 530-534 eV.

Table 4-9. AuNP sample elemental composition determined by XPS.

Particle	**C**[a]	**O**[a]	**N**[a]	**Ni**[b]	**Au**[c]
Citrate@Au$_4$	56.4	42.0	0.69	0	0.96
pHEA$_{46}$@Au$_{40}$	53.8	43.2	1.94	0	0.51
NTA-pHEA$_{45}$@Au$_{40}$	74.9	20.1	4.71	0	0.31
Ni-NTA-pHEA$_{45}$@Au$_{40}$	67.8	23.0	8.28	0.82	0.08
LUMT-Ni-NTA-pHEA$_{45}$@Au$_{40}$	74.8	19.0	6.02	0	0.12

[a] 1s peak; [b] 2p peak; [c] 4f peak.

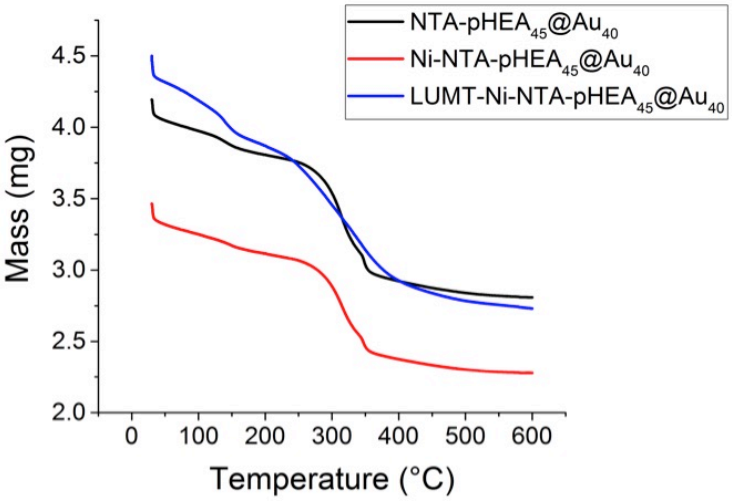

Figure 4-27. TGA temperature curves data for stages of synthesis of LUMT-Ni-NTA-pHEA$_{45}$@Au$_{40}$.

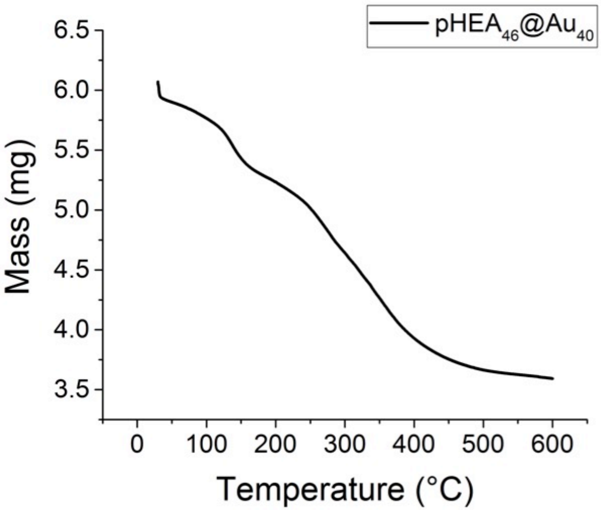

Figure 4-28. TGA temperature curves data for pHEA$_{46}$@Au$_{40}$.

Table 4-10. Masses of organic substances present in LUMT-Ni-NTA-pHEA$_{45}$@Au$_{40}$ samples determined by TGA.

Particle	**Mass present in sample (mg/mL)** [a]
NTA-pHEA$_{45}$ on Au$_{40}$	0.18
LUMT on Au$_{40}$[b]	0.005
pHEA$_{46}$ on Au$_{40}$	0.39

[a] All calculations were taken as the mass difference between 150 and 600, and all AuNP samples were determined to be the same concentration of gold by UV-Vis spectroscopy; [b] All protein-containing sample calculations were blanked relative to HEPES buffer solution, and were then calculated relative to the known organic weight of a protein standard.

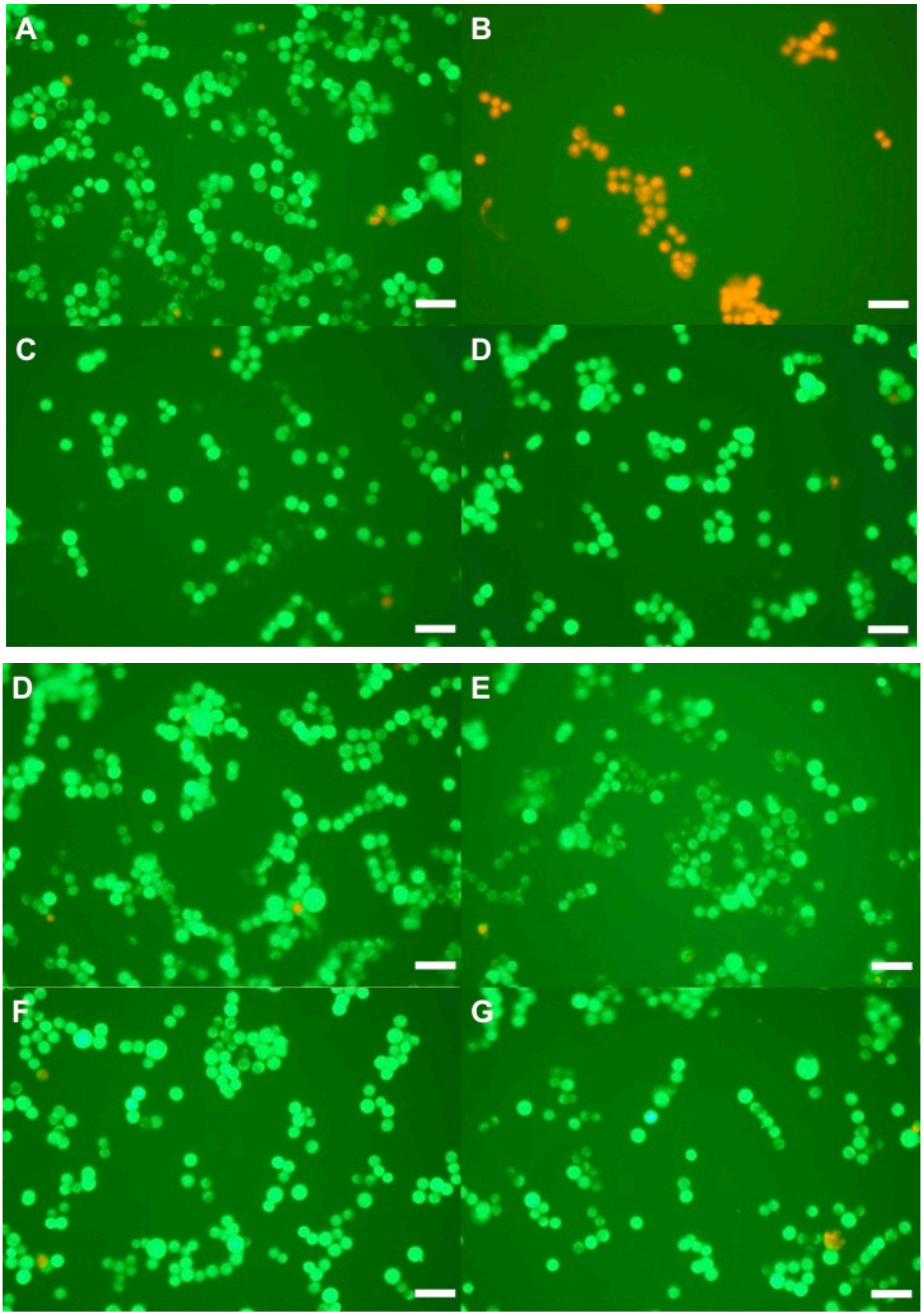

Figure 4-29. Live/dead cell survival assay microscopy images. A) Live control in PBS. B) Dead control in methanol. C/E/G) LUMT-Ni-NTA-pHEA$_{45}$@Au$_{40}$ at 0.3, 0.15 and 0.08 ng/mL AuNP concentration respectively. D/F/H) pHEA$_{46}$@Au$_{40}$ at 0.3, 0.15 and 0.08 ng/mL AuNP concentration respectively. All scale bars 100 µm. Experiments performed with 24 hrs of culture.

Table 4-11. Single-factor ANOVA Statistics completed on cell assays. Each statistical test simply compared the number groups from the control and test groups. The null hypothesis is that the means of these groups are equal (ie. The populations are not significantly different).

Experiment[a]	**F**[b]	**F crit**[b]	**Null hypothesis rejected?**[c]
MTT assay, % viability	0.0007	4.600	No
Live-dead assay, total live cell number	0.4	4.3	No
Hemolysis assay, % lysis	1.4	4.1	No

[a] In each case, data from the LUMT@AuNP incubations was compared to data from pHEA@AuNP incubations. [b] F>F crit results in rejection of the null hypothesis. [c] Null hypothesis rejection suggests there is a significant difference between the test and control groups; if the hypothesis is not rejected, then there is no significant different.

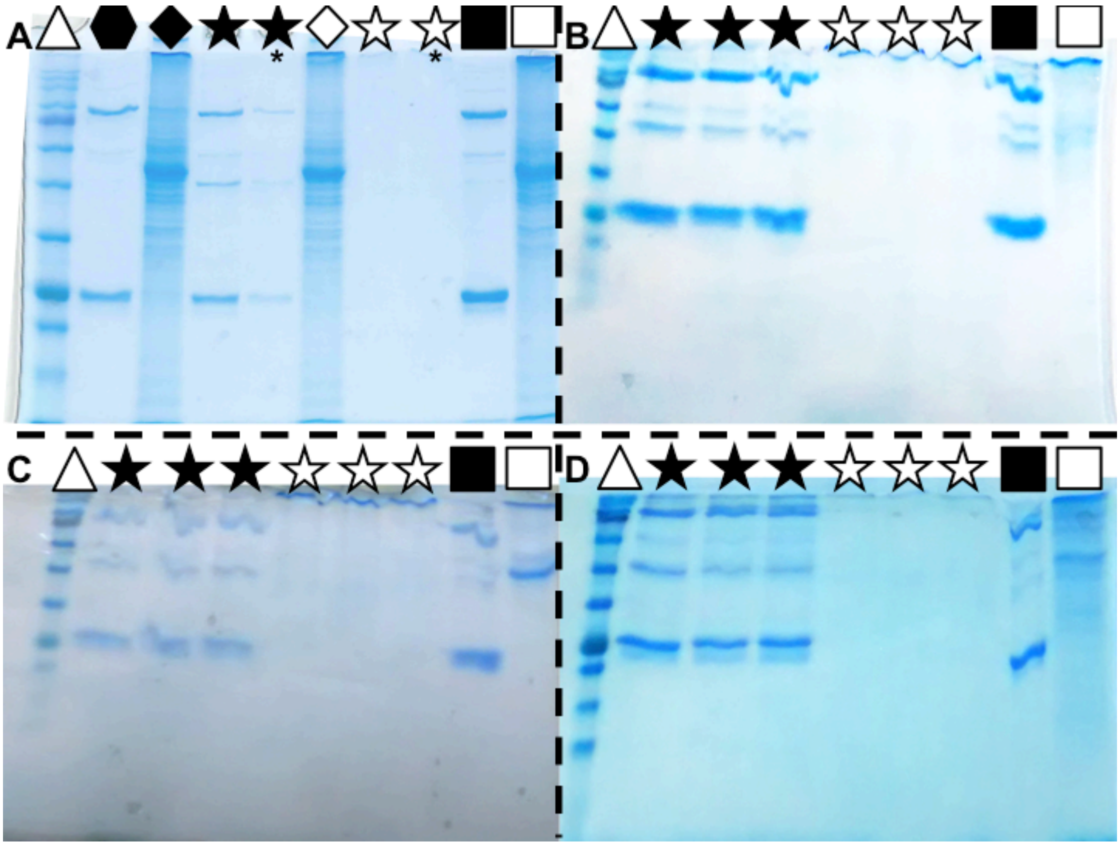

Figure 4-30. SDS-PAGE gels for pull-down experiments using His-tagged recombinant LUMT PVC tail fibre protein in human whole cell lysates. A) A549 human alveolar basal epithelial lysate, B) SW480 human colon adenocarcinoma lysate, C) CACO2 human epithelial colorectal adenocarcinoma lysate, D) THP-1 human monocyte lysate, (see Figure 4-32 for legend).

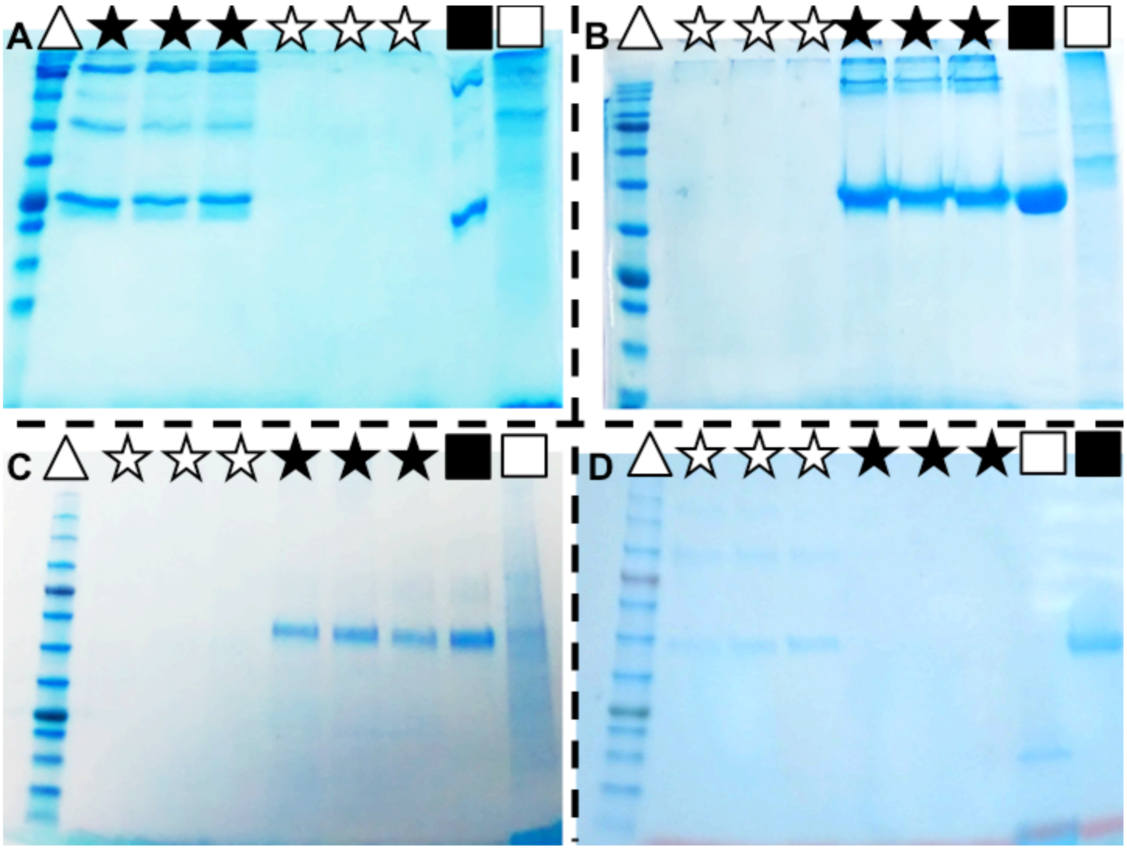

Figure 4-31. SDS-PAGE gels for pull-down experiments using His-tagged recombinant PVC tail fibre protein in whole cell lysates. A-C) Pull-down experiments in S2 *Drosophila melanogaster* macrophage-like cell lysate using bait protein from the LUMT PVC, PNF PVC and Unit 4 PVC constructs respectively. D) Pull-down experiments in *Caenorhabditis elegans* lysate using bait protein from the Unit 4 PVC construct. See Figure 4-32 for legend.

△ Protein ladder

■ Bait protein (recombinant PVC tail fibre from LUMT, PNF or Unit 4 PVC)

□ Lysate

★ Eluent from beads using imidazole solution (sample)
*second elution

☆ Eluent from beads using imidazole solution (control)
*second elution

⬢ Supernatant after bait protein attachment

◆ Supernatant after pull-down with lysate (sample)
*second elution

◇ Supernatant after pull-down with lysate (control)
*second elution

Figure 4-32. Symbol legend for Figures 4-30 and 4-31.

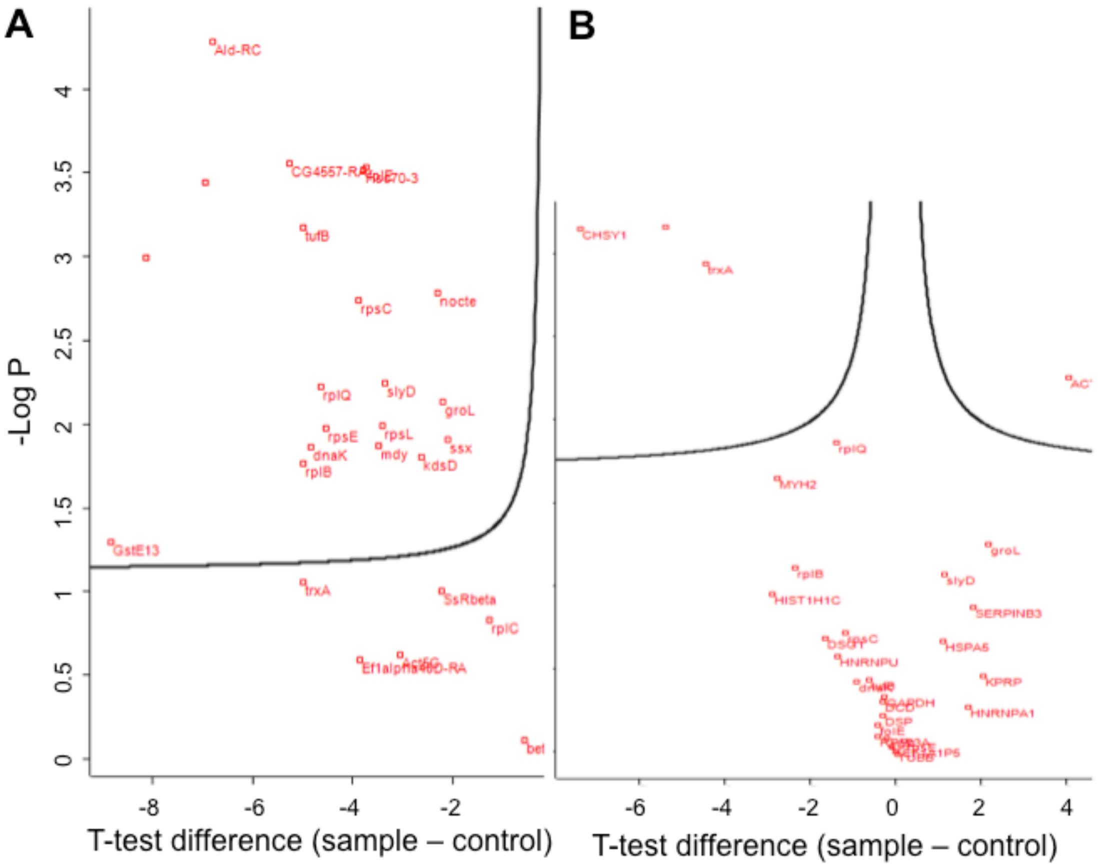

Figure 4-33. Volcano plots from pull-down experiments with His-tagged recombinant tail fibres from the LUMT PVC construct. Experiments with the A) Schneider 2 (S2) *Drosophila melanogaster* macrophage-like cell line and B) SW480 human colon adenocarcinoma cell line.

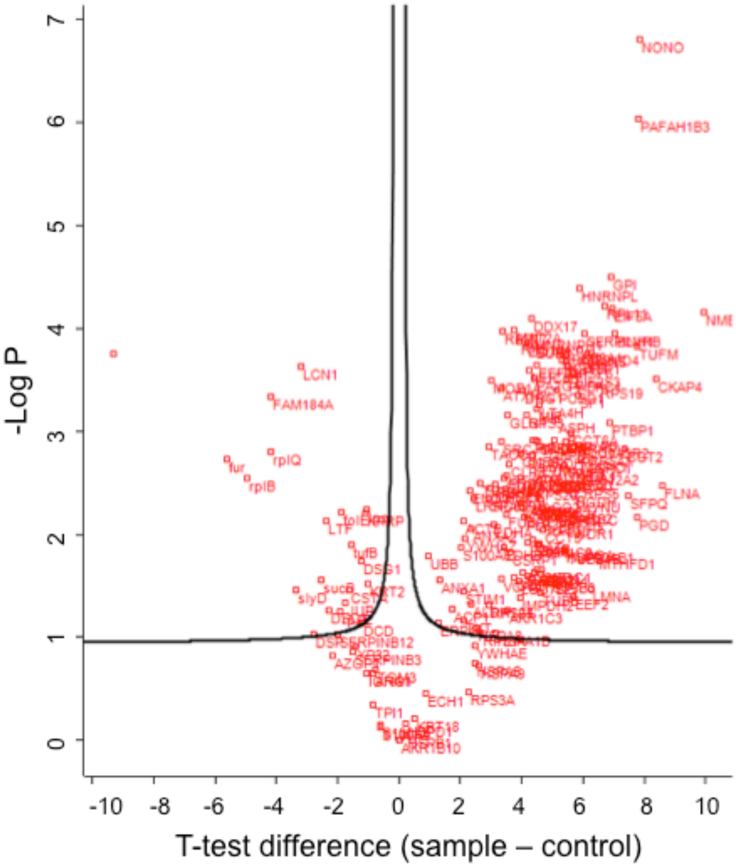

Figure 4-34. Volcano plots from pull-down experiments with His-tagged recombinant tail fibres from the LUMT PVC construct with the A549 human Adenocarcinomic human alveolar basal epithelial cell line.

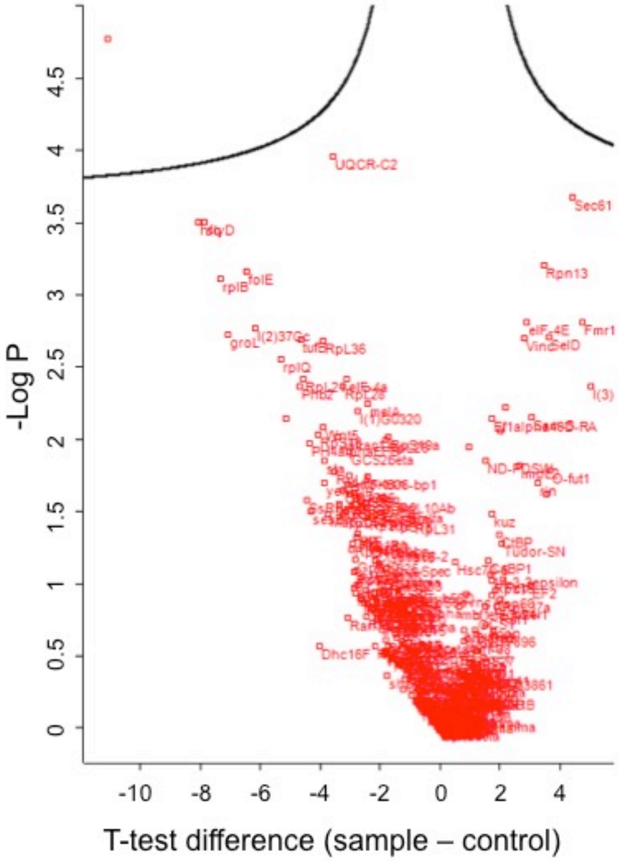

Figure 4-35. Volcano plot from pull-down experiments with His-tagged recombinant tail fibres from the Unit4 PVC construct and Schneider 2 (S2) *Drosophila melanogaster* macrophage-like cell line.

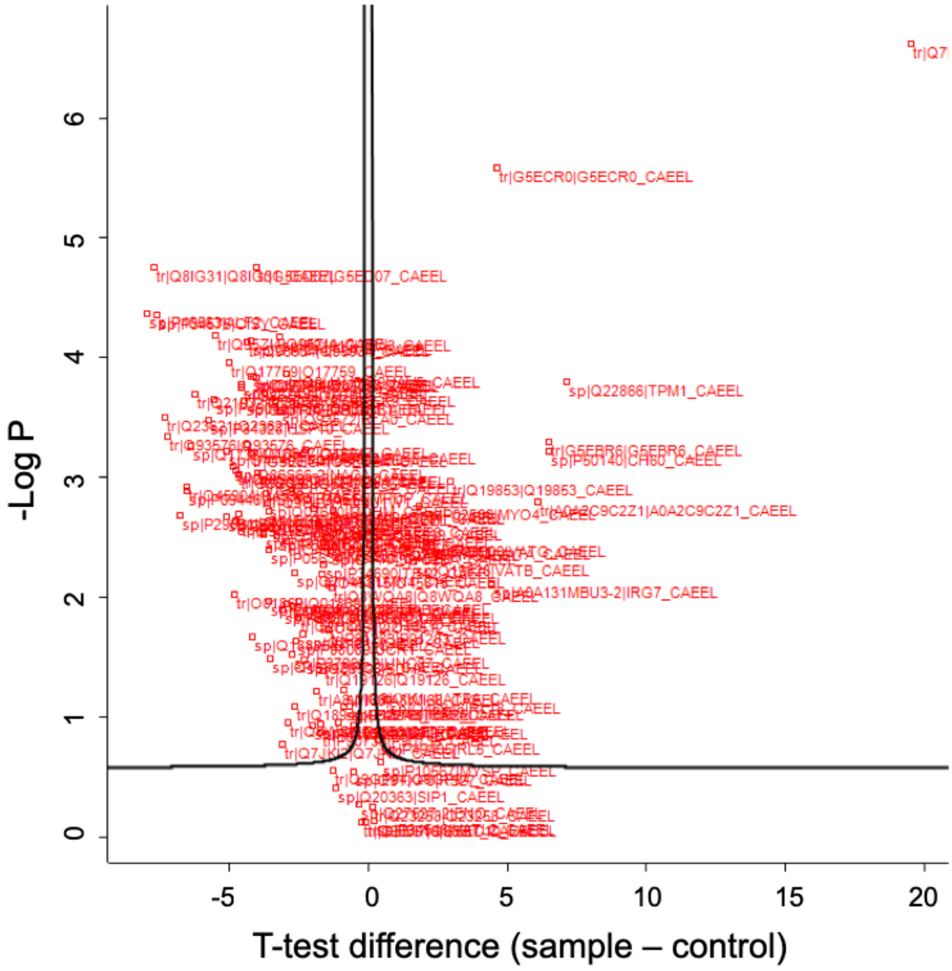

Figure 4-36. Volcano plot from pull-down experiments with His-tagged recombinant tail fibres from the Unit4 PVC construct and *Caenorhabditis elegans* lysate.

Table 4-12. Candidates identified from LUMT pulled down with mammalian lysates: identified in only one experiment

Gene ID	Protein	Lysate with which candidate was identified	Protein expression in human tissue [a]			-Log (p-value) [b]	T-test difference [b]
			Skin	Bone marrow & immune system	Gastro-intestinal tract		
CAP1	Adenylyl cyclase-associated protein 1	THP-1	✓✓	✓✓✓	✓✓✓	8.00 *	4.00 [+]
CLIC1	Chloride intracellular channel protein 1	A549	✓✓	✓✓	✓✓✓	1.53	3.01
CORO1C	Coronin-1C; Coronin	A549	✓✓✓	✓✓✓	✓✓✓	2.48	5.69
CTTN	Src substrate	A549	✓✓	✓✓✓	✓✓✓	2.10	6.02
EZR	Ezrin	SW480	✓✓	✓✓✓	✓✓✓	1.00 *	1.00 [+]
G3BP1	Ras GTPase-activating protein-binding protein 1	THP-1	✓✓	✓✓✓	✓✓✓	0.67 *	0.67 [+]
G6PD	Glucose-6-phosphate 1-	A549	✓✓	✓✓✓	✓✓	2.84	4.80
GNB2L1	Guanine nucleotide-binding protein subunit	A549	n/a	n/a	n/a	1.83	5.80
GSDMA	Gasdermin-A	CACO2	✓✓	✗	✗	0.67 *	0.67 [+]
PDIA6	Protein disulfide-	SW480	✓✓	✓✓✓	✓✓✓	1.00 *	1.00 [+]
PTRF	Polymerase I and transcript release factor	SW480	✓✓	✓✓	✓✓	0.67 *	0.67 [+]

SLC12A2	Solute carrier family 12 member	A549	✓	✓✓✓	✓✓✓	2.61	5.89
SLC3A2	4F2 cell-surface antigen heavy chain	A549	✓	✓	✓✓	1.63	4.03
SLC9A3R2	Na(+)/H(+) exchange regulatory cofactor	A549	✗	✗	✓✓✓	2.87	5.87
SPRR1B	Cornifin-B	SW480	n/a	n/a	n/a	0.67 *	0.67 $^{+}$
STIM1	Stromal interaction	A549	✓✓	✓✓	✓✓✓	2.67	3.06
XP32	Skin-specific	A549	n/a	n/a	n/a	2.00 *	0.67 $^{+}$
CTSG	Cathepsin G	THP-1	✗	✓✓✓	✗	7.67 *	4.00 $^{+}$

[a] The Human Protein Atlas was used to obtain this information, [b] From Perseus software, student's t-test between Sample and Control. ✓✓✓ = high. ✓✓ = medium. ✓ = low. ✗ = not detected. n/a = protein either not in database, or is not annotated with protein expression.

Table 4-13. Candidates identified from S2 lysate pulled down by one recombinant PVC tail fibre, where cellular localisation is known to include the plasma membrane or cell projection

Gene ID	Protein name	Lysate with which candidate was identified	-Log (p-value) [a]	T-test difference [a]
Acsl	Acyl-CoA synthetase long-chain, isoform J	Unit 4	0.67 *	0.67 $^{+}$
alt	Aluminum tubes, isoform G	Unit 4	4.67 *	4.67 $^{+}$
beta-Spec	Spectrin β chain	Unit 4	1.00 *	1.00 $^{+}$
BuGZ	Bub3 interacting GLEBS and zinc finger domain protein, isoform A	Unit 4	1.33 *	1.33 $^{+}$
CD98hc	CD98 heavy chain, isoform D	Unit 4	0.67 *	0.67 $^{+}$
Chc	Clathrin heavy chain	Unit 4	0.67 *	0.67 $^{+}$

cher	Cheerio, isoform I	Unit 4	0.67 *	0.67^{+}
chic	Profilin	Unit 4	2.67 *	1.67^{+}
Chro	Chromator, isoform A	Unit 4	2.33 *	2.33^{+}
Cnx99A	Calnexin 99A, isoform E	Unit 4	1.67 *	1.33^{+}
Cont	Contactin	Unit 4	3.67 *	3.33^{+}
cpa	F-actin-capping protein subunit α	Unit 4	2.33 *	2.00^{+}
Desat1	Desaturase 1, isoform A	Unit 4	0.67 *	0.67^{+}
Dhc93AB	Dynein heavy chain at 93AB, isoform C	PNF	0.67 *	0.67^{+}
Dscam1	Down syndrome cell adhesion molecule 1, isoform CA (Fragment	Unit 4	3.33 *	3.33^{+}
Edem1	α-1,2-Mannosidase	Unit 4	0.67 *	0.67^{+}
EMC1	ER membrane protein complex 1, isoform C	Unit 4	0.67 *	3.67^{+}
ergic53	Ergic53, isoform A	Unit 4		
Fmr1	Fragile X mental retardation syndrome-related protein 1	PNF	2.02	3.29
Gp150	Gp150, isoform E	Unit 4	3.33 *	3.00^{+}
Hmu	FI18644p1	Unit 4	11.7 *	6.00^{+}
Khc	Kinesin heavy chain	Unit 4	0.67 *	0.67^{+}
kst	Karst, isoform E	Unit 4	0.67 *	0.67^{+}
kuk	Kugelkern, isoform A	Unit 4	0.67 *	0.67^{+}
kuz	Kuzbanian, isoform F	Unit 4	1.67 *	1.33^{+}
muc	Midline uncoordinated, isoform A	Unit 4	5.33 *	4.00^{+}
Nap1	LD21576p	Unit 4	1.67 *	1.67^{+}
Nrx-IV	Neurexin-4	Unit 4	1.33 *	1.33^{+}

Phb2	Prohibitin 2, isoform E	Unit 4	21.3 *	10.7 $^+$
Pvr	PDGF-and VEGF-receptor related, isoform G	Unit 4	0.67 *	0.67 $^+$
Ran	GTP-binding nuclear protein	Unit 4	4.67 *	2.67 $^+$
Rap1	Rap1 GTPase, isoform B	Unit 4	0.67 *	0.67 $^+$
Rho1	Ras-like GTP-binding protein Rho1	Unit 4	1.00 *	1.00 $^+$
Sc2	Sc2	Unit 4	2.67 *	1.33 $^+$
sesB	Stress-sensitive B, isoform E	Unit 4	8.33 *	5.33 $^+$
SH3PX1	Sorting nexin	Unit 4	1.00 *	1.00 $^+$
shi	Shibire, isoform F	Unit 4	1.33 *	1.33 $^+$
SrpRbeta	GM04779p	Unit 4	1.67 *	1.00 $^+$
Stim	FI18406p1	Unit 4	4.33 *	3.33 $^+$
Tap42	LD07294p	Unit 4	1.33 *	1.33 $^+$
Tctp	Translationally controlled tumor protein ortholog, isoform B	Unit 4	0.67 *	0.67 $^+$
TER94	TER94, isoform E	Unit 4	0.67 *	0.67 $^+$
Tm1	Tropomyosin 1, isoform Q	Unit 4	0.67 *	0.67 $^+$
UQCR-C2	AT02348p	Unit 4	15.0 *	8.67 $^+$
Vha68-2	MIP16230p	Unit 4	2.00 *	1.33 $^+$
vnc	LD19812p	Unit 4	1.67 *	1.33 $^+$
zip	Zipper, isoform F	Unit 4	0.67 *	0.67 $^+$

[a] From Perseus software, student's t-test between Sample and Control. */$^+$ Identified by Scaffold software analysis, difference in average (over 3 samples and controls) total unique spectra or total unique peptides respectively.

Table 4-14. Candidates identified from S2 lysate pulled down by one recombinant PVC tail fibre, where cellular localisation is unknown.

Gene ID	**Protein name**	**Lysate with which candidate was identified**	**-Log (p-value) [a]**	**T-test difference [a]**
Ahcy	Adenosylhomocysteinase	Unit 4	1.00 *	0.67 $^+$
Aldh-III	Aldehyde dehydrogenase	Unit 4	1.33 *	1.33 $^+$
BcDNA	CG8108, isoform A	Unit 4	7.67 *	6.33 $^+$
cDIP	Common Dpr-interacting protein	Unit 4	6.33 *	4.33 $^+$
CG10166	Probable dolichol-phosphate mannosyltransferase	Unit 4	1.00 *	0.67 $^+$
CG11505	La-related protein CG11505	Unit 4	3.00 *	2.33 $^+$
CG11999	GH21273p	Unit 4	4.33 *	3.67 $^+$
CG12909	CG12909 protein	Unit 4	0.67 *	0.67 $^+$
CG13321	RE03883p	Unit 4	0.67 *	0.67 $^+$
CG1371	CG1371	Unit 4	0.67 *	0.67 $^+$
CG18259-RA	FI13061p	Unit 4	0.67 *	0.67 $^+$
CG31915	Glycosyltransferase 25 family member	Unit 4	3.33 *	2.33 $^+$
CG3224	Zinc finger protein 593 homolog	Unit 4	4.67 *	3.00 $^+$
CG3817	RRP15-like protein	Unit 4	1.33 *	1.33 $^+$
CG5482	Peptidylprolyl isomerase	Unit 4	1.00 *	0.67 $^+$
CG6422	CG6422, isoform A	Unit 4	2.00 *	1.67 $^+$
CG7461	CG7461, isoform B	Unit 4	1.00 *	1.00 $^+$
CG7556	CG7556, isoform A	Unit 4	0.67 *	0.67 $^+$
CG7800-RA	CG7800	Unit 4	5.00 *	3.00 $^+$
CG8326	CG8326	Unit 4	0.67 *	0.67 $^+$

CG8507	CG8507	Unit 4	39.7 *	24.0 $^{+}$
CG9784	CG9784, isoform C	Unit 4	0.67 *	0.67 $^{+}$
CG9911	CG9911, isoform A	Unit 4	9.00 *	7.67 $^{+}$
CNBP	CG3800, isoform B	Unit 4	0.67 *	0.67 $^{+}$
CT23145	CG7565	Unit 4	0.67 *	0.67 $^{+}$
fl	Female lethal d, isoform C	Unit 4	2.33 *	1.67 $^{+}$
Gale	UDP-glucose 4-epimerase	Unit 4	5.33 *	3.67 $^{+}$
muc	Midline uncoordinated, isoform A	Unit 4	5.33 *	4.00 $^{+}$
nolo	No long nerve cord	Unit 4	3.00 *	2.67 $^{+}$
O-fut1	GDP-fucose protein O-fucosyltransferase 1	PNF	2.43	5.57
Pdi	Protein disulfide-isomerase	Unit 4	3.33 *	3.00 $^{+}$
spidey	CG1444	Unit 4	1.00 *	1.00 $^{+}$
Ubi-p63E	Ubiquitin-63E, isoform C	LUMT	0.67 *	1.00 $^{+}$
Ugt58Fa	RE07815p	Unit 4	5.67 *	3.67 $^{+}$

[a] From Perseus software, student's t-test between Sample and Control. */$^{+}$ Identified by Scaffold software analysis, difference in average (over 3 samples and controls) total unique spectra or total unique peptides respectively.

Table 4-15. Candidates identified from *Caenorhabditis elegans* lysate pulled down by Unit 4 recombinant PVC tail fibre, where cellular localisation is unknown or not to plasma membrane.

Accession Number [a]	**-Log (p-value)** [b]	**T-test difference**	**Protein name** [a]	**Function** [c]
CH60	3.22 7.33 *	6.49 7.00 $^{+}$	Chaperonin homolog Hsp-60, mitochondrial	Localised to mitochondria. Involved in protein import and macromolecular assembly, preventing misfolding and promoting refolding
CON__P07477	0.33 *	0.33 $^{+}$	Uncharacterised protein	Unknown
CON__P67983	0.33 *	0.33 $^{+}$		
G5EBR6	3.30 0.33 *	6.49 0.33 $^{+}$		
Q18577	0.33 *	0.33 $^{+}$	Uncharacterised protein	Unknown
Q19336	0.33 *	0.33 $^{+}$		Unknown, potentially localised to nucleus
Q21889	0.33 *	0.33 $^{+}$		Unknown
SIP1	0.33 *	0.33 $^{+}$	Stress-induced protein 1	Binds to unfolded proteins, localised to cytosol
Q564R5_CAE	0.67 *	0.67 $^{+}$	Uncharacterised protein	Unknown
Q95XI9	0.33 *	0.33 $^{+}$		Proton-transporting ATPase activity, rotational mechanism
YQI7	1.00 *	1.00 $^{+}$		Unknown

[a] For Uniprot database (note that those from *Caenorhabditis elegans* also have “CAEEL” after their accession number, [b] From Perseus software, student’s t-test between Sample and Control, [c] According to Uniprot database (including data from Wormbase database). */$^{+}$ Identified by Scaffold software analysis, difference in average (over 3 samples and controls) total unique spectra or total unique peptides respectively.

4.10. References

(1) Waterfield, N. R.; Ciche, T.; Clarke, D. *Annu. Rev. Microbiol.* **2009**, *63* (1), 557.

(2) Brachmann, A. O.; Kirchner, F.; Kegler, C.; Kinski, S. C.; Schmitt, I.; Bode, H. B. *J. Biotechnol.* **2012**, *157* (1), 96.

(3) Tounsi, S.; Blight, M.; Jaoua, S.; de Lima Pimenta, A. *Int. J. Med. Microbiol.* **2006**, *296* (8), 521.

(4) Yin, J.; Zhu, H.; Xia, L.; Ding, X.; Hoffmann, T.; Hoffmann, M.; Bian, X.; Müller, R.; Fu, J.; Stewart, A. F.; Zhang, Y. *Nucleic Acids Res.* **2015**, *43* (6), e36.

(5) Waterfield, N. R.; Daborn, P. J.; Ffrench-Constant, R. H. *Physiol. Entomol.* **2004**, *29* (3 SPEC. ISS.), 240.

(6) Blackburn, M.; Golubeva, E.; Bowen, D.; Ffrench-Constant, R. H. *Appl. Environ. Microbiol.* **1998**, *64* (8), 3036.

(7) Bowen, D. J.; Ensign, J. C. *Appl. Environ. Microbiol.* **1998**, *64* (8), 3029.

(8) Wilkinson, P.; Waterfield, N. R.; Crossman, L.; Corton, C.; Sanchez-Contreras, M.; Vlisidou, I.; Barron, A.; Bignell, A.; Clark, L.; Ormond, D.; Mayho, M.; Bason, N.; Smith, F.; Simmonds, M.; Churcher, C.; Harris, D.; Thompson, N. R.; Quail, M.; Parkhill, J.; Ffrench-Constant, R. H. *BMC Genomics* **2009**, *10*, 1.

(9) Rodou, A.; Ankrah, D. O.; Stathopoulos, C. *Toxins (Basel).* **2010**, *2* (6), 1250.

(10) Bowen, D.; Rocheleau, T. A.; Blackburn, M.; Andreev, O.; Golubeva, E.; Bhartia, R.; Ffrench-Constant, R. H. *Science (80-.).* **1998**, *280* (5372), 2129.

(11) Yang, G.; Dowling, A. J.; Gerike, U.; Ffrench-Constant, R. H.; Waterfield, N. R. *J. Bacteriol.* **2006**, *188* (6), 2254.

(12) Ciche, T. A.; Darby, C.; Ehlers, R. U.; Forst, S.; Goodrich-Blair, H. *Biol.*

Control **2006**, *38* (1), 22.

(13) Ciche, T. A.; Kim, K. S.; Kaufmann-Daszczuk, B.; Nguyen, K. C. Q.; Hall, D. H. *Appl. Environ. Microbiol.* **2008**, *74* (8), 2275.

(14) Ffrench-Constant, R. H.; Dowling, A.; Waterfield, N. R. *Toxicon* **2007**, *49* (4), 436.

(15) Gaudriault, S.; Duchaud, E.; Lanois, A.; Canoy, A. S.; Bourot, S.; DeRose, R.; Kunst, F.; Boemare, N.; Givaudan, A. *J. Bacteriol.* **2006**, *188* (2), 809.

(16) Shikuma, N. J.; Pilhofer, M.; Weiss, G. L.; Hadfield, M. G.; Jensen, G. J.; Newman, D. K. *Science* **2014**, *343* (6170), 529.

(17) Rybakova, D.; Radjainia, M.; Turner, A.; Sen, A.; Mitra, A. K.; Hurst, M. R. H. *Mol. Microbiol.* **2013**, *89* (4), 702.

(18) Heymann, J. B.; Bartho, J. D.; Rybakova, D.; Venugopal, H. P.; Winkler, D. C.; Sen, A.; Hurst, M. R. H.; Mitra, A. K. *J. Biol. Chem.* **2013**, *288* (35), 25276.

(19) Hurst, M. R. H.; Glare, T. R.; Jackson, T. A.; Ronson, C. W. *J. Bacteriol.* **2000**, *182* (18), 5127.

(20) Gerrard, J. G.; Joyce, S. A.; Clarke, D. J.; Ffrench-Constant, R. H.; Nimmo, G. R.; Looke, D. F. M.; Feil, E. J.; Pearce, L.; Waterfield, N. R. *Emerg. Infect. Dis.* **2006**, *12* (10), 1562.

(21) Gerrard, J.; Waterfield, N.; Vohra, R.; Ffrench-Constant, R. *Microbes Infect.* **2004**, *6* (2), 229.

(22) Kuwata, R.; Yoshiga, T.; Yoshida, M.; Kondo, E. *Microbes Infect.* **2008**, *10* (7), 734.

(23) Plichta, K. L.; Joyce, S. A.; Clarke, D.; Waterfield, N.; Stock, S. P. *J. Helminthol.* **2009**, *83*, 309.

(24) Chaston, J. M.; Suen, G.; Tucker, S. L.; Andersen, A. W.; Bhasin, A.; Bode, E.; Bode, H. B.; Brachmann, A. O.; Cowles, C. E.; Cowles, K. N.; Darby, C.; de Léon, L.; Drace, K.; Du, Z.; Givaudan, A.; Herbert Tran, E. E.; Jewell, K. A.; Knack, J. J.; Krasomil-Osterfeld, K. C.; Kukor, R.; Lanois, A.; Latreille, P.;

Leimgruber, N. K.; Lipke, C. M.; Liu, R.; Lu, X.; Martens, E. C.; Marri, P. R.; Médigue, C.; Menard, M. L.; Miller, N. M.; Morales-Soto, N.; Norton, S.; Ogier, J. C.; Orchard, S. S.; Park, D.; Park, Y.; Qurollo, B. A.; Sugar, D. R.; Richards, G. R.; Rouy, Z.; Slominski, B.; Slominski, K.; Snyder, H.; Tjaden, B. C.; van der Hoeven, R.; Welch, R. D.; Wheeler, C.; Xiang, B.; Barbazuk, B.; Gaudriault, S.; Goodner, B.; Slater, S. C.; Forst, S.; Goldman, B. S.; Goodrich-Blair, H. *PLoS One* **2011**, *6* (11).

(25) Mulley, G.; Beeton, M. L.; Wilkinson, P.; Vlisidou, I.; Ockendon-Powell, N.; Hapeshi, A.; Tobias, N. J.; Nollmann, F. I.; Bode, H. B.; Van Den Elsen, J.; Ffrench-Constant, R. H.; Waterfield, N. R. *PLoS One* **2015**, *10* (12), 1.

(26) Wilkinson, P.; Paszkiewicz, K.; Moorhouse, A.; Szubert, J. M.; Beatson, S.; Gerrard, J.; Waterfield, N. R.; Ffrench-Constant, R. H. *FEMS Microbiol. Lett.* **2010**, *309* (2), 136.

(27) Weissfeld, A. S.; Halliday, R. J.; Simmons, D. E.; Trevino, E. A.; Vance, P. H.; O'Hara, C. M.; Sowers, E. G.; Kern, R.; Koy, R. D.; Hodde, K.; Bing, M.; Lo, C.; Gerrard, J.; Vohra, R.; Harper, J. *J. Clin. Microbiol.* **2005**, *43* (8), 4152.

(28) Costa, S. C. P.; Girard, P. A.; Brehélin, M.; Zumbihl, R. *Infect. Immun.* **2009**, *77* (3), 1022.

(29) Brugirard-Ricaud, K.; Givaudan, A.; Parkhill, J.; Boemare, N.; Kunst, F.; Zumbihl, R.; Duchaud, E. *J. Bacteriol.* **2004**, *186* (13), 4376.

(30) Gerrard, J. G.; McNevin, S.; Alfredson, D.; Forgan-Smith, R.; Fraser, N. *Emerg. Infect. Dis.* **2003**, *9* (2), 251.

(31) Costa, S. C. P.; Chavez, C. V.; Jubelin, G.; Givaudan, A.; Escoubas, J. M.; Brehélin, M.; Zumbihl, R. *Microbes Infect.* **2010**, *12* (3), 182.

(32) Akhurst, R. J.; Boemare, N. E.; Janssen, P. H.; Peel, M. M.; Alfredson, D. A.; Beard, C. E. *Int. J. Syst. Evol. Microbiol.* **2004**, *54* (4), 1301.

(33) Zhou, Q. *Biomedicines* **2017**, *5* (4), 64.

(34) Horlacher, T.; Seeberger, P. H. *Chem. Soc. Rev.* **2008**, *37* (7), 1414.

(35) Heimburg-Molinaro, J.; Song, X.; Smith, D. F.; Cummings, R. D. *Curr. Protoc. Protein Sci.* **2011**, *SUPP.64*, 1.

(36) Lee, A. G. *Lipid-protein interactions in biological membranes: A structural perspective*; **2003**; Vol. 1612.

(37) Glatz, J. F. C. *Prostaglandins Leukot. Essent. Fat. Acids* **2015**, *93*, 45.

(38) Zhao, H.; Lappalainen, P. *Mol. Biol. Cell* **2012**, *23* (15), 2823.

(39) Alberts, B.; Johnson, A.; Lewis, J.; Raff, M.; Riberts, K.; Walter, P. In *Molecular Biology of the Cell*; Garland Science: New York, 2002; pp 1–7.

(40) Park, S.; Lee, M. R.; Shin, I. *Chem. Commun.* **2008**, No. 37, 4389.

(41) Rudd, P. M.; Elliott, T.; Cresswell, P.; Wilson, I. A.; Dwek, R. A. *Science* **2001**, *291* (5512), 2370.

(42) Willats, W. G. T.; Rasmussen, S. E.; Kristensen, T.; Mikkelsen, J. D.; Knox, J. P. *Proteomics* **2002**, *2* (12), 1666.

(43) Fukui, S.; Feizi, T.; Galustian, C.; Lawson, A. M.; Chai, W. *Nat. Biotechnol.* **2002**, *20* (10), 1011.

(44) Wang, D.; Liu, S.; Trummer, B. J.; Deng, C.; Wang, A. *Nat. Biotechnol.* **2002**, *20* (3), 275.

(45) Ambrosi, M.; Cameron, N. R.; Davis, B. *Org. Biomol. Chem.* **2005**, *3* (9), 1593.

(46) Lee, Y. C.; Lee, R. T. *Acc. Chem. Res.* **1995**, *28* (8), 321.

(47) Beshr, G.; Sikandar, A.; Jemiller, E. M.; Klymiuk, N.; Hauck, D.; Wagner, S.; Wolf, E.; Koehnke, J.; Titz, A. *J. Biol. Chem.* **2017**, *292* (48), 19935.

(48) Lenman, A.; Liaci, A. M.; Liu, Y.; Frängsmyr, L.; Frank, M.; Blaum, B. S.; Chai, W.; Podgorski, I. I.; Harrach, B.; Benkő, M.; Feizi, T.; Stehle, T.; Arnberg, N. *Proc. Natl. Acad. Sci.* **2018**, *115* (18), 201716900.

(49) Bejsovec, A.; Anderson, P. *Genes Dev.* **1988**, *2*, 1307.

(50) Anderson, P.; Brenner, S. *Proc. Natl. Acad. Sci. U. S. A.* **1984**, *81* (14), 4470.

(51) Higgs, H. N.; Peterson, K. J. *Mol. Biol. Cell* **2004**, *15*, 2782.

(52) Kumar, A.; Sýkorová, P.; Demo, G.; Dobeš, P.; Hyršl, P.; Wimmerová, M. *J. Biol. Chem.* **2016**, *291* (48), 25032.

(53) Haiss, W.; Thanh, N. T. K.; Aveyard, J.; Fernig, D. G. *Anal. Chem.* **2007**, *79* (11), 4215.

(54) Walhout, A. *Biochemistry and molecular biology.* [ONLINE] Available at: http://www.wormbook.org/chapters/www_biochemmolbio/biochemmolbio.html. [Accessed 13 September 2018].

5.Conclusions

The development of materials to interact with or capture proteins remains a challenge, with current synthetic methods often limited by kinetics, the need for cytotoxic reagents and low selectivity/specificity (as described in Chapter 1). Macromolecular materials (polymers and nanoparticles) are proposed as excellent biomolecule mimics, but also as excellent scaffolds for bioconjugation to probe function.

In this work, a glycopolymer library with controlled chain length, carbohydrate density, side chain length and functionality was synthesised to target a pathogenic lectins (CTxB). In chapter 2, these glycopolymers were synthesized using RAFT polymerization and “click”-like post-polymerization double modification. These polymers were assayed for CTxB binding *via* both a competitive assay (against the native ligand, GM-1) and with bio-layer interferometry. Glycopolymers with a hydrophilic glucosamine secondary modification and low carbohydrate density showed greater specificity and binding activity towards CTx over another galactose specific lectin (RCA_{120}). These results suggest that the implementation of greater complexity proximal to the primary glycan binder can further enhance their anti-adhesive activity *via* improved selectivity.

In chapter 3, the impact of multivalent presentation on the ice-binding protein AFP type III was investigated by immobilisation onto a ~4 nm AuNP scaffolds. Two bioorthogonal linker types were used, with the large, covalent SNAP fusion tag/BG-AuNP linkage found to retain all AFP activity in several assays, in comparison to His-tag (non-covalent). This showed that conjugating proteins on NP surfaces is a useful tool to evaluate activity, even though the effective molar concentration was lower. Ice binding assays suggested the AFPs could span multiple faces, unlike monovalent AFP. Poly(vinyl alcohol) was also immobilised onto AuNP scaffolds, *via* the polymer’s thiol end functionality, to form fully-synthetic spherical antifreeze protein mimics. The branched spherical structure was found to have no significant impact on ice recrystallisation inhibition of longer (DP ~150) PVA relative to linear PVA of the same concentration. These experiments showed the potential of using these AuNP scaffolds to form branched-type materials with enhanced antifreeze activity, and that both synthetic and natural antifreezes have similar design rules.

In Chapter 4, ICP-OES was utilised to assess cell binding of recombinant His-tagged proteins of *Photorhabdus* virulence cassette tail fibre immobilised on AuNPs. NTA-pHEA polymers synthesized by RAFT polymerization, followed by post-polymerisation modification of the end group, were first conjugated to AuNPs, and Ni^{2+} added to form surface Ni-NTA groups. PVC*lumt*_Pvc13 was then conjugated to ~40 nm AuNPs using this His-Ni-NTA-pHEA linkage. Cell based assays suggest cytotoxicity at high concentrations, but interestingly no significant binding nor uptake. Glycan and lipid arrays were also used to assess PVC*lumt*_Pvc13 binding, and some glycan candidate hits were identified for the first time. Pull-down assays were then conducted in a variety of whole cell lysates using recombinant His-tagged tail fibre proteins of three *Photorhabdus* virulence cassettes (PVC*lumt*_Pvc13, PVC*pnf*_Pvc13 and PVC*unit4*_Pvc13) attached to Ni-NTA-coated magnetic beads. These pull-down experiments identified proteins of interest (such as immunogenic proteins and actin-binding proteins). The identification of actin-binding proteins or glycans/proteins present on immune cells may suggest a potential route to pathogenicity for these PVC constructs, but also guide their exploitation as a future biosynthetic drug delivery vector.

Awards, Grants and conference proceedings

Oral Presentations

- **August 2018:** 256th National Meeting & Exposition of the American Chemical Society, Boston, USA.
- **July 2018:** Macro Group UK Young Researcher's meeting, Dublin, Ireland.
- **May 2018:** Warwick Chemistry Postgraduate Symposium, University of Warwick, Coventry, UK.
- **June 2015:** MOAC DTC Annual Conference, Wilderhope Manor

Poster Presentations

- **June 2017:** Warwick Chemistry Postgraduate Symposium, University of Warwick, Coventry, UK.
- **May 2017:** APME 2017, University of Ghent, Belgium.
- **October 2016:** RSC Carb 50th Meeting, University of Warwick.
- **July 2016:** Warwick Polymers 2016, University of Warwick. *"Glycopolymer Anti-infectives against Cholera"*
- **June 2015:** MOAC DTC Annual Conference, Wilderhope Manor.
- **August 2013:** Poster Presentation; 11th European Association of Clinical Pharmacology and Therapeutics Congress, Geneva, Switzerland. *"Complex regulation of Alpha-adrenoreceptor-mediated vasoconstriction in human internal thoracic arteries"*
- **April 2013:** British Microcirculation Society Early Career Investigators Symposium, University of Warwick. *"Pleiotropic regulation of alpha-*

adrenoceptormediated vasoconstriction in human internal mammary arteries".

- **April 2012:** 4th BPS Focused Meeting on Cell Signalling, University of Leicester. *"Stereoselective and biphasic S-BEL sensitive pathways regulate receptor-mediated but not high-K induced tone in human conduit arteries".*

Grants and Bursaries

- Biochemical Society General Travel Grant (£400) to support attendance at the 256th National Meeting & Exposition of the American Chemical Society, Boston, USA.
- RSC Chemical Biology Interface Division Travel Grant (£600) to support attendance at the 256th National Meeting & Exposition of the American Chemical Society, Boston, USA.
- European Association for Clinical Pharmacology and Therapeutics (EACPT) and British Pharmacological Society (BPS) travel grants for 11th EACPT Congress 2013, Geneva, Switzerland.
- BPS travel grant for 4th BPS Focused Meeting on Cell Signalling, Leicester 2012.
- Undergraduate Research Scholarships (research grants awarded July-September 2011 and 2012), Department of Chemistry, University of Warwick and the Clinical Sciences Research Laboratories, University Hospitals Coventry and Warwickshire (UHCW). Project title: "*Pleiotropic regulation of alpha-adrenoceptor-mediated vasoconstriction in human arteries.*"

Curriculum vitae

PERSONAL DETAILS

Name: Laura Wilkins

Date of Birth: 05/09/1991

Email: laurawilkins28@gmail.com

Telephone: +447504195714

Address: Department of Chemistry, University of Warwick, Gibbet hill road, Coventry, CV4 7AL, UK

Website: www.warwick.ac.uk/gibsongroup/members/laura_wilkins

EDUCATION

St Hugh's College, University of Oxford

- Currently undertaking accelerated Graduate Entry Medicine (4-year) course. Expected 2018-2022.

University of Warwick

- PhD student (3rd year) joint with Chemistry Department and Medical School, 2015-18.
- Molecular Analytical Science (MSc) degree, passed with distinction, 2014-15.
- Chemical Biology (MChem) degree, upper second class honours, 2010-14

AWARDS, GRANTS AND AFFILIATIONS

- Biochemical Society General Travel Grant to support attendance at the 256th National Meeting & Exposition of the American Chemical Society, Boston, USA.
- RSC Chemical Biology Interface Division Travel Grant to support attendance at the 256th National Meeting & Exposition of the American Chemical Society, Boston, USA.

- European Association for Clinical Pharmacology and Therapeutics (EACPT) and British Pharmacological Society (BPS) travel grants for 11th EACPT Congress 2013, Geneva, Switzerland.
- BPS travel grant for 4th BPS Focused Meeting on Cell Signalling, Leicester 2012.
- Associate member of the Royal Society of Chemistry (AMRSC)
- Postgraduate student member of both the Biochemical Society and British Pharmacological Society.
- Student member of British Medical Association.

PUBLICATION RECORD

- **Wilkins, LE.,** Phillips, DJ, Deller, RC, Davies, G-L, Gibson, MI., *Carbohydrate Research* (Special issue on GlycoNanomaterials), 2015, **405**, 47-54.
- **Richards, S-J.,** Isufi, K., Wilkins, LE., Lipecki, J., Fullam, L.*, Gibson, MI.*, *Biomacromolecules*, 2017, **19** (1), 256-264.
- **Stubbs, C.,* Wilkins, LE.,*** Fayter, AER., Walker, M., Gibson, MI., *Langmuir*, 2018, *accepted and published online*.
- **Wilkins, LE.,** Badhi, N., du Prez, F., Gibson, MI., 'Double-modified glycopolymers from thio-lactones to module lectin selectivity and affinity', *ACS Macroletters,* 2018, **7** (12), 1498-1502.
- **Wilkins, LE.,** Hasan, M., Fayter, AER., Biggs, C., Walker, M., Gibson, MI., ' Site-specific conjugation of antifreeze proteins onto polymer-stabilized nanoparticles ', *Polym. Chem.,* 2019, *accepted and published online*.
- **Lee, GH.,** Wayte, S., Stubbs, C., Wilkins, LE., Hutchinson, CE., Gibson, MI., Davies, G-L., *Chem. Comms.*, *submitted.*

CONFERENCE ATTENDANCE

Attendance at 17 conferences and workshops covering topics from synthesis to applied medical materials. Over the course of my PhD I have delivered 3 oral and 4 poster presentations, including:

- 256th National Meeting & Exposition of the American Chemical Society, Boston, USA: Oral presentation.

- APME 2017, University of Ghent, Belgium: Poster presentation

REFEREES

Prof. Matthew I. Gibson (PhD Supervisor)
Professor between Chemistry and Warwick Medical School
Department of Chemistry
University of Warwick
Coventry
CV4 7AL
m.i.gibson@warwick.ac.uk

Dr. Nicholas Waterfield (PhD Supervisor)
Reader
WMS – Microbiology and Infection
University of Warwick
Coventry
CV4 7AL
n.r.waterfield@warwick.ac.uk

Prof. Timothy D. H. Bugg (MChem course director)
Professor of Biological Chemistry
Department of Chemistry
University of Warwick
Coventry
CV4 7AL
t.d.h.bugg@warwick.ac.uk

Dr. Ann M. Dixon (MSc project supervisor)
Associate Professor of Biological Chemistry
Department of Chemistry
University of Warwick
Coventry
CV4 7AL
a.m.dixon@warwick.ac.uk

Contributions to published work

The following details personal contributions to published work subjected to peer review.

Wilkins, LE., Phillips, DJ, Deller, RC, Davies, G-L, Gibson, MI., 'Synthesis and Characterisation of Glucose-Functional Glycopolymers and Gold Nanoparticles: Study of their Potential Interactions with Ovine Red Blood Cells', *Carbohydrate Research* (Special issue on GlycoNanomaterials), 2015, **405**, 47-54.

> *Performed all experimental work including synthesis and application of materials to red blood cells, and data analysis on all data generated.*

Richards, S-J., Isufi, K., Wilkins, LE., Lipecki, J., Fullam, L.*, Gibson, MI.*, (DOI: 10.1021/acs.biomac.7b01561) 'Multivalent Antimicrobial Polymer Nanoparticles Target Mycobacteria and Gram-Negative Bacteria by Distinct Mechanism', *Biomacromolecules*, 2017, **19** (1), 256-264.

> *Performed transmission electron microscopy and size analysis of generated images for the purpose of nanoparticle characterisation.*

Stubbs, C.,* Wilkins, LE.,* Fayter, AER., Walker, M., Gibson, MI., 'Multivalent presentation of ice recrystallization inhibiting polymers on nanoparticles retains activity', *Langmuir*, 2018, *accepted and published online*.

> *Performed synthesis and characterisation of PVA@Au*$_4$ *materials and related data analysis for characterisation Also performed a significant amount of the writing process.*
>
> **These authors contributed equally.*

Wilkins, LE., Badhi, N., du Prez, F., Gibson, MI., 'Double-modified glycopolymers from thio-lactones to module lectin selectivity and affinity', *ACS Macroletters,* 2018, **7** (12), 1498-1502.

> *Performed all experimental work including synthesis, characterisation and application of glycosylated materials to CTx and RCA lectins. Performed data*

analysis on all data generated and a significant part of the article writing process.

Wilkins, LE., Hasan, M., Fayter, AER., Biggs, C., Walker, M., Gibson, MI., 'Multivalent display of antifreeze proteins on nanoparticles using site specific conjugation', *Polym. Chem.* 2019, *accepted and published online*.

Performed synthesis and characterisation of AFP@Au_4 materials. Also performed data analysis on all data except XPS, sucrose and SPLAT assays, and a significant part of the writing process.

Lee, GH., Wayte, S., Stubbs, C., Wilkins, LE., Hutchinson, CE., Gibson, MI., Davies, G-L., 'Hybrid organic-inorganic nanocomposites: thermally triggerable MRI contract agents for non-invasive diagnosis', *Chem. Comms.*, *submitted*.

Performed transmission electron microscopy for the purpose of nanoparticle characterisation.